

Fermi-Bose mixtures —
From mean-field interactions to ultracold chemistry

Dissertation
zur Erlangung des Doktorgrades
des Departments Physik
der Universität Hamburg

vorgelegt von
Christian Ospelkaus

aus Wuppertal

Hamburg
2006

Gutachterin/Gutachter der Dissertation: Prof. Dr. Klaus Sengstock
Prof. Dr. Werner Neuhauser
Prof. Dr. Randall G. Hulet, USA

Gutachter der Disputation: Prof. Dr. Klaus Sengstock
Prof. Dr. Günter Huber

Datum der Disputation: 21.12.2006

Vorsitzender des Prüfungsausschusses: Dr. Klaus Petermann

Vorsitzender des Promotionsausschusses: Prof. Dr. Günter Huber

Dekan der Fakultät für Mathematik,
Informatik und Naturwissenschaften: Prof. Dr. Arno Frühwald

Abstract

Starting with the observation of Bose-Einstein condensation in single-component bosonic gases and Fermi degeneracy in spin-polarized Fermi gases, the (still relatively young) field of ultracold quantum gases is rapidly expanding to studies of mixed systems. Ultimately, mixtures of different atomic species with different statistics, different trapping properties, interactions and masses open up the widest spectrum of possibilities for quantum simulation, ultracold chemistry, exotic pairing phases, disorder-related many-body physics and long-range interacting systems.

This thesis presents experiments in a system of interacting quantum degenerate fermionic ^{40}K and bosonic ^{87}Rb atoms. An experimental setup for producing Fermi-Bose mixtures which has been set up together with S. Ospelkaus is described in detail. The observation of both bosonic and fermionic degeneracy is demonstrated; in the case of fermionic atoms, showing the quantum behavior requires thorough analysis, which is rewarded by the observation of an ideal macroscopic Fermi sea.

This thesis presents mixtures with the so far largest particle numbers for the ^{40}K - ^{87}Rb system and discusses measurements with high densities where strong mean-field contracting interaction effects affect the behavior of the mixture. Clear signatures of the mean field collapse of large mixtures are observed, the dynamics of the collapsing sample is studied and important consequences for the interaction parameters are discussed.

Tuning of interactions in a harmonically trapped heteronuclear mixture by means of Feshbach resonances is demonstrated for the first time, allowing all phases of the harmonically trapped mixture to be observed: stable heteronuclear interaction and repulsion as well as phase separation and a controlled Feshbach-induced collapse.

From the very beginning, the setup described here has been designed for experiments in 3-dimensional optical lattices. In recent years, an impressive series on experiments with homonuclear systems has shown that such perfect optical crystals can be used as quantum simulators for condensed-matter phenomena. Within this thesis, a heteronuclear system, in particular a Fermi-Bose mixture, has been loaded into a 3D optical lattice for the first time, and only a very small fraction of fermionic “impurities” has been found to significantly reduce the coherence in the bosonic cloud. The observations are currently the subject of intense theoretical analysis, and there are important connections to thermodynamics, advanced mean field models and disorder physics.

As a long-awaited step for heteronuclear systems, formation of ultracold Feshbach molecules from two different atomic elements is demonstrated. This ultracold chemical reaction takes place at temperatures in the nK regime at a heteronuclear Feshbach resonance. A detailed understanding of the observed energy spectrum and the molecular association process has been developed in collaboration with F. Deuretzbacher, K. Plassmeier and D. Pfannkuche in terms of a universal model. Long-lived molecules are produced within single wells of the 3D-optical lattice in a well-defined rovibrational state, which makes them an ideal basis for coherent transfer into both the external and internal ground state using readily available femtosecond technology. Such all ground state polar molecules open up the way towards ultracold long-range dipolar interacting systems. They may be used as building blocks of novel quantum gases, scalable quantum computation schemes and for fundamental measurements of P and T violating effects in atoms.

Parts of this thesis have been published in the following papers:

- C. Ospelkaus *et al.*, Phys. Rev. Lett. **97**, 120402 (2006) [1].
- S. Ospelkaus *et al.*, Phys. Rev. Lett. **97**, 120403 (2006) [2].
- S. Ospelkaus *et al.*, Phys. Rev. Lett. **96**, 180403 (2006) [3].
- C. Ospelkaus *et al.*, Phys. Rev. Lett. **96**, 020401 (2006) [4].
- S. Ospelkaus, *et al.*, Journal of Modern Optics, advanced online publication (2006) [5].

Zusammenfassung

Seit der Beobachtung von Bose-Einstein-Kondensation in einkomponentigen bosonischen Gasen und der Realisierung von spin-polarisierten idealen Fermigasen entwickelt sich das (noch sehr junge) Feld der ultrakalten Quantengase rasch in Richtung mehrkomponentiger Gase. Das letztendlich weiteste Spektrum an Möglichkeiten für quantenmechanische Simulation, ultrakalte Chemie, exotische Paarbildungsmechanismen, Unordnungsphänomene und langreichweitige Wechselwirkung wird eröffnet durch Mischungen unterschiedlicher atomarer Elemente mit unterschiedlicher Statistik, unterschiedlichen Wechselwirkungen und Massen.

Diese Dissertation stellt Experimente in einem System wechselwirkender, entarteter Mischungen aus fermionischen ^{40}K und bosonischen ^{87}Rb Quantengasen vor. Ein zusammen mit S. Ospelkaus aufgebautes Experiment zur Erzeugung von Fermi-Bose Mischungen wird detailliert vorgestellt. Bose-Einstein-Kondensation von ^{87}Rb und die Erzeugung eines quantenentarteten Fermigases aus ^{40}K wird demonstriert.

Im Rahmen dieser Arbeit wurden Mischungen aus ^{40}K und ^{87}Rb mit den bislang größten Teilchenzahlen realisiert. Die entsprechend hohen Dichten führen zur Beobachtung starker kontrahierender Effekte der attraktiven Fermi-Bose-Wechselwirkung, die das Verhalten der Mischung fundamental beeinflussen. Eindeutige Signaturen eines Kollapses für große Mischungen werden aufgezeigt, und das dynamische Verhalten der kollabierenden Mischung wird untersucht. Die beobachteten Instabilitäten haben wichtige Konsequenzen für die Bestimmung der Wechselwirkungsparameter.

Erstmals wird die Durchstimmung heteronuklearer Wechselwirkung mittels Feshbach-Resonanzen demonstriert. Dies führt zur Beobachtung aller Phasen harmonisch gespeicherter Mischungen: stabile, attraktiv oder repulsiv wechselwirkende Mischungen sowie Phasenseparation und ein kontrollierter Feshbach-induzierter Kollaps.

Das hier beschriebene Experiment wurde von Beginn an für Messungen in dreidimensionalen optischen Gittern ausgelegt. Für homonukleare Systeme hat weltweit eine beeindruckende Reihe von Ergebnissen gezeigt, dass solche perfekten optischen Kristallgitter als Quantensimulatoren für Festkörperphänomene dienen können. In dieser Dissertation wurde erstmalig eine Fermi-Bose Mischung in ein dreidimensionales optisches Gitter geladen. Dabei wird beobachtet, dass schon eine kleine Beimengung von fermionischen Atomen die Kohärenz der bosonischen Wolke in beträchtlichem Maße beeinflusst. Diese Beobachtung ist momentan Gegenstand intensiver theoretischer Untersuchungen; es werden Beziehungen zu Thermodynamik im Gitter, Modellen in "mean field" Näherung und unordnungsgetriebenen Lokalisierungsphänomenen in Festkörpern diskutiert.

Als wichtiger Schritt für heteronukleare Systeme wird die Erzeugung ultrakalter Feshbach-Moleküle vorgestellt. Diese ultrakalte chemische Reaktion findet an einer heteronuklearen Feshbachresonanz statt. Das beobachtete Spektrum der Bindungsenergien und die Effizienz der Molekülassoziation werden im Rahmen eines universellen Modelles (in Zusammenarbeit mit F. Deuretzbacher, K. Plassmeier und D. Pfannkuche) untersucht. Die langlebigen Moleküle werden an einzelnen Gitterplätzen eines dreidimensionalen optischen Gitters in einem wohldefinierten Rovibrationszustand erzeugt, was sie zu idealen Kandidaten für einen weiteren Transfer in den absoluten internen und externen Grundzustand mittels Femtosekunden-Frequenzkammtechnologie macht. Solche ultrakalten polaren Moleküle eignen sich als Bausteine neuartiger skalierbarer Quantencomputer, für Quantengase mit langreichweitiger Wechselwirkung und für fundamentale Messungen zu diskreten Symmetrieverletzungen in Atomen.

Teile dieser Dissertation sind in den folgenden Arbeiten veröffentlicht worden:

- C. Ospelkaus *et al.*, Phys. Rev. Lett. **97**, 120402 (2006) [1].
- S. Ospelkaus *et al.*, Phys. Rev. Lett. **97**, 120403 (2006) [2].
- S. Ospelkaus *et al.*, Phys. Rev. Lett. **96**, 180403 (2006) [3].
- C. Ospelkaus *et al.*, Phys. Rev. Lett. **96**, 020401 (2006) [4].
- S. Ospelkaus, *et al.*, Journal of Modern Optics, advanced online publication (2006) [5].

Contents

1	Introduction	1
2	Fermions and bosons	5
2.1	Statistical considerations	5
2.1.1	Fermi energy	7
2.1.2	Bose-Einstein condensation	8
2.2	Density distributions	9
2.2.1	Maxwell-Boltzmann gas	9
2.2.2	Fermi gas at zero temperature	10
2.2.3	Bose-Einstein condensate	10
2.3	Free expansion	11
2.3.1	Non-condensed samples	11
2.3.2	Bose-Einstein condensate	12
2.4	Interacting mixtures	13
2.4.1	Noninteracting limit	15
2.4.2	Attractive interactions	16
2.4.3	Mean field collapse	17
2.4.4	Repulsive interactions	18
2.4.5	Phase separation	19
2.4.6	Full phase diagram	19
3	Experimental setup	23
3.1	Vacuum system	25
3.2	Atomic sources	26
3.3	Laser systems	27
3.3.1	Rubidium laser system	27
3.3.2	Potassium laser system	28
3.3.3	Putting it all together	33
3.4	Two species 2D/3D-magnetooptical trap	33
3.5	Magnetic trapping	36
3.5.1	Magnetic trap concept	38
3.5.2	Trap simulation	39
3.5.3	Trap characterization	39
3.5.4	Magnetic trap in the experiment	40
3.5.5	Trap control	42
3.6	Other coils	44

3.7	Dealing with the gravitational sag	44
3.8	A magic crossed dipole trap	45
3.9	Evaporation and state preparation	46
3.9.1	Versatile frequency control	47
3.9.2	Hyperfine manipulation	49
3.10	Optical lattice setup	50
3.10.1	Lattice laser system	51
3.10.2	Frequency stabilization	52
3.10.3	Intensity stabilization	56
3.10.4	Lattice setup	57
3.11	Imaging	58
3.11.1	Optical setup	60
3.11.2	Detection techniques	60
3.11.3	State selective imaging	64
3.12	Timing	66
3.13	CAD rendering	68
4	Fermions, Bosons and Mixtures	69
4.1	Observation of BEC	70
4.2	Sympathetic cooling	72
4.3	A “degenerate” Fermi gas	74
4.4	Three-body losses	78
4.5	Stages of evaporative cooling	81
4.6	Observation of a mean field induced collapse	84
4.7	Stability analysis of Fermi-Bose mixtures	86
5	Tuning interactions in degenerate mixtures	91
5.1	Experimental procedure	92
5.2	Identifying the resonances	93
5.3	Attractive interactions	94
5.4	An induced mean field collapse	96
5.5	Repulsive interactions and phase separation	96
6	Fermions and bosons in 3D optical lattices	101
6.1	Experimental procedure	104
6.2	Loss of coherence for deep lattices	105
6.3	Quantitative analysis	105
6.4	Understanding the role of the fermions	108
7	Heteronuclear molecules in a 3D optical lattice	111
7.1	The quest for ultracold polar molecules	111
7.1.1	Polar molecules and anisotropic interactions	111
7.1.2	Polar molecules and quantum computation	112
7.1.3	Polar molecules and the EDM	112
7.1.4	Possible routes to molecular degeneracy	112
7.2	Ultracold heteronuclear Feshbach molecules	116
7.2.1	Rf association of molecules	116

7.2.2	Experimental protocol	120
7.2.3	Rf spectrum	121
7.2.4	Energy spectrum	122
7.2.5	Modelling strong heteronuclear interactions in the lattice	124
7.2.6	Transfer efficiency	129
7.2.7	Lifetime of the molecular sample	129
7.2.8	Experimental implementation of rf spectroscopy	132
8	Conclusions and Outlook	139
A	High field detection and frequency offset lock	143
B	Atomic parameters	147
C	Transport in lattices and phase stabilization	149
D	Numerical algorithms and software	155

Chapter 1

Introduction

In 1924, the Indian physicist Satyendra Nath Bose started a revolution in statistical mechanics working on the question of distinguishability of particles. Bose was at the time working on a derivation of Planck's formula for blackbody radiation by treating the photons in the *Hohlraum* as a gas of photons [6]. Bose's approach to the problem boiled down to asking the question of *how many particles / photons occupy a certain energy state of the system* instead of *which particle occupies which energy level*. The latter gives rise to the classical Maxwell-Boltzmann gas of distinguishable particles, whereas the former leads to either Bose-Einstein or Fermi-Dirac statistics, depending on the choice of statistical weight factor for microstates of the ensemble.

In Bose-Einstein statistics, each single particle state can be occupied by an arbitrary number of particles. The original work of Bose was extended to massive particles by Albert Einstein [7, 8] who immediately recognized the importance of Bose's work. Particles obeying Bose-Einstein statistics are called *bosons*. Einstein discovered that an ensemble of bosons would undergo a phenomenon later called *Bose-Einstein condensation* characterized by a massive occupation of the single particle ground state of the system if the particle number is increased beyond the maximum capacity of the excited states.

Following the formulation of Pauli's exclusion principle in 1925 [9], Fermi introduced Fermi-Dirac statistics [10] for a class of particles nowadays known as *fermions*. The statistical weight factor for fermions allows only microscopic states where no more than one identical fermion occupies a single energy state of the system. Fermi-Dirac statistics and the Pauli exclusion principle were found to be essential for the electron theory of metals, the stability of atoms and white dwarf stars.

It took until 1939 before the connection between the spin of a particle and its quantum statistics was fully discovered: Particles with half-integer spin such as the electron obey Fermi-Dirac statistics and particles with integer spin such as the photon and the phonon obey Bose-Einstein statistics. Composite particles also fall into one of these categories, depending on the total spin. As such, the basic building blocks of an atom (electron, neutron, proton) are all fermions. Nevertheless, an atom as a whole can be either a boson or a fermion, depending on the total number of electrons and nucleons.

Although introduced by Einstein in 1925, Bose-Einstein condensation remained a theoretical concept for some time. It was then used by London in 1938 [11, 12] to discuss the superfluidity of liquid ^4He . ^4He is generally not considered a prototype weakly interacting Bose-Einstein condensed system due to the importance of interactions in this peculiar liquid.

Bose-Einstein condensation was also discussed in the context of superconductivity of Cooper paired electrons in metals. Realistic perspectives of observing BEC in dilute gaseous systems appeared with work on spin-polarized hydrogen [13, 14] which was expected to remain in a gaseous state even below the temperature of Bose-Einstein condensation. Techniques developed for atomic hydrogen, namely magnetic trapping and evaporative cooling, were also applied to alkali atoms. Connected with efficient laser cooling, this has led to the observation of BEC of ^{87}Rb and ^{23}Na in 1995 [15, 16]. Work on ^7Li [17] explored condensates with attractive interaction. The field of atomic Bose-Einstein condensates has since exploded, and today many groups worldwide study the properties of these BECs.

Parallel to the work on bosonic atoms, there was growing interest in fermionic gaseous ensembles motivated by the perspective of observing cooper pairing between atoms in such a system. Compared to bosonic systems, fermion experiments were subject to a considerable delay. In part, this is due to the technical difficulty in applying techniques of evaporative cooling to fermionic systems, and partly due to the popular misconception that fermions “don’t interact”. There is some truth to this above statement: *s* wave scattering between identical fermions is forbidden due to the Pauli exclusion principle, and at the low temperatures that we are talking about, higher order scattering processes are usually energetically forbidden. The final step which is so successful in producing atomic BECs, evaporative cooling, relies on redistribution of energy in the ensemble through elastic collisions, and it becomes tremendously inefficient when applied to a spin-polarized Fermi gas. Nevertheless, fermions in different spin states (distinguishable fermions) do interact, and the observation of a quantum Fermi gas of atoms [18] (often also called a “degenerate” Fermi gas) as a result of evaporative cooling of an interacting spin mixture triggered an exciting development. The identification of Feshbach resonances [19, 20, 21], the advent of rf spectroscopy [22, 23], formation of long-lived bosonic molecules from an interacting Fermi gas [24, 25, 26, 27, 28], BEC of these molecules [29, 30, 31] and the exploration of the full BCS-BEC crossover [32, 33, 34, 35, 36], the observation of the pairing gap [37], and studies of imbalanced gases [38, 39] proved that fermions do interact, even strongly. Fermionic gases have been loaded into optical lattices [40, 41, 42, 43, 44, 45, 46] and used for atom interferometry [47]. When the experiment described in this thesis produced its first “degenerate” Fermi gas in August 2004, we were only the ninth institution worldwide to dispose of such a sample, while there were already about a hundred BEC experiments.

At that time, three of these experiments [18, 48, 28] used a spin mixture of atoms to circumvent Pauli blocking of collisions, six of the other experiments (including this one) have used a gas of bosons as a refrigerator to sympathetically cool the fermions [49, 50, 51, 52, 53, 40]. In most of these two-species setups, the bosonic component was completely removed during the evaporation process. To date, most experiments have either studied bosons or fermions or bosonic molecules created from fermions, and mostly studying *one* particular atomic isotope at a time. Heteronuclear systems such as degenerate mixtures of different bosonic atoms [54], fermionic and bosonic atoms or two different fermionic atoms significantly extend the class of phenomena which can be studied in quantum gases. This is due to the different interactions between constituents which can be realized in these mixed systems. At the same time, the differences in masses and trap frequencies raises interesting questions of universality and possible pairing phases. As can be seen from the introductory discussion of chapter 6, mixtures possess interesting prospects for simulating disorder related localization phenomena. Molecules formed from heteronuclear samples as demonstrated in chapter 7 are candidates for measurements with fundamental relevance in physics. They may allow studies of P- and T- violating effects, result in novel quantum gases with large long-range anisotropic

interactions and may be used as building blocks for future molecular quantum computers [55].

As a special case of heteronuclear mixtures, the study of Fermi-Bose mixtures as discussed in this thesis has been motivated by a particularly compelling analogy with traditional condensed matter systems, namely the prospect of observing boson-mediated Cooper pairing in this system [56, 57]. I have already mentioned that with the observation of the BCS-BEC crossover for fermionic atoms, an atomic approach to fermionic superfluidity has been realized. In that approach, the attractive interaction required for Cooper pairing is provided by direct scattering between fermions in different spin states. In a mixture of fermionic and bosonic atoms, this attractive interaction can be realized by using bosonic atoms as the attractive “glue” provoking the fermion pairing. This would provide a strong analogy to solid state systems, where the attractive interaction between electrons is provided by phonons. Pushing the analogy even further, by performing the experiment in an optical lattice, the atomic fermions would take over the role of the electrons, the solid would be replaced by an artificial crystal made out of light, not matter, and the phonons (quasiparticles) would be replaced by bosonic atoms. While this analogy may not be true in every sense, it demonstrates the fascinating prospects of Fermi-Bose mixtures for quantum simulation.

Mixtures of fermionic and bosonic atoms have been studied in ^6Li - ^7Li [49, 50], ^6Li - ^{23}Na [52], and ^{40}K - ^{87}Rb [51, 53]. The focus of the first experiments has been on understanding the effects of mean-field interactions in this rich system [51, 58, 59] and to constrain the heteronuclear interaction parameter [60, 53, 61]. At the point where this experiment reached simultaneous degeneracy in August 2004, heteronuclear Feshbach resonances allowing a much wider parameter space to be explored had only just been identified through inelastic losses [62, 63], and a significant discrepancy in observed stability limits of ^{40}K - ^{87}Rb mixtures had not yet been understood. Measurements presented in this thesis have demonstrated that, in contrast to what was previously believed, large ^{40}K - ^{87}Rb mixtures can be created (chapter 4). This thesis demonstrates that elastic scattering in heteronuclear mixtures can be tuned by means of Feshbach resonances (chapter 5; see also ref. [2, 64]). By loading the mixture into a 3D optical lattice (chapter 6; see also [3, 65]), we have accessed a regime of fascinating many-body effects in the experiment, and, by combining all of the acquired techniques, ultracold heteronuclear molecule formation has been achieved (chapter 7 and ref. [1]). This thesis documents these experimental achievements and is organized as follows:

- Chapter 2 describes basic properties of degenerate Fermi and Bose gases, introduces an interaction between the two and discusses the various limiting cases of an interacting mixture trapped in a harmonic trap in terms of numerical simulations and simple physical arguments.
- Chapter 3 describes the experimental setup for studying degenerate Fermi-Bose mixtures in 3D optical lattices which has been setup together with Silke Ospelkaus. Short research publications, often limited in page number, do not give details of experimental techniques due to space constraints. This chapter discusses relevant experimental techniques for cooling and trapping in detail. Many of the techniques used in the experiment were not previously available in our institution and required significant development effort.

The frequency and intensity stabilization of our VersaDisk lattice laser, the experiment control system using an ADWIN digital signal processor, the precise rf and microwave control system, advanced imaging techniques and a lot of software, electronics and optics development is just a small part of this technological “side effect” of experimental

physics. All of these techniques have been relevant to the measurements presented in this thesis and are discussed in detail here.

- In the following chapter, I describe how Bose-Einstein condensates and Fermi gases with the so far highest particle numbers for ^{40}K - ^{87}Rb experiments are produced in this apparatus. Based on chapter 2, chapter 4 discusses experiments performed on the harmonically trapped mixture in this limit of large particle numbers. I discuss what we can learn about the interaction of ^{40}K - ^{87}Rb mixtures in this regime from the experiment. The relatively strong attractive interaction in ^{40}K - ^{87}Rb mixtures gives rise to a collapse instability beyond certain critical conditions. I present effects of the heteronuclear interaction before the onset of the collapse and analyze in detail how the collapse affects time of flight images and the time evolution of the mixture. I also discuss the stability limit resulting from these experiments, its important consequences for interaction parameters in this system and a study of 3-body losses which resulted in a loss coefficient an order of magnitude lower than previously reported. The result have been partly published in C. Ospelkaus *et al.*, Phys. Rev. Lett. **96**, 040201 (2006) [4] and are extensively discussed here.
- In chapter 5, I discuss effects of arbitrary interaction between ^{40}K and ^{87}Rb , which can be realized by exploring heteronuclear Feshbach resonances. The results document the first realization of tunable heteronuclear interactions as a prerequisite for heteronuclear molecules (chapter 7). This chapter closely follows S. Ospelkaus *et al.*, Phys. Rev. Lett. **97**, 120403 (2006) [2]; a very broad and detailed analysis is contained in Silke's PhD thesis [66].
- Chapter 6 describes the first realization of Fermi-Bose mixtures confined in three-dimensional optical lattices and closely follows S. Ospelkaus *et al.*, Phys. Rev. Lett. **96**, 180403 (2006) [3]. Again, an in-depth discussion can be found in [66].
- Finally, chapter 7 reports on the first creation of ultracold long-lived heteronuclear molecules in a 3D optical lattice. This is an important step towards ultracold ground-state polar molecules for novel quantum computation schemes, studies of dipolar quantum gases and fundamental measurements. The chapter contains a detailed description of the experimental technique of rf association for producing molecules developed in this thesis. It contains a measurement of the molecular binding energy across the Feshbach resonance and develops a theoretical approach to the binding energy and transfer efficiency by treating arbitrary heteronuclear interactions in the lattice through a pseudopotential approach (in collaboration with F. Deuretzbacher, K. Plassmeier and D. Pfannkuche). This chapter provides an extensive in-depth discussion of the results published in C. Ospelkaus *et al.*, Phys. Rev. Lett. **97**, 120402 (2006) [1] and an upcoming publication.

As mentioned above, this thesis contains a comprehensive discussion of the experimental techniques which have been used in this thesis, with particular emphasis on the reasons why we used and developed certain techniques, not only how they were implemented (chapter 3), and all of these techniques have been essential to the results presented in this thesis. Readers who want to start directly with main experimental results can begin with chapter 4; I have included backreferences to chapter 3 whenever talking about specific features of the apparatus.

Chapter 2

Fermions and bosons

In this introductory chapter, I discuss basic concepts for trapped Fermi-Bose mixtures. I start my discussion with a thermodynamic approach. This corresponds to the textbook treatment of fermionic and bosonic gases for the harmonically trapped case. The treatment is valid for noninteracting particles. This approximation is perfect for single-component ultracold fermionic gases where s wave interactions are completely absent due to the Pauli exclusion principle and higher partial wave scattering is energetically suppressed. In later chapters, I will show that such a perfect Fermi gas can be realized in the experiment and present results on the thermodynamic behavior of this textbook example of statistical physics (see chapter 4). The non-interacting approximation is also reasonable for thermal bosonic gases and provides us with a good estimate for the critical temperature for Bose-Einstein condensation. Even though the atomic Bose-Einstein condensates are weakly interacting and dilute, interactions do play a fundamental role for the condensed phase, and I review basic properties of these condensates as discussed in this thesis, such as their density distributions and the expansion behavior.

Based on the separate discussion of Bose and Fermi gases, I then switch to the description of interacting mixtures in a mean field picture of interactions between bosons and fermions. I calculate density profiles of trapped mixtures for the basic phases (stable attractively and repulsively interacting mixtures, phase separation and collapse). I show how the phase diagram of the mixture can be calculated. This discussion of phases of harmonically trapped mixtures is highly relevant both for understanding how mixtures are produced, what the limits of stability are and which signatures of interactions we can see in the experiment. In chapters 4 and 5, we will see that all of these phases can be observed in the experiment.

For corresponding literature, see [67, 68, 69, 70, 71, 72, 73, 74]. Here, I have attempted to derive results relevant for non-interacting and interacting Fermi-Bose mixtures as discussed in this thesis with the maximum degree of parallelism in treating both constituents.

2.1 Statistical considerations

This chapter begins with a discussion of the statistics of harmonically trapped ideal gases. Most of the formulas that are derived are directly relevant to the experiment, in particular to thermometry. The symmetrization or antisymmetrization postulate for bosons and fermions, respectively, leads to the mean occupation number of a single-particle energy eigenstate with

energy ε_n given by [73]

$$f(\varepsilon_n) = \frac{1}{\zeta^{-1}e^{\beta\varepsilon_n} + a} \quad (2.1)$$

where $\zeta = e^{\beta\mu}$ is the fugacity, a parameter which is sometimes convenient to use instead of the chemical potential μ . $\beta = 1/kT$ corresponds to the temperature of the system. In order to treat the Fermi-Dirac, Bose-Einstein and classical Maxwell-Boltzmann cases alike, it is convenient to introduce a defined by

$$a = \begin{cases} -1 & \text{Bose-Einstein statistics} \\ +1 & \text{Fermi-Dirac statistics} \\ 0 & \text{Maxwell-Boltzmann statistics} \end{cases} \quad (2.2)$$

In the case of Fermi-Dirac statistics, the mean occupation number can become at most one (Pauli principle), whereas in the case of Bose-Einstein statistics, it features a singularity which can occur when the denominator in eq. 2.1 tends to zero. This singularity is closely connected to the phenomenon of Bose-Einstein condensation.

In this chapter, I will introduce thermodynamic relationships which are relevant for harmonically trapped gases, whereas the most simple case, the homogeneous gas, is the classic textbook example. To introduce some basic notation, the 3D harmonic oscillator potential considered here is given by:

$$V(\vec{r}) = \frac{1}{2}m\omega_1^2x_1^2 + \frac{1}{2}m\omega_2^2x_2^2 + \frac{1}{2}m\omega_3^2x_3^2 \quad (2.3)$$

In order to calculate thermodynamic properties of the system, it is convenient to switch from a representation of discrete energy levels ε_n to a continuous density of energy eigenstates. This is a very good approximation, except for the ground state of systems following Bose-Einstein statistics, as we shall see. The density of states as a function of energy ε is given by:

$$g(\varepsilon) = \frac{\varepsilon^2}{2(\hbar\bar{\omega})^3} \quad (2.4)$$

where $\bar{\omega} = \sqrt[3]{\omega_1\omega_2\omega_3}$ is the geometric mean trapping frequency. Note that eq. 2.4 fails for very small energies – it ascribes a weight of zero to the ground state, which is significant only for a Bose-condensed case due to the possible massive occupation of the ground state, but not for a Fermi gas where the ground state can be occupied by at most one identical fermion. The excited state number of particles can thus be calculated according to

$$N_{ex} = \int_0^\infty f(\varepsilon)g(\varepsilon) d\varepsilon \quad (2.5)$$

For the given density of states of eq. 2.4, we obtain the following expression for the excited state particle number:

$$N_{ex} = -a \left(\frac{k_b T}{\hbar\bar{\omega}} \right)^3 Li_3(-a\zeta) \quad (2.6)$$

Here, I have introduced $Li_n(\cdot)$, the Polylogarithm of order n ($n > 0$ integer or half integer). The Polylogarithm function belongs to the class of hypergeometric functions and is a special case of the Lerch transcendent. Note that

$$-Li_n(-\zeta) = f_n(\zeta) \quad (2.7)$$

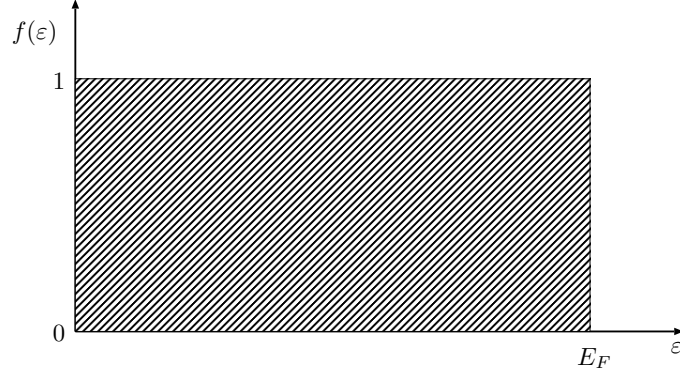


Figure 2.1: Zero-temperature Fermi distribution

where $f_n(\cdot)$ is the Fermi-Dirac function, and

$$Li_n(\zeta) = g_n(\zeta) \quad (2.8)$$

where $g_n(\cdot)$ is the Bose-Einstein function. The Polylogarithm has a branch cut discontinuity in the complex z plane along the line $z > 1$. This discontinuity is responsible for the phenomenon of Bose-Einstein condensation¹, as we shall see. The following series expansion for the Polylogarithm is helpful in many calculations:

$$Li_n(y) = \sum_{l=1}^{\infty} \frac{y^l}{l^n} \quad (2.9)$$

For numerical calculations, it is usually better to make use of predefined implementations of Polylogarithms which rely e. g. on Chebyshev polynomial expansions, such as the ones given in appendix D. In order to derive the particular result of eq. 2.6, the following integral representation for the Polylogarithm is very helpful:

$$\int_0^{\infty} \frac{x^{(n-1)}}{\zeta^{-1}e^x + 1} dx = -\Gamma(n)Li_n(-\zeta) \quad (2.10)$$

2.1.1 Fermi energy

In the case of Fermi-Dirac statistics ($a = +1$), the occupation of any state, in particular the ground state, is not larger than 1, and we can use the approximation $N \approx N_{ex}$. Let us look at the $T = 0$ limit of eq. (2.5). Here,

$$f(\varepsilon) = \frac{1}{e^{\frac{\varepsilon-\mu}{kT}} + 1} \quad , \quad (2.11)$$

and for very small T , the argument of the exponential is either large and positive when $\varepsilon > \mu$ or close to zero when $\varepsilon < \mu$. As a result, $f(\varepsilon)$ is either zero or one, depending on whether ε is above the Fermi edge $\mu(T \rightarrow 0)$ or below the Fermi edge $\mu(T \rightarrow 0)$.

Thus, in this limit, $f(\varepsilon)$ is a step function, and $\mu(T \rightarrow 0)$ is called the Fermi energy. At $T = 0$, all energy levels up to this level are occupied, and none above (see Fig. 2.1). The actual

¹For the most compact and original description of BEC, see footnote on page 234 of ref. [67].

value of the Fermi energy for a given potential and particle number is found by integrating eq. (2.5) with

$$f(\varepsilon) = \begin{cases} 1 & \varepsilon < E_F \\ 0 & \varepsilon > E_F \end{cases} \quad (2.12)$$

The integration yields:

$$N = \int_0^\infty f(\varepsilon)g(\varepsilon) d\varepsilon = \int_0^{E_F} g(\varepsilon) d\varepsilon = \frac{E_F^3}{6(\hbar\bar{\omega})^3} \quad (2.13)$$

and we find the Fermi energy

$$E_F = \hbar\bar{\omega}(6N)^{1/3} \quad (2.14)$$

By dividing the Fermi energy by the Boltzmann constant k_B , we obtain the Fermi temperature T_F which, for a given particle number and trap geometry, sets the scale for the onset of “quantum behavior” deviating significantly from the Maxwell-Boltzmann case:

$$T_F = \frac{\hbar\bar{\omega}}{k_B}(6N)^{1/3} \quad (2.15)$$

For a typical experimental situation with $N = 10^6$ fermions in a spherically symmetric trap with $\bar{\omega} = 2\pi \cdot 50$ Hz, $T_F = 1 \mu\text{K}$. Plugging this expression into eq. (2.6), we can eliminate the particle number and obtain a universal relationship between the fugacity ζ and the degeneracy parameter T/T_F :

$$Li_3(-\zeta) = \frac{-1}{6(T/T_F)^3} \quad (2.16)$$

As we shall see, this relation is of particular importance for thermometry of ultracold Fermi gases, since it connects T/T_F as determined through temperature, trap parameters and particle number to the single fit parameter ζ . Agreement of the two “thermometers” is an indicator that systematics are well controlled.

2.1.2 Bose-Einstein condensation

As mentioned above, the Polylogarithm has a complex branch cut discontinuity for real-valued arguments z with $z > 1$. This means that for a given temperature, the excited states can accommodate no more than

$$N_{ex} = \left(\frac{k_b T}{\hbar\bar{\omega}}\right)^3 g_3(1) \quad (2.17)$$

particles. If there is any number of left-over particles, they need to occupy the ground state of the system:

$$N = N_0 + N_{ex} \quad (2.18)$$

In the non-interacting case, the density distribution would be given by the modulus of the single-particle Gaussian ground state wave function of the harmonic oscillator problem, scaled to reproduce the correct density when integrated over space. This phenomenon of macroscopic ground state occupation is known as Bose-Einstein condensation. The temperature of condensation can be seen from eq. 2.17:

$$T_C = \frac{\hbar\bar{\omega}}{k_B} \left(\frac{N}{g_3(1)}\right)^{1/3} \quad (2.19)$$

For the above-mentioned trap with 10^6 atoms and $\bar{\omega}=50$ Hz, $T_C = 226$ nK. There are small corrections arising to the critical temperature as a result of interactions (see e. g. discussions in [75, 69]). Another important related quantity is the condensate fraction, given by

$$\frac{N_0}{N} = 1 - \left(\frac{T}{T_C} \right)^3 \quad (2.20)$$

which can be used as a thermometer for the partly condensed Bose gas, independent of the width of the thermal component. This may be seen as the bosonic equivalent of eq. 2.16.

In our particular system of ^{40}K and ^{87}Rb with masses m_F , m_B and particle numbers N_F , N_B , temperatures of degeneracy for bosons and fermions are related according to:

$$\frac{T_C}{N_B^{1/3}} = \frac{T_F}{N_F^{1/3}} \cdot \left(\frac{g_3(1)}{6} \right)^{1/3} \sqrt{\frac{m_F}{m_B}} \approx 0.40 \frac{T_F}{N_F^{1/3}} \quad (2.21)$$

Typical experimentally observed ^{40}K - ^{87}Rb mixtures consist of a lot more bosons than fermions which means that the constraints on temperature for coexistence of a degenerate mixture with a thermal cloud as small as possible would not require the production of extremely cold Fermi gases.

2.2 Density distributions

For non-condensed samples, the density distribution in the harmonic trap can be obtained based on a semiclassical approximation, the Thomas-Fermi approach. Particles are described in terms of wave packets with a definite position and momentum, and the density in phase space is given by:

$$w(\vec{r}, \vec{p}, \beta, \zeta) = \frac{1}{h^3} \frac{1}{\zeta^{-1} e^{\beta \mathcal{H}(\vec{r}, \vec{k})} + a} \quad (2.22)$$

Note that in the case of fermions, this distribution limits the number of fermions per phase space volume element to at most one, thereby taking into account Fermi-Dirac statistics. Distributions in position or momentum space can be obtained by integrating over the other coordinate. For non-condensed samples, integration over p results in the density profile

$$n(\vec{r}) = -a \left(\frac{m}{2\pi\beta\hbar^2} \right)^{3/2} Li_{3/2} \left(-a\zeta e^{-\beta V(\vec{r})} \right) \quad (2.23)$$

These density distributions are used in chapter 4, where 3-body loss of ^{40}K - ^{87}Rb mixtures is discussed. In order to measure such density-dependent phenomena in thermal clouds, measured temperature and atom number of the cloud are plugged into the above equation in order to calculate overlap integrals between bosonic and fermionic densities and hence the global instantaneous loss rate.

2.2.1 Maxwell-Boltzmann gas

In the classical limit, we can use the fact that $Li_n(z) \rightarrow z$ as $z \rightarrow 0$ and recover the well-known distribution of the harmonically trapped Maxwell-Boltzmann gas:

$$n(\vec{r}) = N \cdot \left(\frac{m\beta\bar{\omega}^2}{2\pi} \right)^{(3/2)} e^{-\beta V(\vec{r})} \quad (2.24)$$

where I have used the same limit for Li_n in equation (2.6) ($\zeta \approx N \cdot (\beta\hbar\omega)^3$) in order to eliminate the fugacity.

2.2.2 Fermi gas at zero temperature

At $T = 0$, the density in phase space assumes a very simple form:

$$w(\vec{r}, \vec{p}, E_F) = \frac{1}{h^3} \begin{cases} 1 & \text{for } V(\vec{r}) + p^2/2m < E_F \\ 0 & \text{otherwise} \end{cases} \quad (2.25)$$

In this case, integration of w over p is trivial and results in

$$n(\vec{r}) = \begin{cases} \frac{(2m)^{3/2}}{6\pi^2\hbar^3} (E_F - V(\vec{r}))^{3/2} & \text{for } V(\vec{r}) < E_F \\ 0 & \text{otherwise} \end{cases} \quad (2.26)$$

which means that the Fermi gas “fills up” the external trapping potential up to the Fermi energy. The ideal spin-polarized Fermi gas discussed above is characterized by the complete absence of interactions. This is a very good approximation for the situations that are discussed within this thesis. Expanding scattering between particles in terms of partial waves, the s wave scattering between identical fermions is forbidden by the Pauli exclusion principle – the scattering wave function needs to be antisymmetric with respect to particle exchange. The next higher order, p wave scattering, is not forbidden by the Pauli principle, but its importance scales with T^2 , making it energetically forbidden in most experiments reported to date. The absence of interactions and hence also of rethermalizing collisions is the reason why evaporative cooling of a spin-polarized Fermi gas is so inefficient, and also explains why the simple theory outlined above describes the basic properties of such a macroscopic Fermi sea so well.

2.2.3 Bose-Einstein condensate

For a spin-polarized Bose gas, interactions *do* play a significant role, and achieving BEC through evaporative cooling relies on interactions in a fundamental way. In the absence of interactions, all condensed bosons occupy the lowest single particle harmonic oscillator state; in the presence of interactions, the ground state of the sample can be found by introducing a macroscopic wave function ψ with

$$n(\vec{r}) = |\psi(\vec{r})|^2 \quad , \quad (2.27)$$

usually called the condensate wave function. This corresponds to the assumption that all particles occupy the same single-particle state. By variation of the energy functional of the system, one obtains the following equation for ψ :

$$\left[-\frac{\hbar^2}{2m}\Delta + V(\vec{r}) + g_{BB}n(\vec{r}) \right] \psi(\vec{r}) = \mu\psi(\vec{r}) \quad (2.28)$$

which is usually called a “non-linear” Schrödinger equation due to the term involving the wave function in a nonlinear way through the density and is known as the Gross-Pitaevskii

equation for the condensate wave function. $g_{BB} = 2\pi\hbar^2 a_{BB}/\mu_{BB}$ is the well-known coupling parameter, a_{BB} the s wave scattering length for collisions between bosons, $\mu_{BB} = m/2$ the Bose-Bose reduced mass and μ the chemical potential. Under typical experimental conditions, the kinetic energy term is small compared to interactions and the external potential. Under these circumstances, the solution for the density is given by

$$n(\vec{r}) = \begin{cases} \frac{1}{g_{BB}} (\mu - V(\vec{r})) & \text{for } V(\vec{r}) < \mu \\ 0 & \text{otherwise} \end{cases} \quad (2.29)$$

Due to the striking similarity with eq. (2.26), this approximation is often given the same name, ‘‘Thomas-Fermi approximation’’. For a harmonic trap, the shape of the condensate wave function takes the form of an inverted three-dimensional parabola. The spatial extension of the condensate in the i direction is characterized by the so-called Thomas-Fermi radius of the sample, which is the value of the spatial coordinate where the Thomas-Fermi density drops to zero. At this point, the trapping potential becomes equal to the chemical potential:

$$R_i(\mu(N, \bar{\omega}), \omega_i) = \frac{1}{\omega_i} \sqrt{\frac{2\mu}{m}} \quad (2.30)$$

2.3 Free expansion

By looking at eq. 2.30, we can estimate the size of the trapped sample. For a typical cigar-shaped magnetic trap ($\omega_1 = \omega_2 \equiv \omega_{rad} = 2\pi \cdot 214$ Hz and $\omega_3 \equiv \omega_{ax} = 2\pi \cdot 11$ Hz as used in this experiment) and an atom number in the condensate of 10^6 atoms, the axial Thomas-Fermi radius is $57 \mu\text{m}$, and the transverse radius is smaller ($2.9 \mu\text{m}$). This object is surprisingly large given the fact that it can well be described by a single macroscopic wave function. Nevertheless, the length scales can be smaller than or on the order of typical ‘‘diagnostic’’ length scales such as the pixel size of CCD chips, resolutions of optical imaging systems and imaging artefacts. Most experiments therefore probe the behavior of the system by suddenly releasing the sample from the trap and recording the density distribution after a typical time of flight of 10 to 25 ms when the sample has expanded to a size which is larger than the in-trap extension.

2.3.1 Non-condensed samples

For non-condensed samples of bosons and for fermions, the time-of-flight distribution in the Thomas-Fermi approximation can be derived much in the same way as the density distribution. This is accomplished by integrating the density in phase space w over coordinate space, not over momentum space. In order to perform the integration of eq. 2.22 in position space, the trick is to introduce new coordinates $\tilde{x}_i \equiv x_i/\sqrt{\omega_i}$, which makes the integrand isotropic and allows the use of spherical coordinates:

$$n(\vec{p}) = -a \frac{1}{\bar{\omega}} \left(\frac{1}{2\pi\beta\hbar^2 m} \right)^{3/2} Li_{3/2} \left(-a\zeta e^{-\beta \frac{p^2}{2m}} \right) \quad (2.31)$$

In contrast to the density distribution, the momentum distribution is isotropic. Let us consider the limit where the cloud expands to a final size which is much larger than the in-trap size.

Let t_E be the time of free expansion. In this case, the momentum distribution is converted into the time of flight density distribution according to the substitution $\vec{p} = m/t_E \cdot \vec{r}$, and the distribution is isotropic, in contrast to the in-trap density distribution. In the intermediate regime, we can introduce the width

$$\sigma_i^2 = \frac{1}{m\beta\omega_i^2} [1 + (\omega_i t_E)^2] \quad (2.32)$$

For general t_E , it has been shown [68] that the density distribution after time of flight is given by

$$n(\vec{r}) = -a \left(\frac{1}{2\pi\beta^2\hbar^2\bar{\omega}^2} \right)^{3/2} \cdot \frac{1}{\sigma_1\sigma_2\sigma_3} Li_{3/2} \left(-a\zeta e^{-\sum_i \frac{x_i^2}{2\sigma_i^2}} \right) \quad (2.33)$$

The density after time of flight is thus given by a simple rescaling of coordinates. The above equation contains the large t_E limit discussed before since for large t_E , the trap frequency ω_i drops out of the σ_i . When equation 2.33 is integrated over one spatial coordinate (the z direction in this case), we obtain the two-dimensional column density of the expanded cloud which is the basis of thermometry for ideal Fermi gases. The trick in doing the integral is to write the Polylogarithm as its series representation (eq. 2.9), perform the integration on the individual terms and then go back to the Polylogarithm representation. For each integration over a spatial coordinate, we get a prefactor of $\sqrt{2\pi}\sigma_i$, we need to increase the order of the Polylogarithm by 1/2 and we need to remove one of the terms in the exponential:

$$n(x_1, x_2) = -a \left(\frac{1}{2\pi\beta^2\hbar^2\bar{\omega}^2} \right)^{3/2} \cdot \frac{1}{\sigma_1\sigma_2} \sqrt{2\pi} Li_2 \left(-a\zeta e^{-\sum_{i \neq 3} \frac{x_i^2}{2\sigma_i^2}} \right) \quad (2.34)$$

A one-dimensional profile is obtained by integrating over y :

$$n(x_1) = -a \left(\frac{1}{2\pi\beta^2\hbar^2\bar{\omega}^2} \right)^{3/2} \cdot \frac{1}{\sigma_1} 2\pi Li_{5/2} \left(-a\zeta e^{-\frac{x_1^2}{2\sigma_1^2}} \right) \quad (2.35)$$

As an additional check, we can integrate this over x to obtain:

$$N = -a \left(\frac{1}{\beta\hbar\bar{\omega}} \right)^3 Li_3(-a\zeta) \quad (2.36)$$

which is nothing but the thermodynamic relationship between particle number and fugacity which we have already seen in eq. 2.6.

2.3.2 Bose-Einstein condensate

The evolution of the condensate density during time of flight can be obtained by using a set of hydrodynamic equations for the superfluid density. The derivation which is outlined for example in ref. [69] scales the equilibrium Thomas-Fermi radii of the sample by time-dependent coefficients but as an ansatz keeps the same parabolic shape as the equilibrium distribution, only with the re-scaled coefficients. One can then derive a set of coupled equations for the scaling of the radii. For a commonly used experimental condition, the trapping potential corresponds to an elongated cigar-shaped trap, and these equations can be expanded in the

trap asymmetry parameter $\lambda = \omega_{ax}/\omega_{rad}$. In terms of the dimensionless expansion time $\tau = \omega_{rad}t_E$, the resulting time of flight Thomas-Fermi radii are given by:

$$R_{rad}(\tau) = R_{rad}(0)\sqrt{1 + \tau^2} \quad (2.37)$$

$$R_{ax}(\tau) = R_{ax}(0) \left[1 + \lambda^2 \left(\tau \arctan \tau - \ln \sqrt{1 + \tau^2} \right) \right] \quad (2.38)$$

where $R_{rad}(0)$ and $R_{ax}(0)$ are given by eq. 2.30.

2.4 Interacting mixtures

So far, I have separately discussed the behavior of degenerate bosonic and fermionic gases. When simultaneous degeneracy of bosonic and fermionic gases is achieved in a harmonic trap, interactions between the two can fundamentally affect the behavior of the system, as we shall see. Interaction in degenerate mixtures of a single bosonic and fermionic component are characterized by two parameters, one of them, a_{BB} , the s wave scattering length for identical bosons which I have already introduced, and a_{FB} , the scattering length between bosons and fermions. For a spin polarized fermionic component, there is no scattering between identical fermions for ultracold temperatures due to the Pauli exclusion principle, hence the absence of a scattering parameter for Fermi-Fermi scattering.

This section discusses interacting clouds of many fermions and bosons under the influence of global harmonic confinement for the whole cloud, the so called mean field limit, in connection with experiments discussed in chapter 4 and 5. A different scattering problem is discussed in chapter 7, where I discuss interactions of exactly one fermion and one boson at a single site of an optical lattice. To some approximation, the latter can be described as a model harmonic trap, and with exactly two particles per site, the discussion of chapter 7 is complementary to the many-body approach discussed here.

The question of interacting mixtures in a harmonic trap is intimately related to the question of phases of harmonically trapped mixtures. Phases of harmonically trapped Fermi-Bose mixtures have first been analyzed theoretically by K. Mølmer in 1998 [71]. The density profiles of both the fermionic and the bosonic cloud are strongly affected by the presence of an interspecies interactions a_{FB} . Depending on the sign of the heteronuclear interaction, the interaction will either mutually enhance the density of the components for attractive interactions ($a_{FB} < 0$) or push the constituents apart in the case of repulsive interactions ($a_{FB} > 0$). In both cases, instabilities can occur - a collapse of the sample for strong attractive interactions and phase separation for strong repulsive interactions.

In order to quantitatively discuss the behavior of the mixture under the influence of heteronuclear interactions, let us consider a model where we use the full Gross-Pitaevskii equation for the bosonic component and the Thomas-Fermi limit for the fermionic component. The heteronuclear interaction is introduced through a mean field potential entering both the fermionic and bosonic equations. The modified system of equations is [72, 76]:

$$\left[-\frac{\hbar^2}{2m_B} \Delta + V_B(\vec{r}) + g_{BB} \cdot n_B(\vec{r}) + g_{FB} \cdot n_F(\vec{r}) \right] \psi = \mu_B \psi \quad (2.39)$$

$$n_F(\vec{r}) = \frac{(2m_F)^{3/2}}{6\pi^2 \hbar^3} \max[\mu_F - V_F(\vec{r}) - g_{FB} \cdot n_B(\vec{r}), 0]^{3/2} \quad (2.40)$$

The coupling parameters are defined by

$$g_{BB} = 2\pi\hbar^2 a_{BB}/\mu_{BB} \quad (2.41)$$

$$g_{FB} = 2\pi\hbar^2 a_{FB}/\mu_{FB} \quad (2.42)$$

and μ_{BB} and μ_{FB} are corresponding reduced masses. Using the Thomas-Fermi approximation for the bosonic equation, we obtain a new set of equations:

$$n_B(\vec{r}) = \frac{1}{g_{BB}} \max[\mu_B - g_{FB} \cdot n_F(\vec{r}) - V_B(\vec{r}), 0] \quad (2.43)$$

$$n_F(\vec{r}) = \frac{(2m_F)^{3/2}}{6\pi^2\hbar^3} \max[\mu_F - V_F(\vec{r}) - g_{FB} \cdot n_B(\vec{r}), 0]^{3/2}$$

and the bosonic and fermionic chemical potentials are fixed by the particle numbers:

$$N_B = \int_0^\infty n_B(\mu_B, \vec{x}) d^3x \quad (2.44)$$

$$N_F = \int_0^\infty n_F(\mu_F, \vec{x}) d^3x$$

Let us consider a situation where the trapping potential for the bosonic component and the fermionic component are related to each other by a simple factor, as is the case for magnetically trapped mixtures. For magnetically trapped mixtures of ^{40}K and ^{87}Rb

$$V_{\text{Rb}}(\vec{r}) = V_{\text{K}}(\vec{r}) \quad , \quad (2.45)$$

and the ratio of the trap frequencies is

$$\omega_{\text{K}}/\omega_{\text{Rb}} = \sqrt{m_{\text{Rb}}/m_{\text{K}}} = \sqrt{87/40} \quad . \quad (2.46)$$

We can introduce rescaled coordinates

$$\tilde{x}_i = \sqrt{\frac{m_F}{2}} \omega_{F,i} \cdot x_i \quad . \quad (2.47)$$

In this case, $\tilde{r}^2 = V_B = V_F$, and the coupled Thomas-Fermi problem becomes:

$$n_B(\tilde{r}) = \frac{1}{g_{BB}} \max[\mu_B - g_{FB} \cdot n_F(\tilde{r}) - \tilde{r}^2, 0] \quad (2.48)$$

$$n_F(\tilde{r}) = \frac{(2m_F)^{3/2}}{6\pi^2\hbar^3} \max[\mu_F - \tilde{r}^2 - g_{FB} \cdot n_B(\tilde{r}), 0]^{3/2} \quad (2.49)$$

and the problem only depends on $\tilde{r} = \sqrt{\tilde{x}_1^2 + \tilde{x}_2^2 + \tilde{x}_3^2}$. In the new set of coordinates, equation 2.44 becomes

$$N_B = \left(\frac{2}{m_F}\right)^{3/2} \frac{1}{(\bar{\omega}_F)^3} \int_0^\infty 4\pi^2 \tilde{r}^2 \cdot n_B(\tilde{r}) d\tilde{r} \quad (2.50)$$

$$N_F = \left(\frac{2}{m_F}\right)^{3/2} \frac{1}{(\bar{\omega}_F)^3} \int_0^\infty 4\pi^2 \tilde{r}^2 \cdot n_F(\tilde{r}) d\tilde{r} \quad , \quad (2.51)$$

where I have used the spherical symmetry of the problem in the new coordinates. As one can see, the above problem can be formulated solely in terms of the potential energy \tilde{r}^2 of the

mixture, and the trapping potential only enters the calculation through the geometric mean trapping frequency $\bar{\omega} = \sqrt[3]{\omega_1\omega_2\omega_3}$. This will be particularly relevant in chapter 4, where mixtures produced in different experiments and different harmonic traps are discussed; the fact that the discussed mixtures had different aspect ratios, yet the same $\bar{\omega}$, allows direct comparison to other experiments.

Moreover, the fact that the problem only depends on the modulus \tilde{r} allows the system of equations to be solved in a 1-dimensional calculation, although the result is fully applicable to the 3D case. Numerically, a self-consistent solution to the above equations starts by initializing the bosonic distribution $n_{B,0}$ to a Thomas-Fermi distribution of a pure condensate. The next step is to calculate the fermionic density distribution $n_{F,0}$ which results from eq. 2.49 and $n_{B,0}$. Yet, at this point, μ_F has not yet been fixed, and we can find the corresponding value using

$$N_F = \frac{4}{(\hbar\bar{\omega}_F)^3} \int_0^\infty d\tilde{r} \max [\mu_F - \tilde{r}^2 - g_{FB}n_B(\tilde{r}), 0]^{3/2} \tilde{r}^2 \quad (2.52)$$

μ_F is initialized with the Fermi energy and iterated over until the right-hand side is equal to the total particle number. When $\mu_{F,0}$ has been determined, we obtain $n_{F,0}$. The latter can be used to start the next global iteration and calculate $n_{B,1}$ through eq. 2.48. Again, we need to fix the value of the chemical potential $\mu_{B,1}$. This is done by solving

$$N_B = \frac{4\pi}{g_{BB}} \left(\frac{4}{m_F^2\bar{\omega}_F} \right)^3 \int_0^\infty d\tilde{r} \max [\mu_B - \tilde{r}^2 - g_{FB}n_F(\tilde{r}), 0] \tilde{r}^2 \quad (2.53)$$

We obtain $\mu_{F,2}$ and $n_{F,2}$ by solving 2.52 with the new bosonic input data, and so forth. After some of these iterations, several outcomes are possible:

- The densities converge. We obtain a self-consistent solution of the full problem.
- The bosonic density converges, and the fermionic density becomes zero at the center. This is really a special case of the above situation and corresponds to phase separation, as we shall see.
- Both densities diverge, corresponding to collapse (see below).

In the following, I will discuss four different phases of the harmonically trapped mixture which have all been observed in the experiment and are discussed in chapter 4 and 5. I illustrate these phases with numerical solutions to the above Thomas-Fermi model. The solutions of the Thomas-Fermi model which I am going to discuss have been calculated for equal boson and fermion numbers of 10^5 atoms in a harmonic trap with mean oscillator frequency $\bar{\omega} = 2\pi 50$ Hz for ^{87}Rb . I have used $a_{BB} = 98.98a_0$ [77], corresponding to ^{87}Rb . The heteronuclear interaction is parametrized by comparing it to the ^{87}Rb interaction parameter through the definition of the ratio

$$\gamma := \frac{g_{FB}}{g_{BB}} \quad . \quad (2.54)$$

2.4.1 Noninteracting limit

In this situation ($\gamma = 0$), where the two clouds do not influence each other at all, the solutions to eq. 2.43 are the well-known Thomas-Fermi profiles of an atomic Bose-Einstein condensate and a degenerate Fermi gas at $T = 0$. As a starting point for our discussion, the non-interacting limit can be used to estimate the relative influence of one species on the other

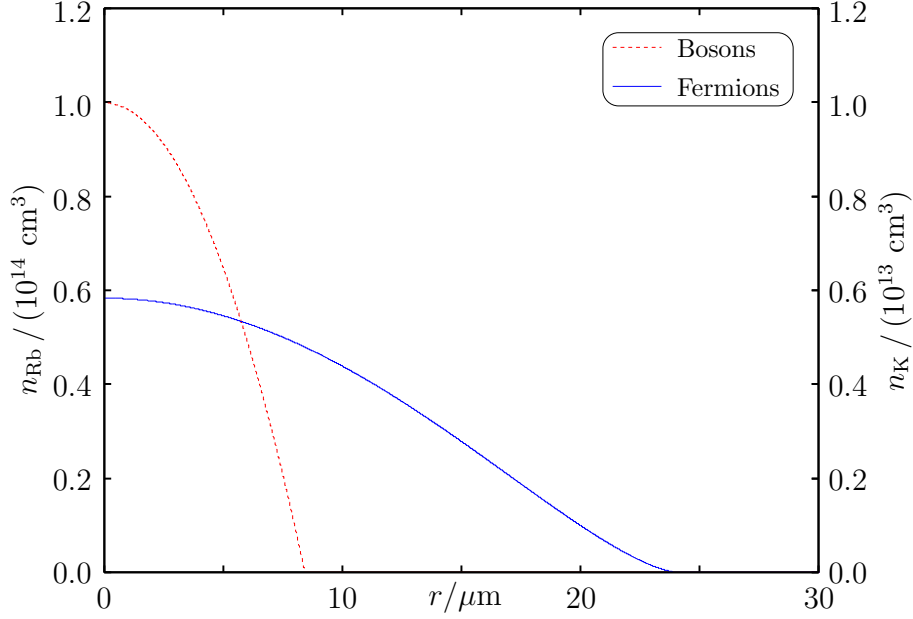


Figure 2.2: Non-interacting Fermi-Bose mixture in the Thomas-Fermi model.

as the interaction between the two is gradually turned on. I have plotted the corresponding $T = 0$ noninteracting density profiles of the Fermi gas and the BEC in Fig. 2.2. The density of the BEC is shown in red, and the corresponding scale is on the left y axis. The fermionic density is plotted in blue, and the corresponding scale is the right y axis in the figure, with the scale increased by a factor of 10 compared to the bosonic density.

The central density of the BEC in our example trap in this case is $1 \cdot 10^{14} \text{ cm}^{-3}$, and the Fermi gas is much more dilute, $6 \cdot 10^{12} \text{ cm}^{-3}$, about one and a half orders of magnitude smaller. At the same time, the spatial extension of the Fermi cloud is much larger than the size of the condensate. The Bose-Einstein condensate has a Thomas-Fermi radius of $8 \mu\text{m}$, and the Fermi cloud is about three times as large. In terms of volume occupied inside the trap, this corresponds to a factor of 3^3 .

Leaving the non-interacting discussion, weak interactions between fermions and bosons will affect the density distributions mostly in the overlap region with the Bose-Einstein condensate, i. e. within the Thomas-Fermi radius of the condensate. Since the bosonic density is so much larger, a good first order intuitive picture is to only look at how the large bosonic density affects the fermionic cloud, since the corresponding mean field potential $g_{FB} \cdot n_B$ is an order of magnitude larger than $g_{FB} \cdot n_F$.

2.4.2 Attractive interactions

For attractive interaction between bosons and fermions ($\gamma = -4$ in Fig. 2.3), the effect of the first order correction on the fermions is the appearance of an additional mean field dimple in the external trapping potential due to the narrow bosonic cloud. This mean field dimple, $g_{FB} \cdot n_B$, increases the fermionic density distribution in the center of the harmonic trap where it overlaps with the BEC and gives rise to a bimodal density distribution of the fermionic component in the trap. For small enough interactions, the bosonic density is mostly unaffected

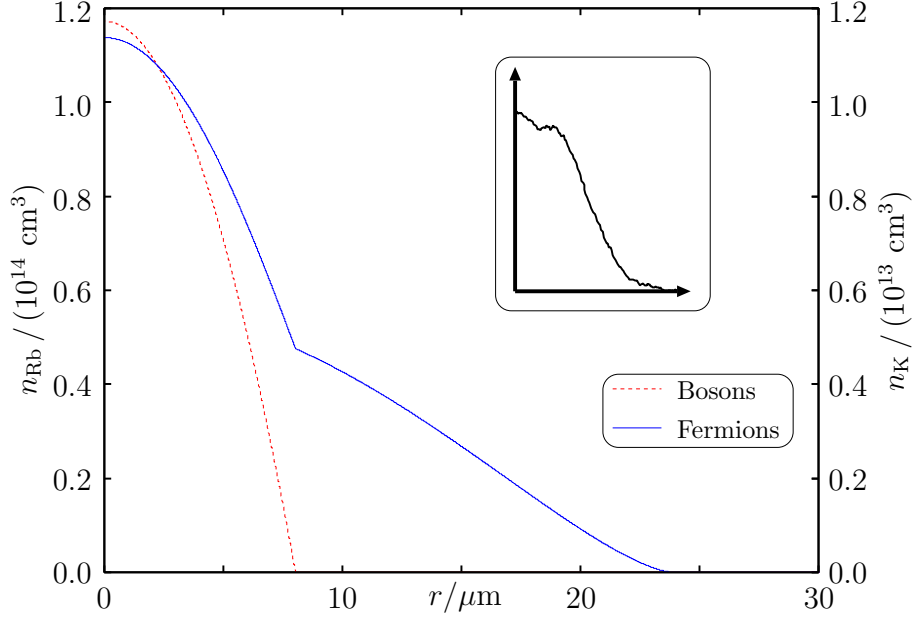


Figure 2.3: Fermi-Bose mixture with moderately attractive interactions.

by the presence of the fermions, and this first order correction in the iterative solving procedure of the coupled problem remains valid even after several iterations of eq. (2.43). This situation is illustrated in Fig. 2.3.

In this situation, where the Fermi-Bose attraction is four times as strong as the Bose-Bose repulsion, the fermionic density is increased by a factor of two in the center of the trap, while the bosonic density increases only by about 20% for this relatively strong attraction. In the inset of Fig. 2.3, I have shown the measured axial density profile of an attractively interacting cloud of bosons and fermions in our magnetic trap in order to show that we can observe this phase in the experiment. The short time of flight chosen here ensures that the time of flight distribution is close to the in-trap distribution, and the bimodality in the fermionic density distribution is clearly visible. I will say more about the experimental observation of this regime of stable attractive interactions in chapter 4 and 5.

2.4.3 Mean field collapse

For strong attractive interactions, the outward bound Pauli pressure of the Fermi gas [18, 50] and the repulsive interactions within the BEC can no longer counteract the strong attraction between the two components, and a simultaneous collapse of the two is observed, reminiscent of the collapse of pure Bose-Einstein condensates with attractive interactions [78, 79]. Now, the back-action of the fermionic component on the BEC is significant and so strong that it will compress the Bose-Einstein condensate even more, which in turn will increase the fermionic density, ultimately leading to a self-accelerating contraction in a kind of runaway process.

In the mean field model, this is seen from the fact that each of the subsequent steps in solving equations (2.43) yields significant contracting contributions, and convergence can no longer be achieved. Since densities cannot become arbitrarily large, the consequence is that no stable solutions for the densities exist beyond certain critical combinations of

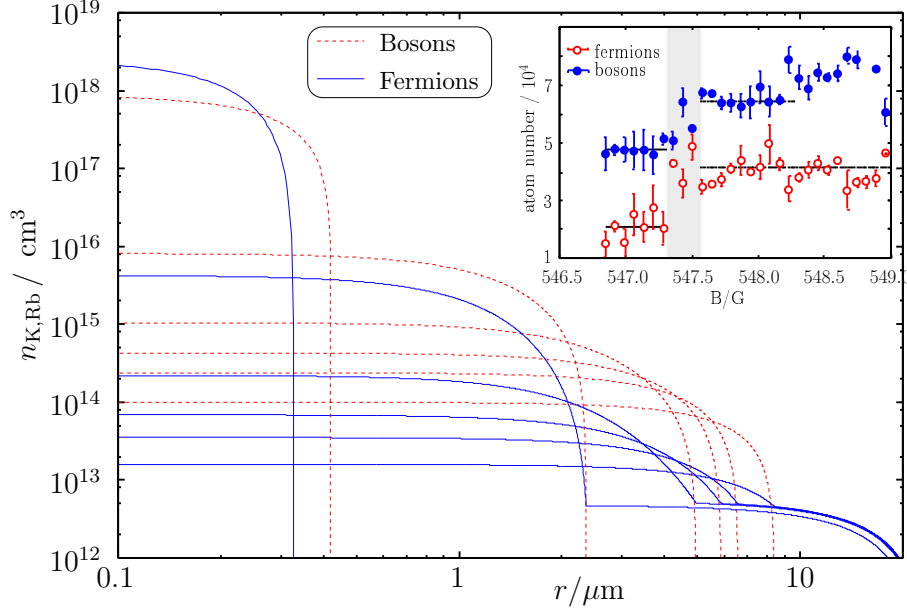


Figure 2.4: Iterations of the coupled Thomas-Fermi model leading to a collapse of the mixture.

particle numbers, interaction strength and external confinement. For the particle numbers and trapping frequencies mentioned above, the critical γ for the onset of collapse is $-6.992(8)^2$ (see below). Fig. 2.4 illustrates successive steps (in fact, every third step) of the iterative solution procedure for $\gamma = -8$ (beyond the critical conditions for collapse), demonstrating this contraction in the simulation. First, the overlap region of condensate and Fermi gas becomes narrower and narrower, and more and more fermions are trapped inside the BEC. At the same time, the central densities of both clouds increase more and more. Once complete self-trapping of the mixture has been achieved, both components contract together and the densities grow to infinity. In order to be able to visualize the evolution of the algorithm over these large density and position scales, I have plotted the iterations in a full logarithmic plot for both the density and the spatial coordinate. In chapter 4 and 5, I will show how we observe the onset of collapse in the experiment. One of the symptoms of collapse is a sudden drop in particle number when the mixture becomes overcritical as seen in the plot of ^{87}Rb and ^{40}K particle number in the inset in Fig. 2.4. The inset shows a sudden drop as the interactions strength at a Feshbach resonance is more and more increased (from right to left). I will say more on the experimental observation of the onset of collapse in chapter 4 and 5.

2.4.4 Repulsive interactions

For weak repulsive heteronuclear interactions (here: $\gamma = 4$), the mean field dimple in the center of the trap which I have discussed in the limit of weak attractive interactions is inverted. Now, it effectively repels fermions from the center of the trap. This repulsive “bump” leads to a fermionic density distribution which reaches its maximum on an ellipsoid around the origin as seen in the simulation in Fig. 2.5.

As a result of the additional fermionic “curvature”, the BEC will feel an effectively deeper

²The error stems from the interval process determining stability limits.

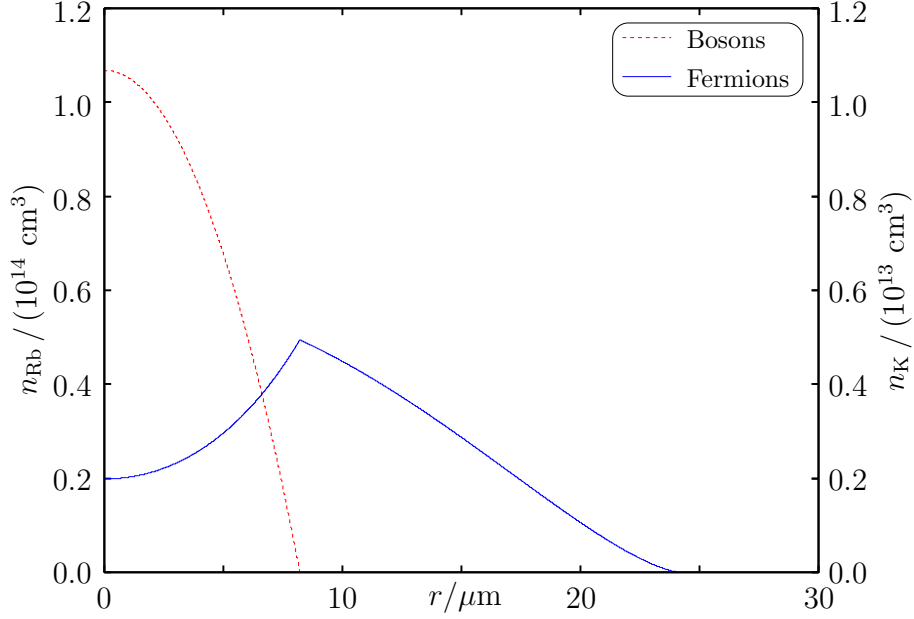


Figure 2.5: Fermi-Bose mixture with moderately repulsive interactions.

external potential due to the presence of the fermions. In chapter 5, I will show how we can observe this compression of the condensate and the increased potential energy of the fermions in time of flight through a faster expansion of the system.

2.4.5 Phase separation

When the repulsive BEC bump in the center becomes so strong that the associated potential is larger than the fermionic chemical potential, the fermionic density distribution at $\vec{r} = 0$ vanishes completely. In this limit, the mixture phase separates into a dilute fermionic shell surrounding a dense BEC core, as seen in the simulation in Fig. 2.6 for $\gamma = 8$. In the center of the trap, where the bosonic density vanishes completely, the BEC only feels the external trapping potential. The effect of the heteronuclear interaction is seen in the outer overlap region between the dense BEC and the Fermi cloud and has the shape of a very steep mean field potential as seen in Fig. 2.6. For the particle numbers and trapping frequencies mentioned above, the critical γ for the onset of phase separation is 7.008(8).

The inset in Fig. 2.6 shows a time of flight image of ^{40}K atoms in the regime of phase separation which is discussed in chapter 5 from an experimental perspective. Most of the fermionic density is concentrated in the upper part of the image. This is due to the fact that in the presence of gravity, phase separation occurs in a slightly different way where the light fermions will tend to sit above the heavy bosons in the trap. In chapter 5, I will show how we can observe this vertical phase separation in the experiment.

2.4.6 Full phase diagram

After I have shown these four limiting phases of harmonically confined mixtures, let us look at the full phase diagram of the mixture. I only discuss the case of repulsion between bosons here. Even for moderate attractive interactions, an atomic Bose-Einstein condensate is quickly

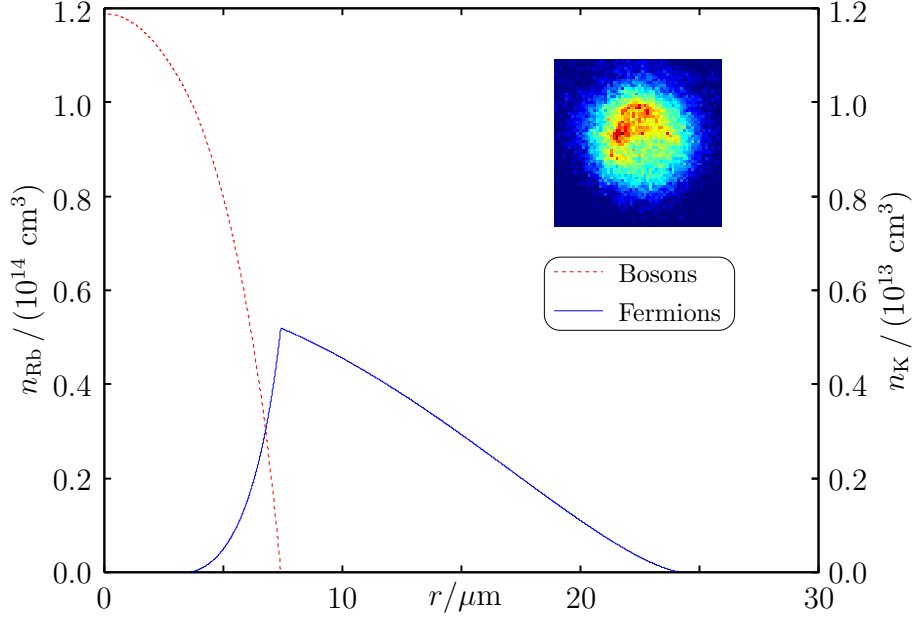


Figure 2.6: Fermi-Bose mixture undergoing phase separations for strong repulsive interactions.

subject to collapse all by itself. In the case of repulsive interactions *between bosons*, the self-consistent solution of equations 2.43 allows us to calculate a phase diagram of the mixture [72] by looking at convergence or divergence of the algorithm. The algorithm determines the phase boundary by initializing γ with -1 or 1 , depending on the phase boundary to be determined (collapse or phase separation). In successive iterations, γ is then multiplied by two until either phase separation or collapse occurs at $\gamma_0 = 2^n \cdot 1$. Now, an interval procedure initialized with a lower value $\gamma_L = 0$ and a higher value $\gamma_H = \gamma_0$. In each step, the stability of the mixture is determined for

$$\gamma_C = \frac{\gamma_L + \gamma_H}{2} \quad (2.55)$$

and, depending on the outcome, either the lower or upper interval boundary is updated to γ_C and thus the length of the interval halved. The algorithm continues until the interval length is inferior to a threshold reflecting the desired precision. The resulting phase diagram is shown in Fig. 2.7.

In the phase diagram, I have plotted the phase boundaries as a function of the boson-boson repulsion and the Bose-Fermi interaction, parametrized through the respective scattering length. From the phase diagram, we can see that stable mixtures, either attractively or repulsively interacting, exist as long as the Fermi-Bose interaction is not too strong compared to the Bose-Bose interaction. For too strong attractive Fermi-Bose interactions, the mixture collapses. If interactions between fermions and bosons become large and repulsive, phase separation occurs, where stable density distributions do exist, but the overlap of the constituents is reduced to a small region.

In this chapter, I have treated interacting fermions and bosons from a mean field perspective. I have shown the various limiting cases of harmonically trapped mixtures and established a basis for thermometry. In the following chapter, I will present experimental techniques which have been used in this thesis to create ultracold mixtures of bosons and fermions and

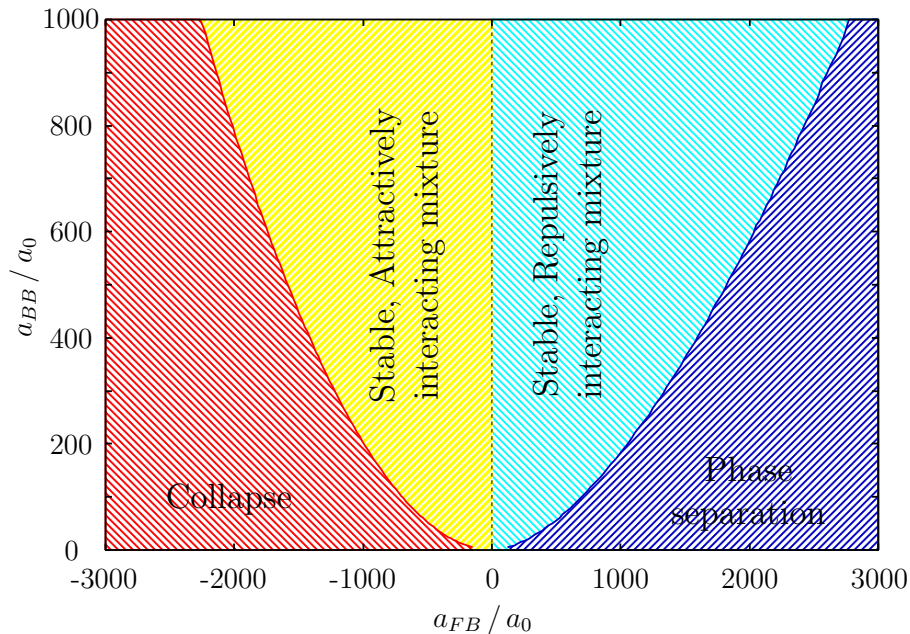


Figure 2.7: Phase diagram of a harmonically trapped Fermi-Bose mixture for $N_B = 10^6$ and $N_F = 5 \cdot 10^5$

then show in chapter 4 and chapter 5 how we can make use of these techniques to measure temperatures of degenerate gases and understand the various experimentally observed phases.

It is important to keep in mind that all of the calculations performed in this chapter assume equilibrium conditions. In particular, the phase boundaries with respect to collapse determined here are only valid for thermal equilibrium. In chapter 4, we will see that excitations in the cloud may significantly lower critical conditions for the onset of collapse, since shape oscillations can cause an overcritical increase in density in an otherwise undercritical mixture.

A complementary problem to the mean field many particle treatment of this chapter is considered in chapter 7, where I will experimentally and theoretically study scattering between only *two* particles in the steep potential of an optical lattice well and show that this leads to formation of two-body bound states (heteronuclear Feshbach molecules).

Chapter 3

Experimental setup

In this chapter, I will describe the experimental setup for quantum degenerate Fermi-Bose mixtures of ^{40}K and ^{87}Rb in 3D optical lattices which has been realized together with S. Ospelkaus. The experiments presented in chapters 4 to 7 have required the development and implementation of a lot of experimental techniques which are described in depth here. Readers who wish to continue with the main experimental results can continue with chapter 4; I have included backreferences to this chapter in order to highlight where the experimental techniques discussed here have been particularly relevant.

In this introductory paragraph, I will briefly sketch our experimental approach to going from 400°C to the nanokelvin regime within a few centimeters, covering more than ten orders of magnitude on the absolute temperature scale. Fig. 3.1 illustrates the basic concept of the experiment. A vapor of ^{40}K and ^{87}Rb is produced within a rectangular glass cell (2D-MOT cell) at a pressure of between 10^{-8} and 10^{-9} mbar using alkali metal dispensers. When current is run through these tiny metal boats, a chemical reduction reaction takes place in the interior and atomic alkali vapor is released into the vacuum system. From this background vapor, a cold atomic beam is produced using two pairs of horizontal, orthogonal laser beams forming a two-dimensional magneto-optical trap [80] for both species. The beam is collimated in the horizontal direction and directed along the vertical axis of the apparatus.

The flux towards the lower part of the apparatus is enhanced by using a resonant pushing beam which is optimized to match the velocity distribution with the capture range of a 3D two-species magneto-optical trap which is located in the lower part of the apparatus in a second glass cell. This region is separated from the 2D-MOT region by a differential pumping stage, thereby achieving UHV conditions in the 3D-MOT region. From the cold atomic beam, atoms are accumulated in the 3D-MOT for typically ten seconds with final particle numbers on the order of $1 \cdot 10^{10}$ for ^{87}Rb and $2 \cdot 10^8$ for ^{40}K ($5 \cdot 10^7$ in the presence of ^{87}Rb). After some additional optical molasses cooling, final achievable temperatures of the laser cooled atoms are on the order of $50 \mu\text{K}$ for ^{87}Rb . Although already seven orders of magnitude in temperature reduction have been achieved at this stage, the ensemble is still about three orders of magnitude away from the quantum regime, and the atoms still behave like little billiard balls in a classical Maxwell-Boltzmann gas.

In order to further decrease temperature and increase phase space density, evaporative cooling in a magnetic trap is used. The magnetic moments of the atoms allows them to be held in an inhomogeneous magnetic field, which is produced at the same place where the atoms have been accumulated in the 3D-MOT. Radio frequency transitions are used to

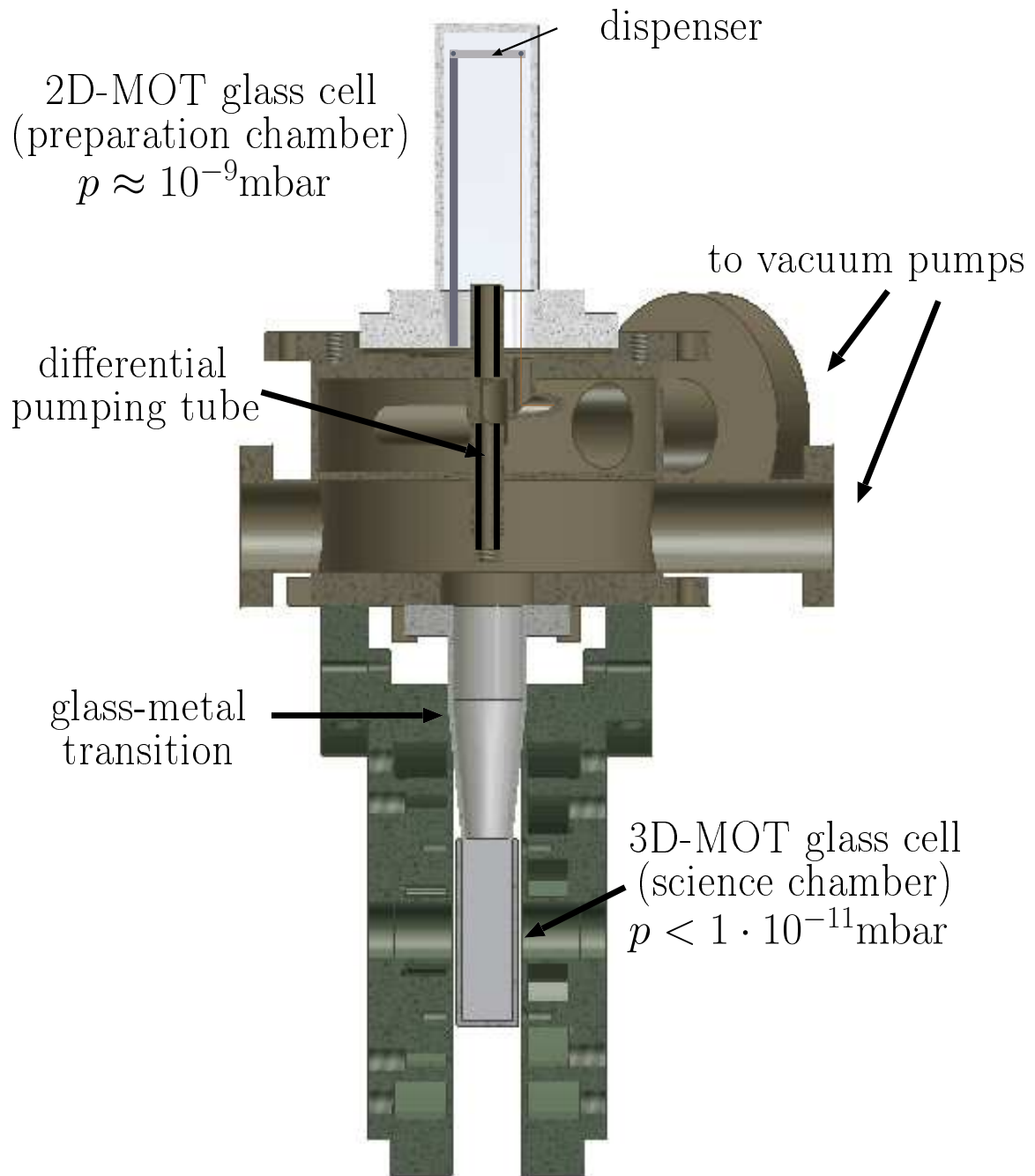


Figure 3.1: Sketch of the basic experimental setup, excluding all laser systems, optics and electronics. In the 2D magneto-optical trap, a cold atomic beam is produced, sent through a differential pumping stage and recaptured in a 3D-MOT. Atoms are transferred into a magnetic trap, sympathetically cooled into the degenerate regime and then transferred into optical traps and optical lattices for further experiments.

remove atoms from the trap in a velocity-selective way. We start to induce spinflips into antitrapped states in the outer region of the trap and thereby remove atoms with the highest overall energy from the sample. Cutting away part of the atomic velocity distribution triggers rethermalization through collisions between atoms, resulting in fewer atoms, yet at a lower temperature and with a higher phase space density. Evaporative cooling proceeds by cutting from the outer regions of the trap to the center with the “rf knife” until the thermal deBroglie wavelength of the atoms is on the order of the interparticle spacing. At this time, the quantum nature of the atoms in their external degrees of freedom becomes apparent, which results in Bose-Einstein condensation for ^{87}Rb and a macroscopic Fermi sea for ^{40}K . The success of evaporative cooling relies on several factors:

- **Low background gas scattering during evaporative cooling.** This is the main reason for using a double-MOT setup which fulfills the otherwise incompatible requirements of UHV conditions and efficient and fast loading from a background vapor by splitting the system up into two regions.
- **Low intrinsic collisional losses in the gas.** This concerns 3-body and 2-body inelastic collisions in the sample which lead to trap loss and / or heating. This thesis contains a measurement of 3-body loss in the ^{40}K - ^{87}Rb system which demonstrates that 3-body loss in the magnetically trapped states is much weaker than previously believed.
- **Presence of rethermalizing collisions.** ^{87}Rb has very favorable properties for evaporative cooling. Any spin-polarized fermionic gas alone suffers from Pauli-blocking of s -wave collisions at the temperatures in the magnetic trap, making evaporative cooling of such a system very inefficient. In the mixture system, this limitation is overcome by removing essentially ^{87}Rb atoms with the rf knife and by cooling ^{40}K in the thermal bath of the ^{87}Rb atoms. The ^{40}K - ^{87}Rb system has very favorable interspecies rethermalization properties [81].

In order to perform experiments with the degenerate mixture, we can either transfer it into an optical dipole trap where the spin of the atoms is an experimental degree of freedom or ramp up the power in three retroreflected laser beams forming a 3D perfect optical crystal, the optical lattice. Inside the dipole trap and the optical lattice, Feshbach resonances allow interactions between atoms to be tuned practically arbitrarily. In order to extract information on the sample, the atoms are imaged using one or more of the four imaging systems in various directions after release from the trap.

3.1 Vacuum system

The vacuum system of our experiment is based on the design by Holger Schmaljohann [82] for the spinor BEC experiment in our group and has been further optimized for optical access and two-species operation. Initial evacuation of the apparatus has been performed using a rotary vane roughing pump in a neighboring room connected to the main system by a flexible PVC tube. A turbomolecular pump together with a Titanium Sublimation pump allowed us to reach 10^{-10} mbar in the main chamber. Both the turbomolecular pump and the roughing pump are then disconnected from the vacuum system using two UHV valves. After this step, the only remaining connection between the 2D and 3D MOT parts of the vacuum system is the differential pumping tube. Each of the two regions is pumped separately by a 55 l/s

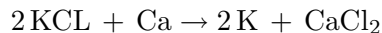
Ion pump, and possess a cold cathode vacuum gauge allowing us to measure the pressure in both regions separately. After bakeout at roughly 300 °C during one week, the pressure in the lower region drops below 10^{-11} mbar, while the pressure in the upper part is on the order of 10^{-10} mbar. Note that we cannot directly measure the pressure in the 2D MOT glass cell, which is higher due to additional differential pumping. We estimate this pressure to be between 10^{-8} mbar and 10^{-9} mbar, based on the estimated performance of the differential pumping stage.

The one exception where pressure in the lower part of the vacuum system was above the 10^{-11} level happened in July 2005 where a ceramic part of one of the current feedthroughs for our 2D MOT dispenser sources broke for no apparent reason. The situation was fixed by applying a lot of heated TorrSeal vacuum compatible glue (Varian) to the outside of the current feedthrough, switching on the roughing pump again, selectively baking out the ion pumps and firing the Titanium sublimation pump a few times. Removing all of the 3D MOT and lattice optics was also necessary. We had degeneracy again about one month later at a pressure of $5 \cdot 10^{-11}$ mbar, and pressure dropped below $1 \cdot 10^{-11}$ mbar within one more month.

3.2 Atomic sources

It is now common in laser cooling experiments to use Alkali Dispensers to produce a background vapor from which a 3D collection or 2D MOT [80] is loaded. Dispensers are tiny metal boats containing an alkali salt and a reduction agent. When the boat is heated by sending current through it, the reduction reaction takes place and atomic alkali atoms are released into the surrounding vacuum vessel. These dispensers are usually employed in producing photosensitive surfaces of photocathodes, and their entire content is “fired” within a few seconds in these applications. As a source of atoms in laser cooling experiments and run at much lower current, they last for years. We haven’t seen any degradation in the output of our commercial ^{87}Rb dispenser until the above mentioned cracking of the corresponding current feedthrough.

Being a mass product, dispensers are inexpensive sources and the manufacturer usually charges an extra fee for the small quantities that an atomic physicist will buy. They are, however, only available for the naturally occurring isotope mixture of a particular element. ^{40}K has a natural abundance of 0.01%, making enriched sources highly desirable, but these are not available commercially. In the group of D. S. Jin, a technique to build dispensers based on small quantities of enriched salts (\$6000 for 200 mg) has been developed [83], and we have been following this approach. The reduction reaction is



and takes place at around 400°C. The very fine powder required both for the hygroscopic salt and the delicate Ca powder required us to perform the whole production process including several days of filing Ca for just a few mg of material under Ar atmosphere in a glovebox at the University’s chemistry department. Assembly of the whole dispenser setup was also performed in this box, and the transport to our institute inside a CF tube under Ar atmosphere. Details of the production process and the characterization can be found in [66].

3.3 Laser systems

I will now describe the laser systems which are used for the initial laser precooling in the 2D/3D magneto-optical trap combination and for detection. I will start with the ^{87}Rb laser system, then describe techniques developed for ^{40}K and finally discuss how the different laser beams are overlapped in order to be delivered to the experiment.

3.3.1 Rubidium laser system

A schematic sketch of the ^{87}Rb laser setup is given in Fig. 3.3. The concept of the ^{87}Rb laser system is similar to the one described in [82, 84] and relies on having two extended cavity master diode lasers for laser frequencies close to the $|1, X\rangle \rightarrow |2, X\rangle$ repumping transition and the $|2, X\rangle \rightarrow |3, X\rangle$ cycling transition for laser cooling, trapping, optical pumping and detection. Each of these two master lasers is locked to a saturated absorption FM spectroscopy setup; the light is then amplified in several injection locked slave lasers and frequency shifted using Acousto-Optical Modulators (AOMs). The frequency locking scheme is shown in Fig. 3.4.

The cooling master M1 runs approximately 160 MHz blue-detuned with respect to the $F = 2 \rightarrow F' = 3$ cycling transition. A probe beam is shifted by -267 MHz to the red (using a 120 MHz AOM in double pass configuration) allowing the laser frequency to be locked to the $F = 2 \rightarrow F' = 2, 3$ crossover resonance. The output power of M1 is then amplified by injection seeding of a slave diode laser S1. The latter is frequency shifted to the red by an 80 MHz AOM in double pass configuration to provide near-resonant light for detection, optical pumping and the pushing beam.

The resonant detuning for the detection beam has been determined by taking images of thermal clouds with varying AOM frequency and recording the detected pixel count (see Fig. 3.2). An absorptive Lorentzian

$$N(\nu_{AOM}) = \frac{N_0}{1 + ((\nu_{AOM} - \nu_0)/w)^2} \quad (3.1)$$

has been fitted to the data, yielding a resonance center position of

$$\nu_0 = 66.50(05) \text{ MHz} \quad (3.2)$$

AOM frequency and a half width of $w = 1.59(3)$ MHz. This half width needs to be multiplied by two in order to obtain the frequency half width due to the double pass configuration and by four in order to compare it to the natural linewidth. The result of 6.36(12) MHz is only slightly above the natural linewidth of 6.065(9) MHz, possibly due to slight saturation.

Two other identical beam paths originating from S1 involve another -160 MHz frequency shift using an 80 MHz double pass AOM, another injection seeded slave laser (S1a and S1b) which in turn produces enough power to seed a tapered amplifier (T1a and T1b) for the 2D and 3D MOTs, respectively. Of course, these beams will also be resonant for an AOM frequency of 66.5 MHz, and a larger frequency corresponds to a red-detuned situation.

In order to run a large ^{87}Rb MOT, the original setup relied on using broad area diodes as a last power amplification stage [85]. While this was a good option at a time where previously used tapered amplifier chips from SDL were no longer available and other options simply a lot more expensive, we found another option when setting up our system: tapered amplifier chips from Eagleyard Photonics proved to provide a long lifetime and largely sufficient output

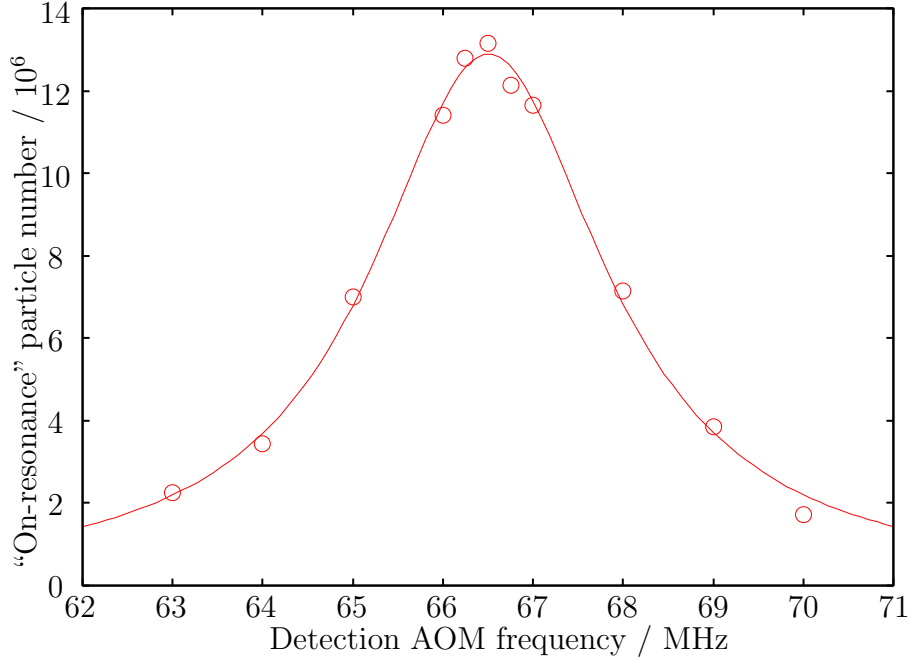


Figure 3.2: Determination of ^{87}Rb detection AOM resonance frequency. The figure shows the detected particle number (assuming zero detuning) as a function of AOM frequency. The displayed particle number therefore only corresponds to the real particle number exactly on resonance.

power (≈ 500 mW) at the same price as the previously used broad area diodes. In terms of adjustment, they offer the advantage of the injection being completely independent of fiber coupling of the output beam, which is incredibly useful in daily maintenance. In order to transfer atoms from the MOT into the magnetic trap with an additional step of molasses cooling, we need to be able to quickly switch the T1b intensity. This is done using an Electro-Optic Modulator (EOM).

The repumper master M2 is directly locked to the $F = 1 \rightarrow F' = 1, 2$ crossover resonance. Its output power is amplified by injection locking a slave laser S2. The output of the latter is frequency shifted 80 MHz to the blue using an AOM in single pass and is then resonant with the $F = 1 \rightarrow F' = 2$ repumping transition. It is split into two beams and coupled into the same optical fibers as the 2D MOT and 3D MOT using orthogonal polarizations. The ^{87}Rb laser system is described in detail in the diploma thesis of Jürgen Fuchs [86]; the interested reader is referred to this thesis for details on the tapered amplifier setup.

3.3.2 Potassium laser system

An important aspect to bear in mind when working with some of the light Alkali atoms (such as ^{40}K) is that hyperfine splittings, especially in the excited state, may be small and that even on a cycling transition, there is a relatively high probability of atoms being excited into a state where they can decay into the “blind” ground hyperfine manifold. As a result, there may be need for more repumping power than in the case of ^{87}Rb . At the time when we were planning the laser system for ^{40}K , inexpensive tapered amplifiers providing enough power

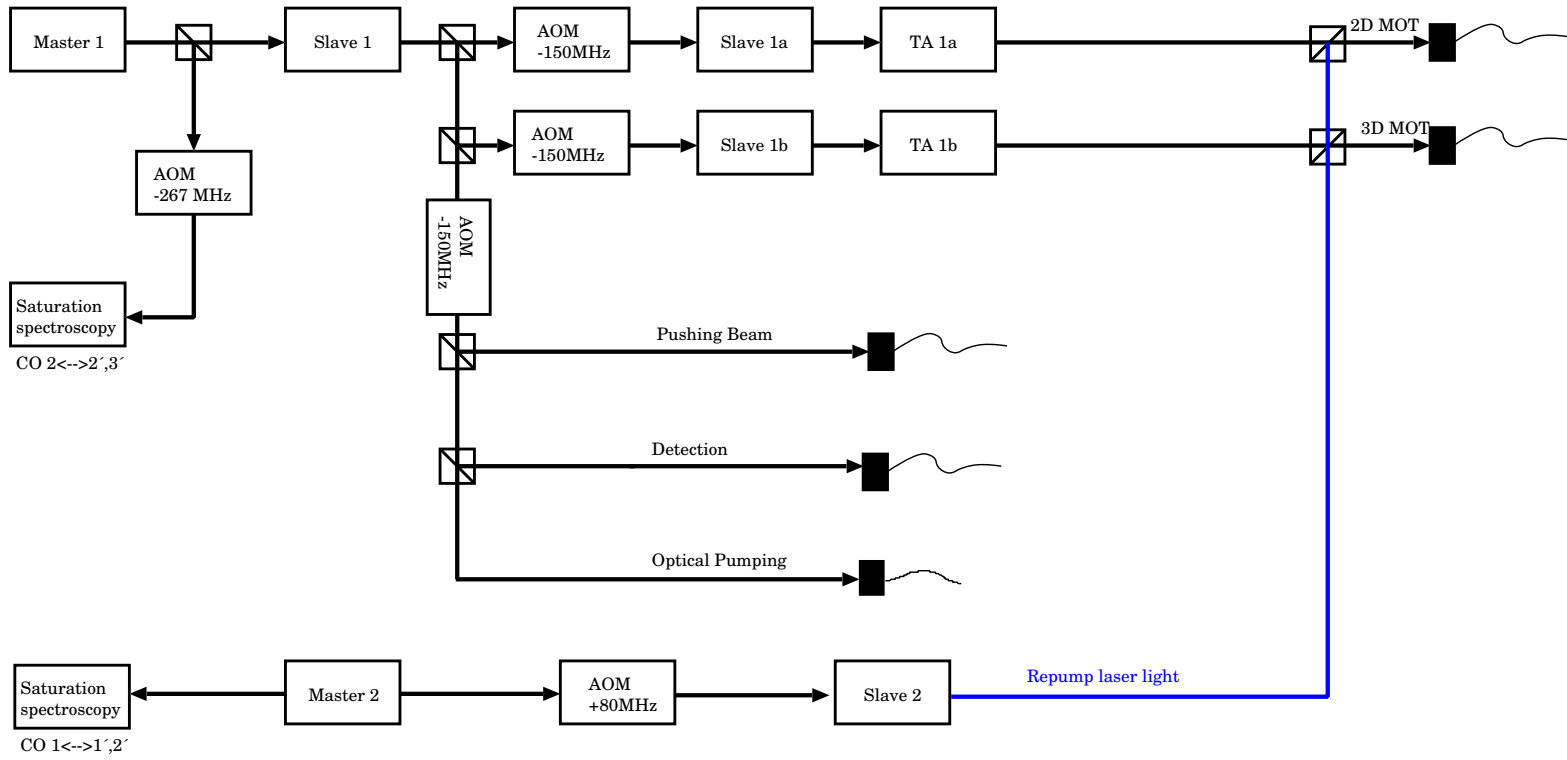
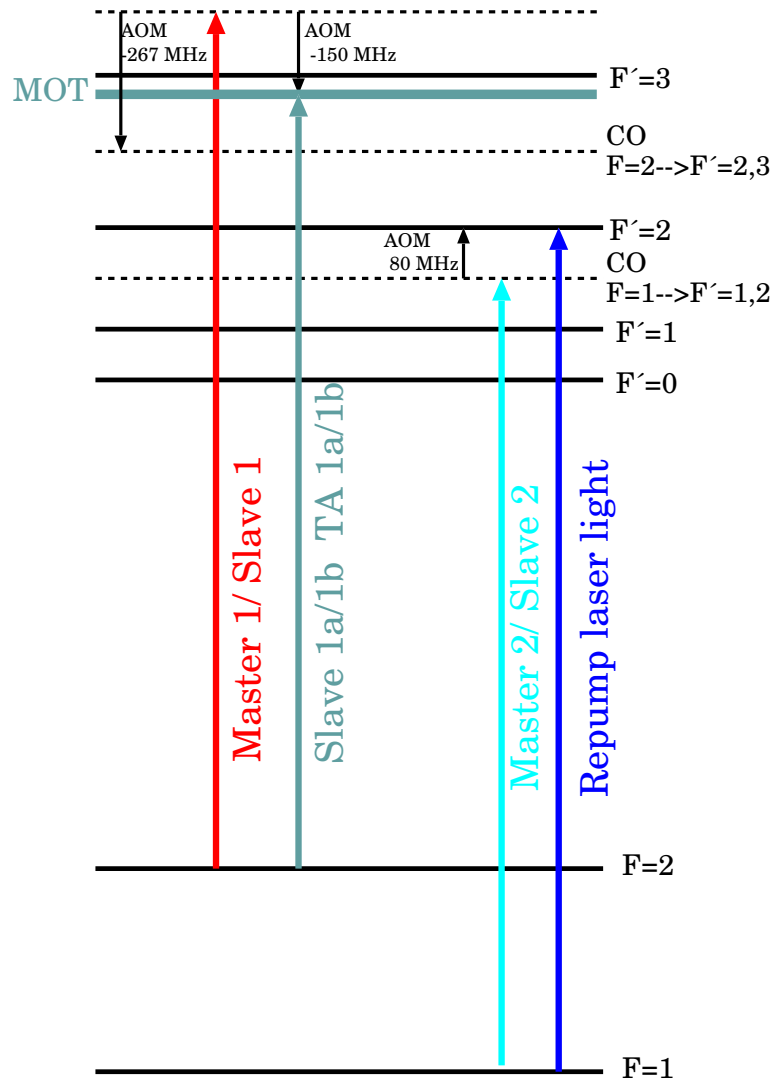


Figure 3.3: Simplified sketch of ^{87}Rb laser system

Figure 3.4: Laser locking scheme for ^{87}Rb .

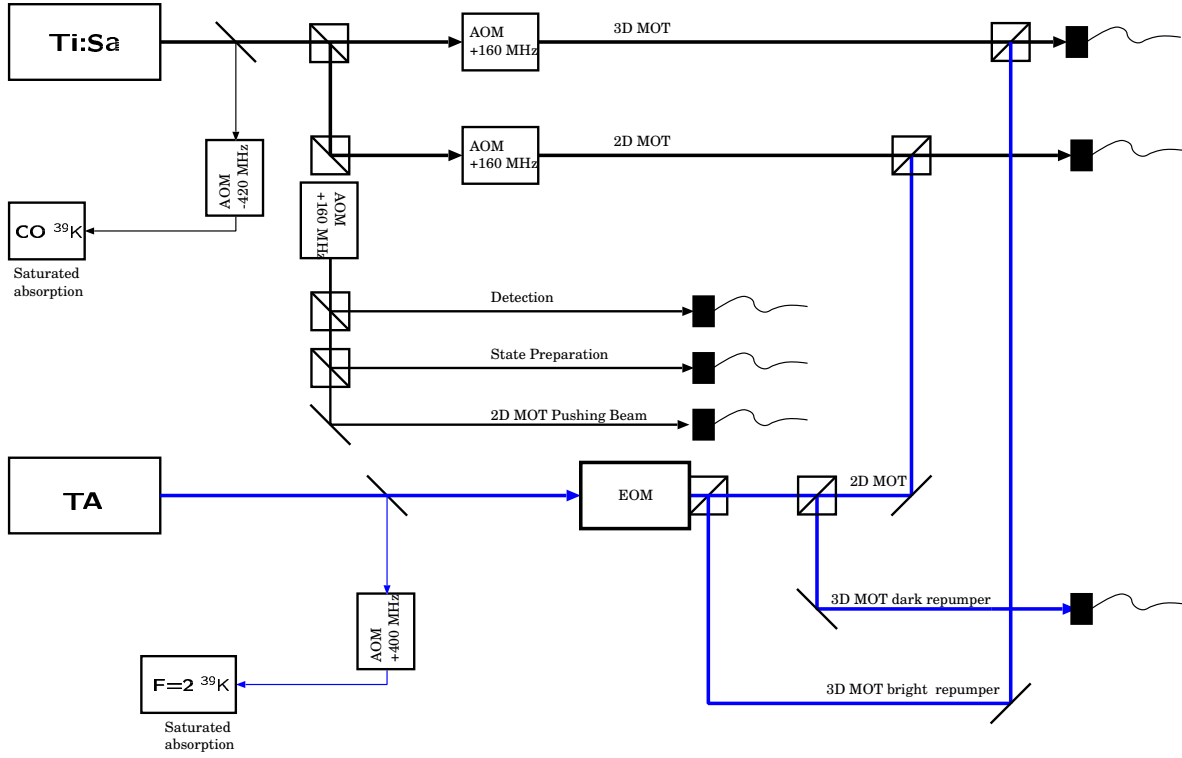
both for cooling and a repumper were not available. We decided to base this part of the setup on commercially available laser systems.

A sketch of the ^{40}K laser system can be found in Fig. 3.5. For repumping, we rely on a tapered amplifier system from Toptica Photonics. The system consists of an extended cavity diode laser injecting a Tapered amplifier with a specified output power of 500 mW. This laser system runs slightly red-detuned with respect to the ^{40}K $F = 7/2 \rightarrow F' = 9/2$ transition. Vapor cells containing non-negligible concentrations of ^{40}K for frequency stabilization are not affordable, and the stabilization of the laser can equally well be done by using the known isotope shifts relative to the most abundant isotope ^{39}K . In our case, the ^{39}K line closest to the ^{40}K repumping transition is the $F = 2 \rightarrow F' = X$ transition¹. This transition is blue-detuned by approximately 415 MHz with respect to the repumping transition. We therefore use a 200 MHz AOM in double pass configuration to shift part of the repumper light towards higher energy and make it resonant with the the aforementioned ^{39}K transition for frequency stabilization using a standard saturated absorption FM spectroscopy setup. In order to obtain a decent signal-to-noise ratio, we heat the vapor cell to about 60-70°C.

As will become clear from the discussion of our 3D magneto-optical trap for ^{40}K , our dark-SPOT MOT [87] for ^{40}K relies on two different paths for the repumping light, depending on whether we run only a bright 3D-MOT or a 2D-MOT and a dark SPOT 3D-MOT. We therefore need a possibility to quickly switch between these two configurations. Since we do not have an AOM after the MOPA, we also need the possibility to quickly switch off the repumper. All this is accomplished by using an Electro-Optical Modulator (EOM). It basically works as an electronically controllable waveplate in front of a polarizing beam splitter cube allowing us to send light either of two ways. For loading the 3D-MOT, we use one output port which feeds a separate fiber for the dark SPOT repumper and sends some of the repumping light into the 2D-MOT fiber together with the corresponding cooling beam. For transfer into the magnetic trap, we have a short period of bright MOT only. This uses the other output port of the cube, and all of the repumping light is coupled into the same fiber as the 3D MOT cooling beam.

Our cooling laser for ^{40}K is a commercial Coherent MBR110 Titanium-Sapphire ring laser pumped by a 10 W Verdi-V10 laser at 532 nm. The MBR110 has an internal reference cavity resulting in an inherent linewidth of about 100 kHz. Two years ago, this laser produced about 1.6 W of output power at 767 nm; the power has dropped to about 800 mW in between, which is still largely sufficient for running our 2D/3D MOT combination. One well known complication when working with lasers with lengthy resonators at 767 nm is the presence of molecular O_2 absorption features in this region. These losses can lead to an important gain reduction in the laser cavity and make the laser feel more happy on a different spectral mode than desired. This can be avoided by purging the resonator housing with nitrogen (see discussion in [88, 89]). The Ti:Sa runs approximately 160 MHz below the ^{40}K $F = 9/2 \rightarrow F' = 11/2$ cycling transition and is shifted to frequencies near the resonance for laser cooling, detection and optical pumping by 80 MHz AOMs in double pass configuration. These are also used for rapid switching, intensity control and small changes in the detuning. The Ti:Sa initially used to have its own saturated absorption spectroscopy setup stabilizing it relative to the ^{39}K groundstate crossover resonance as shown in Fig. 3.5. In experiments on molecule formation (chapter 7), we have found it necessary to detect atoms at high magnetic fields (see section 3.11.3.2 and thus detune the imaging laser by up to -800 MHz. For this purpose,

¹The largest excited state hyperfine splitting is 21 MHz and is only barely resolved.

Figure 3.5: Simplified sketch of ^{40}K laser system

we have instead implemented a frequency offset lock relying on the beat signal between the Ti:Sa frequency and the repumper frequency recorded on a fast photodiode. For this purpose, we have adapted a scheme from the group of Martin Weitz [90] which relies on comparison between the flat frequency characteristic of a -3 dB attenuator and the -3 dB point of an rf low pass filter. The output of the two is compared in a rectifier circuit and results in a zero-crossing of the spectroscopy signal at an input rf frequency of 161 MHz. This technique has the advantage of being robust and providing a large capture range for the lock. In fact, we can unlock and scan the repump MOPA while the Ti:Sa remains locked relative to the MOPA. In order to be able to set the desired beat frequency to a wide range of desired values and thus tune the Ti:Sa laser frequency, we mix the beat signal from the photodiode with the output of a commercial rf synthesizer and then stabilize the difference frequency to 161 MHz using the above mentioned error signal circuit (ESC). By changing the output frequency of the synthesizer via GPIB, we can then detune the Ti:Sa laser over a wide range². The ⁴⁰K offset locking scheme is described in detail in appendix A.

3.3.3 Putting it all together

So far, the ⁸⁷Rb and ⁴⁰K systems have been discussed separately; both the 2D-MOT and the 3D-MOT are operated simultaneously at the same place; here I will discuss how we make a separate ⁸⁷Rb and ⁴⁰K laser system *one* laser system for a two-species MOT. The idea is to have four fibers delivering the main cooling and repumping light to the experiment. Cooling and bright repumping light for one species in the 3D-MOT are overlapped using orthogonal polarizations and coupled into the same polarization non-maintaining single mode fiber. This makes one 3D-MOT ⁴⁰K fiber, one 3D-MOT ⁸⁷Rb fiber and another set of two fibers for the 2D-MOT. This allows us to adjust the ⁴⁰K and ⁸⁷Rb MOTs independently at the experiment and to have the bright repumper always automatically overlapped with the cooling light.

Then there is another set of three auxiliary beams for optical pumping, detection and the pushing beam enhancing the flux of atoms from the 2D to the 3D MOT. These frequencies are always near the cycling transition, and are never needed at the same time. We therefore use one common AOM to shift them near the cycling transition, then divide the power into three separate paths. We then use dichroic mirrors which reflect ⁴⁰K light under 20 to 25 degrees angle of incidence and transmit ⁸⁷Rb light to overlap ⁴⁰K detection light with ⁸⁷Rb detection light, ⁴⁰K optical pumping light with ⁸⁷Rb optical pumping light etc. and send each of these overlapped beams through a mechanical shutter and couple it into a single mode fiber.

3.4 Two species 2D/3D-magneto-optical trap

Having described how all of the laser light for cooling and trapping is produced, I will now explain the concept of the two-species magneto-optical trap setup. The description will only cover the 3D magneto-optical trap, since it is the more complex of the two and also requires a discussion of imaging and overlapping with the optical lattice beams. The most significant part of the setup is sketched in Fig. 3.6. The idea underlying our two-species MOT is to divide both ⁴⁰K (c) and ⁸⁷Rb (b) cooling and repumping light up into three different beam

²One of the shortcomings of the current setup is that as the synthesizer frequency comes closer to 161 MHz, the other mixer products will disturb the ESC, so that one MHz of rf synthesizer frequency change no longer *exactly* corresponds to one MHz change in beat frequency change. This is a simple matter of applying a small correction on the set frequency.

paths (e) and (d). One ^{40}K and one ^{87}Rb path are then overlapped using a dichroic mirror (f), forming three two-species cooling beams. Each of these is sent through a beam expansion telescope (g) and split up into two of the counter-propagating beams for the MOT using a large 30 mm polarizing beam splitter cube. Care is taken to make the length of the beam paths of the counter-propagating beams approximately equal for ease of adjustment and a beam profile of both which is as balanced as possible.

At the experiment, two of the MOT beams run at 45° with respect to the laser table (m) and one beam is running in the horizontal direction. Fig. 3.6 shows only two of the three MOT axes. The whole setup has been mounted on a custom made vertically oriented fiber hardened epoxy board (a). The choice of the material is due to its low thermal expansion coefficient and vanishing conductivity, thereby avoiding eddy currents upon switchoff of the magnetic trap³. Much of the geometry is influenced by the characteristics of the mirrors that are used for overlapping ^{40}K and ^{87}Rb light (f). These are HR coated for 767 nm and AR coated for 780 nm, all at an angle of incidence of 20 to 25° , so that they will reflect ^{40}K (e) cooling light and transmit ^{87}Rb cooling light (d). Producing such an optical filter with an edge of only 13 nm between HR and AR is only possible using the ion beam sputtering technique⁴. The angle of incidence of these mirrors means that the 1:3 setup for ^{40}K (e) is rotated by 45° with respect to the ^{87}Rb 1:3 (d) setup before the $2 \cdot 3$ beams are overlapped (f) and sent through a common telescope (g) for each direction of the MOT. All of the beam preparation is done on the back side of the 3D-MOT (a) board in order not to compromise the optical access close to the atoms. Finally, each of the beams is sent onto a diagonal beam path on the “atomic” side of the MOT board using a beam walk consisting of two mirrors, one on each side of the board (i). Before going through the glass cell, each of the beams passes another edge filter which transmits the MOT light, but reflects 1030 nm light. These mirrors are used to shine in the optical lattice beams (l).

The horizontal beam path for the MOT is built very much in the same way, except that the overlapping and beam expansion is done on two stainless steel boards parallel to the optical table and 65 mm below the MOT center. This setup allows flexible imaging and lattice configurations in the horizontal direction.

There are of course other aspects to the MOT setup. One aspect is imaging in the direction of the MOT and dipole beams. Many of the MOT beams can be blocked individually during evaporative cooling using low-vibration “shutters” made from servo motors and cardboard so that imaging can be done in the direction of the lattice / MOT beams using the MOT beam. Another aspect is that as soon as ^{40}K and ^{87}Rb light has been overlapped, achromatic waveplates need to be used for polarization manipulation.

I have already briefly mentioned the dark SPOT scheme [87] which is used for the ^{40}K 3D-MOT. The repumping light for this dark SPOT is delivered to the experiment using a separate fiber. It is sent through a glass plate with a 0.5 mm diameter dark spot in the center and imaged to the atoms by sending it through a lens system into the unused port of the ^{40}K cube which produces the two diagonal MOT beams (e), thus resulting in a repumper beam profile in the MOT which is characterized by a roughly 5 mm dark area in the center. The effect of the dark area is that repumping is very weak in the center of the trap and atoms can easily fall into the “uncooled” $F=7/2$ hyperfine state as long as they stay in the center

³The field lines from the magnetic trap run directly through the board

⁴The edge filters used in this experiment were produced by Laserzentrum Hannover and have transmission / reflection of better than 95% for both species.

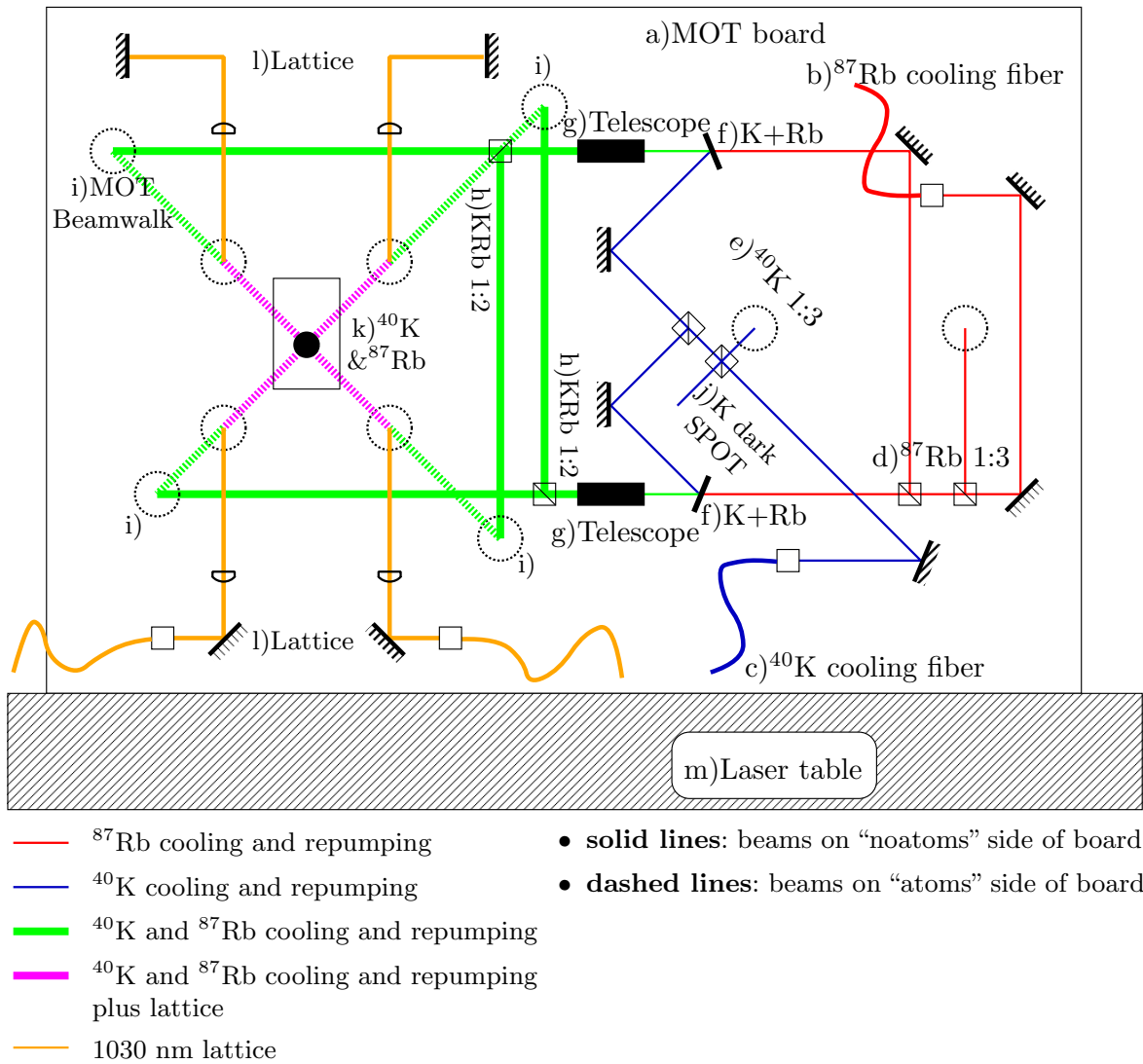


Figure 3.6: Two-species 3D magneto-optical trap beam preparation and lattice overlapping setup.

of the MOT, i. e. as long as they are “cold enough”. Atoms which leave this area will be repumped into the “bright” $F=9/2$ state and pushed into the center of the trap by radiation pressure as in a traditional MOT. The dark SPOT scheme allows one to overcome limitations due to the density in the center of the trap, related to radiation trapping and excited-ground state collisions. Before implementing the dark SPOT MOT, very low magnetic field gradients and very weak cooling power had been required to run a ^{40}K MOT, particularly in the presence of ^{87}Rb , which is a typical indication of light-assisted collisional losses. A detailed characterization of the double MOT system can be found in [66, 91, 5]; for a pure ^{40}K dark SPOT, see [67].

3.5 Magnetic trapping

Since the initial experiments on Bose-Einstein condensation in dilute atomic gases, magnetic trapping and evaporative cooling of samples precooled by laser cooling techniques has been the workhorse of ultracold quantum gases. Magnetic trapping relies on the potential energy of an atom with a magnetic moment $\vec{\mu}$ in an external inhomogeneous magnetic field:

$$V = -\vec{\mu} \cdot \vec{B}$$

Let us consider the limit where the precession of the magnetic moment of the atom around the \vec{B} -field is fast compared to the motion of the atom along the field lines. Let F be the total angular momentum of the atom, m_F its projection on the z -axis and g_F the g-factor of the atom. In this case,

$$V = -g_F \cdot m_F \mu_B \cdot |\vec{B}|$$

Atoms in states with $g_F \cdot m_F < 0$ (“weak-field seeking states”) will be attracted towards a local minimum of the modulus of the magnetic field and atoms with $g_F \cdot m_F > 0$ (“high-field seeking states”) would tend to stay at a local maximum of the magnetic field. According to a result from classical electrodynamics, such a local maximum of the magnetic field cannot be created in a time-independent field configuration (Earnshaw theorem). Magnetic trapping of atoms has hence been limited to the weak-field seeking states. In the presence of an external magnetic field, any weak-field seeking state cannot be the absolute ground state of the atom. Inelastic losses related to this internal energy can therefore limit the practicability of magnetic trapping, as observed in Cs. This atom was initially thought to be one of the best candidates for achieving BEC in alkali gases, but showed strong dipolar losses in magnetic traps and has only been condensed in 2003 using a sophisticated optical evaporation scheme.

The simplest configuration of a magnetic trap is given by two coils in anti-Helmholtz configuration, see Fig. 3.7a). The magnetic field at the center is then given by a zero at the trap center and a linear increase in $|\vec{B}|$ away from the center. While conceptually simple, this trap has one important shortcoming: When the temperature of the trapped sample becomes low and approaches the degenerate limit, the time that an atom spends near $B = 0$ will increase. In this case, spin flips of the atoms can occur and transfer atoms from the trapped to the anti-trapped state. These so-called Majorana losses remove just the coldest atoms from the trap, making cooling to the degenerate regime impracticable in pure quadrupole traps. Traps relying on AC fields for confinement such as the TOP trap [15] can make use of this hole by making it revolve around the trap center, and thus exploit it for “circle of death”-evaporation. In experiments at MIT [16], the magnetic-field zero at the center of the trap has been “plugged” with a blue-detuned repulsive laser beam.

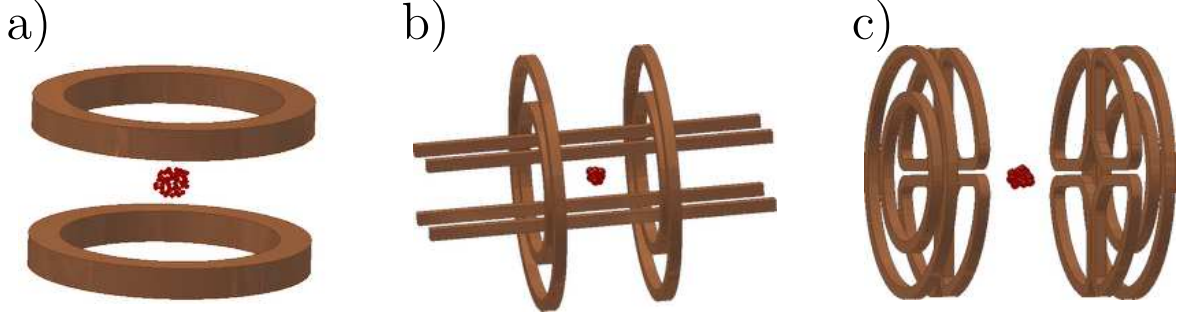


Figure 3.7: Illustration of three different magnetic trap types: **a)** Quadrupole trap **b)** Ioffe-Pritchard trap **c)** A variant of the original Ioffe-Pritchard trap, the cloverleaf trap.

Today, the majority of experiments use a configuration with a non-zero magnetic field minimum at the trap center and a quadratic increase of the magnetic field away from the center, the Ioffe-Pritchard trap [92], see Fig. 3.7b). The most simple realization relies on four horizontal bars on the edges of a square to provide a radial gradient field. Two axial coils with a radius significantly smaller than required for a pure Helmholtz configuration provide a non-zero magnetic field at the trap center and weak curvature for axial confinement. The relatively large bias field can be tuned by additional anti-Bias coils in Helmholtz configuration. The magnetic field of such a trap at the trap center is:

$$\vec{B} = B_0 \begin{pmatrix} 0 \\ 0 \\ 1 \end{pmatrix} + B' \begin{pmatrix} x \\ -y \\ 0 \end{pmatrix} + \frac{B''}{2} \begin{pmatrix} -xz \\ -yz \\ z^2 - 1/2(x^2 + y^2) \end{pmatrix}$$

where B_0 is the bias field, B' the radial gradient and B'' the axial curvature. B' and B'' are generally given by the winding pattern and the maximum current allowed in the wires, and the trap geometry is changed as a function of the bias field B_0 . The confinement in the axial direction is always harmonic and the corresponding curvature is independent (except for the sign) of B_0 and given by B'' . There are three limiting cases as a function of the bias field:

- For $B_0 = (2B'^2)/(3B'')$, the resulting trapping potential is isotropic and harmonic with a common curvature of B'' . This configuration is generally used for mode-matched transfer of laser cooled atoms into the magnetic trap, and the resulting trap frequency is:

$$\omega_{iso} = \sqrt{\frac{g_F m_F \mu_B}{m} B''} \quad (3.3)$$

- For B_0 slightly larger than 0 (typical values between 300 mG and 1 G) we obtain a compressed cigar-shaped trap. In the axial direction, the potential is harmonic; in the radial direction, the potential is linear far from the center and has a harmonic minimum near the origin. In this tightly confining configuration, one obtains the highest collision rate for evaporative cooling; the trapping frequencies in the harmonic minimum are:

$$\omega_{ax} = \sqrt{\frac{g_F m_F \mu_B}{m} B''} \quad (3.4)$$

$$\omega_{rad} = \sqrt{\frac{g_F m_F \mu_B}{m} \tilde{B}''} \quad (3.5)$$

where $\tilde{B}'' = \frac{B''^2}{B_0} - \frac{B''}{2}$ is the radial curvature which strongly depends on the offset field.

- For $B_0 < 0$, we obtain a situation similar to the above case, except that in the axial direction, we now obtain two magnetic field zeros symmetric to the origin. In the center of the trap, the potential is confining in the radial direction and expelling in the axial direction or vice versa, depending on the product $g_F \cdot m_F < 0$. We have sometimes used this configuration when experimenting with elongated single-beam dipole traps to provide some additional very weak axial confinement. The atomic states in this configuration are high field seekers; the antitrapping in the radial direction in this case is overcompensated by the single beam dipole trap along the axis of the magnetic trap.

A significant simplification of this scheme [93] replaces the original Ioffe bars with a cloverleaf-shaped configuration, resulting in 2π optical access in the radial direction. The cloverleaf trap still requires the quadrature and anti-bias coils for axial confinement and bias field tuning, see Fig. 3.7c). A variant of the cloverleaf trap is the 4Dee trap [94]. This trap drops two of the cloverleaves on each side of the trap and thus achieves both radial gradient and axial curvature with one set of coils. The resulting trapping potential is relatively isotropic, compared to the strongly elongated cigar-shaped potential of the cloverleaf trap.

3.5.1 Magnetic trap concept

The magnetic trap designed for this experiment is a hybrid between the cloverleaf trap and the 4Dee trap and is based on developments by Markus Kottke [95] for the Spinor BEC experiment set up by Holger Schmaljohann and Michael Erhard in Hamburg [82, 84]. The idea is to build an “unbalanced” cloverleaf trap where on each half of the trap two of the leaves feature less windings than the other two. The main features of this trap are:

- In its optimized configuration, the aspect ratio of this trap is somewhat between the strongly elongated cloverleaf trap and the relatively isotropic 4Dee trap. At $B_0 = 1$ G, the aspect ratio is 19.
- It offers the full 2π optical access of the cloverleaf trap
- The trap obtains its strongly confining cigar shape when the current in the bias coils is close to zero, in contrast to the cloverleaf trap which is tightly confining when the field from the antibias and curvature coils almost exactly cancel each other. This has the advantage that the current in the antibias Helmholtz coils can be supplied by a separate power supply, eliminating the need for current control through MOSFETs.
- There is no need for separate z curvature coils, as the confinement in the axial direction is provided by the unbalanced winding pattern of the cloverleaves.

The winding pattern chosen here consists of 6 layers of 7 windings for the strong leaves each covering an angle of 112 degrees and 2 layers of 7 windings for the weak leaves covering an angle of 68 degrees has been chosen. The winding pattern is illustrated in Fig. 3.8.

Additionally, a set of Helmholtz coils providing both the magnetic field gradient for the magneto-optical trap (in anti-Helmholtz configuration) and spatially homogeneous magnetic fields of up to 1 kG allowing manipulation of atoms with Feshbach resonances has been integrated.

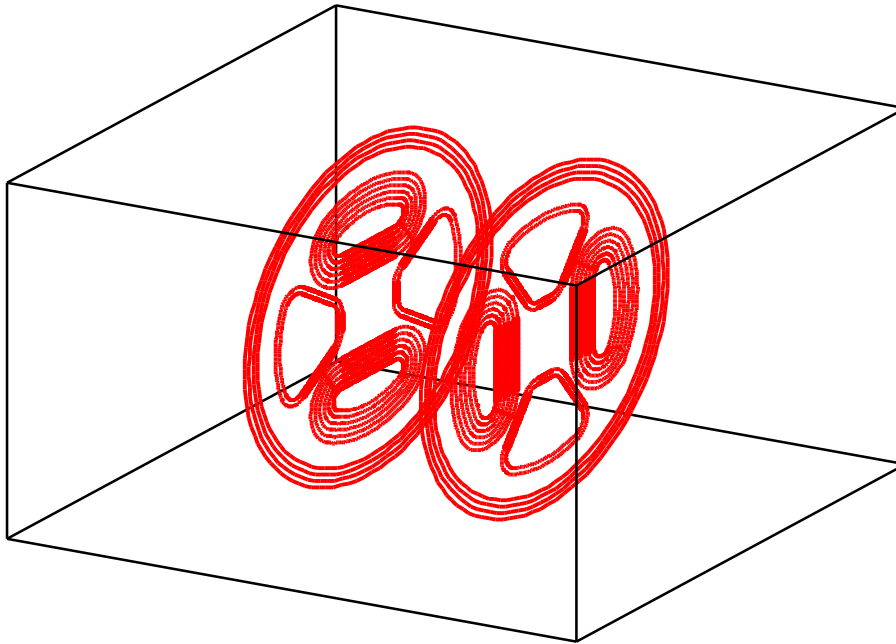


Figure 3.8: Trap winding pattern of cloverleaf / 4Dee hybrid magnetic trap

3.5.2 Trap simulation

Due to the significantly improved simulations using a numerical integration of Biot-Savart's law, it has become possible to predict the resulting trap parameters very precisely (see below) and to calculate the inductivity of the complex winding pattern. The outcome of the simulation is a radial gradient of $B' = 167.7$ G/cm and an axial curvature $B'' = 77.1$ G/cm². This corresponds to a radial ⁸⁷Rb trap frequency of $2\pi \cdot 214$ Hz in the $|F = 2, m_F = 2\rangle$ state for $B_0 = 1$ G and an axial frequency of $2\pi \cdot 11.2$ Hz. The calculated inductivity of the combination of all leaves is 226 μ H. The Helmholtz coil wound outside of the curvature coil consists of 9 windings in 6 layers, producing a calculated magnetic field of 7.645 G/A in Helmholtz configuration and an axial gradient of 113 G/(cm·A) in anti-Helmholtz configuration.

3.5.3 Trap characterization

The magnetic trap has been characterized before being integrated into the experiment by performing a magnetic field scan using a combination of 3 stepper motors and a 3-axis Hall probe. The equipment (see Fig. 3.10) has been developed by Michael Erhard [84] for the spinor BEC experiment in our group. Fig. 3.9(a) shows the obtained field scan for the quadrupole field of the MOT configuration. From the image, one can see that on the symmetry axis of the quadrupole coils, the gradient is twice as large as in the perpendicular direction. The isotropic trap for transfer from the MOT into the magnetic trap is shown in Fig. 3.9(b), resulting from a 243 G offset field, whereas the compressed cigar-shaped trap with an offset field of 1 G is shown in Fig. 3.9(c). Fig. 3.9(d) is a representation of the field of the trap right after mounting with current only in the Dee coils. In this case, we can see that the bias field is overcompensated, leading to the characteristic double-well structure. This overcompensation can be fixed by connecting a few Helmholtz windings in series with the Dee coils (see below).

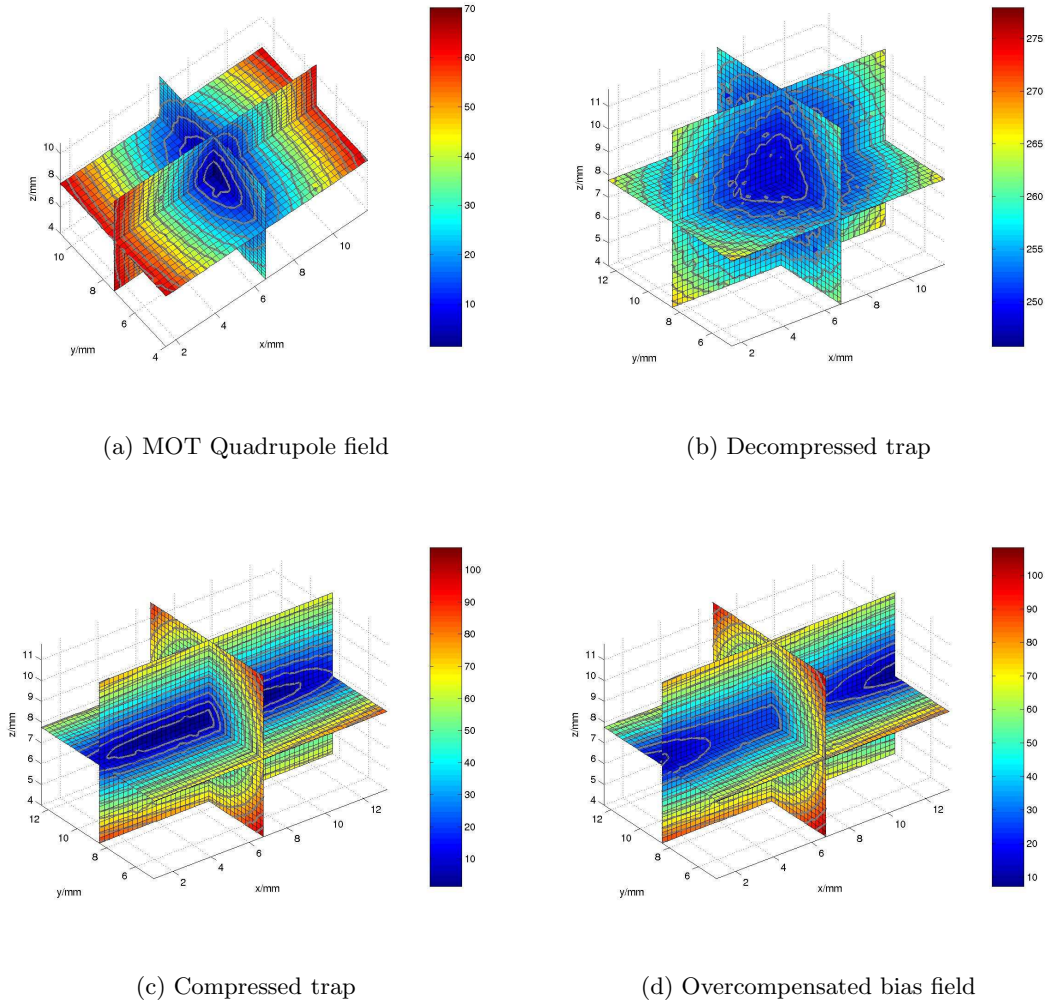


Figure 3.9: Magnetic field scans of various trap configurations. The modulus of the magnetic field is encoded in a pseudocolor representation in Gauss.

From the experimental data of the field scans, we can extract experimental results for the radial gradient and the axial curvature. The agreement with the calculated values as seen in Table 3.1 is remarkable. Note that the inductivity will be discussed in the context of current switching. Details of the magnetic trap characterization can be found in Ralf Dinter’s diploma thesis [96].

3.5.4 Magnetic trap in the experiment

When working with magnetic traps of the Ioffe-Pritchard type, one of the most important aspects is to maintain a stable bias field in the trap. When performing rf induced evaporative cooling, the final frequency of the rf knife is only slightly above the frequency corresponding to the bias field; temporal unintended changes in the bias field can therefore be a source of significant trouble in the experiment. This requirement is somewhat relaxed when the final



Figure 3.10: Stepper motor setup for magnetic field scans

Quantity	Measured	Simulation	Unit
B''	78	77.1	G/cm ²
B'	168	167.7	G/cm
L	237	226	μ H

Table 3.1: Characterization of magnetic trap based on field scan (gradient, curvature) and switch off behavior (inductance). Calculated values are from a numerical solution for the Biot-Savart law.

stage of evaporation is performed in an optical dipole trap, but it is still a key concern. The actual bias field of the trap without any current in the Helmholtz coils is one of the aspects of our magnetic trap that can only vaguely be predicted from field simulation, thereby shining light on the main possible source of bias field instability: the exact distance between the two trap housings. Possible thermal expansion of the trap and temperature drifts therefore should be minimized as much as possible. Our trap has adapted concepts from the spinor BEC experiment in our group which have proved successful in minimizing bias field drifts.

The magnetic trap is cooled by water flowing through the trap housing at a pressure of approximately 2 bar. This water is provided by a separate water cooling system with a 40 to 70 l reservoir. Water from the reservoir is pressed into the trap housing from below by a pump, followed by a pressure regulator. The recycled cooling water is then sent through a heat exchanger cooled by the institute's closed cooling system and sent back into the reservoir. The temperature in the system is measured by a PT100 style temperature probe in the reservoir and controlled by a commercial fuzzy logic self-optimizing regulator which controls the water flow through the heat exchanger on the institute's closed cooling circuit side by means of a motorized valve.

Bias field control is the most sensitive aspect of magnetic trapping; at the same, the bias field of the compressed trap in the absence of current in the Helmholtz coils can only be predicted to within a few Gauss. The field depends a lot on how the trap is wound and on the precise coil distance achieved in the experiment. After the trap has been integrated into the experiment, the bias field is determined by looking for the trap bottom in initial evaporation experiments. A rough compensation is performed by having a few additional Helmholtz windings in series with the cloverleaves. Fine control of the bias field is then

performed as outlined in the following section.

3.5.5 Trap control

The magnetic trap is powered by two Delta Electronica SM45-140 power supplies capable of delivering 140 A at a voltage of 45 V. Needless to say that an interlock system prevents these supplies from working when there is insufficient water flow in the closed trap cooling circuit or when the temperature is too high. It is clear from the previous discussion that switching of magnetic fields and controlling the polarity of the Helmholtz coils is critical to operation of the trap. We control the main current through the cloverleaf magnetic trap by remote current programming the Delta supply from an analog output of the experiment control system. Fast switching is performed using IGBT (Insulated Gate Bipolar Transistor) modules produced by Powerex, now Mitsubishi (PM200HA-24H). These devices have a switching time of a few hundred nanoseconds. Combined with the inductivity of a magnetic trap, this extremely short switching time would lead to an extraordinarily high induction voltage of a few kilovolts upon switchoff, which is far beyond the voltage handling capability of the modules (1200 V). The modules are therefore protected by connecting a varistor across collector and emitter of the device. The varistor will clamp the collector-emitter voltage to a value of about $U_0=800$ V. The coil is thereby “discharged” at constant voltage, and the resulting switch-off time for an initial current I_0 and an inductivity L is given by

$$T = L \cdot I_0 / U_0 \quad . \quad (3.6)$$

For the calculated inductivity of the magnetic trap proper, this results in a switch-off time of 40 μ s as observed in the experiment (see Fig. 3.11, where the voltage across the varistor is plotted as a function of time). The observed oscillatory behavior of the voltage at switchoff is possibly due to capacitive effects in the varistor, but is not seen in the current. Taking into account that the switch-off voltage is not exactly constant, we can calculate the inductivity according to

$$L = \int_0^T U(t) dt / I_0 \quad . \quad (3.7)$$

The result (237 μ H) is slightly larger than the calculated value (226 μ H, see table 3.1), which is due to the fact that the voltage across the varistor is measured, not across the coil. The power supply may introduce some additional non-constant contribution to the overall voltage. Intended just as a check of the calculated inductivity (to be sure that switchoff is fast enough), the agreement is excellent.

Whereas for the cloverleaves, a single IGBT is for sufficient switching, control of current in the Helmholtz coils is more sophisticated. A total of three power supplies is used for the Helmholtz coils; their current is added by means of a set of three diodes. This fulfills several purposes: The delta power supply in constant voltage programming mode can provide the current for the magneto-optical trap gradient field and the bias field for the decompressed magnetic trap for initial trapping of the laser cooled atoms. Its control voltage is then ramped down for compression of the magnetic trap; when its output voltage goes to zero, a HAMEG 8143 supply will take over and provide a current in the range of 400 mA in order to maintain a precise bias field for evaporation. This power supply is remote controlled using an analog modulation input. A third diode allows up to 3 A of current to be sent through the Helmholtz coils produced by one channel of a HAMEG 7044 quadruple power supply, thereby

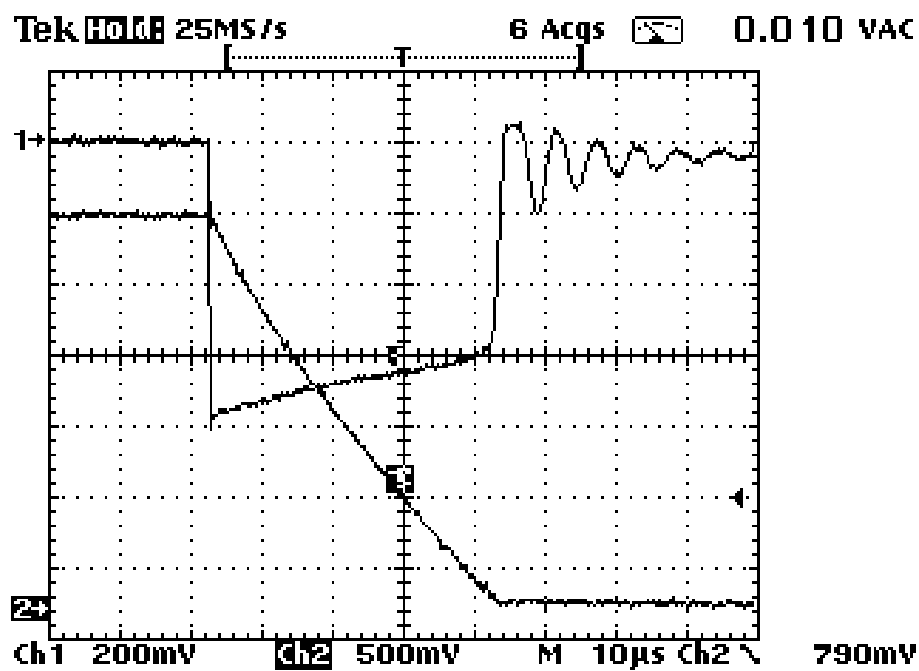


Figure 3.11: Magnetic trap switching behavior. Trace 1 shows the behavior of the varistor voltage upon switchoff; due to the presence of a 1:1000 voltage probe, the oscilloscope reading needs to be multiplied by 1000. Trace 2 shows the behavior of the current, measured through a current transducer (1 V / 50 A)

producing a field of approximately 20 G. The field is controlled by a MOSFET, and used as an offset field for Landau-Zener state transfer in the optical dipole trap.

So far, I have only talked about meeting various current stability requirements; there is also the necessity to change between Helmholtz and anti-Helmholtz configuration for magneto-optical trapping and Stern-Gerlach imaging on the one hand and bias / Feshbach fields on the other hand. The polarity in one of the coils can be changed using a H-bridge configuration of four IGBT modules.

One last IGBT module is located in between the H-bridge configuration and the power supply return. Its function is to provide precise regulation of the Helmholtz current for control of Feshbach magnetic fields; a DANFYSIK ULTRASTAB 867-200I magnetic field probe is used as a current probe for this same purpose.

3.6 Other coils

Besides the magnetic trap proper, there are a couple of other magnetic fields in the experiment. All of these are provided by a compensation cage of three sets of Helmholtz-like coils in the x -, y - and z -direction. Each of these coils consists of three packages of ten windings of 1.2 mm diameter wire. Each of these sets can be connected separately. We use one package per direction for offset field compensation using the other three channels of the quadruple HAMEG 7044 power supply already mentioned above. In the axial (z) direction, one package is connected to a ELA 5 A max. power supply controlled by a MOSFET and used for providing a 1 G bias field for optical pumping and imaging. The third package in this direction is connected to a 20 A power supply which allows us to add a strong bias field for Stern-Gerlach imaging independent of the proper Helmholtz coils which are switched to Anti-Helmholtz for this purpose. Note that the compensation coils will under no circumstances withstand more than 10 A CW; they are protected from accidentally running for a long time at 20 A by means of a slow 10 A fuse.

3.7 Dealing with the gravitational sag

This part of my thesis is motivated by experiments on Fermi-Bose mixtures in dipole traps (chapters 5 and 7) as a prerequisite for being able to confine arbitrary spin states. A special interest is in relatively weak confinement, allowing optical lattice geometries which are as close as possible to a homogeneous situation. The “magic” crossed dipole trap discussed below has allowed us to successfully overcome one of the main limitations of experiments working with atoms with sufficiently different masses. An atom with mass m confined in a harmonic trap with trap frequency ω in the presence of gravity experiences a gravitational sag given by the expression

$$s = -(g/\omega^2) \quad (3.8)$$

This expression is found by calculating the local minimum of the combined potential. Different atomic species and even the different spin states of the same atomic species will in general experience a different trapping frequency when confined in the same magnetic or optical dipole trap, giving rise to a difference in gravitational sag. The importance of this issue depends on the value of the trap frequency. It is generally a non-issue for the compressed magnetic trap or for strong dipole traps. It does however play a significant role in the weak isotropic magnetic trap used for transfer of laser precooled atoms and for experiments in shallow and weak dipole

Trap type	ν_{Rb}	ν_{K}	$s_{\text{Rb}} / \mu\text{m}$	$s_{\text{K}} / \mu\text{m}$	$\Delta s / \mu\text{m}$
Decompr. mag. trap	11.2	16.5	1981	913	1068
Compr. mag. trap	214	315	5.4	2.5	2.9
Far-detuned ODT	50	71	99	50	49
Magic trap	50	50	99	99	0

Table 3.2: Examples for differential gravitational sag in various trap configurations

traps such as the ones used in experiments with optical lattices aiming at a situation close to homogeneous systems. The difference in gravitational sag can then lead to a significantly reduced overlap of the two species. Table 3.2 gives examples of the gravitational sag for ^{87}Rb and ^{40}K in various scenarios. Another possible issue, especially relevant for shallow optical dipole traps is that the presence of gravity can remove the local potential minimum of such a trap, thereby preventing trapping completely. These effects have been seen in the BEC experiment in our group; details can be found in [82].

Let us look more closely both at the weak magnetic trap and at the shallow optical dipole trap. In our experiment, the position of the magneto-optical trap is overlapped with the equilibrium position of ^{87}Rb $|2, 2\rangle$ atoms in the decompressed magnetic trap (2 mm below the trap center of the compressed trap according to Table 3.2). We use magnetic offset fields which are proportional to the MOT gradient in order to achieve fine-tuning of the MOT position independent of the MOT gradient. While this provides optimum transfer for the ^{87}Rb component, ^{40}K is not optimally transferred. The ^{40}K atom number is, however, usually at least two orders of magnitude smaller. If ^{87}Rb transfer is good and ^{40}K is transferred at all, the subsequent compression of the magnetic trap will immediately provide a sufficiently large collision rate and the amount of heating due to mismatched ^{40}K transfer is negligible.

3.8 A magic crossed dipole trap

Let us next have a look at shallow dipole traps. In experiments with bosonic atoms in optical lattices, external confinement with trapping frequencies as low as a few 24 Hz has been used [97], bringing systems closer to a homogeneous configuration. Note that other considerations, such as desired filling factors, may influence the choice of the external confinement. The differential gravitational sag may be overcome to some degree by mean field confinement in a system with strong heteronuclear attraction as in the ^{87}Rb – ^{40}K system. It will become even more important for repulsive interactions – see the discussion in chapter 5. As seen from table 3.2, the difference in gravitational sag for a trapping frequency of 50 Hz is on the order of the extension of the cloud, thereby significantly reducing the overlap of the two samples. This effect could in principle be overcome by applying a magnetic field gradient in the direction of gravity as in experiments with Cs [98]; it would however restrict the range of practically usable spin states and magnetic fields.

The idea for solving this issue was based on the expression for the gravitational sag itself: If we can make the trap frequency in the direction of gravity the same for both species, the gravitational sag will automatically be the same for ^{87}Rb and ^{40}K . In an optical dipole trap, this can be done by a suitable choice of the dipole laser wavelength for confinement in the direction of gravity. This so-called “magic wavelength” can be calculated to be 806.7 nm taking into account contributions from the D1 and D2 lines. The calculation has been performed by

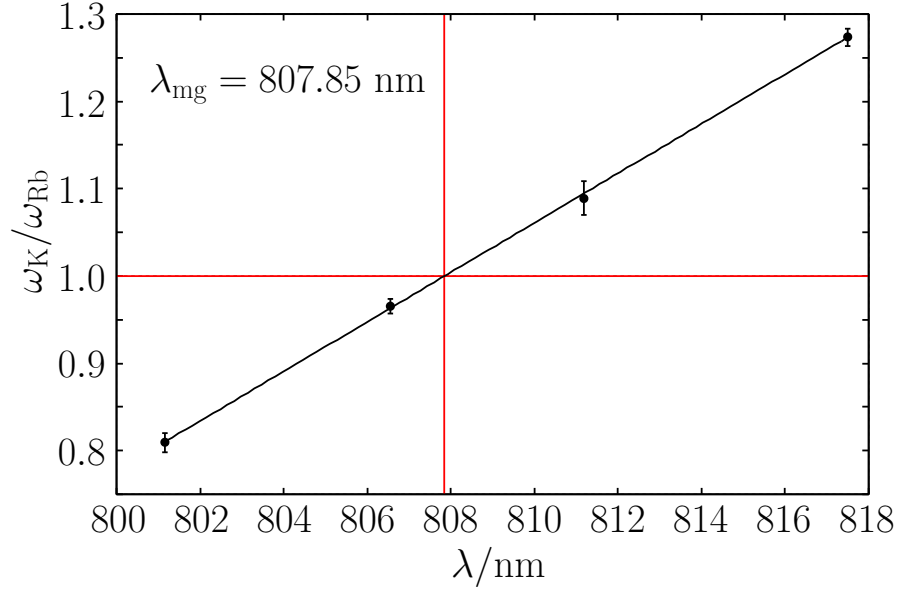


Figure 3.12: Measurement of the magic wavelength for our dipole trap.

Silke and is described in her thesis [66].

With this idea in mind, we first performed a measurement of the magic wavelength by measuring the ratio of ^{40}K and ^{87}Rb trap frequencies in a dipole trap as a function of wavelength and found the magic wavelength to be 807.9 nm (see Fig. 3.12)⁵. Based on this information, a crossed beam optical dipole trap was designed with one beam at the magic wavelength providing confinement in the z and x direction. The potential minimum of the atoms in this beam is made to overlap with the position in the magnetic trap. We tend to hold the intensity of this beam constant. A second beam is derived from our Yb:YAG lattice laser ($\lambda = 1030$ nm) and provides confinement in the y and z direction. This beam is made to overlap with the atomic position in the “magic” beam. This is also the beam that we use for optical evaporation in the crossed dipole trap by lowering its intensity after transfer of atoms into the optical trap. This optical dipole trap allows us to go to weak optical dipole traps ($\omega = 2\pi \cdot 50$)Hz without having issues with reduced overlap of the two clouds. It has been the basis for our experiments on tuning of interactions (chapter 5) and heteronuclear molecules in 3D optical lattices (chapter 7). A detailed discussion of this novel dipole trap can be found in [66].

3.9 Evaporation and state preparation

This section is dedicated to manipulation techniques within the ground state manifold, covering both transitions between individual Zeeman sublevels of one of the two hyperfine ground states as well as transitions from one hyperfine submanifold to the other. The associated frequencies are in the MHz regime (for Zeeman transitions) and in the GHz range for hyperfine transitions. These transitions are used at several stages in the experiment:

⁵The magic wavelength may be influenced by the choice of polarization and spin state. For a comprehensive discussion, see [66].

- **Evaporation.** During evaporative cooling of ^{87}Rb in $|2, 2\rangle$ and ^{40}K in $|9/2, 9/2\rangle$, we drive transitions between neighboring Zeeman sublevels with frequencies between 40 MHz and a few 100 kHz. This corresponds to magnetic field regions in the trap between 50 G and a few 100 mG. Assuming thermal equilibrium between ^{40}K and ^{87}Rb , evaporation mostly affects ^{87}Rb . This is a result of

$$\nu_{\text{Rb}}/B = g_F m_F \mu_B / h = 700 \text{ kHz/G} \quad , \quad (3.9)$$

whereas

$$\nu_{\text{K}}/B = 311 \text{ kHz/G}. \quad (3.10)$$

- **Zeeman state preparation at low fields.** At magnetic fields of 20 G, the quadratic energy splitting between the sublevels of the ground state in ^{40}K and ^{87}Rb allows separate addressing of individual transitions. By describing the atom-rf interaction in a dressed state picture, one obtains a series of avoided crossings in the energy spectrum as a function of radio frequency. By sweeping the radio frequency across the individual Zeeman resonances, arbitrary spin compositions can be produced within one hyperfine manifold. This technique has been discussed in detail e. g. in [84, 99].
- **Hyperfine transfer.** The above Zeeman manipulation technique can be generalized to hyperfine transitions. In general, transitions have been used which allow the assumption of a two-level system. By sweeping a microwave frequency close to the ^{87}Rb hyperfine splitting, ^{87}Rb can be transferred from the magnetically trapped $|2, 2\rangle$ state to the $|1, 1\rangle$ absolute ground state where heteronuclear Feshbach resonances occur (chapters 5 and 7). The same technique has also been used to transfer ^{40}K from the $|9/2, -7/2\rangle$ state to the upper hyperfine manifold at magnetic fields around 547 G.
- **Rf spectroscopy.** At magnetic field values around the heteronuclear Feshbach resonances used in this thesis, the energy separation between the ^{40}K $|9/2, -7/2\rangle$ and $|9/2, -9/2\rangle$ states is about 80 MHz. This transition is used for magnetic field calibration in chapters 5 and 7 as well as for rf spectroscopy to measure interaction shifts and binding energies in chapter 7. In the latter case, Gaussian amplitude modulated pulses have been beneficial in order to obtain a quasi-Gaussian frequency response of the atomic system to pulses and improve the energy resolution.

This section describes a versatile frequency synthesis setup which has been used to generate all of the above frequencies and fulfill the corresponding modulation requirements. The setup can be used in order to fulfill in principle arbitrary frequency, phase and amplitude modulation requirements on time scales down to 5 ns with a minimal experimental complications.

3.9.1 Versatile frequency control

The rf / microwave manipulation setup described here has been crucial to all of the experiments presented in this thesis. The versatility and simplicity of operation as well as the precise timing down to the nanosecond level has greatly enhanced the experimental possibilities and tremendously reduced the usual rf and evaporation debugging. The setup was developed based on the observation that many of the commercially available frequency generators provide a plethora of modulation options, whereas they are usually unable to rapidly and accurately perform for example simple linear frequency sweeps or AM modulation with a

given envelope. The usual Rapid Adiabatic Passage (RAP) sequences for Zeeman state preparation require sweep times on the order of 10 ms, whereas the dwell time of many commercial synthesizers, i. e. the time duration of each individual “slot” in a linear sweep, is limited to precisely 10 ms. Most experiments work around this issue by operating these generators in FM modulation and sweeping the FM modulation control voltage. This approach is not very versatile, it sacrifices expensive analog output channels and many devices require long times for switching such as from fixed frequency operation to FM. I have seen delays as long as a second, and due to this inflexibility, one usually ends up with a whole stack of these expensive devices just for a couple of sweeps, and all of them want to be programmed separately.

Here, I will describe a solution which relies on *one* versatile and precise synthesizer which controls all of the rf and microwave transitions in this experiment. The setup is based on a device developed by Thilo Hannemann, at the time in the group of C. Wunderlich at Hamburg, now Siegen. The synthesizer (VFG-150) developed by Thilo Hannemann is based on FPGA technology, allows frequency, phase and amplitude to be updated every 5 ns and generates frequencies between a few kHz and 150 MHz. It has been developed for quantum computation schemes with trapped ions in order to apply pulse sequences known from the NMR literature to realize quantum gate operations through selective addressing with microwave radiation in magnetic field gradients. The device is programmed via a fast USB 2.0 link from a host computer. This link can sustain data rates >50 MB/s. The device’s internal buffer allows about 1000 “modulation slots” to be stored. This means that “short” sweeps are possible with a resolution of 5 ns and not exceeding the internal buffer of 1000 slots. “Long” sweeps with more than 1000 “slots” can be run with a dwell time of shorter than 200 ns. In addition to its rf output, the device has four optically isolated digital outputs and a trigger input which can be used to synchronize it with external events. A frequency reference input allows the internal reference frequency to be locked to an external high-quality low-drift frequency reference. This device can be used directly for evaporation on Zeeman transitions, for rf spectroscopy on ^{40}K as described in chapter 7 and for state preparation using rapid adiabatic passage within the ground state manifold. When higher frequencies were required, the output of the VFG has been mixed with a fixed frequency reference close to the desired frequency range. This has been done by connecting its rf output to the input of an rf multiplexer which is digitally controlled by two of the four digital outputs of the VFG. One of the four outputs of the rf multiplexer is directly connected to an rf amplifier and an rf antenna for the frequency range from a few kHz to 150 MHz. The other three are connected to mixer setups for various microwave transitions as described below.

When it came to integration of this incredibly versatile device into the experiment, several approaches could have been pursued. One would have been to directly implement support for this USB 2.0 connected device in the experiment control software which to date supports analog and digital channels as well as National Instruments VISA devices. The disadvantage would have been that

- Over time, adding more and more classes of devices makes the experiment control software overburdened and difficult to understand and maintain.
- The experiment control computer may be overburdened with the load, since for fast sweeps, a low latency is critical.

The solution was to keep things simple and implement a separate piece of software controlling the VFG over the USB link. This piece of software listens on a TCP/IP port of its host

computer for incoming network connections and expects modulation commands in a simple syntax developed for this purpose. Within the server application, these are translated into sequences of slots in the wire level protocol of the VFG USB link. Since the National Instruments VISA library admits TCP/IP connections besides the more commonly used GPIB, parallel or serial port device classes, this allows integration into the experiment without any modifications to the experiment control software and without sacrificing its versatility. Also, the control software can run on the same computer as the experiment control software or on a different host. In practice, I have always run it on one of our two CCD control computers. The remaining question is how we synchronize the VFG timing with the rest of the experiment, since delays on TCP/IP links and in the underlying network stack of the operating system can be considerable. The solution consists in preprogramming the full sequence over the VISA link and then triggering various key points through the digital trigger input of the VFG connected to a digital output of the experiment control DSP system. For a description of the VFG server software syntax developed as part of Manuel Succo's diploma thesis, see [99].

3.9.2 Hyperfine manipulation

Here, I will briefly describe the approach followed in this thesis for manipulating the atomic hyperfine state, in particular for ^{87}Rb . In their experiments on $F = 1$ spinor BECs, the BEC experiment in our group had initially used a Raman laser setup in order to transfer a condensate from $F = 2$ to $F = 1$. For this thesis, a setup based on direct microwave coupling has been developed and implemented, which has later been ported back to the BEC experiment in order to produce $F = 2$ condensates from $F = 1$ condensates obtained through direct evaporation. The scheme is a simple extension of rapid adiabatic passage within one hyperfine manifold to hyperfine transitions. Due to the nature of the transitions (principally the $|2, 2\rangle \rightarrow |1, 1\rangle$ transition), we can generally assume a two-level system. The oscillating B field which is used to drive these transitions is perpendicular to the axis of quantization. Following discussions with Th. Fickenscher at Universität der Bundeswehr (HSU), Hamburg, it seemed easiest to use a cut-off microwave waveguide in order to produce the required oscillating B field. Such a waveguide has a rectangular shape and produces a B field along the long axes of its cross-section. The waveguide fits perfectly directly below the science chamber glass cell with a distance of about 4 cm to the trapped atoms. In this near field regime, the field at the location of the atoms is well approximated by the field distribution in the waveguide for our purposes. Since waveguides are usually not designed to be operated with an open end, a significant fraction of the microwave power may be retroreflected into the amplifier and even destroy the latter or adversely affect its performance. I have never seen more than -10 dB of retroreflected power in the experiment, which may be due to the additional metallic elements (magnetic trap coils, vacuum vessel) modifying the near field behavior and reflection properties at the open end. Nevertheless, it is a good idea to protect the amplifier by using a circulator and a proper high-load termination behind the amplifier.

It was initially unclear how much microwave power would be required for RAP, and initial experiments were performed using a 20 W solid state amplifier. In practice, we have never exceeded 1 W of microwave power due to the efficient waveguide "antenna", and after a defect of the 20 W amplifier, we have used a much less expensive 1 W solid state amplifier from Minicircuits. So in order to transfer ^{87}Rb atoms from the magnetically trapped $|2, 2\rangle$ to the high field seeking $|1, 1\rangle$ absolute ground state (magnetic field sensitivity of the transition ca. 2.1 MHz/G), a 10 ms long 400 kHz sweep over the hyperfine transition at 20 G is fully

sufficient to transfer ^{87}Rb with almost 100% efficiency from one hyperfine state to the other.

The remaining question is how to generate these rapid sweeps on the microwave transition. As mentioned above, the microwave frequency is generated by mixing the VFG output with a fixed reference frequency close to 6.8 GHz. In this case, the fixed reference is a Rohde & Schwarz SMR 20. Its output is sent into a double-balanced mixer from Minicircuits, and the other input port of the mixer is connected to one of the VFG multiplexer output ports. In order to not sacrifice too much of the output power of the final amplification stage in useless sidebands, a cavity bandpass filter is used to filter out only the upper sideband of the mixing process. Alternatively, an SSB mixer might have been used.

Another application of such an up conversion is ^{40}K . Manuel’s diploma thesis [99] has a discussion of methods for 1.3 GHz. At the end of the studies presented in chapter 7, it was beneficial to be able to drive ^{40}K hyperfine transitions at high magnetic fields; the corresponding transitions were on the order of 2.4 GHz. While WLAN equipment can be used in this frequency range, good results were also achieved using a single turn coil-shaped device in combination with double-stub tuning for “impedance matching”.

A third application of this setup consisted in the initial field calibration method for Feshbach spectroscopy where the ^{87}Rb $|1, 1\rangle \rightarrow |1, 0\rangle$ transition was used. For magnetic fields around 547 G, this transition occurs at 355 MHz. The transition has been driven using a 2 W amplifier from MTS Systemtechnik operated way beyond its frequency specification and a directly connected single turn coil-shaped device; the 355 MHz signal has been generated using the VFG, mixed with the fixed frequency output of a Rohde & Schwarz SML 02.

To summarize the state preparation discussion, the highly versatile frequency generation setup based on the VFG synthesizer has fulfilled all the requirements of this thesis for advanced state manipulation and rf spectroscopy, as will also become clear from chapter 7 with “plenty of room at the bottom” both in terms of time resolution and possible extensions of modulation schemes and complexity. Only a fraction of the potential of this scheme has been necessary to use in this thesis, yet the scheme is both very simple to apply in the experiment and highly cost-effective.

3.10 Optical lattice setup

In this section, I will present the optical lattice setup realized within this thesis and used for the measurements presented in chapter 6 and 7. The lattice laser described here has of course also been used for the measurements in optical dipole traps discussed in chapter 5.

The lattice setup used in this experiment is based on three mutually orthogonal retroreflected standing wave laser beams. All beams have mutually orthogonal polarizations in order to avoid interference between the different beams. Moreover, a frequency difference of at least 10 MHz is introduced between individual beams by means of an AOM. This ensures that any cross-interferences between the beams are averaged out over the experimentally relevant time scales.

Together, these three laser beams create spatially modulated intensity pattern. This 3D standing wave creates a perfect periodic potential for atoms confined in the intersection of the three lattice laser axes.

I will start my discussion of optical lattices with considerations which influence the choice of the lattice laser wavelength and the laser source. Based on these considerations, an ELS VersaDisk Yb:YAG disc laser with a specified power of 20 W has been chosen for this ex-

periment. While offering a high output power, these lasers have never been used in optical lattice experiments so far, and an analysis of the frequency noise of the laser source showed that a frequency stabilization would be necessary in order to avoid heating in the lattice. A scheme for frequency stabilization is presented; the required bandwidth has only been achievable by modifying elements in the laser cavity itself, resulting in a combination of power and linewidth of >20 W and 20 kHz short term. In order to avoid parametric heating due to intensity fluctuations and in order to increase the reproducibility of the system, an intensity stabilization for the optical lattice has been implemented together with O. Wille [100].

The optical setup realizing this 3D standing wave configuration is described, including overlapping with the magneto-optical trap beams and a discussion of imaging along the lattice axes. The latter is an essential prerequisite for lattice adjustment and diagnosis.

As part of this thesis, I have also looked into extensions of this scheme which might prove useful for this setup in future experiments and also added the relative options to the design of the lattice / MOT setup. Ideas developed in this context have influenced the design of this experiment and may be used later for transport measurements in accelerated optical lattices. More details on these options are given in appendix C.

3.10.1 Lattice laser system

The choice of the lattice laser system is influenced by several boundary conditions:

- **Wavelength.** The wavelength of the laser source determines the detuning from the main atomic resonances. For a given atomic species, it therefore determines the relationship between power and lattice depth. While for far detuned lattices, this is a mostly technical consideration in single species experiments, there are important considerations when working with multiple species in the same lattice. In general, for the same total laser power, tunneling will be different for both species, and the choice of the wavelength is a choice of the relative mobility of both species.
- **Power.** At the wavelength of choice, spectrally narrow single frequency lasers with the necessary output power to achieve deep lattices may not be available.
- **Spectral quality.** Frequency jitter of the lattice laser frequency directly translates into translational jitter of the lattice laser interference pattern and can be a source of significant heating. In order to assess the importance of this effect, the frequency domain of the jitter is important. Slow drifts of the laser frequency over a timescale of seconds are completely harmless, whereas frequency noise happening at the trapping frequency in the optical lattice can severely limit the lifetime in the lattice.
- **Intensity noise.** Intensity noise coupling to the band separation can also cause significant heating. Intensity noise can to some degree be compensated for by using a fast intensity servo.

The design of our experiment is based on creating the interference pattern for the optical lattice at the same position where a two-species 3D-MOT and a magnetic trap are present. This imposes some boundary conditions: From the beginning, we opted for overlapping the lattice beams with the magneto-optical trap beams in order to preserve the excellent optical access. As a consequence, the wavelength had to be sufficiently far detuned from the atomic

resonance lines so that dichroic mirrors would allow overlapping the optical lattice beams with the two-species MOT beams.

Taking together all the available options in terms of laser power and available wavelengths, we opted for a wavelength of 1030 nm, where high power Yb:YAG disc lasers were available. At this far detuned wavelength, lattice potentials for K and Rb are approximately equal; this is different when the lattice depth in units of the atomic recoil energy

$$E_r = \hbar^2 k^2 / 2m \quad (3.11)$$

is considered, setting the scaling behavior for tunneling and interactions in terms of the particle's mass. In this sense, for equal absolute potentials, tunneling is about twice as likely to occur for ^{40}K as for ^{87}Rb .

The following sections discuss both frequency and intensity stabilization for the lattice laser source as well as the actual lattice setup at the experiment.

3.10.2 Frequency stabilization

The light for the optical lattice setup is produced by a commercial 20 W Yb:YAG disc laser (VersaDisk) manufactured by ELS. The disc laser is basically a diode pumped solid state laser where the active medium is a thin Yb doped YAG crystal glued onto a copper mount. This allows the generated heat to be removed efficiently. A thin etalon in combination with a birefringent filter ensures single mode operation of the laser; the resonator geometry is a linear Fabry-Perot cavity. The specified linewidth of the laser is 5 MHz, measured over 50 ms, so an external frequency stabilization would be required in order to further quench the linewidth.

Previous attempts at stabilizing these lasers that I have heard of have focused on absolute stabilization to an atomic reference line and have made no attempt at reducing the short term linewidth of the laser. For the optical lattice, short term stability is important; within this thesis, stable single mode operation of the lasers locked to the reference cavity has routinely been achieved over 5-10 hours at a short time linewidth of 20kHz; I will hence discuss the scheme in some detail.

The frequency stabilization used in this thesis is based on FM (frequency modulation) spectroscopy of the light reflected from an optical reference cavity (Pound, Drever, Hall) and has been described in [101]. The setup is shown in Fig. 3.13. A small portion of the output beam from the laser is sent through an Electro-Optic Modulator operated at a frequency of 17 MHz given by the resonance frequency of the LRC enhancement circuit connected to its electrodes. The EOM imprints sidebands separated by the modulation frequency from the carrier onto the laser light. The light is then coupled into a confocal cavity. The fraction reflected from the cavity is detected on a fast photodiode; the signal component at the modulation frequency is filtered out by mixing it with the modulation frequency.

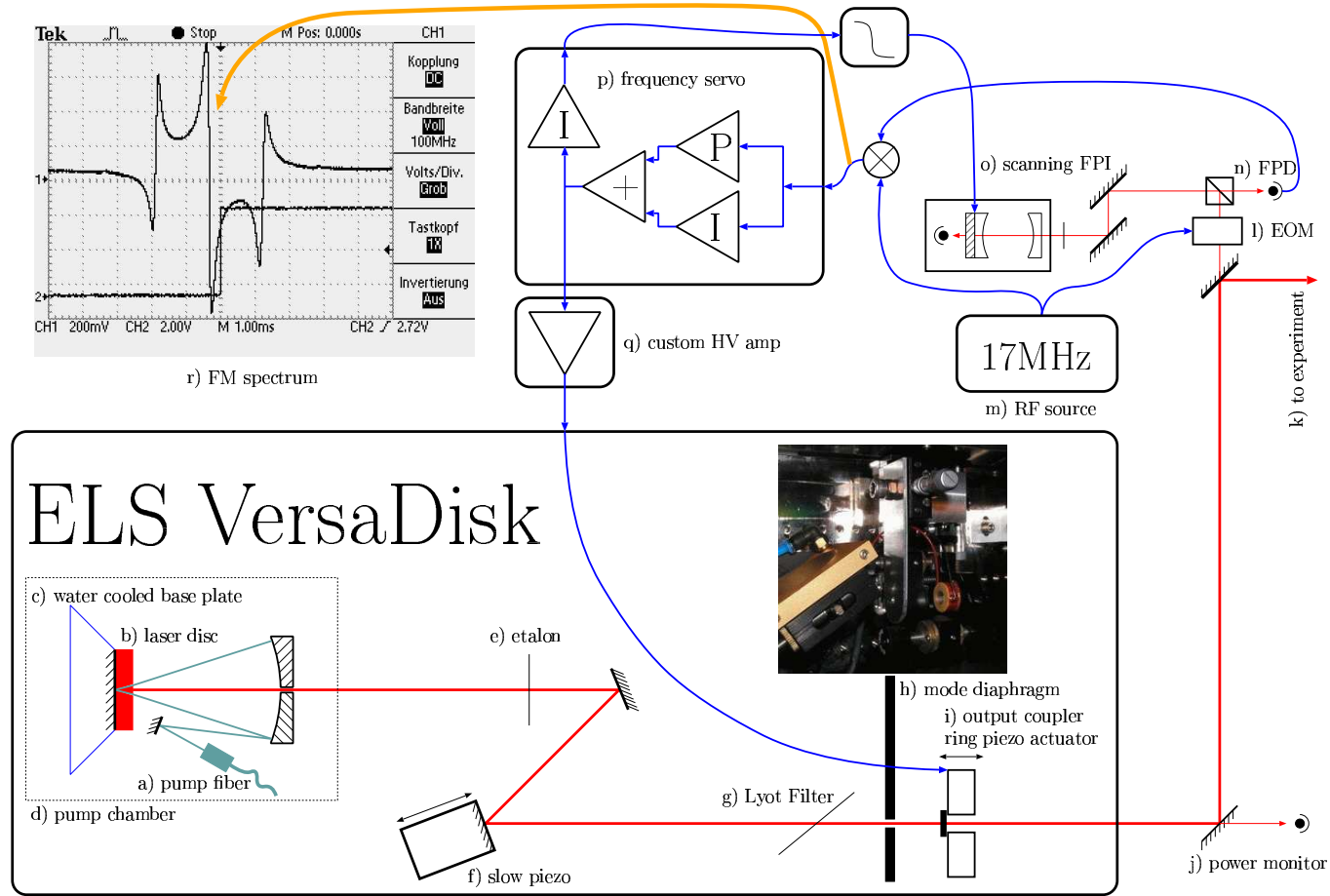


Figure 3.13: Lattice laser frequency stabilization setup. The lower part of the image shows the VersaDisk lattice laser and the modifications to the laser cavity for frequency stabilization. The upper right part shows the spectroscopy and servo setup; top left: FM spectroscopy signal.

A first step in the frequency stabilization consisted in analyzing the spectral distribution of the frequency noise of the laser. This was performed by using a low finesse cavity (finesse $\mathcal{F} \approx 15$). This realizes the limit of FM spectroscopy where the linewidth of the medium is large compared to the modulation frequency and where the observed line shape is the derivative of the absorption (or reflection) coefficient. The line has a wide central zero crossing with the two central extrema about 100 MHz apart. Since the central zero crossing is linear within the expected frequency excursion range, this can be used to characterize the spectral distribution of frequency noise. Most of the frequency noise was found to happen at frequencies in the acoustic range below 1 kHz, consistent with the statement by the manufacturer that the noise could be produced by turbulent water flow in the cooling plate of the laser disc.

A first attempt to compensate for this acoustic noise was performed using a mirror mounted on pre-stressed piezo element (Piezomechanik HPSt 150/14-10/12 VS22) inside the laser cavity and provided by ELS. While it was possible to lock the laser frequency to the cavity resonance, the result was disappointing – with optimized lock parameters, the lock merely compensated for the long-term drift of the laser frequency relative to the cavity, but it was not possible to tighten the servo loop and reduce the short-term linewidth. On the other hand, it was easy to lock a cavity with a (relatively) high finesse of $\mathcal{F} \approx 500$ and an internal piezo element to the laser output frequency and obtain a residual short term linewidth of about 20 kHz. It was therefore clear that the reason for the bandwidth constraint would be found in the laser itself, and more precisely in the pre-stressed piezo.

This picture was confirmed by measuring the bandwidth of the piezo using the low finesse cavity. The laser frequency was manually held at the central zero crossing of the cavity resonance, and a modulation signal plus a dc offset from the generator output of a Rohde & Schwarz UPV audio analyzer applied to the piezo element. The frequency response of the laser was measured in the central zero crossing of the FM spectroscopy signal using the audio input of the UPV. The result can be seen in Fig. 3.14. The frequency response of the piezo exhibits several pronounced resonances between dc and 4 kHz; the most prominent one is at 2.8 kHz and (at least in Fig. 3.14) has a total gain increase of 3. In fact, the situation is much worse because for these large resonance oscillations, the signal has long left the central linear portion of the FM spectroscopy signal. The estimated increase in gain is about 10. This was clearly the reason why, using this piezo actuator, a frequency lock with a bandwidth of 2 kHz was impossible to achieve.

Since the piezo actuator has a specified intrinsic resonance frequency significantly above 10 kHz, and the mirror glued onto the mount was not heavy enough to significantly alter the behavior, the reason had to be the mirror mount in which the actuator was sitting. Specifications of the dynamical behavior of piezo actuators usually assume that the actuator is fixed to some infinitely heavy object on one end. The large oscillations in the system were due to the fact that already at 1 kHz, dynamic forces of piezo actuators can be on the order of several 10 N, even when moving small masses. The mirror mount is simply not able to withstand the back-action of the moving piezo.

In order to resolve this issue, the laser cavity had to be modified to provide a faster “tuning knob”. In a first attempt, the original piezo was replaced by a very small stack actuator (PI Picma PL055.31) and a 0.7 mm diameter and 0.8 mm thick mirror glued on top of it. The frequency response of this element was flat up to 30 kHz, and it was possible to achieve a 20 kHz linewidth relative to the high finesse cavity immediately. Over time, the scheme nevertheless showed some limitations, notably the presence of strong stray reflections from the thin etalon. Using a small mirror, these reflections would not be reflected onto the laser

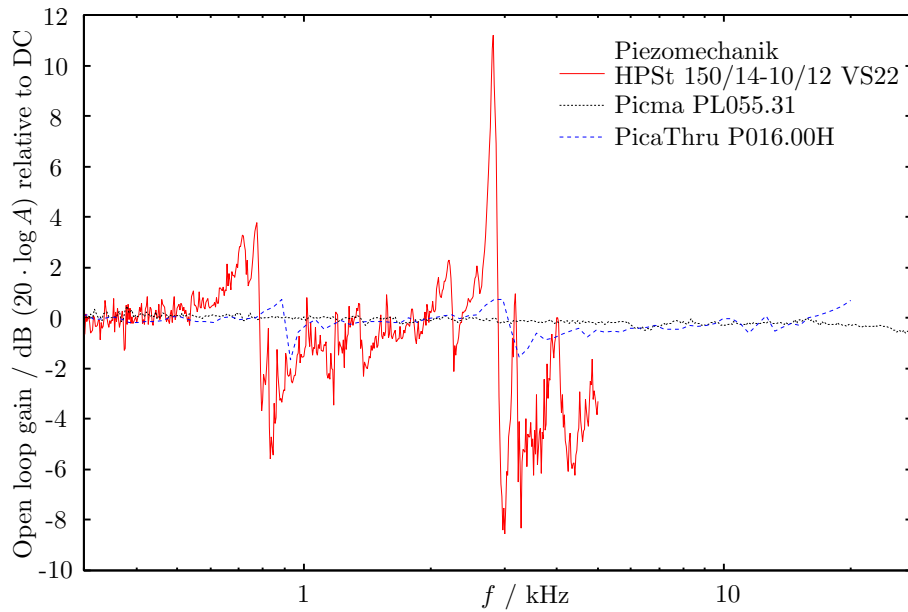


Figure 3.14: Bandwidth of piezo actuators used in the VersaDisk and measured with a low finesse cavity. The performance of these actuators is relative to the mounting; the relatively large moving mass and mounting in a mirror mount is the main reason for the many mechanical resonances in the Piezomechanik actuator. Its specified resonance frequency when fixed to a rigid wall is 15 kHz. The PicaThru actuator used in the final setup still features some (much smaller) resonances at roughly the same positions as the Piezomechanik actuator. This indicates that the origin of the resonances is really the mirror mount in which all piezos were mounted, combined with a large moving mass. In the case of the PicaThru actuator, the resonant behavior is so small that it has not affected the possibility to use the Piezo for frequency stabilization.

housing wall by the mirror, but instead heat up the mount to sometimes 50°C . The solution that would overcome all of these issues was to use a ring actuator (PI PicaThru P016.00H) at the output coupler with a tiny mirror glued onto it and a mode diaphragm on an xy translation stage directly in front of the output coupler. The solution developed in this thesis is shown in Fig. 3.13; note that the original “slow” actuator has been put back into its original position. Using the fast actuator on the output coupler, any short-term acoustic frequency jitter can be compensated. The mode diaphragm has proven beneficial in maintaining a stable spatial output mode of the laser and protects the ring actuator from reflections that might still be present in the resonator. The ring actuator suffers from significant bending when operated over its full specified 1 kV voltage range; it is therefore desirable to operate the latter at a fixed average voltage in order to maintain the same output power.

This is performed using a servo loop with two different output paths. One relatively fast PI regulator acts onto the output coupler (note the presence of a voltage amplifier to achieve a 0-200 V piezo voltage). The average voltage can be maintained at about 100 V by carefully having the reference cavity follow the laser drift on a timescale of seconds using the piezo actuator inside the reference cavity. The latter is controlled using a very slow integrator and additional low pass filtering at the second output of the regulator. The advantage of this lock scheme is that the ring actuator is always run at the same average voltage and maintains a constant output power. Moreover, the laser will always run where it prefers to; forcing it to follow the cavity could also quickly break the lock because of the relatively small longitudinal resonator mode spacing of about 200 MHz. In addition, the cavity does not need to be temperature stabilized at all since it will automatically remain resonant with the laser. Note that this scheme relies on the fact that an absolute frequency stabilization is not required for an optical lattice setup, but short term stability is important.

Using the setup presented in this section, the laser frequency remained locked to the reference cavity for hours once the experiment was up and running; some nights, we have forgot about the frequency lock altogether until the early morning when an acoustic signal connected to the regulator indicated that the laser had left the lock after more than ten hours stable single mode operation.

3.10.3 Intensity stabilization

Intensity stabilization for the optical lattice and for all dipole traps was an essential prerequisite in the optical lattice experiments described in this thesis. It makes the confinement independent of laser intensity fluctuations and drifts, provides reproducible operation from day to day as long as enough light is coupled into the optical fibers and allows a very flexible characterization of the lattice depth by modulating the set value of the regulator and observing parametric heating. Together with part of the frequency stabilization, our locking scheme has been developed by Oliver Wille as part of his diploma thesis [100].

The idea of the setup is the following: optical fibers are used to deliver optical lattice and dipole trap beams to the experiment proper. Behind the optical fiber, a pickup sends a small fraction of the light onto a photodiode (Thorlabs PDA255-EC). The regulator compares the measured intensity to a set value from the computer and compensates for non-zero error signals by adjusting the rf power in an acousto-optic modulator in front of the optical fiber. When designing the stabilization, the goal was to achieve a high bandwidth of the servo loop. For moderately deep optical lattices, parametric heating occurs at frequencies of several 10 kHz, and the servo loop should be able to suppress any noise at these frequencies. In achieving a

bandwidth of roughly 100 kHz, we found that the main limiting factor is the choice of the rf attenuator used for controlling the intensity through the AOM. The AOM itself can switch off the light on time scales significantly below 500 ns, depending on adjustment. Many VCAs (Voltage-Controlled Attenuator) either feature high nonlinearity, thereby practically limiting the bandwidth, or a modulation input with a large overshooting behavior (such as the ZX-73 from Minicircuits or the RVA-2500). It turned out that the best solution is to use a mixer and control the rf power coupled from LO to RF by means of a voltage applied to the IF terminal. The mixer has the disadvantage of being insensitive to the polarity at the control port. A diode in series with the control signal is therefore necessary in order to avoid inverting the loop gain. The regulator also features a digital control input which allows resetting of the integrator in the regulator and nulling of the output while the respective beam is not used. Since the achievable rf extinction of the mixer is not perfect, it can be beneficial to also connect the disable signal for the regulator to the digital rf on/off input of the VCO box generating the rf itself.

Another feature of the intensity regulation is the presence of two modulation inputs, one for “slow” modulation and one for “fast” modulation. The slow modulation input can be used for frequencies within the bandwidth of the regulator, i. e. for frequencies up to 100 kHz. It is internally added to the set value input. We have used this input in connection with a gated frequency generator in order to determine the depth of the optical lattice for a given set value by means of modulation spectroscopy. The transition used for this measurement is a direct excitation from the first to the third band of the optical lattice and a measurement of the excitation spectrum can be compared to a band structure calculation in order to determine the lattice depth calibration factor.

The “fast” modulation input is added directly to the output of the regulator and may be used for modulation significantly above the bandwidth of the regulator. It may be used for modulation spectroscopy in very deep lattices, although care has to be taken since the response in terms of intensity modulation depth depends on the set value of the regulator.

3.10.4 Lattice setup

Fig. 3.15 shows a general view of the beam preparation scheme for the optical lattice setup. Behind an optical diode and pickups for laser power monitoring and frequency stabilization (see 3.10.2), the light from the lattice laser is split up into 4 independent beam paths using polarization optics. Each of these beam paths has an AOM in single-pass configuration for intensity control and is coupled into an optical fiber (fc-apc – fc-apc to avoid back-reflections from the fiber end surfaces and resulting superlattices). All of the AOM frequencies are detuned by roughly 10 MHz with respect to each other in order to make the interference terms in the experiment between the individual beams so fast that they are averaged out on any experimentally relevant time scale. Three of the beam paths are used for three orthogonal retroreflected lattice beams with mutually orthogonal polarizations, and one of them is used for one of the two beams of the “magic” crossed optical dipole trap.

After passing through the optical fiber, each of the lattice beams is collimated and focused using the scheme developed in Oliver Wille’s diploma thesis [100] which relies on one lens for reducing the numerical aperture of the beam leaving the fiber, a second lens for collimation, a pickup for intensity stabilization as discussed in 3.10.3, a polarizing beam splitter cube to produce a fixed polarization and a third lens with a focal length of 400 mm to focus the beam down to its final size. Having passed this third lens, the lattice beam is delivered to the

atoms using one adjustable mirror with precision micrometer screws and one last fixed mirror which is the edge filter overlapping the lattice beam with the MOT beam. After initial course adjustment, additional degrees of freedom needed for lattice fine adjustment are provided by a lateral displacement of the focussing lens using a pair of translation stages.

The standing wave configuration for the optical lattice is produced by separating the MOT and lattice beams again after passing the glass cell using an identical “disentangling” edge filter, recollimating the beam using a second lens identical to the focussing lens and retroreflecting it using a mirror. Not shown in Fig. 3.15 are imaging systems in all of the three lattice axes and the two dipole beams. Along the horizontal (LA) lattice axis, imaging is performed using the optical pumping beam. This axis can also image the LA lattice beam and the “magic” beam of the crossed dipole trap onto the CCD chip. On the diagonal axes, the MOT beams are used for imaging. In the direction of the main detection axis, the 1030 nm beam of the crossed dipole trap can also be imaged.

Three of the four detection systems share the direction of detection with a pair of MOT beams. This means that the detection light which is to be imaged onto the camera needs to be somehow separated from the counter-propagating MOT beam which has of course exactly the same wavelength. This has been realized using flipper mirrors installed between the “disentangling” edge filter in the counter-propagating MOT beam path and the next MOT mirror. The flipper mirror is moved into place during evaporative cooling and directs the detection light through a two-lens imaging configuration onto a CCD chip.

3.11 Imaging

In this section, I will show how information about the atomic samples stored in magnetic traps, dipole trap or optical lattices is obtained. The technique used in this thesis, absorption imaging, is now discussed in many introductory texts, e. g. [75]. It relies on sending a resonant light beam onto the atomic cloud which absorbs photons and scatters them into 4π . The shadow cast by the atoms is imaged onto a CCD chip using a set of lenses. Here, I will only discuss destructive imaging. Non-destructive imaging techniques such as phase-contrast imaging would allow one to observe the time evolution of a single sample which may be interesting for example in connection with the mean field collapse. For the experiments described here, destructive imaging fulfilled all the experimental requirements.

The standard resonant imaging procedure is based on taking three to four different images. After releasing the atoms from the trap, a first image, \mathcal{A} (absorption image), is taken. This is essentially an image of the detection laser beam with the shadow cast by the atoms. This image is usually very ugly to look at, since it contains all of the beam imperfections of the imaging beam and the interference features which arise as a result of the spatially coherent nature of the light which is being used for imaging. As such, it is of little use for extracting any quantitative information on the sample. A second image, \mathcal{R} (reference image) is taken as soon as the CCD camera is ready for the next image. The image is taken with the same exposure time and intensity as \mathcal{A} , but without any atoms in the field of view of the imaging system. These have either fallen out of the imaging area by the time the exposure is made or wear some other “cloak of invisibility” (see discussion below). By taking the ratio \mathcal{R}/\mathcal{A} , one can thus eliminate the laser beam profile through image processing.

In some experiments, there may be a disturbing background signal which is present even in the absence of any imaging light. This should generally be suppressed as much as possible, but

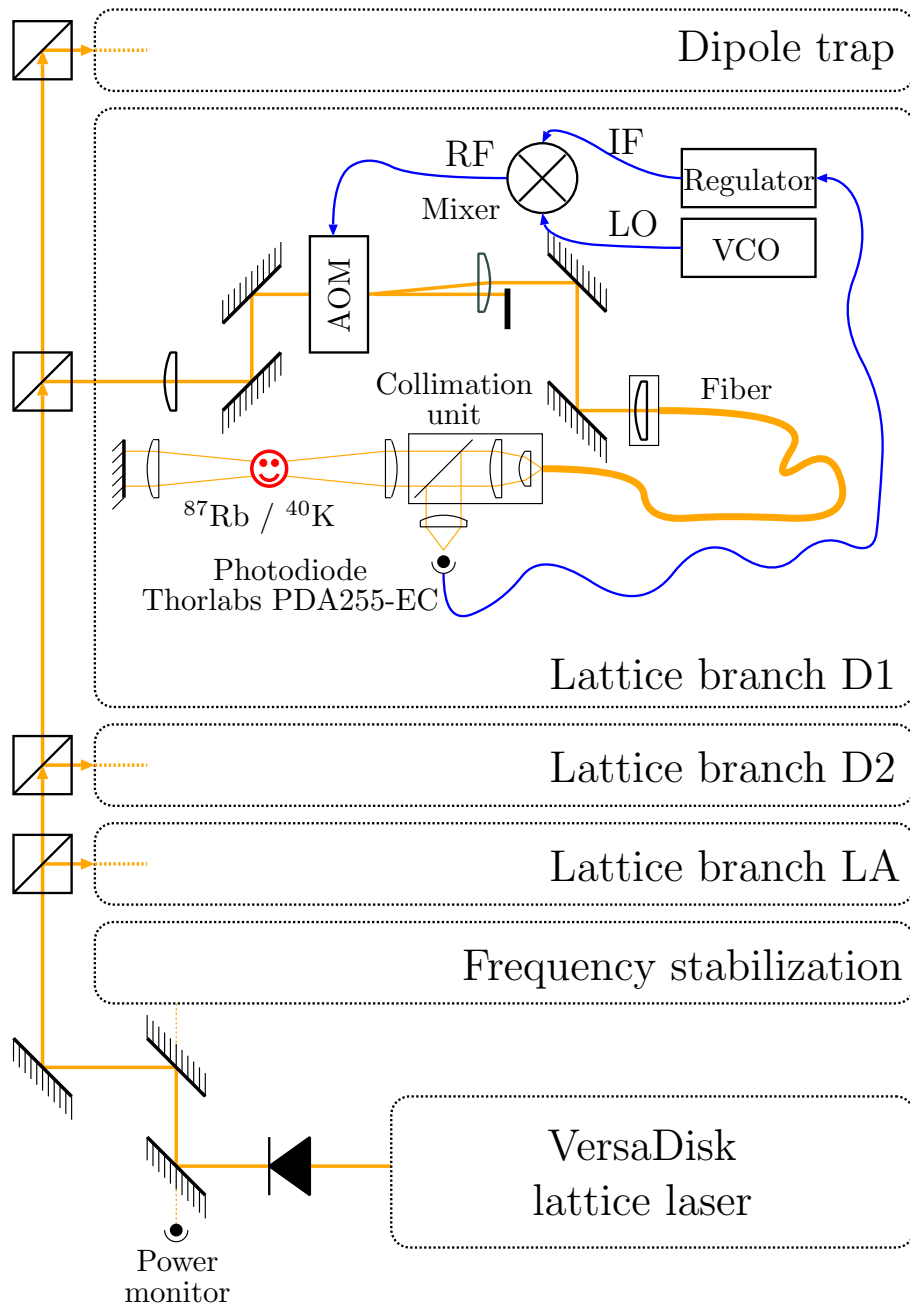


Figure 3.15: Optical lattice setup with beam preparation, intensity stabilization, collimation unit and retroreflection. Not shown: Imaging along lattice axes and edge filters for overlapping with MOT beams.

can never be completely avoided. The residual signal can be eliminated by taking a third and fourth exposure \mathcal{D}_A and \mathcal{D}_R (dark images) which are taken exactly like the corresponding \mathcal{A} and \mathcal{R} images, but without the detection flash. In most cases, $\mathcal{D}_A \equiv \mathcal{D}_R$. These dark images are subtracted from absorption images before calculating the ratio. The line of sight integrated optical column density can then be obtained by taking the logarithm of the ratio:

$$\mathcal{OD} = \log \frac{\mathcal{R} - \mathcal{D}_R}{\mathcal{A} - \mathcal{D}_A} . \quad (3.12)$$

Below, I will first only briefly look at the optical imaging setup and then describe advanced properties of CCD chips used for absorption imaging in this experiment and present two implementations of absorption imaging which have been developed in this thesis and rely on advanced features of Interline Transfer CCD chips. I will then discuss two implementations of state-selective imaging, the more traditional Stern-Gerlach imaging and imaging at high magnetic fields. These techniques have been essential to chapters 5 and 7.

3.11.1 Optical setup

The optical setup for all of our four imaging systems is based on two-lens configurations on all four imaging axes. A first lens collimates light from the imaging plane, and a second lens focusses the collimated beam onto a CCD chip. The numerical aperture of the first lens limits the imaging resolution, and depending on the focal lengths used for the lenses, various magnifications can be realized. In most experiments described in this thesis, a 1:2 magnification has been used for detection on the main detection axis and on the horizontal MOT axis; the detection systems on the diagonal axes have mostly been used for lattice adjustment and have a 1:1 lens configuration. A detailed description of the optical aspects of imaging as used on this experiment can be found in [66].

3.11.2 Detection techniques

In this section I will discuss various detection techniques that have been crucial for the experiments presented in this thesis. These techniques are related to the readout possibilities that modern interline CCD chips offer, achieving interframing times on the order of 200 μs . I will first discuss a technique of imaging two species onto the same CCD chip in one experimental run. This has been most important with respect to experiments on Fermi-Bose mixtures in the high particle number limit where it was important to look at the behavior of the cloud in the axial direction comparing the two species in a regime of instability where large shot-to-shot variations are possible (chapter 4). Another possibility to take advantage of interline CCD chips is to take absorption and reference images in very quick succession in order to improve on the image quality and the number of detectable particles for one particular species. This has been relevant to experiments on heteronuclear molecule formation (chapter 7).

3.11.2.1 Charge coupled devices

This short paragraph is not meant to be a comprehensive discussion of CCD technology, but merely as an introduction to the terminology needed for the discussion of fast imaging with interline CCD chips. Initially developed in the context of memory technology, Charge Coupled Device (CCD) and CMOS sensors are today used in microscopy, astronomy, consumer products, digital cameras, x-ray applications, spectroscopy, medicine, and this list is by no

means exhaustive. A CCD element is a collection (row or matrix) of semiconductor potential wells in which charge can be accumulated as a result of exposure to light. By applying a series of voltage pulses on gate electrodes, charge can be transferred between neighboring wells. CCD rows are often used in spectroscopic applications or for telefax machines or barcode scanners. Matrix elements are commonly used in imaging applications. In the simplest (Full Frame CCD, FF CCD) case, readout of such a matrix of potential wells is performed by shifting the charges in individual wells in the parallel direction by one pixel. The outermost row is shifted into the serial shift register, which is then in turn shifted into an Analog-Digital Converter (ADC). A full readout of an $N_P \times N_S$ matrix therefore involves N_P parallel shift operations and $N_S \cdot N_P$ serial shift and ADC steps. There are two main shortcomings in this scheme:

- **Readout time.** The readout process is dominated by the time for the individual ADC process. Total readout times are typically on the order of at least a few 100 ms. During readout, no further images can be taken.
- **Image smear.** During readout and shift, the chip is still sensitive to light. This may not be such a problem in absorption imaging where the exposure is controlled through a few μs flash of light and stray light falling onto the CCD chip can be reduced to the maximum.

The readout time limitation is the most important aspect in atomic absorption imaging. Imaging is usually done with coherent light leading to the typical interference fringes in the absorption image. For stationary interference patterns, these can be eliminated by taking a second reference image and a suitable normalization procedure. The location of the interference fringes usually drifts as a function of time; in addition, the sudden switch-off of the magnetic trap for absorption imaging may produce vibrations in the experiment, thereby also causing similar fluctuations. A long time delay between absorption and reference image will thus lead to significant fringes even in the normalized output image. At the same time, it is often desirable to take more than one absorption image in one experimental run, either when working with two species and imaging with one camera or when using non-destructive phase contrast imaging.

One extension of the simple scheme is the Frame Transfer CCD (FT CCD) chip. In this case, one half of the chip close to the serial register is covered with an opaque mask. This allows one image to be taken, subsequently shifted under the mask quickly by a given amount of parallel shifts, then a second image etc. until the area under the mask is full and ready for readout. This technique has been used in non-destructive imaging of Bose-Einstein Condensates [102]. In terms of speed, a full parallel transfer still requires a time on the order of milliseconds.

Another extension is the Interline Transfer CCD (IT CCD). In this scheme, each pixel is made up of two potential wells. One is exposed to light falling onto the chip, and the other is covered by an opaque mask. Within a few microseconds, the whole image can be shifted under the mask and a second exposure of the bright pixels can start. Note that the chip remains sensitive to light for the whole readout period of the first image. This technique is widely used in consumer devices and has the advantage of a very fast electronic shutter without any need for mechanical shutters. In the limit of exposure time and readout time being equal, this technique can double the achievable frame rate. In general, IT CCDs are also less expensive than FT CCDs. The inherent disadvantage of a lower filling factor, i. e. only half of the detector area being sensitive to light, has been overcome by placing microlenses above each

pixel which will focus almost all of the incoming light onto the bright half of the pixel. There is also a scheme combining FT CCDs and IT CCDs into Frame Interline Transfer CCDs (FIT CCDs).

Of course, there are other relevant aspects to choosing a CCD element, such as front illuminated vs. back illuminated, quantum efficiency, single photon detection capability, electron multiplication technology which are not discussed here. Absorption imaging for the experiment described in this thesis has been implemented using IT CCDs because of the above mentioned advantages; the following sections discuss absorption imaging using these elements in more detail. Two camera types have been used in these experiments, a Roper Scientific Coolsnap HQ camera equipped with a special firmware and a PCO Pixelfly double shutter in the enhanced quantum efficiency version. In both cases, the glass cover in front of the CCD chip has been removed by the manufacturer in order to further reduce interference fringes. Both cameras use the same CCD chip (SONY ICX205AL).

3.11.2.2 Two species imaging

This detection technique takes advantage of the extremely short interframing time of interline CCD cameras for taking two absorption images of two different species with one experimental run. The detection sequence consists of three double frames. The first double frame contains absorption images of ^{40}K and ^{87}Rb . Usually, the ^{40}K absorption images is taken after a relatively short time delay of 5-10 ms. 100 μs before the begin of the exposure, the camera is triggered with an exposure time of 500 μs programmed into the camera. The exposure flash itself is typically 50 μs long and controlled using an AOM. After the 500 μs exposure time is over, the image is shifted under the mask and the chip remains sensitive to light in the second half of the first double frame for the readout time which is approximately 100 ms. In a conservative approach, I have usually allowed 200 ms for readout of this first double frame. Afterwards, the second double image is taken in exactly the same way, but by this time, the atoms have fallen out of the imaging area and reference images for ^{40}K and ^{87}Rb are recorded. These are again read out of the chip during 200 ms, and then two dark images are recorded in order to subtract the background count rate. This is particularly relevant to the second half of each double frame (usually ^{87}Rb), since the exposure time is considerably longer than for the first half (^{40}K). Afterwards, the optical density of the two half frames is computed separately and displayed on screen in a configurable false color representation, together with 1D profiles through the center of the trap and 1D column sums for both the serial and parallel directions of the CCD chip. The set of three double exposures can be saved to disk when taking data; a corresponding filename for the protocol file containing the full experimental sequence in an `xml` (eXtensible Markup Language) format is sent to the experiment control computer at the same time.

It has been of particular help in optimizing the experiment that the CCD control software developed in this thesis has a built-in fit feature which allows the experimenter to fit both a one-dimensional bimodal distribution for a Bose-Einstein condensate with a thermal cloud and also a two-dimensional Fermi-Dirac profile given by eq. 2.34 to the experimental data, display the result of the fit and output relevant fit results such as absolute temperature and relative temperature (T/T_C and T/T_F), total particle number, condensate fraction, and fugacity. This has become possible through use of very efficient implementations of thermodynamic integrals contained in Bose-Einstein and Fermi-Dirac functions as well as an efficient implementation

of the Levenberg-Marquardt nonlinear least-squares fit algorithm⁶. The algorithms used in this software are given in appendix D.

3.11.2.3 Fast imaging

This detection technique makes quite different use of the short interframing time of IT CCDs. In this scheme, both absorption and reference image for one *single* species are recorded in the first double frame. There is a pretrigger of 100 μs for the camera, followed by an exposure time of the first frame set to 300 μs ⁷, and the second half of the double frame is imaged immediately after the first half has been shifted under the mask. After absorption and reference image have been read out, a double dark exposure is taken. In this scheme, since the time during which exposure and reference image are sensitive to stray light is really a lot different, it is indispensable to record two separate dark images for each of the two absorption images.

The advantage of this scheme is that the short interframing time between reference and absorption image leads to a huge reduction in interference fringes in the resulting optical density. The extremely short interframing time does not allow the interference fringes of the laser beam to move over a considerable distance between the two images, which allows them to be cancelled almost completely in the normalization procedure. This has particular advantages when detecting very small particle numbers, such as in the experiments on ultracold heteronuclear molecules discussed in chapter 7.

A different aspect of the extremely short time between absorption and reference image is that we somehow need to get the atoms “out of the way” in order to take the reference image because the time of flight distance during a few microseconds is negligible for all practical purposes. Several approaches can be taken:

- We have typically combined this technique with experiments with Feshbach resonances where ^{87}Rb was in the absolute ground state of the system ($|F = 1, m_F = 1\rangle$). In this state, the atoms are not seen by the $F = 2 \rightarrow F' = 3$ detection laser. This allows us to take the reference image first. In the short interframing time, the MOT repumper is used to transfer population to the $F = 2$ manifold. A maximum of one photon per atom is scattered in this repumping process. The absorption image is then taken in the second half of the double frame on the aforementioned cycling transition.
- For almost all experiments discussed in this thesis, ^{40}K has been prepared in the $F = 9/2$ manifold. Therefore, optical pumping tricks as for ^{87}Rb cannot be used to provide a “cloak of invisibility” for the atoms. Instead, I have used the fact that in the case of the experiments discussed in chapter 7, a high magnetic field for Feshbach resonances has been used. This allows the following trick: for ^{40}K , we take the absorption image in the first half of the first double frame with the detection laser detuned to reflect the presence of a high magnetic field of 547 G. The detection transitions in this case are cycling transitions in the Paschen-Back regime between individual $|m_I, m_J\rangle$ states, and typical detunings are on the order of 800 MHz (see discussion in 3.11.3.2). The magnetic field is then rapidly switched off in the interframing time; this can be done in a few 10 μs . The detection laser, still running at the same detuning, cannot see these

⁶The netlib library (<http://www.netlib.org/>) is an incredible resource full of very efficient algorithms for various applications in numerical mathematics and physics.

⁷The length of the detection flash is 50 μs as before

zero-field atoms. The ^{40}K reference image can therefore be recorded in the second half of the double frame.

As I have already mentioned, the gain in sensitivity due to the high imaging quality of this detection scheme has been essential to the experiments discussed in chapter 7.

3.11.3 State selective imaging

I will now discuss two possibilities of state-selective imaging, i. e. techniques which allow the experimenter to independently image atoms in various sublevels of the ground state hyperfine manifolds. These techniques rely on the possibility of being able to both prepare and confine arbitrary spin states. The latter becomes possible using purely optical confinement from dipole traps and optical lattices, and the former can be achieved using e. g. Raman lasers and techniques of rapid adiabatic passage (see 3.9). Below I will discuss Stern-Gerlach imaging and detection at high magnetic fields as two possibilities of state-selective detection and point out their respective advantages and limitations and the particular realization in the experiment presented in this thesis.

3.11.3.1 Stern-Gerlach imaging

This technique, reminiscent of a seminal experiment by Stern and Gerlach in 1921 [103], employs inhomogeneous magnetic fields to spatially separate atoms with different magnetic moments. Michael Erhard's thesis [84] has an extensive discussion of Stern-Gerlach imaging. In these studies, it was found to be best to operate the pair of Helmholtz coils in Helmholtz configuration and then switch off one of the coils in order to produce a strong gradient with a strong offset field ensuring that the axis of quantization remains well-defined. We have found this to be not very practicable in the case of ^{40}K . This atom has a total of 10 different Zeeman sublevels in the lower hyperfine manifold, requiring one to separate them as much as possible in order to resolve the different components. On the other hand, one can not really afford a large time of flight with fermions because much more kinetic energy is stored in the gas, and it quickly becomes very dilute in time of flight. The solution is therefore to increase the force on the atoms and make the time short. Increasing the force means increasing the magnetic field gradient. However, with the above mentioned method, the offset field increases as much as the gradient when the current in the coils is increased. As a consequence, compared to ^{87}Rb , one quickly leaves the quasi-Zeeman regime and enters the Paschen-Back regime where the lowest nine of the available states begin to have the same magnetic field sensitivity and are essentially pushed into the same direction altogether – there is no longer a significant differential force on the spin states.

Efficient Stern-Gerlach imaging for ^{40}K is therefore best performed with a very high field gradient, but an offset field small enough to stay in the Zeeman regime and high enough to maintain the quantization axis. The solution implemented in this thesis and used for the measurements in chapter 5 consisted in using the Helmholtz coils in anti-Helmholtz configuration and quickly switching on an additional current of 20 A through a z pair of coils in the compensation cage in order to have a bias field high enough to maintain the quantization axis⁸. Fig. 3.16 shows that this technique of spin-selective imaging can resolve all of the 10 Zeeman

⁸Note that these coils cannot withstand the high current over a long time. They are protected against melting by accidental long-time operation by a slow 10 A thermal fuse

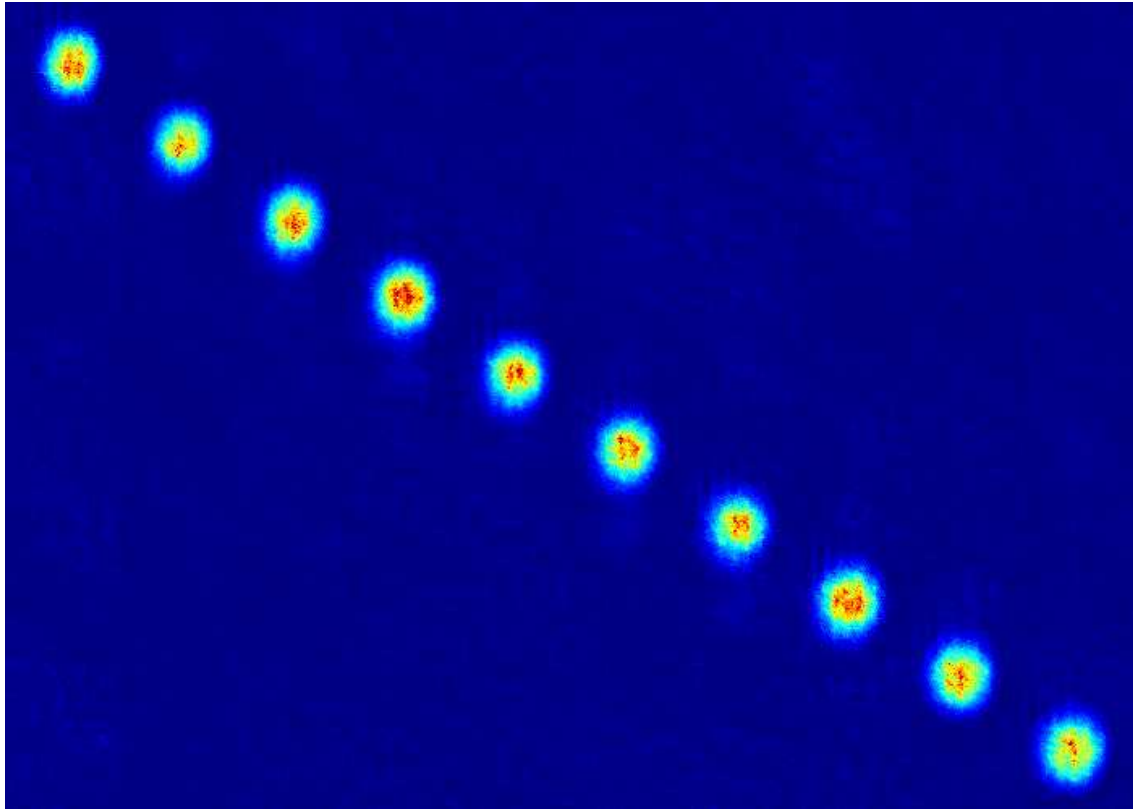


Figure 3.16: Stern-Gerlach imaging of ^{40}K with low bias field and high gradient. The image combines ten individually recorded images where RAP (Rapid Adiabatic Passage) was used to selectively prepare all of the ten sublevels of the lower $F = 9/2$ hyperfine manifold, from the magnetically trapped $|9/2, 9/2\rangle$ state (top left) to the absolute ground state $|9/2, -9/2\rangle$ (bottom right).

sublevels within the $F = 9/2$ hyperfine manifold with an equidistant separation between the individual components.

3.11.3.2 Detection at high magnetic fields

As outlined in the previous section, high bias fields are mostly undesirable when performing Stern-Gerlach imaging. This section discusses imaging at high magnetic fields (in our case often close to a Feshbach resonance) without any magnetic field gradient to spatially separate the Zeeman components. In this case, we make use of the energy separation between the different states at high magnetic fields. The different spin components are no longer imaged in the same image, but using different laser frequencies in different imaging steps (either using the above-mentioned two-species imaging by taking two images on the same chip in rapid succession or by using different CCD chips for different spin states). Just to mention the scale of absolute and relative detunings: at magnetic fields of typical KRb Feshbach resonances (say 547 G), the absolute detuning with respect to the usual $9/2 \rightarrow 11/2$ cycling transition is -834 MHz for the $|9/2, -9/2\rangle$ state, and -765 MHz for the $|9/2, -7/2\rangle$ state. At these high magnetic fields, it makes more sense to speak of these two states as the $|m_I = -4, m_J = -1/2\rangle$

and $|m_I = -3, m_J = -1/2\rangle$ states. The transitions that we drive in this example case are then $| -4, -1/2\rangle \rightarrow | -4, -3/2\rangle$ and $| -3, -1/2\rangle \rightarrow | -3, -3/2\rangle$ transition. Note that because of the $\Delta m_I = 0$ selection rule, these transitions are cycling transitions! In fact, once in the Paschen-Back regime, it is always possible to construct a cycling transition on the D2 line by driving $m_J = +1/2 \rightarrow m_J = +3/2$ or $m_J = -1/2 \rightarrow m_J = -3/2$ with $\Delta m_I = 0$. If the magnetic field is too low, this imaging technique will no longer work as the involved transitions have significant probability of falling back into a different substate in the lower hyperfine manifold. While this imaging technique works in the case of ^{40}K at magnetic fields of 200 G, it does not for ^{87}Rb . Detecting at high magnetic fields has the disadvantage of making a maximum number of two to three spin states detectable due to practical limitations in the number of imaging paths in an experiment, but it has several important advantages:

- **Short TOF.** This technique makes it possible to image even small atom numbers because detection can start right after releasing atoms from the trap. There is no need to apply a field gradient or even wait for the bias field to change.
- **Imaging Feshbach molecules.** In the vicinity of Feshbach resonances, weakly bound molecules can directly be detected by means of absorption imaging, removing the need to convert them back into atoms by magnetic field sweeps or rf dissociation.

Implementing high field imaging has therefore been essential to experiments on heteronuclear ultracold molecule formation discussed in this thesis in chapter 7.

3.12 Timing

This section discusses computer control of the experiment. Aspects of the experiment that need remote control include frequency and intensity control through Acousto-Optic Modulators and EOMs, blocking of beams through mechanical shutters and servo motors, control of currents in coils and fast switching of magnetic fields. This task is performed by the combination of a DSP processor controlling 16 analog output channels and 64 digital TTL output lines and a host PC for user control and VISA synchronization. Each experimental sequence is defined as a number of time slots with a length of a multiple of $10\ \mu\text{s}$. In each slot, both the state of all digital and analog channels and strings to be sent to arbitrary devices controlled by the National Instruments VISA library are defined. The user interface running on the host PC groups these slots into a tabular representation. The user interface allows linear ramps of analog channels to be performed; these are discretized into a predefined number of constant slots. In addition, pre- and post- delays for digital outputs can be specified; this is most useful for beam shutters which typically need to be triggered 2 to 20 ms prior to blocking the beam path.

The National Instruments VISA library is an interface allowing GPIB, VXI, PXI, Serial, Parallel, Ethernet and USB interfaces to be transparently controlled from a high-level programming environment. Usage of VISA in our experiment covers control of power supplies and frequency synthesizers through RS232 and GPIB connections as well as TCP/IP connections with other application software such as the server software for the VFG-150 (see section 3.9.1).

At the beginning of each experimental sequence, the user interface program running on the host PC will discretize all analog ramps into individual constant slots, generate pre- and post-triggering slots for the digital channels and send the resulting pattern for the analog and

digital channels over an ethernet link to the DSP system. Once the transfer is complete, a firmware running on the DSP system will execute the predefined sequence. The user interface maintains a loose time synchronization with the DSP system (updated every few ms) and performs VISA output to attached devices when the respective slot has been reached. After the sequence is over, the user interface will accept a text string from the camera software and save a file in `xml` format containing the whole sequence definition. This file can later be reloaded into the interface.

Tight control of timing can thus be achieved by making use of analog and digital outputs of the DSP system. Usual delay involved in VISA transmission are on the order of a few 10 ms; the loose synchronization with the host PC therefore does not cause any issues. When tight time synchronization with VISA devices is necessary, these can often be preprogrammed and precisely triggered by a digital input, such as the VFG-150 rf synthesizer.

The system developed in this thesis replaces an earlier hardware implementation based on National Instruments DAQ boards. The advantages of using a separate DSP system for computer control are obvious:

- **Reliability.** PC operating systems are not designed with real time capability in mind. Other operating system activity can unduly delay the experiment cycle when timing is performed by the host PC and lead to buffer underruns. With the PCI card based system, the user interacting with the control interface would often cause the same effect.
- **EMC.** The analog and digital PCI boards previously used had shown to be quite sensitive to electrical back-action from the experiment, although the relevant outputs connecting to the magnetic trap circuitry had all been electrically separated from the PC using isolation amplifiers and optocouplers. This has even lead to unintended reboots of the host PC. The embedded DSP system proved insensitive to these perturbations.
- **Elimination of ground loops.** A modern PC is a hostile environment for processing of precision analog signals. The PC itself is usually one of the most important points where ground loops are created. The fact that the DSP system has been designed with precision analog signal processing in mind and is only connected to the host PC using one twisted pair ethernet cable makes elimination of ground loops and a strict ground separation with respect to the PC a lot easier.
- **Separating PC and experiment.** The rack-mount DSP system can be relatively close to the experiment, thereby limiting the length of signal lines.

The control system presented above has proved to be a very uncomplicated and reliable method to run our experiment; we have rarely had issues with unexpected triggers of edge-triggered digital inputs when switching strong magnetic fields, which is a common problem with magnetic traps. The timing has proved to be extremely reliable and exact, and the possibility to control arbitrary VISA-compatible devices allows us to access practically all the available measurement and instrumentation equipment without changes to the control software itself.

The solution developed here has later been adopted by two other experiments in our group and the metastable Ca experiment in the group of A. Hemmerich.

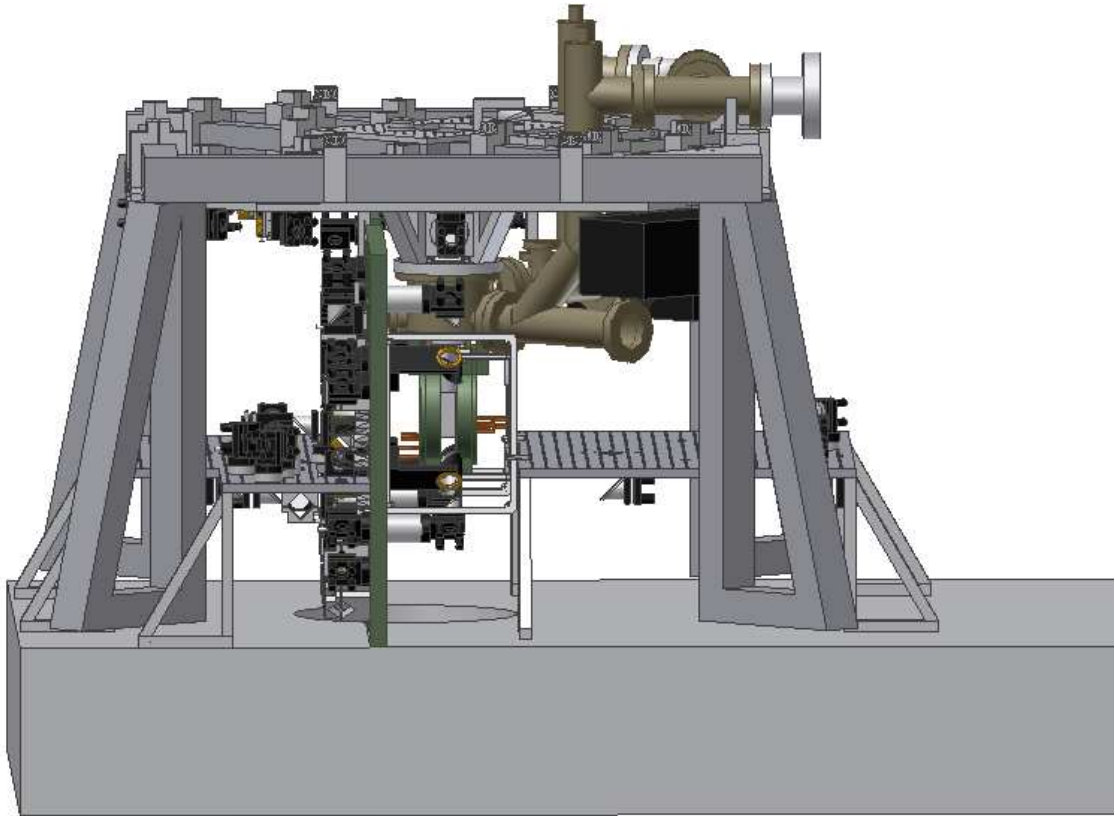


Figure 3.17: CAD rendering of full apparatus, including vacuum system, magnetic trap, MOT optics, and most optical lattice optics.

3.13 CAD rendering

Finally, Fig. 3.17 shows a CAD rendering of the whole apparatus discussed in this chapter. The whole vacuum system is suspended from a baseframe which also carries the 2D-MOT optics (suspended from the top of the baseframe). The magnetic trap is attached from below to the main vacuum chamber with the glass cell clearly visible between the two parts of the cloverleaf trap. Left of the magnetic trap, one can see the MOT board where all of the 3D MOT and lattice optics are located. Most of the optics has been put on the side of the board which is pointing “away from the atoms”, so that the excellent optical access is maintained. The two horizontal boards carry the optics for the z axis of the 3D magneto-optical trap, the magic dipole trap and for flexible lattice setups. Not shown in this rendering is of course all of the electronics and computer equipment as well as the cooling and electricity connections.

Chapter 4

Fermions, Bosons and Mixtures

In chapter 2, I have introduced basic concepts for interacting Fermi-Bose mixtures, described limits on the stability of the samples related to the strength of Fermi-Bose interactions and discussed density distributions of trapped samples and resulting expansion distributions, both for single-component fermionic and bosonic gases and for mixtures.

This chapter looks at fermions and bosons from an experimental perspective. I will show how we produce an atomic Bose-Einstein condensate in the experiment, present sympathetic cooling of ^{40}K by ^{87}Rb in our magnetic trap and show how a degenerate Fermi gas is produced through sympathetic cooling. I discuss how the temperature of such an ideal trapped Fermi gas is determined from absorption images and explore the parameter space in terms of particle number and temperature covered in the experiment.

Next, I start my discussion of ^{40}K - ^{87}Rb mixtures with thermal samples. By stopping the evaporation above the onset of degeneracy, we are in a regime where the density distributions are not yet significantly effected by the presence of interactions and can study 3-body recombination in the mixture as an important prerequisite for understanding the regimes of degenerate mixtures accessible in the experiment and for adjusting the speed of evaporation.

I will then discuss interacting degenerate mixtures and show from an experimental point of view how we can observe aspects of the interaction for the harmonically trapped mixture. In this chapter, I will follow an approach which starts with a fixed value of the heteronuclear interaction and explores various regimes of interactions by taking particle numbers in the mixture as a free parameter. Historically, this is the first experimental approach to interacting Fermi-Bose mixtures which has been pursued; tunable interactions have only become available very recently (see chapter 5) and opened up the second perspective on harmonically trapped interacting mixtures.

Saying that we are going to look at the phase diagram as a function of the particle number is easy to say from a theoretical point of view. Yet from an experimental perspective, particle numbers are subject to both technical and fundamental constraints, and the work reported here has become possible mainly because the experiment described in this thesis has allowed the production of the so far highest particle numbers reported in ^{40}K - ^{87}Rb mixtures. The observed stability limits have imposed constraints on values of the interaction parameter, the s wave ^{40}K - ^{87}Rb scattering length a_{FB} . For a long time, this scattering length had been believed to be exceedingly large in the community (e. g. $-395(15) a_0$ from [60]). For this reason, it seemed that particle numbers in ^{40}K - ^{87}Rb mixtures would be severely limited by the onset of the mean-field collapse discussed in section 2.4.3. The observations presented

in this chapter constrain $|a_{FB}|$ to values below $284 a_0$, which has important implications for experiments described in later chapters of this thesis. At the same time, entering the regime of mean field instability allows us to study the dynamical behavior of the system after the onset of collapse. The dynamics of the mixture in this regime is a feature which has received little attention from theory, but allows interesting insights into mixture physics, as for example the observation of revivals of the collapse.

4.1 Observation of BEC

As a prerequisite for sympathetic cooling to Fermi degeneracy of ^{40}K or even simultaneous degeneracy of ^{40}K and ^{87}Rb , I will now describe the experimental procedure which leads to observation of BEC of ^{87}Rb in our experiment. Over 10 to 20 s, depending on desired final particle numbers, atoms are captured from the background pressure of the 2D magneto-optical trap and sent through the differential pumping stage into the lower part of the vacuum system. Here, the atoms are recaptured in the 3D magneto-optical trap at a magnetic field gradient of typically 10 G/cm and a detuning of -20 MHz with respect to the cycling transition. During the whole MOT phase, a homogeneous magnetic field proportional to the MOT gradient is applied in the vertical direction in order to shift the center of the MOT approximately 2 mm below the center of the pure quadrupole field. This position corresponds to the equilibrium position of ^{87}Rb in the decompressed magnetic trap as a result of the gravitational sag.

When enough atoms have been accumulated, the loading from the 2D magneto-optical trap is stopped by blocking the 2D-MOT beams and the pushing beam using mechanical shutters. 70 ms later, the MOT beams are blocked using an Electro-Optic Modulator (EOM), the MOT quadrupole field is rapidly switched off using IGBT modules, and the detuning of the MOT beams changed to -29.5 MHz. After 200 μs , a 10 ms optical molasses phase is initiated by again switching on the MOT light using the EOM. After the optical molasses phase, the MOT light is switched off and blocked using mechanical shutters as quickly as possible in order to avoid heating. An auxiliary power supply is connected to one of the auxiliary coil cage layers in Helmholtz configuration along the z (magnetic trap) axis using a MOSFET switch, and after 50 μs , the AOM of the repumping beam oriented along the z axis in the positive z direction is flashed on for another 50 μs . Optical pumping on the ^{87}Rb $F = 2 \rightarrow F' = 3$ cycling transition transfers atoms predominantly into the ^{87}Rb $|F = 2, m_F = 2\rangle$ state which is magnetically trappable. For ^{87}Rb , optical pumping typically gives a factor of 2 improvement in the transfer efficiency into the magnetic trap.

After the optical pumping flash, we wait another 50 μs and then switch on the IGBT modules for the magnetic trap. The power supplies have been preprogrammed to deliver a current of 110 A in the cloverleaf and Dee coils and 31.8 A in the Helmholtz coils, which corresponds to a round

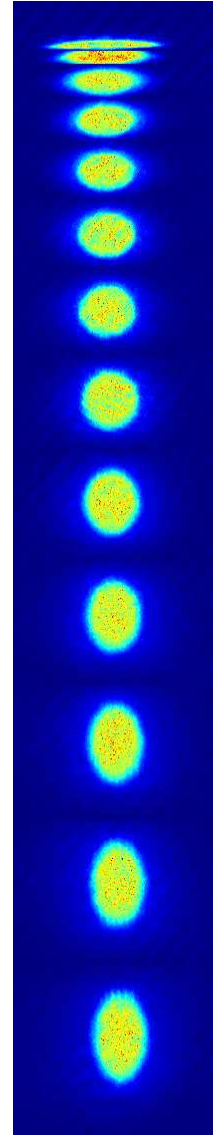


Figure 4.1: BEC in time of flight

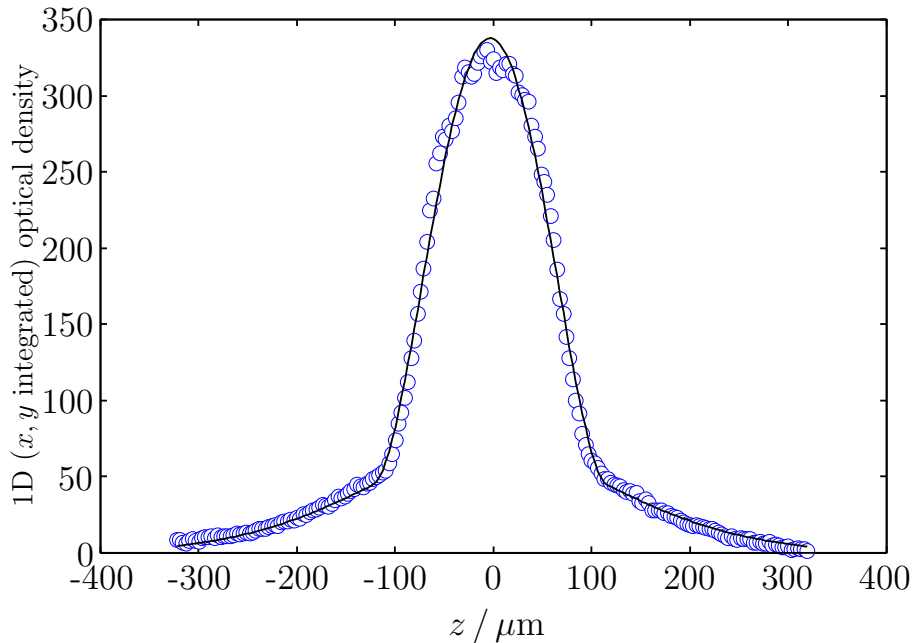


Figure 4.2: 1D optical density of ^{87}Rb Bose-Einstein condensate with thermal cloud (broad wings) after 25 ms TOF. The fitted bimodal distribution would drastically underestimate the condensate atom number, since the condensate is completely optically dense and practically does not transmit any light.

trap with a trap frequency of $2\pi \cdot 11.2$ Hz. After 100 ms, the optical pumping field MOSFET is switched off and the trap compression stage begins. Over 1 s, the current in the Helmholtz coils is ramped down to 5 A, and then more carefully down to 0 A over 500 ms. During this last ramp, a HAMEG 8143 power supply takes over and finally provides the remaining bias field current of typically 400 mA. Radial trapping frequencies in the cigar-shaped trap after compression depend on the value of the bias field current and are typically between $2\pi \cdot 200$ and $2\pi \cdot 300$ Hz, whereas the axial (z) trap frequency is independent of the bias field and remains at $2\pi \cdot 11.2$ Hz during compression. Immediately after compression, the evaporation sequence is started by sending a digital trigger pulse to the VFG synthesizer. This triggers a sequence of linear ramps which has been preprogrammed into the VFG server software during the MOT phase over a VISA network link as described in section 3.9.1. The evaporation sequence typically consists of 3 linear negative chirp frequency ramps starting at 35 to 40 MHz and ending at rf frequencies corresponding to slightly above the trap bias field. To give a specific example that has been used in the experiment, the first sweep goes from 40 to 5 MHz in 7 seconds, the second down to 1 MHz in 4 seconds, and degeneracy is reached with the last sweep, where the sweep speed depends on the actual experiments. Large degenerate mixture with comparatively high losses for high densities require a fast sweep of 1 MHz/s, although this may create strong excitations, and producing a ^{87}Rb BEC with a minimum of excitations is usually achieved with a ramp speed of 250 kHz/G.

The onset of Bose-Einstein condensation is observed as in Fig. 4.1, where I have shown the evolution of the sample as a function of a time of flight of 1 ms, 3 ms, 5 ms, 7 ms,... (top to bottom). One immediately recognizes the cigar-shaped in-trap distribution of the

sample. Over time, the condensate first becomes spherical and then inverts its aspect ratio which is the signature of the large mean field energy stored in the radial direction. At the same time, we observe that the tiny residual thermal cloud (visible as a weak background in the large TOF images) tends to become completely round during time of flight as expected from eq. 2.31.

From Fig. 4.1, it might look as if the condensate first shrinks in the axial direction. This is not the case. The condensate is optically dense during the whole time of flight shown here, whereas the thermal cloud is dense for short TOF and then expands very rapidly and becomes very dilute. So for very short time of flight, where both components are optically dense, we cannot really distinguish between condensate and thermal cloud.

For illustration, Fig. 4.2 shows the 1D optical column density of the sample after 25 ms. Since the BEC is optically dense, it practically does not transmit any light over most of its area. Determining the condensate atom number from the area under the central peak would drastically underestimate the condensate size. When quantitative information is desired, off-resonant imaging may be used to increase the transmission. The latter has been done in our experiments with large particle numbers (see below).

4.2 Sympathetic cooling

In order to create quantum degenerate Fermi gases or degenerate mixtures, the experimental procedure leading to the observation of BEC is modified as follows: Generally, the loading phase for the dark ^{40}K MOT is initiated a few seconds before the ^{87}Rb MOT begins to load. For transfer into the magnetic trap, the 70 ms 3D-MOT only phase after the 2D-MOT has been switched off is split into two parts. In the last 50 ms, the dark ^{40}K MOT is switched to a bright configuration by use of an EOM: Instead of sending ^{40}K repumping light into the dark SPOT fiber and the 2D-MOT setup, the full repumping power is sent onto the same path as the 3D-MOT ^{40}K cooling laser. Before the bright MOT phase, ^{40}K is predominantly in the upper $|F = 7/2, X\rangle$ manifold; the bright MOT brings these atoms back into the $|F = 9/2, X\rangle$ manifold for magnetic trapping. The length of this slot is determined empirically so that losses in the bright MOT do not spoil the large atom number accumulated in the dark MOT, but long enough so that we do not leave a significant fraction in the “wrong” hyperfine state for magnetic trapping.

In contrast to ^{87}Rb , where optical pumping improves transfer into the magnetic trap by a factor of two, it is much more important for ^{40}K . This due to two different factors: ^{40}K in $|9/2, X\rangle$ has twice as many Zeeman substates as ^{87}Rb in $|2, X\rangle$; in the magnetic trap, only the $|9/2, 9/2\rangle \otimes |1, 1\rangle$ is studied, meaning that there is a lot to gain from efficient optical pumping! Even worse, if a significant fraction of ^{40}K is left over in other Zeeman sublevels, this might compromise the stability of the fraction of the mixture which is in the “good” states through inelastic decay. It is generally easiest to optimize the ^{40}K optical pumping power by looking at the ^{40}K atom number after some initial evaporation or even with the degenerate or close to degenerate gas.

The transfer of ^{40}K into the isotropic magnetic trap is generally not optimized with respect to gravitational sag, since this can be only done for one species at a time due to the differential sag between the two components. However, the ^{40}K atom number is usually much smaller, and the suboptimal transfer therefore does not harm too much.

Assuming thermal equilibrium, the sympathetic cooling using rf transitions removes prefer-

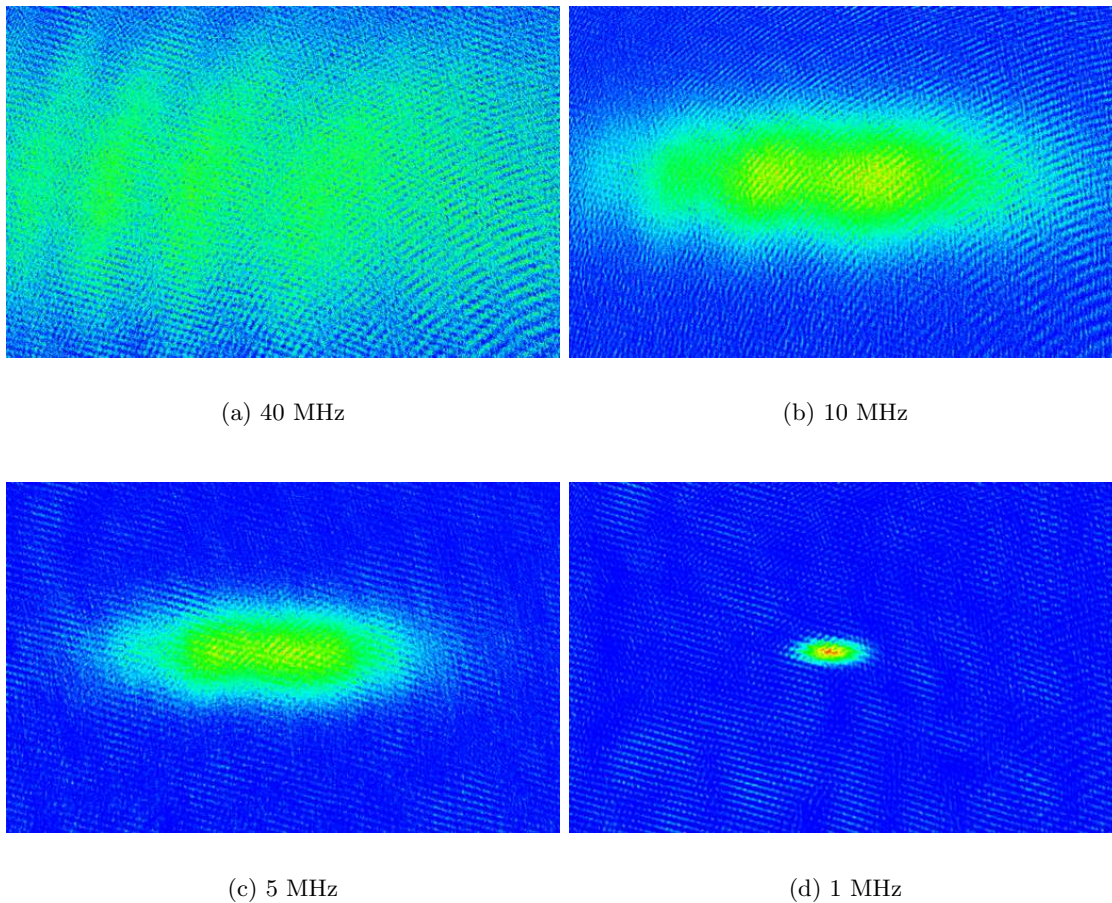


Figure 4.3: Sympathetic cooling of ^{40}K by ^{87}Rb . The time of flight images show the ^{40}K images as a function of evaporation end frequency (given below the image).

entially ^{87}Rb from the trap, and ^{40}K is cooled in the thermal bath, since $\nu_{\text{Rb}}/B = g_F m_F \mu_B / \hbar = 700 \text{ kHz/G}$, whereas $\nu_{\text{K}}/B = 311 \text{ kHz/G}$. In principle, it is also possible to perform the evaporation on a microwave transition for ^{87}Rb , and the Zürich experiment does precisely that. I have been told that it results in a factor of two in ^{40}K particle number increase compared to the rf scheme. However, care has to be taken in order not to accumulate ^{87}Rb atoms in $|2, 1\rangle$. Usually, two microwave knives or a cleaning sweep are required to avoid this. We have not felt in any way limited by particle number, so all of the sympathetic cooling described here as been performed using rf, although microwave evaporation could be easily done using the existing existing setup for microwave manipulation described in section 3.9.1.

Fig. 4.3 shows time of flight images of the ^{40}K cloud during the early stages of the sympathetic cooling process. Fig. 4.3(a) shows a dilute ^{40}K cloud right after compression of the magnetic trap, and the subsequent evaporation of ^{87}Rb leads to more and more dense ^{40}K samples. Fig. 4.4 has corresponding atom numbers in ^{40}K and ^{87}Rb throughout the non degenerate parts of the sympathetic cooling process.

As can be seen, the slope in atom number loss is much steeper for ^{87}Rb than for ^{40}K , which shows that the sympathetic cooling process preferentially removes ^{87}Rb as expected,

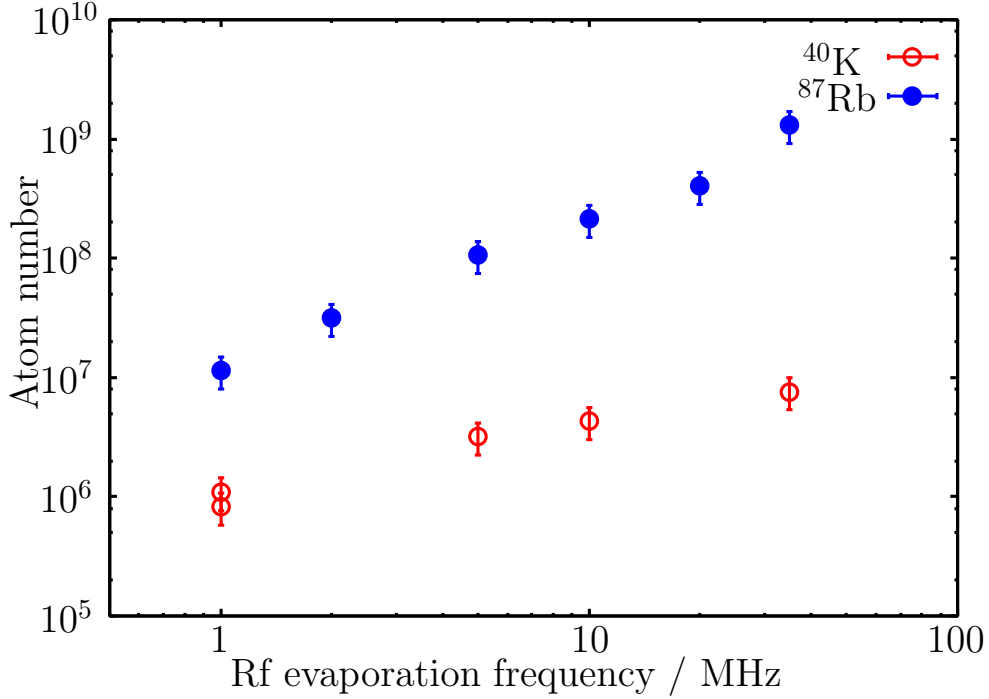


Figure 4.4: Sympathetic cooling of a ^{40}K - ^{87}Rb mixture.

and the residual loss may be due to the finite ^{40}K trap depth. At the end of the evaporation sequence shown here, where the evaporation end frequency is 1 MHz, degeneracy is not yet achieved. Throughout the shown evaporation ramp, we lose two orders of magnitude in ^{87}Rb atom number due to evaporation and about a factor of eight in ^{40}K atom number. If we remove all of the ^{87}Rb atoms in the evaporative cooling process, we obtain a “degenerate” Fermi gas as explained in the next section.

4.3 A “degenerate” Fermi gas

In discussing the onset of degeneracy for ^{87}Rb , I have shown the striking features of Bose-Einstein condensation, such as the appearance of a bimodal distribution in time of flight and the (more indirect) evidence through the inversion of the aspect ratio. A spin-polarized Fermi gas lacks such a drastic transition as the temperature is lowered. The onset of degeneracy happens gradually and is seen as the appearance of a macroscopic Fermi sea. The degree of degeneracy can only be extracted through careful image analysis [67]. Correctly calibrating the overall particle number vs. absorption imaging optical density is particularly important, since the total atom number influences the reference temperature, the Fermi temperature T_F . Fortunately, we dispose of two independent “thermometers” for the Fermi cloud which can be compared using eq. 2.16.

Fig. 4.5 shows the outcome of thermometry for a typical experimental situation. The red curve is the optical column density as observed in imaging, integrated along the direction of the detection beam and the horizontal direction. The green curve is the result of a two-dimensional nonlinear least squares fit of the time of flight expansion profiles discussed in

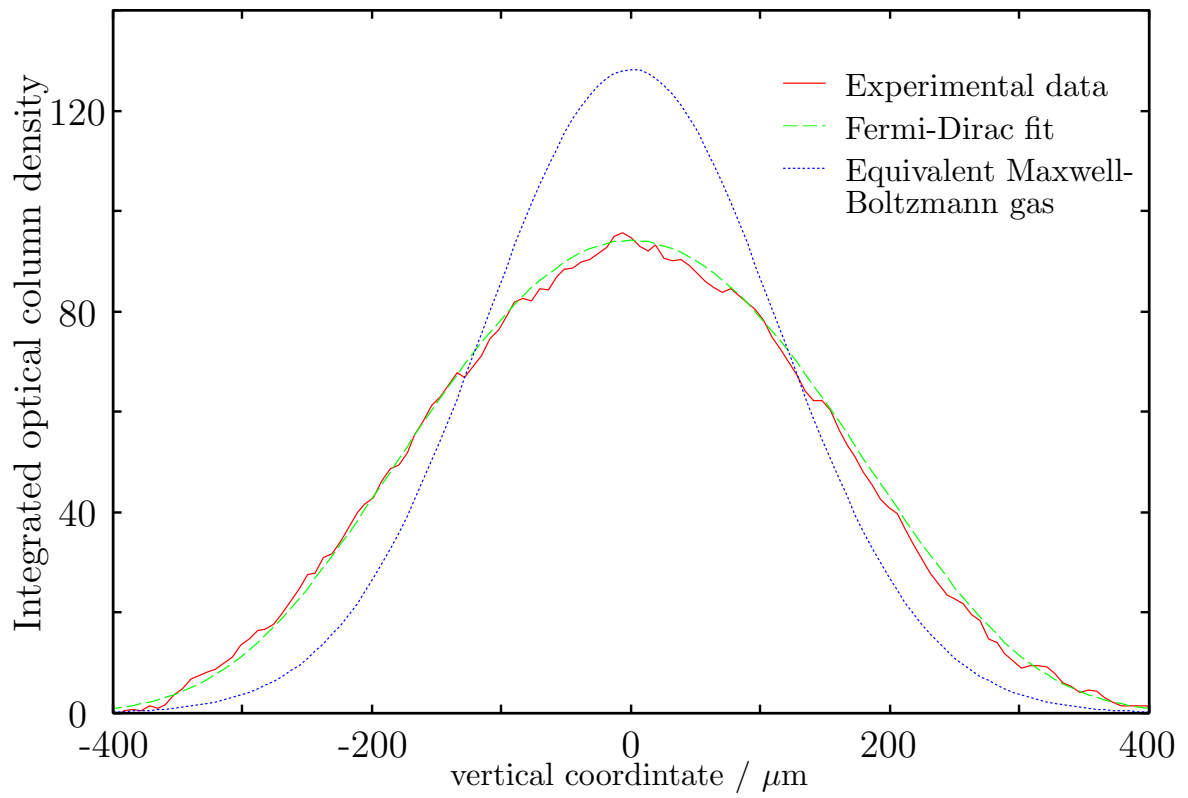


Figure 4.5: Thermometry for a degenerate Fermi gas.

chapter 2 to the experimental data. The fit function is derived from equation 2.34:

$$n(x_1, x_2) = - \left(\frac{1}{2\pi\beta^2\hbar^2\bar{\omega}^2} \right)^{3/2} \cdot \frac{1}{\sigma_v\sigma_h} \sqrt{2\pi} Li_2 \left(\zeta e^{-\sum_{i=v,h} \frac{x_i^2}{2\sigma_i^2}} \right) \quad (4.1)$$

It is however more convenient to use a different set of fit parameters than in the above equation. The set of fit parameters which proved most useful are horizontal and vertical center position, the widths σ_h and σ_v , the peak optical density a and the logarithm of the fugacity. The latter makes more sense as a fit parameter than the fugacity since it can assume both positive and negative values and does not potentially cause problems in the fit algorithms due to temporal excursions of the fugacity into undefined parameter regions. In terms of these fit parameters, equation 2.34 becomes:

$$\mathcal{OD}(x_1, x_2) = A \cdot \frac{Li_2 \left(-\text{Exp} \left[\ln(\zeta) - \sum_{i=v,h} \frac{x_i^2}{2\sigma_i^2} \right] \right)}{Li_2(-\text{Exp}[\ln(\zeta)])} \quad (4.2)$$

From the time-dependent widths $\sigma_{v,h}$, temperatures are calculated according to

$$T_{v,h} = \sigma_{v,h} \omega_{v,h} \sqrt{\frac{m}{k} \cdot \frac{1}{1 + (\omega_{v,h} t_E)^2}} \quad (4.3)$$

The total particle number is obtained by integrating the fit function equation 4.2 over both remaining coordinates. The result is

$$B = A \cdot 2\pi\sigma_v\sigma_h \frac{Li_3(-\text{Exp}[\ln(\zeta)])}{Li_2(-\text{Exp}[\ln(\zeta)])} \quad (4.4)$$

This expression has the dimension of an area, and is related to the particle number by dividing B by the absorption cross section

$$\sigma = 2\lambda^2/(2\pi) \quad , \quad (4.5)$$

where λ is the detection wavelength. Based on the known trap frequencies, the total particle number and the vertical and horizontal temperatures, T/T_F can be calculated both for the vertical and the horizontal direction. A third value for T/T_F is based on the fugacity, combined with equation 2.16:

$$T/T_F = \sqrt[3]{-1/(6 \cdot Li_3(-\zeta))} \quad (4.6)$$

The benchmark for thermometry is agreement of the three independent thermometers. In the above typical situation, the trapping frequencies for ^{40}K in the magnetic trap are $2\pi \cdot 16.6$ Hz in the axial direction and $2\pi \cdot 447$ Hz in the radial direction. The measured particle number is $N = 1.99(60) \cdot 10^6$ ¹, resulting in a Fermi temperature of $1.64(16) \mu\text{K}$. The resulting degeneracy parameters are:

$$T_v/T_F = 0.221(22) \quad (4.7)$$

$$T_h/T_F = 0.217(22) \quad (4.8)$$

$$T_\zeta/T_F = 0.19 \quad (4.9)$$

¹30% is the estimated particle number calibration uncertainty

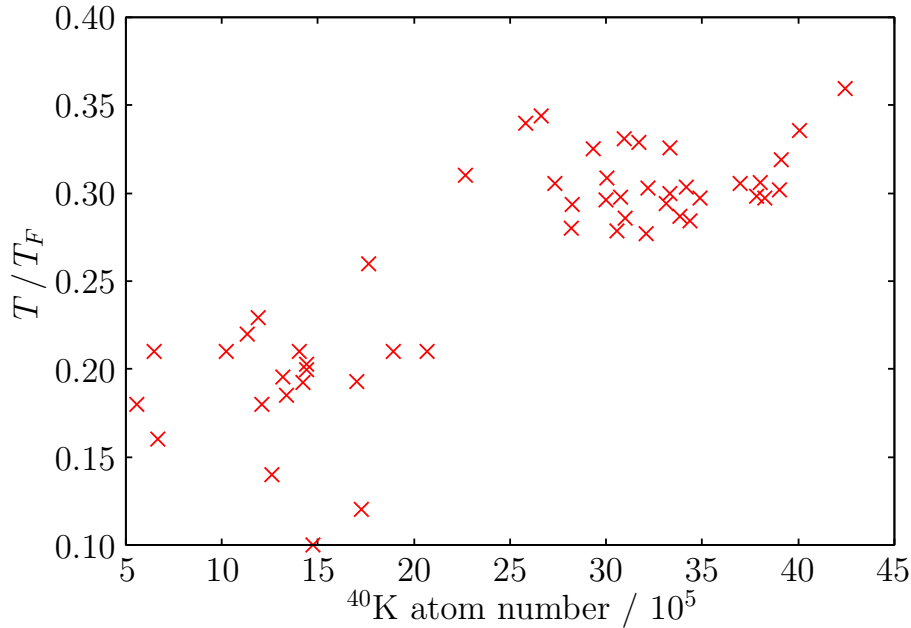


Figure 4.6: Parameter space of degenerate Fermi gases covered in the experiment.

The horizontal and vertical temperatures agree very well; within the limit set by the particle number calibration uncertainty, both do not fully agree with the temperature from the fugacity – the latter is a little bit lower, which may be an indication that the particle number calibration for ^{40}K might still have to be corrected upwards a little bit. A reason for this could be the relatively small hyperfine splitting in the excited ^{40}K levels, which can lead to quick losses into the dark hyperfine ground state when multiple photons are scattered per atom. This effect is not easy to account for in the experiment, although it has been compensated to some degree here by calibrating the atom number against the number of scattered photons.

Overall, the temperature in this particular case is below 25% of the Fermi temperature. For comparison, I have included a blue line in Fig. 4.5, showing the calculated time of flight image of a hypothetical Maxwell-Boltzmann gas with the same absolute temperature and particle number as the Fermi gas. The outward bound Pauli pressure of the Fermi gas, leading to a significantly flattened distribution compared to the classical gas, is clearly visible.

So far, I have shown only one particular, yet typical example for thermometry. The parameter space covered by this experiment is shown in Fig. 4.6, where I have plotted particle number vs. degeneracy parameter T/T_F . The temperature shown is the temperature as extracted from the width of the cloud, which is the more conservative estimate (because it yields slightly higher temperatures as seen above). As can be seen, Fermi gasses with four million atoms at $T/T_F = 0.4$ and 1 million atoms at close to 10% of the Fermi temperature can be created. In these experiments, the initial number of ^{40}K atoms transferred from the magneto-optical trap into the magnetic trap has been varied in order to vary the final particle number. In general, lower temperatures come at the expense of fewer particles which seems to indicate that the final temperature is limited by the ^{87}Rb cloud which is completely used up in the cooling.

I have explained above that the fugacity ζ and the width of the cloud, combined with the total particle number, give us two independent thermometers for the cloud. Fig. 4.7 shows a

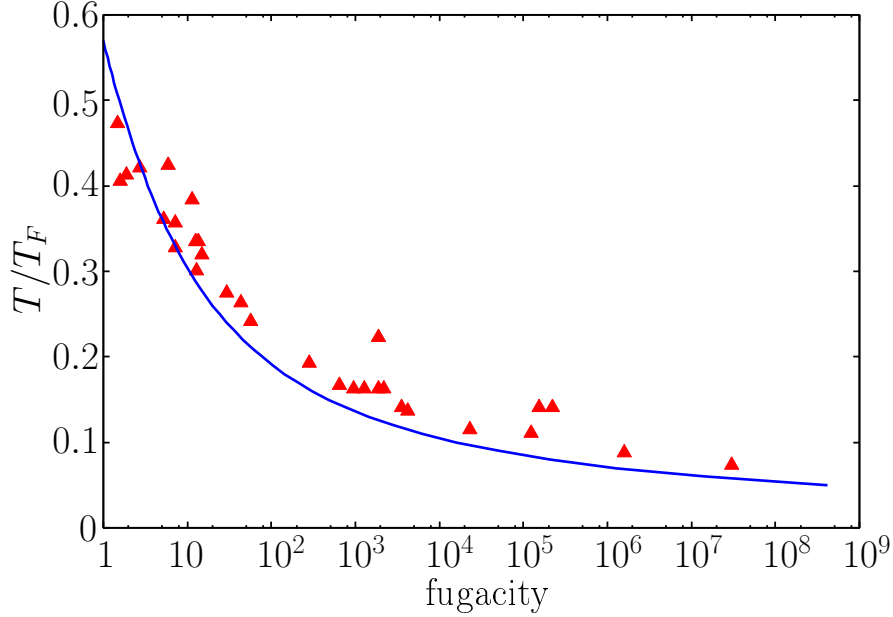


Figure 4.7: Fugacity ζ vs. degeneracy parameter T/T_F , compared to the prediction of eq. 2.16.

comparison of the two thermometers connected by eq. 2.16. As far as the temperature from the width of the cloud is concerned, the horizontal and vertical temperature usually agree very well as seen above in one particular case, so I have taken the average of both temperatures here. This average is plotted as a function of the fugacity resulting from the full Fermi-Dirac fit to the experimental data. The corresponding theoretical relation is given by equation 4.6. This relation is also plotted as a solid line in Fig. 4.7, together with the experimental data. As can be seen, both curves agree very well for moderate degeneracy (fugacity on the order of 1 to 10). For deeper degeneracy, the universal relationship eq. 2.16 lies slightly below the experimental data. Calculating the temperature based on the fugacity would therefore result in even slightly deeper degeneracy as already seen above.

Fig. 4.7 thus verifies an important universal relationship for ultracold Fermi gases and demonstrates, based on both of the independent thermometers, that we achieve at least 10% of the Fermi temperature in the experiment, even for the more conservative thermometer.

4.4 Three-body losses

After this separate discussion of bosonic and fermionic degeneracy as observed in the experiment, I will switch over to discuss mixtures and start my discussion with thermal mixtures and a measurement of three-body loss in ultracold ^{40}K - ^{87}Rb mixtures. Three-body loss is an important parameter of ultracold atomic gases. This process, where two atoms combine to form a molecule and a third atom takes away the binding energy (generally leaving the trap as a result of the excess energy), ultimately limits the lifetime of the trapped samples and timescales of evaporative cooling (in the absence of 2-body losses which are generally less important apart from some notorious and well-known examples). When this experiment produced its first degenerate mixtures, little was known about three-body loss in ^{40}K - ^{87}Rb mixtures. An

experiment at LENS [59] had reported a three-body loss coefficient of $2(1) \cdot 10^{-27} \text{ cm}^6/\text{s}$ measured in thermal mixtures at 300 nK. Values extracted for 3-body loss coefficients strongly depend on particle number calibrations and may also depend on temperature. For this reason, it is crucial to control the systematics of the experiment very well. One of the advantages of the high particle numbers produced in the experiment described in this thesis is that it allowed the production of large thermal ^{40}K - ^{87}Rb thermal samples, which has enabled studies of 3-body loss over a wide range of densities until clouds become undetectable.

For 3-body loss to occur, three particles need to come close to another. In a Fermi-Bose mixture where scattering between fermionic atoms is forbidden by the Pauli exclusion principle, the dominant 3-body loss mechanism is collisions between two ^{87}Rb and one ^{40}K atom. The 3-body loss coefficient K_3 then characterizes the local loss rate in the fermionic cloud according to

$$\dot{n}_F(\vec{r}, t) = -\frac{n_F(\vec{r}, t)}{\tau} - K_3 n_F(\vec{r}, t) n_B^2(\vec{r}, t) \quad (4.10)$$

where τ is the background loss rate. In order to measure K_3 in the experiment, a thermal mixture is prepared in the magnetic trap in the $^{40}\text{K} \otimes ^{87}\text{Rb} |9/2, 9/2\rangle \otimes |2, 2\rangle$ state by stopping the rf knife before condensation sets in. We then vary the hold time in the magnetic trap typically up to a few seconds and take absorption images of ^{40}K and ^{87}Rb perpendicular to the symmetry axis of the magnetic trap. From the 2D distributions recorded after a total time of flight of 5 ms (^{40}K) and 21 ms (^{87}Rb), both particle number and temperature as a function of time can be extracted. In the following, I will explain how the 3-body loss coefficient can be extracted from such a dataset. Some of the ideas have been inspired by a precision measurement of ^{87}Rb 3-body loss in Paris [104] and at JILA [105].

Since we do not have experimental access to the in-trap distributions, we would rather like to work in terms of total particle numbers. Integrating equation 4.10 over position yields

$$\dot{N}_F(t) = -\frac{N_F(t)}{\tau} - K_3 \int d^3r n_B^2(\vec{r}, t) \cdot n_F(\vec{r}, t) \quad (4.11)$$

This expression still contains the derivative of the particle number. By dividing by N_F and integrating this over time, we obtain

$$\ln \frac{N_F(t)}{N_F(0)} + \frac{t}{\tau} = -K_3 \int_0^t dt' \int d^3r n_B^2(\vec{r}, t') \cdot \frac{n_F(\vec{r}, t')}{N_F(t')} \quad (4.12)$$

By introducing the time-dependent quantities

$$\mathcal{N}(t) = \ln \frac{N_F(t)}{N_F(0)} + \frac{t}{\tau} \quad (4.13)$$

and

$$\mathcal{K}_3(t) = \int_0^t dt' \int d^3r n_B^2(\vec{r}, t') \cdot \frac{n_F(\vec{r}, t')}{N_F(t')} \quad (4.14)$$

we obtain the following simple expression:

$$\mathcal{N}(t) = -K_3 \cdot \mathcal{K}_3(t) \quad (4.15)$$

and the idea for the measurement of the 3-body loss rate is to determine K_3 from a linear fit to \mathcal{N} as a function of $-K_3 \cdot \mathcal{K}_3(t)$. The remaining question is how $\mathcal{K}_3(t)$ and $\mathcal{N}(t)$ are

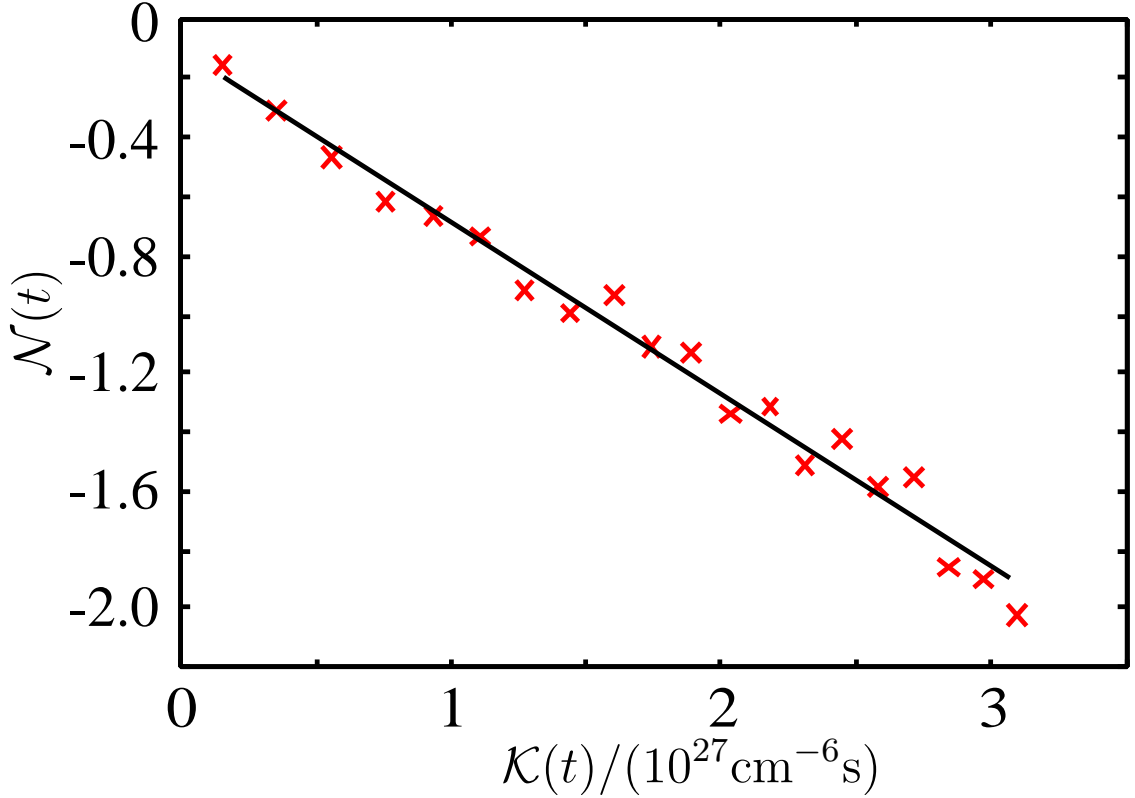


Figure 4.8: Decay analysis of thermal ^{40}K - ^{87}Rb mixtures.

determined. For different values of the hold time t , the $\mathcal{N}(t)$ can be calculated based on the measured ^{40}K atom number. The double integral $\mathcal{K}_3(t)$ is treated in the following way: For each time step in a decay series, we determine temperature and ^{87}Rb and ^{40}K particle number from 2-dimensional fits to time of flight absorption images using eq. 2.34. Using equation 2.23, we can calculate the overlap integral of the two distributions. In order to evaluate the integral over t' , we use the values of the inner integral for each time step and create a linear interpolation as a function of time which is integrated directly (trapezoidal rule).

Fig. 4.8 shows the left-hand side logarithmic expression $\mathcal{N}(t)$, of eq. 4.12 vs. the right-hand side double integral $\mathcal{K}_3(t)$ of eq. 4.12. From a linear fit, we can extract a value for the loss coefficient K_3 for each individual measurement. We then take the weighted average of twelve values. The corresponding error budget is determined as follows: The statistical error from the weighted average is the standard deviation, and the systematic error comes from the estimate of the atom number calibration. In equation 4.12, $\mathcal{K}_3(t)$ does not depend on the ^{40}K atom number calibration, since the density is divided by the total atom number in the integration. The ^{87}Rb atom number calibration does enter the calibration, since the bosonic density enters to the power of 2. With an estimated uncertainty on the ^{87}Rb atom number of 20%, this leads to a systematic uncertainty of $\mathcal{K}_3(t)$ of 40% given by

$$\Delta_{\text{sys}} K_3 = 0.4 K_3 \quad (4.16)$$

Altogether, we obtain:

$$K_3 = 2.8 (1.1)_{\text{syst}} (0.3)_{\text{stat}} \cdot 10^{-28} \text{ cm}^6/\text{s} \quad (4.17)$$

In order to cross-check the validity of our approach, we have measured 3-body decay of a pure ^{87}Rb thermal cloud with the same technique. In this case, the decay law is

$$\mathcal{N}_{\text{Rb}}(t) = -K_{\text{Rb}}(t) \cdot \mathcal{K}_{\text{Rb}}(t) \quad (4.18)$$

with $\mathcal{K}_{3,\text{Rb}}(t)$ and $\mathcal{N}_{\text{Rb}}(t)$ defined by

$$\mathcal{N}_{\text{Rb}}(t) = \ln \frac{N_B(t)}{N_B(0)} + \frac{t}{\tau} \quad (4.19)$$

$$\mathcal{K}_{\text{Rb}}(t) = \int_0^t dt' \int d^3r \frac{n_B^3(\vec{r}, t')}{N_B(t')} \quad (4.20)$$

From seven different individual decay series, we obtain

$$K_{3,\text{Rb}} = 2.20 (0.88)_{\text{syst}} (0.08)_{\text{stat}} \cdot 10^{-29} \text{ cm}^6/\text{s} \quad (4.21)$$

by taking the weighted average of the individual measurements. The systematic error is again due to the atom number calibration uncertainty of 20%. The precision result from ref. [104] is

$$K_{3,\text{Rb}} = 1.80 (0.40)_{\text{syst}} (0.06)_{\text{stat}} \cdot 10^{-29} \text{ cm}^6/\text{s} \quad (4.22)$$

and both values agree within the systematic errors. Coming back to 3-body decay of the mixture, the obtained value was:

$$K_3 = 2.8 (1.1)_{\text{syst}} (0.3)_{\text{stat}} \cdot 10^{-28} \text{ cm}^6/\text{s} \quad (4.23)$$

The resulting loss coefficient is thus an order of magnitude smaller than the value reported in [59]. The experimental outcome that 3-body loss in the ^{40}K - ^{87}Rb system is so much lower than previously believed, even when the mixture is not in the absolute internal ground state, is good news both in view of producing large and dense samples as demonstrated in this thesis, but it is also an important input parameter for theoretical calculations of the dynamical behavior of the cloud at the onset of collapse. 3-body loss is the ultimate loss mechanism in this mean-field implosion and thus an important input parameter for theory (see e. g. ref. [106]).

4.5 Stages of evaporative cooling

In the previous paragraph, I have limited my discussion to thermal mixtures. Now we will further lower the “evaporation knife” and see which regimes of degenerate mixtures are accessible in the experiment. When the ^{87}Rb atoms are not completely evaporated, various regimes of mixtures are accessible, ranging from dense thermal ^{87}Rb clouds of 10^7 ^{87}Rb atoms right at the phase transition point interacting with a moderately degenerate Fermi gas of $2 \cdot 10^6$ ^{40}K atoms to deeply degenerate mixtures with almost pure condensates. We achieve $> 1 \cdot 10^6$ atoms in the condensate coexisting with $7.5 \cdot 10^5$ ^{40}K atoms, limited by the onset of the collapse discussed in section 2.4.3.

My introductory discussion will be based on the experimental approach to mixture creation which has been to look at time of flight images of both clouds at various stages in the evaporative cooling cycle when large samples are transferred from the MOT to the magnetic trap.

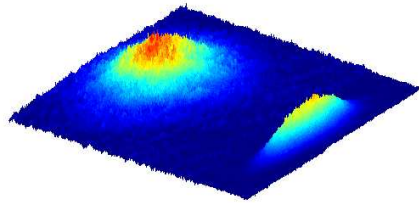
Throughout this section, the ^{40}K images were recorded with a time of flight T_E of 3 to 5 ms. With an axial ^{40}K trap frequency of $\omega_{ax} = 2\pi \cdot 16.6$ Hz, this means that $\omega_{ax} \cdot T_E$ is on the order of 0.3 to 0.5, and with the relatively large size of the Fermi gas in the trap, we can still deduce information on the axial *spatial* distribution in the magnetic trap from the time of flight image. In the experiment, this has allowed the extraction of information about the outer regions of the Fermi gas where it is noninteracting and about the inner regions where it overlaps with the dense Bose-Einstein condensate.

The ^{87}Rb atoms, on the other hand, are imaged after a total time of flight of 20ms. All of the experiments described in this chapter are based on imaging using the two-species detection technique (see section 3.11.2.2) which has allowed us to extract information about both species on the same CCD chip in one run although only one camera was used. With these prerequisites, the choice of the ^{87}Rb time of flight is motivated as follows: While it would in principle be beneficial to increase the time of flight even more in order to make the samples more dilute and allow an easier extraction of particle numbers, this is limited by the size of the CCD chip which must image both the ^{40}K and the ^{87}Rb image. Imaging on two different axes could have been also possible, but would have made the direct comparison of both observed density profiles more cumbersome.

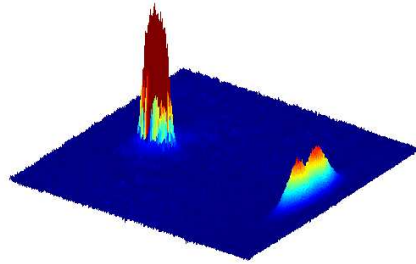
Fig. 4.9 shows resulting time of flight images for various evaporation end frequencies, with the final evaporation ramp being carried out at a speed of 1 MHz/s. In Fig. 4.9a), the mixture is still thermal. Due to the long time of flight, the thermal ^{87}Rb cloud has already reached its isotropic aspect size; the ^{40}K cloud still reflects the initial cigar-shaped trap profile. As the evaporation knife further cuts into the ^{87}Rb thermal cloud, a condensate starts to grow out of the thermal cloud as seen in Fig. 4.9b). At the same time, a hole appears in the axial direction in the ^{40}K cloud which is most pronounced in Fig. 4.9d), where the condensate is already almost pure. The hole in the fermionic distribution appears at the same time as the growth of the large condensate and in the spatial region where the condensate overlaps with the fermionic cloud and is accompanied by massive particle loss in ^{40}K , whereas the ^{87}Rb loss is essentially due to evaporation which acts mainly on the ^{87}Rb component. In Fig. 4.9f), evaporation has reduced the condensate size considerably, and the ^{40}K cloud no longer exhibits the pronounced hole; instead, it is rather peaked at the center, as we shall see later. In the following, I will present arguments which show that the appearance of the hole in the center of the cloud is due to the mean field collapse of the mixture. The collapse gives rise to an interesting dynamic behavior of the ^{40}K cloud which tends to refill the overlap region of rapid losses from the outer regions of the cloud.

A more direct visualization of the various stages of interacting mixtures is found in the vertical axial 1d profile of the interacting cloud (see Fig. 4.10). Here, I have analyzed in more detail three different stages. In a), the Fermi cloud exhibits a small peak in the center on top off a flat profile. This peak is due to the Fermi-Bose attraction increasing the fermionic density in the center of the trap where the BEC is formed. Once critical conditions for the onset of the collapse have been met as in b), the collapse localized in the overlap region removes the overlapping fraction of the Fermi gas. The hole which is left behind can be refilled from the outer regions of the trap, and, as we shall see, this refilling process can even lead to a second collapse of the mixture. The peaked structure which is shown in c) is stable

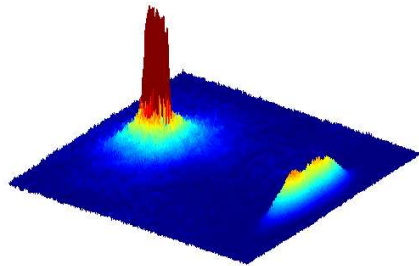
a) $f - f_0 = 90$ kHz



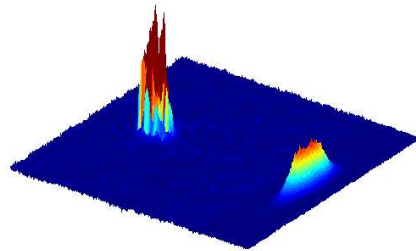
d) $f - f_0 = 30$ kHz



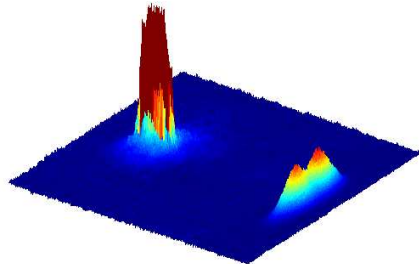
b) $f - f_0 = 60$ kHz



e) $f - f_0 = 25$ kHz



c) $f - f_0 = 40$ kHz



f) $f - f_0 = 20$ kHz

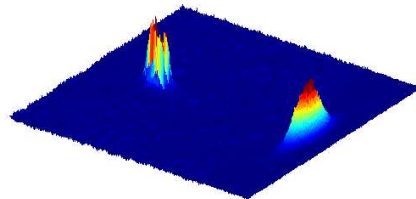


Figure 4.9: Time of flight absorption images of ^{87}Rb (left-hand side) and ^{40}K (right-hand side) at various stages of the final evaporation ramp. The figure indicates the difference between the evaporation and frequency and the absolute trap bottom where all atoms would be removed.

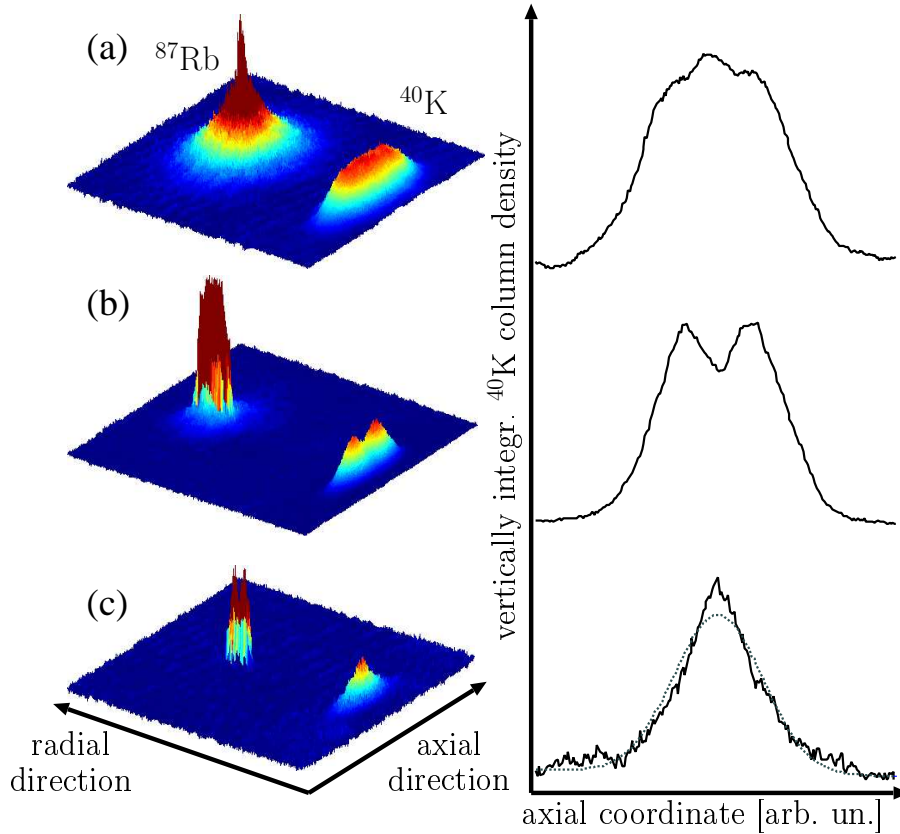


Figure 4.10: Density profiles of interacting ^{40}K - ^{87}Rb mixtures in various stages of the evaporative cooling process

over relatively long timescales of several 100 ms once the total ^{40}K number has been reduced to undercritical values; for comparison, I have included the result of a Fermi-Dirac fit to the experimental data which clearly fails to account for the interactions with the Bose-Einstein condensate in the center. In contrast to the situation depicted in a), which results from overcritical initial conditions and is on the edge to collapse, the condition of subfigure c) is a signature of Fermi-Bose interactions in a stable mixture.

4.6 Observation of a mean field induced collapse

In the discussion of the density profiles, I have claimed that the appearance of the hole in the center of the trap is due to the mean field collapse of the mixture. The distinction from localized loss processes in the presence of high densities is most apparent when looking at the associated time scales. In order to study the time scale of atom loss, I will discuss a situation where an only slightly overcritical mixture has been prepared. This time, I will discuss the behavior of the mixture not as a function of evaporation end frequency, but as a function of hold time in the magnetic trap. During the first few milliseconds of the hold time, where the rf knife is held at a fixed frequency, the condensate will still grow out of the thermal cloud and reach critical conditions after some initial delay. The result of the measurement is shown in Fig. 4.11. The figure shows the particle number contained in the central part of the ^{40}K

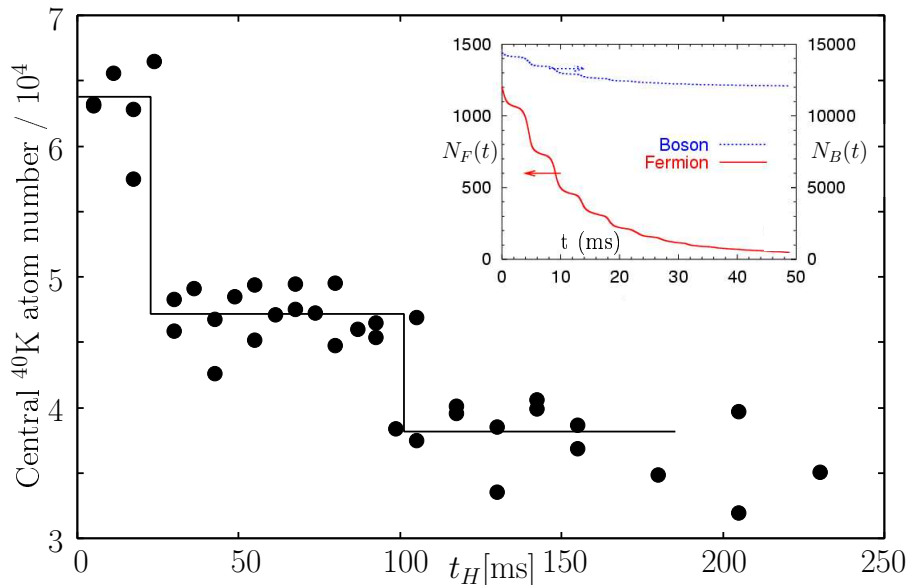


Figure 4.11: Sudden drop in atom number as a result of the initial collapse, followed by one revival of the collapse out of a non-equilibrium situation.

absorption image which helps enhance the visibility of the effect. Between 10 and 20 ms after the start of the measurement, a sudden drop reduces the integrated particle number in this area to about two thirds of its original value. The atom number then remains constant for some time and at 100 ms again undergoes a second sudden drop, which is due to a refilling of the cloud in the center from the outer regions and a subsequent second collapse. Looking at Fig. 4.11, one might argue that this refilling should become apparent in the center particle number going up again after the initial collapse. There is no such evidence from the data. One must however take into account that the central atom number from the time of flight image only approximately reflects the particle number in the overlap region. The occurrence of excitations and strong nonequilibrium conditions following the initial collapse may modify the expansion behavior and in particular lower the collapse conditions for the second occurrence of this mean-field instability. The message of Fig. 4.11 is the step-like feature which shows a very sudden drop of the particle number which is characteristic for this rapidly contracting mean-field implosion. From Fig. 4.11, we can constrain this timescale to below 10 ms, which is incompatible with pure 3-body loss in the absence of the collapse. The inset in Fig. 4.11 shows results from numerical modelling of the mixture in the regime of mean field instability based on hydrodynamic equations [106]. The numerical simulations qualitatively predict the same behavior for the particle number as a function of time. Note that these simulations make explicit use of the three-body loss coefficient for ^{40}K - ^{87}Rb which demonstrates the importance of this parameter discussed in section 4.4.

One of the experimental challenges in measuring data as in Fig. 4.11 is that over many runs, the initial conditions must be stable enough so that the time evolution can be well controlled. This is most important with respect to initial particle numbers and transfer from the MOT to the magnetic trap. When large overcritical mixtures are initially prepared, the steps shown in Fig. 4.11 can no longer be resolved initially due to initial fluctuations and the very complex dynamism. Instead, in this limit the collapse is observed as a very rapid overall

decay when measurements with independently prepared samples are visualized together as in Fig. 4.11. It would be an interesting perspective to analyze the behavior of the cloud in the regime of instability using phase-contrast imaging which would allow several subsequent nondestructive measurements of the same sample.

4.7 Stability analysis of Fermi-Bose mixtures

During the above discussion, I have mentioned conditions of criticality of mixtures and critical particle number of the mean field collapse several times. Here, I will summarize experimental findings on stable and unstable mixtures and discuss the relation with the value of the s wave scattering length for collisions between ^{40}K and ^{87}Rb . Two criteria for instability have been used here:

- Particle number combinations where the overall decay of the mixture is much too fast for normal 3-body decay in connection with the appearance of the pronounced hole are considered as unstable.
- The observation of the step-like drop as discussed in context with Fig. 4.11 is a sign of instability.

Other situations are identified as stable. The resulting atom number combinations are plotted in Fig. 4.12. Stable atom number combinations are plotted in blue, and combinations found to be unstable in the experiment in red. Atom numbers observed as stable are e. g.

$$\begin{aligned} N_F &= 7 \cdot 10^5 \\ N_B &= 1.2 \cdot 10^6 \\ \bar{\omega} &= 2\pi \cdot 91 \text{ Hz} \end{aligned} .$$

The error bars (c) result from an estimate of the ^{87}Rb and ^{40}K atom number uncertainty of 20% and 30%, respectively. The uncertainty in the ^{40}K atom number is less important than for ^{87}Rb , since in the regime considered here the dependence of critical conditions on ^{40}K is much smaller than on ^{87}Rb . Also shown in Fig. 4.12 are particle number combinations from two other experiments, namely the one at LENS and the JILA ^{40}K - ^{87}Rb setup. The particle number combination (a) of

$$\begin{aligned} N_F &= 2 \cdot 10^4 \\ N_B &= 1.5 \cdot 10^5 \\ \bar{\omega} &= 2\pi \cdot 91 \text{ Hz} \end{aligned}$$

has been reported as critical for the onset of collapse in ref. [60], but is an order of magnitude smaller than the stable particle number combination observed in Hamburg. Data point (b) is the stable particle number reported at JILA in ref. [53] without any sign of instability:

$$\begin{aligned} N_F &= 8 \cdot 10^4 \\ N_B &= 1.8 \cdot 10^5 \\ \bar{\omega} &= 2\pi \cdot 86 \text{ Hz} \end{aligned}$$

which raises the question why mixtures which are observed as stable in this experiment and by the JILA experiment have been reported as unstable at LENS.

When comparing critical particle numbers of different experiments, a few words on the role of the trap parameters are appropriate. Conditions for instability are of course influenced by the trapping potential. In general, the stronger the external confinement, the lower the critical particle numbers or the critical interaction are. The scale for the onset of instability is set by the geometric mean of the trap frequencies $\bar{\omega}$ which is given above for all three experiments. The mean harmonic trap frequency used in this experiment and at LENS are equal, whereas the JILA trap is just slightly shallower.

Within the Thomas-Fermi approximation for bosons and fermions, I have shown in section 2.4 that for fixed harmonic mean trap frequency, the aspect ratio does not influence the point of onset of collapse. This trap and the LENS trap are therefore directly comparable within this approximation, and the JILA trap is only slightly shallower and should therefore be slightly less subject to collapse than the the two other traps for the same particle number.

The only difference between the LENS trap and the trap used here is the trap aspect ratio, with our trap being slightly more elongated. The latter may play a role in the following situations:

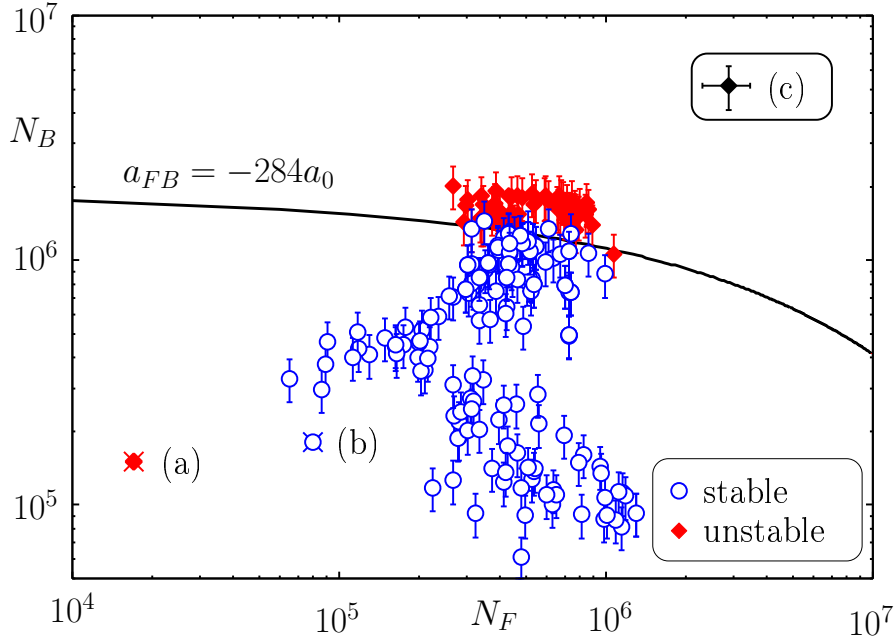
- **Breakdown of the Thomas-Fermi approximation.** This may occur when going to very elongated quasi-1D geometries (which is not the case in any of the experiments discussed here). The breakdown of the Thomas-Fermi approximation in the radial direction would result of radial trap frequencies on the order of kHz. The general effect of such a geometry is a stabilization with respect to collapse. This stabilization is responsible e. g. for the stabilization of bright solitons in a narrow window before the onset of collapse [107]. Another reason may be that particle numbers become below, say, 10^4 . Neither this is the case here.
- **Gravitational sag.** A trap which is radially more tight features a reduced *differential gravitational sag* between atoms of different mass compared to the isotropic situation. This differential sag is given by:

$$-g \left(\frac{1}{\omega_{\text{Rb}}^2} - \frac{1}{\omega_{\text{K}}^2} \right) \quad (4.24)$$

and vanishes for equal trap frequencies (see discussion in section 3.8. Since the differential gravitational sag reduces the spatial overlap of the components, some of the mean field energy is already “used up” in compensating for the gravitational sag. The larger gravitational sag in the Florence experiment thus results in the LENS trap becoming “less subject to collapse” for the same critical particle numbers, while the opposite is observed in the experiment. The role of the gravitational sag has also been discussed in [108].

Therefore, for the purpose of comparing the above-mentioned experimental results, the difference in trap aspect ratio does not play a role and cannot account for the order of magnitude difference in critical particle numbers.

It has been pointed out by the LENS group [60] that with the very sensitive relationship between critical particle numbers and the Fermi-Bose interaction parameter a_{FB} , the observation of the collapse instability can be a very sensitive way to constrain a_{FB} . This picture is true with respect to equilibrium conditions; however, the observation of instabilities during evaporative cooling, where excitations can never be completely avoided, complicates the picture, as we shall see. In this sense, the observation of a given particle number combination as

Figure 4.12: Stability diagram of ^{40}K - ^{87}Rb mixtures

stable imposes an upper limit on the interaction parameter. Observation of a particle loss at lower critical particle numbers means that either some other (possibly technical) mechanism is causing the loss², or that excitations lead to collapse for lower than equilibrium particle numbers.

Excitations

In my discussion of the implications of observed stability limits, I have mentioned several times that the presence of excitations in the sample during evaporative cooling means that an observed stability limit is always an upper limit on the interaction parameter. To illustrate this, fig. 4.13 shows the aspect ratio of the condensate before the onset of collapse in some of our experiments. The strong deviations (factor of ≈ 10) from the equilibrium aspect ratio of 1.3 may be due to fast evaporation compared to the axial trap frequency, thereby creating strong axial excitations.

These excitations can in turn locally increase the density and lead to critical conditions even for particle number combinations which are stable in an equilibrium situation. For example, a twofold increase of the Thomas-Fermi radius of the condensate due to excitations would lead to a fivefold increase in the central density of the condensate, leading to the same densities required for a an equilibrium collapse at $a_{FB} = 200a_0$. The same is true for any experiment observing the collapse during the evaporation ramp: In the absence of more sophisticated theory taking into account the excitations, observation of certain particle number combinations as stable provide an upper limit on scattering parameters.

When putting the observed experimental stability limit from this experiment (which produced the largest degenerate mixtures so far) into mean field theory, we obtain $-a_{FB} < 284a_0$

²in particular if symptoms of the collapse are scarce, such as a sudden loss of atoms and a localized structure

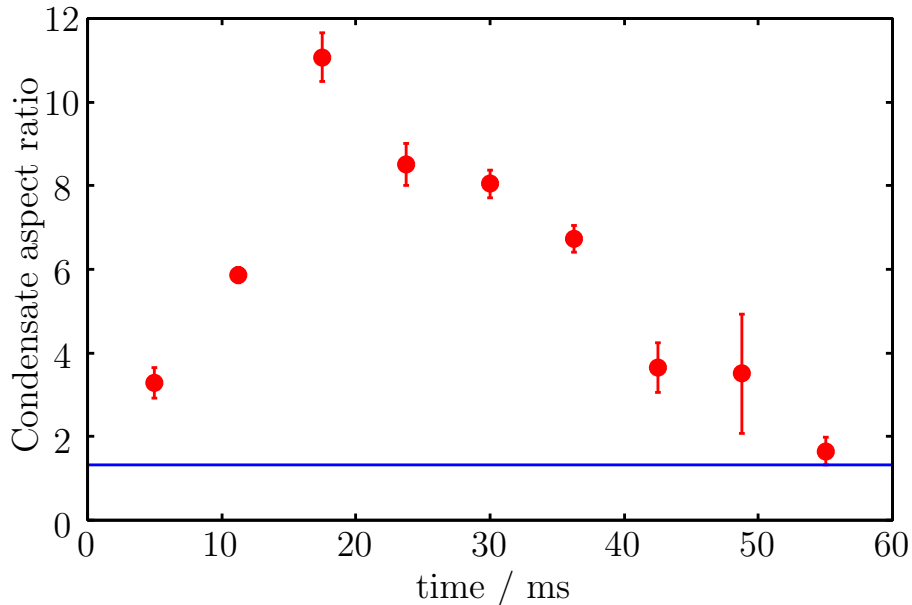


Figure 4.13: Aspect ratio of a forming condensate in a ^{40}K - ^{87}Rb mixtures, compared to the pure BEC expected aspect ratio of 1.3 (blue line).

as an upper limit on the interaction parameter. This upper limit coincides with the value deduced from the first ^{40}K - ^{87}Rb spectroscopy experiment at JILA and the corresponding resonance assignment. The identification of more Feshbach resonances and an upgraded collisional model performed at LENS as well as an improved magnetic field calibration has resulted in a scattering length of $-215(10) a_0$ [109], and the upper limit reported here is compatible with that value. Since the same argument is valid for any experiment, there is no contradiction between the observed stable particle number combinations and $a_{FB} = -215(10) a_0$.

It is an important result from this experiment that large stable ^{40}K - ^{87}Rb particle numbers can be produced, which was not clear *a priori*, and to have identified experimental signatures of the mean field collapse in Fermi-Bose mixtures, which have later been seen in experiments with tunable interactions (see following chapter).

Chapter 5

Tuning interactions in degenerate mixtures

In the previous chapter, I have approached interacting Fermi-Bose mixtures from the point of view of constant attractive interactions. The influence of interactions on the mixture parameters has been studied by varying the particle number. The overall particle number influences the value of the mean field interaction through the achieved densities. In this chapter, I discuss the behavior of the system as a function of scattering length. This approach has only become possible through heteronuclear Feshbach resonances in scattering between ^{40}K and ^{87}Rb which allow the s wave interaction in the mixture to be tuned from large and repulsive to large and attractive.

From a more general point of view, Feshbach resonances are *the* knob in atomic quantum gases which has made them so versatile and well controlled model systems. Tuning of atomic interactions through Feshbach resonances has been the key to a series of groundbreaking experiments in recent years, most recently the exploration of the BCS-BEC crossover in two-component Fermi gases [32, 33, 34, 35, 36]. Intimately connected with crossover physics is molecule creation at Feshbach resonances. Chapter 7 contains a discussion on Feshbach molecules and the first demonstration of heteronuclear Feshbach molecules.

Heteronuclear systems, Fermi-Bose mixtures in this particular case, will benefit a lot from the availability of controlling interactions through Feshbach resonances. It is one of the most important prerequisites in realizing a different and complementary approach to fermionic superfluidity in which the interaction between fermionic atoms is provided by bosonic atoms taking over the role of phonons in the solid state superconductor [110, 111, 112]. Exploiting heteronuclear Feshbach resonances could give access to ultracold polar molecules with novel anisotropic interactions. These molecules may be used as sensitive probes for physics beyond the standard model, such as a measurement of the permanent electric dipole moment of the electron. In chapter 7, this thesis presents the first realization of *heteronuclear* Feshbach molecules as an important and long awaited step towards the production of absolute ground state polar molecules and a more in-depth discussion of Feshbach chemistry.

Tunability of interactions is also a key to accessing the wealth of different phases predicted to exist in Fermi-Bose mixtures in a 3D optical lattice (see chapter 6) or even in a harmonic trap. So far, due to available scattering lengths in reported Fermi-Bose mixtures, only the effects of heteronuclear attraction have been studied in detail experimentally. Heteronuclear Feshbach resonances have already been identified in the systems $^6\text{Li} - ^{23}\text{Na}$ [62] and $^{40}\text{K} -$

^{87}Rb [63] in 2004 through increased atom loss at the resonance, but no tuning of interactions giving access to the above novel phenomena in heteronuclear systems has been reported.

In this chapter, I will report on the demonstration of tuning of elastic collisions through heteronuclear Feshbach resonances as published in [2]. This is the first time that Feshbach tuning of heteronuclear interactions has been observed, more than two years after the initial identification of these resonances through inelastic losses. In addition, we have for the first time realized all phases of harmonically trapped Fermi-Bose mixtures. Due to available heteronuclear mixtures, repulsive interactions between fermions and bosons have never been studied before in the experiment, including the observation of phase separation¹. I will first describe the experimental procedure. Then, I will discuss a determination of the resonance position for three Feshbach resonances. One of them exhibits the doublet structure characteristic for a p-wave resonance, thereby confirming a recent theoretical assignment [113]. In order to tune interactions, we then exploit a broad resonance located at 546.8 G and study both the attractive and repulsive side of the resonance. Strong attractive interaction is identified both through the expansion profile of the Fermi gas, which develops a strong bimodal feature, as well as through the mean field energy stored in the condensate. Furthermore, I will describe how we can induce a mean field collapse in a controlled fashion by tuning the scattering length. On the repulsive side of the resonance, the fermionic component is found to be shifted significantly upwards compared to the background scattering situation, which is explained in terms of vertical phase separation between the light fermionic and the heavy bosonic component in the presence of the symmetry-breaking gravitational force.

This chapter closely follows the S. Ospelkaus *et al.*, Phys. Rev. Lett. **97** (2006), 120403; for an in-depth discussion, see [66].

5.1 Experimental procedure

I have already described in chapter 4 how we create degenerate mixtures in the experiment. To access Feshbach resonances, a few more techniques are required, mostly related to trapping and preparing arbitrary spin states and controlling magnetic fields. In section 3.8, I have discussed an approach to purely optical trapping for mixtures which confines an arbitrary spin state and compensates for the differential gravitational sag between the two species as much as possible. This dipole trap, which is discussed in detail in [66], has been used in the experiments described in this chapter.

We evaporatively cool in the magnetically trapped fully stretched ^{87}Rb $|F = 2, m_F = 2\rangle \otimes$ ^{40}K $|F = 9/2, m_F = 9/2\rangle$ state. Slightly before reaching degeneracy, we shine in the crossed “magic” dipole trap. A last step of rf-induced evaporation is performed in the combined potential before ramping down the magnetic trapping potential and finishing with purely optical evaporation in the crossed dipole trap. The evaporation is done by lowering the intensity in the non-“magic” beam of the crossed dipole trap. We typically end up with a quantum degenerate mixture of $5 \cdot 10^4$ ^{40}K and 10^5 ^{87}Rb atoms and no discernible bosonic thermal fraction. The mean trapping frequency for ^{87}Rb in the dipole trap is $2\pi \cdot 50$ Hz.

As I have already said, the Feshbach resonances that we study occur in the $|1, 1\rangle \otimes |9/2, -9/2\rangle$ absolute ground state. The dipole trap gives us the experimental freedom to prepare and confine this high-field seeking state. This is performed using techniques discussed in section 3.9. We transfer ^{87}Rb atoms from $|2, 2\rangle$ to $|1, 1\rangle$ by sweeping a microwave

¹Independent work has been performed in parallel at Florence [64].

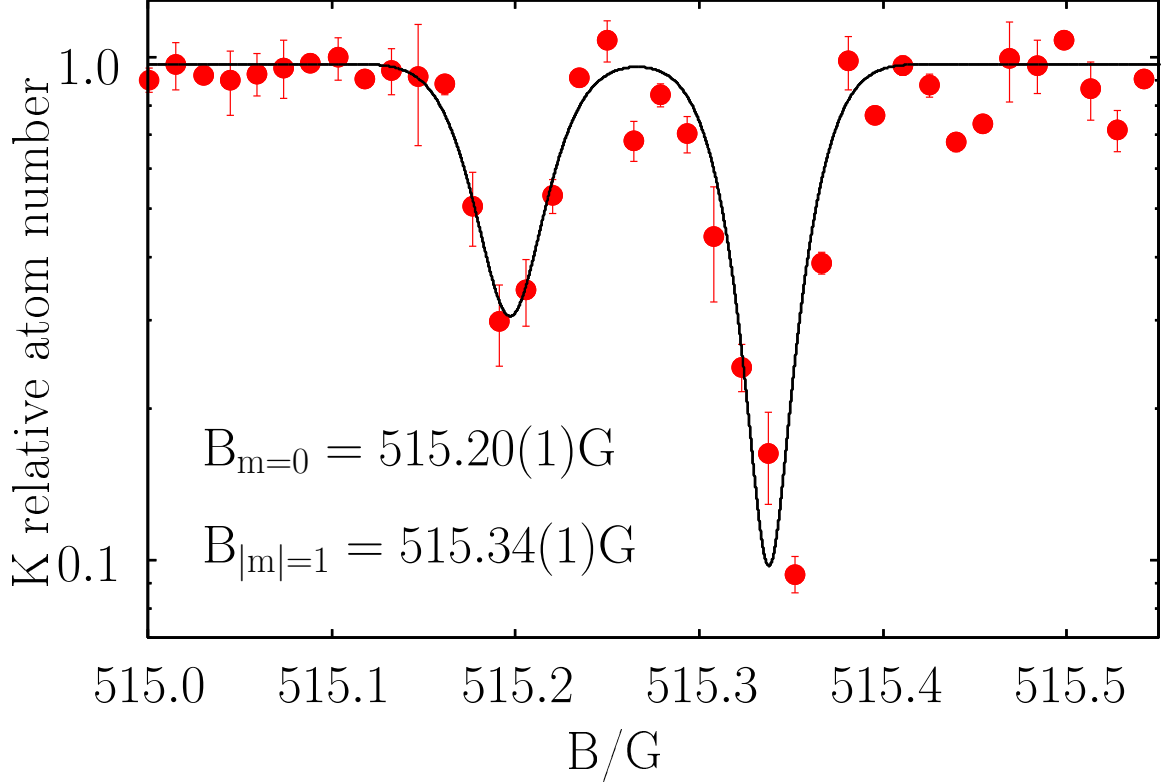


Figure 5.1: Doublet structure observed in ^{40}K atom loss at 515 G, showing the p -wave nature of this heteronuclear resonance.

frequency at a magnetic field of 20 G and remove any residual atoms in the $F = 2$ hyperfine manifold by a resonant light pulse. We then transfer ^{40}K atoms into the $|9/2, -7/2\rangle$ state by performing an rf sweep at the same magnetic field achieving close to 100% efficiency. We subsequently ramp up the magnetic field to a value near the resonance. Magnetic fields near the Feshbach resonances are calibrated by driving both the ^{87}Rb $|1, 1\rangle \rightarrow |1, 0\rangle$ transition and the ^{40}K $|9/2, -7/2\rangle \rightarrow |9/2, -9/2\rangle$ transition².

5.2 Identifying the resonances

In a first measurement, we have identified the position of strong inelastic losses for several previously identified resonances and found positions of 495.28(5) G, 546.8(1) G and (515.20(5) G / 515.34(5) G)³. The measurement is performed by preparing the system in the $|9/2, -7/2\rangle \otimes |1, 1\rangle$ state at the desired magnetic field and then transferring the fermionic component into the Feshbach-resonant $|9/2, -9/2\rangle$ state by a 100 kHz wide rf sweep of 3 ms after the field has settled. We then wait for a given time of 50 ms, 40 ms, (350 ms / 350 ms) for the above resonances. As an important result, the 515 G feature shown in Fig. 5.1 exhibits a dou-

²For a discussion of magnetic field accuracy, see chapter 7. The same equipment has been used here, only that the field sweeps performed in the tuning experiments presented this chapter may mean that the final magnetic field values of the sweeps are not as accurate as $5 \cdot 10^{-6}$

³Note that the observed resonances are systematically shifted by roughly 1 G as compared to [113]

plet structure with a separation between the two peaks of 140 mG. Such a doublet feature has previously been found in p -wave scattering between fermionic atoms [114, 115, 42, 116, 117]. Reference [114] predicted a p -wave resonance to occur in the ^{40}K - ^{87}Rb system at magnetic fields of (540 ± 30) G, with the $|m_l| = 1$ peak located approximately 300 mG above the $|m_l| = 0$ peak. Ref. [113] obtained the most recent resonance assignment in this system by ascribing a p -wave character to the resonance occurring at 515 G. The doublet structure measured in our experiment for the first time provides direct evidence of a heteronuclear p -wave resonance and confirms the resonance assignment. Corresponding loss features for the other observed resonances can be found in [66].

5.3 Attractive interactions

In order to tune interactions in the heteronuclear system, we have studied the broadest of the available s -wave resonances which we observe at $B_0 = 546.8(1)$ G, where the resonance position has been determined by the transition between strong attractive and repulsive interactions (see below). At the resonance, the scattering length varies as

$$a_{\text{FB}} = a_{\text{BG}} \cdot \left(1 - \frac{\Delta B}{B - B_0}\right) \quad (5.1)$$

(see Fig. 5.2d) with a predicted width ΔB of -2.9 G [113] and a background scattering length of $a_{\text{BG}} = -185a_0$ [64]. For these measurements, the $|9/2, -7/2\rangle \rightarrow |9/2, -9/2\rangle$ transfer is performed at fixed fields of 550.5 G (for studies of $a_{\text{FB}} < 0$) or 543.9 G ($a_{\text{FB}} > 0$) after the field has settled. The field is then ramped to varying values near the resonance within 50 ms, thereby changing a_{FB} adiabatically.

Above the center of the heteronuclear resonance, the K-Rb interaction is expected to be attractive. We study tuning of interactions by observing the mean field energy of the BEC confined in the combined potential of the external dipole trap and the heteronuclear mean field potential:

$$U_B(r) = U_{\text{B,ext}}(r) + g_{\text{FB}} \cdot n_{\text{F}}(r) \quad . \quad (5.2)$$

The additional trapping potential due to the fermions becomes evident when both the external trapping potential and the magnetic field are switched off simultaneously. In the case of attractive interactions, the effective trap frequency for the bosonic component increases with interactions due to the additional heteronuclear mean field confinement. This leads to a larger density and thus to a stronger mean field energy of the condensate which has an intrinsic repulsion characterized by $a_{\text{BB}} = 100.4(1)a_0$ [77]. As the simultaneous switchoff occurs, the heteronuclear mean field confinement is reduced to its background value determined by $a_{\text{FB}} \approx a_{\text{BG}}$. The stronger the in-trap interaction is compared to the background interaction, the faster the condensate will expand due the increased mean field energy [51, 118] as shown in Fig. 5.2a above resonance.

Complementary information can be gained from a measurement where we leave on the magnetic field during expansion (Fig. 5.2b). In contrast to Fig. 5.2a, the permanence of strong attraction now slows down the expansion of the BEC as the heteronuclear attraction will tend to keep the sample together during expansion. A peculiar feature arises in the expansion profiles of the Fermi gas which, in our experiment, has a larger extent than the BEC and only overlaps in the center. In this overlapping region, fermions and bosons are held together by the mean field attraction and give rise to a dense feature in the center of the

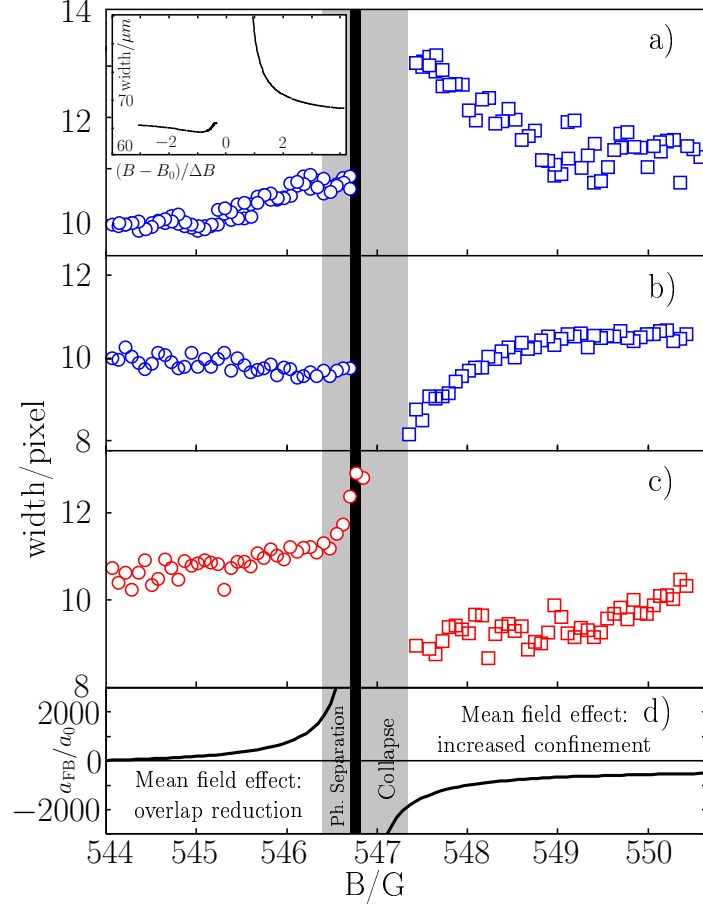


Figure 5.2: Observed width of the components after expansion as a function of magnetic field. The inset shows numerical mean field calculations where the width of the BEC after expansion has been plotted as a function of detuning from resonance. **a)** bosonic component when the resonant interaction is turned off in the same moment as the external potential **b)** corresponding bosonic component with resonant interaction left on during expansion **c)** fermionic width corresponding to **b)**. The region shaded in grey indicates instability with respect to collapse. The black vertical line marks the observed transition from attractive to repulsive interactions. (1 pixel $\hat{=}$ 3.2 μm ; time of flight 25.2 ms for ^{87}Rb and 7.5 ms for ^{40}K) **d)** Heteronuclear scattering length and expected phases.

fermionic cloud, while the non-overlapping fraction gives rise to a broader background. The overall fermionic image thus acquires a bimodal appearance as seen in images in Fig. 5.3d.

5.4 An induced mean field collapse

For even stronger attraction closer to the resonance, the system is expected to become unstable with respect to collapse as explained in chapter 2 and observed as a function of particle number in chapter 4. The corresponding magnetic field region for our experimental parameters is shaded in Fig. 5.2. This region of mean field instability is studied in detail in Fig. 5.3, where we have plotted the atom numbers in the mixture as a function of magnetic field in a). At a detuning of about 0.6 G above resonance, we observe a sudden drop in both the fermionic and the bosonic atom number which is due to the mean field collapse of the mixture. In contrast to previous work observing the onset of instability as a function of atom number (see previous chapter and [59]), the collapse is now due to tuning of interactions above a certain critical interaction strength in an otherwise undercritical mixture. We can also observe the collapse happen as a function of time – see Fig. 5.3b, where we have ramped to a fixed magnetic field in the region of instability and then varied the hold time of the mixture. The onset of the collapse, again visible as a sudden drop in atom number, is retarded by a timescale given roughly by the trap frequency and happens on a timescale < 1 ms (Fig. 5.3d). During the collapse the overlap region of the fermionic cloud with the BEC is destroyed by a three-body implosion which causes significant heating and excitation in the remaining sample, reflected in the width of the remaining cloud in Fig. 5.3c. Possibly due to evaporation of the sample in the shallow dipole trap, the mixture assumes a new equilibrium. The heating leads to significantly reduced densities in the cloud, which means that losses in the remaining cloud are approximately constant as we further approach the resonance (see Fig. 5.3a). Fig. 5.3d shows time of flight images of the Fermionic component with the field left on during expansion, clearly demonstrating the bimodality of the Fermionic distribution, the sudden loss due to the collapse and the remaining fraction.

5.5 Repulsive interactions and phase separation

Phase separation due to repulsive interactions in a composite system of harmonically trapped fermions and bosons has been intensely discussed in theory [71, 72], but never explored in experiment. Tuning of heteronuclear interactions has enabled us to enter the regime of repulsive heteronuclear interactions, where phase separation is expected to occur. In the limit of vanishing differential shift due to gravity and for our experimental parameters, phase separation will occur as a shell of Fermions surrounding a dense BEC core. For weak repulsive interactions, there will still be a non-vanishing fermionic density overlapping with the center of the BEC. In this case, the additional fermionic curvature acting on the condensate will increase the mean field energy in the condensate, again leading to a faster expansion of the BEC as seen on the left-hand side of Fig. 5.2. When the fermionic density at the trap center vanishes at even higher repulsion, the potential felt by the Bose cloud will rather be that of the pure external trapping potential with quite a sharp transition to a very steep higher order potential created by the fermionic density in the outer shell, at the edges of the condensate. We identify this region with the regime from 546.4 G to the center of the resonance at 546.8 G where, as seen in Fig. 5.2a, the width of the condensate saturates. At the onset

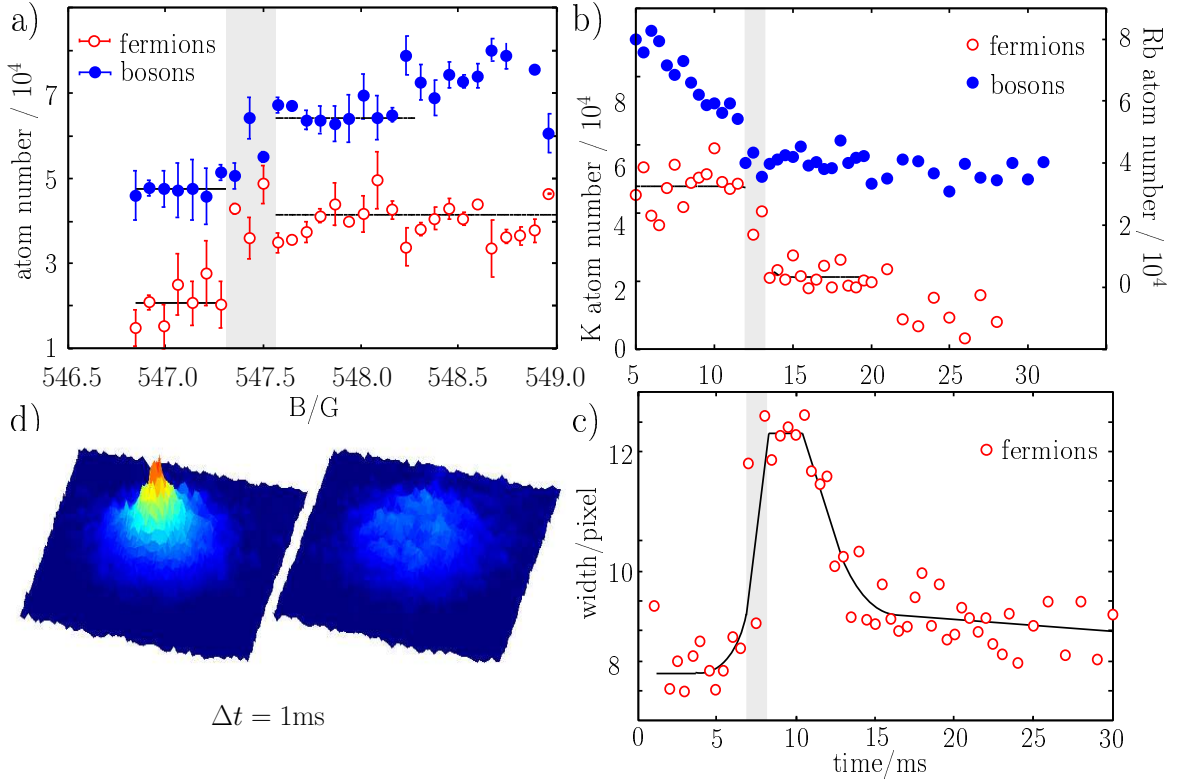


Figure 5.3: Induced mean field collapse of the mixture. **a)** Sudden drop of atom numbers for critical heteronuclear interactions. **b)** Varying hold time in the regime of instability (at $B=547.4$ G). Onset of the collapse is retarded by a timescale given by the trap frequency. **c)** As the collapse happens, the sample is excited and heated, visible in the width of the fragments. **d)** Sample time of flight images showing the bimodal distribution in the fermionic component and the sudden collapse of the system.

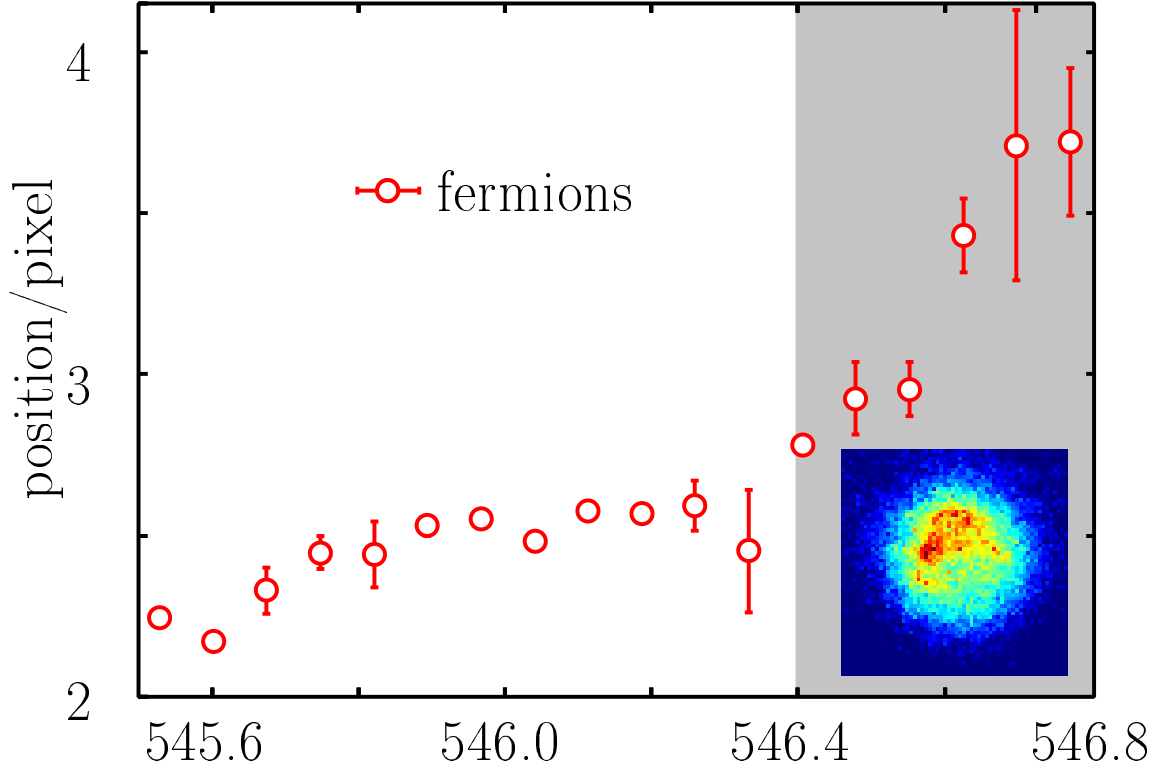


Figure 5.4: Vertical position of the Fermi gas as a function of magnetic field. The grey shaded area indicates the assumed region of full phase separation, where the fermionic density is expected to vanish at the BEC core. Due to gravitational symmetry breaking, the fermions are pushed above the BEC, an effect amplified by time of flight expansion. The inset shows the corresponding fermionic density distribution where most of the density is concentrated in the upper part of the image. Again, 1 pixel corresponds to $3.2 \mu\text{m}$.

of this regime, we also find the width of the Fermi gas with the magnetic field left on during expansion (Fig. 5.2c) to exhibit a change of slope. This may indicate that at complete phase separation, the repulsive interaction leads to a rapid expansion of the Fermi gas suddenly accelerated outside when the external potential is switched off and the repulsive bump of the BEC in the center maintained.

Inside a harmonic trap and in the presence of gravity, atoms experience a gravitational sag given by

$$-g/\omega^2 \quad . \quad (5.3)$$

For systems with different masses, such as the ^{40}K - ^{87}Rb system, this will in general lead to a differential gravitational sag between the components, as the trap frequencies may be different, and I have explained in section 3.8 how our “magic trap” compensates for most of the differential sag. There may however still be some residual differential sag left over, and this becomes particularly important for strong repulsive interactions. A slightly different gravitational sag breaks the symmetry of the system and therefore favors phase separation to occur in the vertical direction (see also [108]). As a consequence, the position of the fermionic component in the time of flight image is shifted upwards as a function of detuning from resonance, with an even stronger slope in the region of complete phase separation (see

Fig. 5.4). An important aspect is that the shift in position between fermions and bosons in the trap is amplified by the repulsive interaction during expansion if we leave on the interaction.

The initial symmetry breaking in the trap may be anything between a differential gravitational sag on the order of $1 \mu\text{m}$ and a Thomas-Fermi radius of a typical BEC in the dipole trap of between 5 to 10 μm . In the latter case, the distance would be directly resolvable using absorption imaging without any amplification in time of flight. Yet, we do not observe the behavior shown in Fig. 5.4 if we switch off the strong repulsive interactions during time of flight. Thus, the small initial symmetry-breaking in the direction of gravity is strongly enhanced by the permanence of repulsive interactions during time of flight and clearly visible in absorption images such as in the inset of Fig. 5.4 where the Fermionic density is concentrated in the upper part of the image.

To summarize this chapter, we have identified a p -wave Feshbach resonance at 515 G in heteronuclear ultracold K-Rb atom scattering. Tuning of interactions at the 546.8 G s-wave resonance enables us to explore the entire phase diagram of the mixture for arbitrary heteronuclear interaction and fixed repulsive Bose-Bose interaction. We have extensively studied both the expansion of the cloud for attractive interactions and induced a mean field collapse of the mixture by tuning the scattering length. On the repulsive side of the resonance, we have entered a thus far inaccessible part of the phase diagram of the harmonically trapped mixture. For sufficiently strong repulsive interactions, we observe the mixture to phase separate. In the presence of gravity, phase separation is found to occur as a “stacking” effect in the vertical direction, with the light fermionic component being repelled above the Bose-Einstein condensate.

Chapter 6

Fermions and bosons in 3D optical lattices

In a seminal paper on ultracold atoms in optical lattices [119], D. Jaksch and coworkers have shown that the Hubbard model discussed in the context of condensed matter systems can be realized using ultracold (bosonic) atoms in optical lattices, making them possible “quantum simulators” for condensed matter Hamiltonians. From the experimental point of view, this potential became apparent in 2002 with the observation of a superfluid to Mott insulator phase transition for bosonic atoms in optical lattices [120]. This and following experiments and theoretical work on atoms in optical lattices demonstrated the main advantages of atomic systems in lattices and also showed important differences from traditional condensed matter systems. Atomic systems are characterized by an enormous degree of control over the properties of the system: The strength of the crystal can be tuned just by changing the laser power. This allows the ratio of tunneling to on-site interaction to be tuned over several orders of magnitude. The optical crystals made of light have perfect periodicity and are completely defect-free. By playing with the laser power in the different beams forming the lattice and “freezing out” degrees of freedom, one- and two-dimensional geometries can be realized. Feshbach resonances allow interactions between atoms to be tuned from repulsive to attractive, and recent years have seen a tremendous increase in diagnostics, from direct imaging of the band structure and the quasimomentum distribution to advanced spectroscopic techniques probing site-dependent interactions. One of the main differences between conventional condensed matter systems and atoms in lattices is the presence of the trap. In fact, the initial demonstration of the Mott insulator transition by increasing the lattice strength has only become possible as a result of the trap and the finite size of the system¹.

Besides offering an interesting approach to condensed matter physics, atoms in optical lattices also have applications in molecule formation, as we shall see in chapter 7, in quantum information processing and in other “quantum engineering” proposals. So far, studies with atoms in 3D optical lattices have been performed using a single atomic species, either bosonic or fermionic, eventually exploiting the spin internal degree of freedom of the atoms. In this chapter, I will report on the first realization of heteronuclear systems in 3D lattices, in this case Fermi-Bose mixtures.

Phase diagrams of Fermi-Bose mixtures in 3D lattices have been calculated in [121, 122].

¹For a fixed mean occupation number in a homogeneous system, the system would remain in the superfluid phase forever.

The system offers an alternative and in many ways complementary approach to fermionic superfluidity, compared to the BCS-BEC crossover in two-component Fermi gases [32, 33, 34, 35, 36]. In the literature, this approach is known as boson-induced Cooper pairing [56, 57]. The analogy is perhaps not perfect in every sense, but a very compelling perspective demonstrating the potential of mixtures in lattices: The role of the crystal in the traditional solid state system is taken over by an artificial crystal made out of light; the lattice potential can be varied practically arbitrarily. The fermionic electrons which make up the Cooper pairs in the superconductor are replaced by fermionic atoms. In the standard superconductor picture, phonons provide the attractive glue between fermions which is responsible for the pairing. In the atomic system, the attractive interaction between the fermions is provided by the Fermi-Bose interaction and the bosonic atoms; the interaction can be varied practically arbitrarily through Feshbach resonances, as seen in the previous chapter. Realizing this goal may of course depend on the ability to tune bosonic interactions at the same time, which is not easy given that they would both be influenced by the same magnetic field at a Feshbach resonance, and it may also require novel diagnostics to be developed, but this perspective alone would be motivation enough for studying Fermi-Bose mixtures in lattices.

Another topic which is currently of great interest for ultracold atoms in optical lattices is the perspective of realizing disorder-related phenomena in such systems. Recently, randomized light potentials have been used in Florence [123] to create such a system, and the findings have been interpreted in terms of a Bose glass phase. For Fermi-Bose mixtures, the experimental perspectives for the realization of disordered systems rely on using atomic “disorder”, i. e. an “impurity” or defect atomic species randomly distributed over the lattice. Several localization scenarios can be imagined. Fig. 6.1 gives an illustration of some possible effects, starting with a pure bosonic superfluid (Fig. 6.1a). Adding fermionic impurities and considering the attractive ^{40}K - ^{87}Rb Fermi-Bose interaction energy as an additional potential for the bosons, the “defects” caused by the fermionic impurities can be described by a local change of the effective optical lattice depth for the bosons due to the interparticle interaction (Fig. 6.1b). If the energy level shift caused by the interaction energy is large enough, the superfluid bosonic wavefunction will not extend into this defect region, but will be scattered by the impurity. If scattering becomes frequent, interference effects along a closed scattering path are predicted to suppress transport and lead to a localization scenario similar to Anderson localization (e.g. [124]) (Fig. 6.1c). A further increase in the impurity density may lead to the formation of “forbidden walls”. Once the walls in this quantum percolation scenario lead to a sufficiently complicated labyrinth like structure for the bosonic wavefunction, a single coherent superfluid phase can no longer be sustained and several separated domains can be formed (Fig. 6.1d). For a filling of one fermion per lattice site (Pauli limit for the lowest band) the localized phase becomes comparable to a pure bosonic Mott-insulator but now the transition is shifted by the interaction energy with the fermionic impurity (Fig. 6.1e). Access to these various regimes in the experiment can be controlled by varying both crystal depth and fermionic impurity concentration and may strongly depend on temperature, external confinement and relative potential depth for the two species.

In this chapter, I describe the first experimental demonstration of Fermi-Bose mixtures in 3D optical lattices. In contrast to chapter 7, which discusses two-body physics in the optical lattice, this chapter deals with many-body systems. The approach described here uses diagnostic techniques developed for pure bosonic systems to probe the behavior of the bosonic component of the mixture in the presence of fermionic atoms. All experiments have been performed in a regime of small fermion number (compared to the total boson number), which

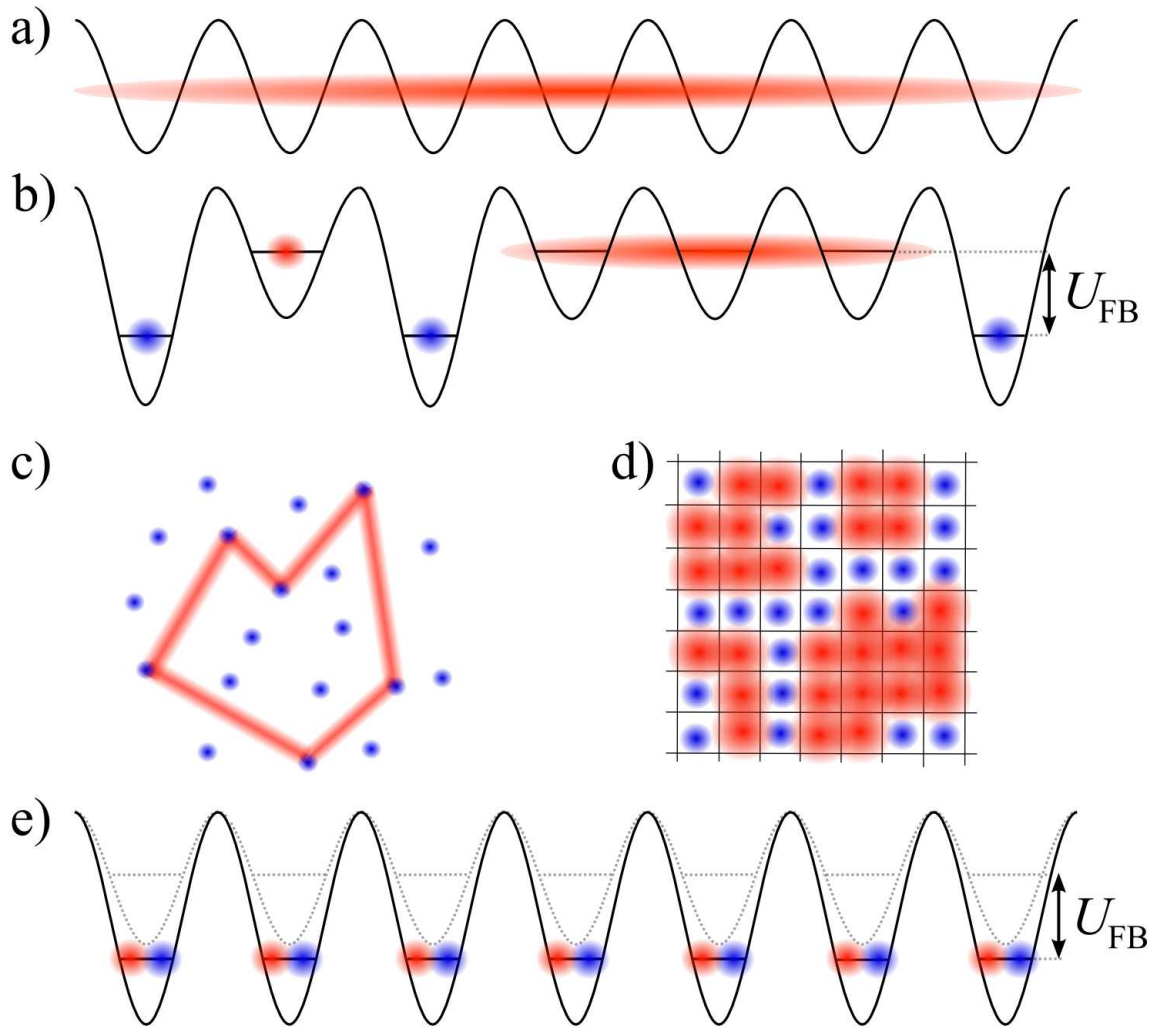


Figure 6.1: Schematic localization scenarios. **a.** Pure bosonic superfluid in an optical lattice. **b.** Shift of the effective potential depth due to fermionic impurities. **c.** Localization by interfering paths of the bosonic wavefunction scattered by randomly distributed fermionic impurities. **d.** Localization due to percolation. A random fermion distribution hampers the establishment of a coherent connection and causes the localization of bosonic ensembles in superfluid “islands”. **e.** Mott insulator transition induced by a uniform distribution of attractive fermionic impurities, resulting in an effectively deeper lattice potential for the bosons.

is the first motivation for calling the fermionic atoms “impurities”. When the mixture is loaded into the optical lattice, I will show that already a small impurity admixture will significantly alter the behavior of the mixture. More specifically, the loss of coherence accompanying the onset of a Mott insulating phase in the case of a pure bosonic system is observed much earlier for a small fermionic admixture than for a pure system. The same is the case for the correlation length in the sample. I will discuss how this effect is studied as a function of impurity concentration. The findings were published in [3] and have generated a lot of theoretical and experimental interest in this novel system. There is an ongoing discussion on the size of the observed shift and possible explication of the effect both in terms of mean field models, DMRG calculations, Monte Carlo simulations, adiabatic thermodynamic processes in the lattice ramp-up sequence and a possible relation to disordered systems. This chapter closely follows our publication ref. [3]; for a more detailed discussion, including basic lattice theory, see [66].

6.1 Experimental procedure

The experiments presented in this chapter rely on techniques discussed in previous chapters for creating degenerate Fermi-Bose mixtures. I have already mentioned the role of the external trap in my introductory discussion. Experiments in optical lattices greatly benefit from a weak external confinement which is as isotropic as possible. Experimental complications arise when trapping several species at the same time due to a possible differential gravitational sag between the two resulting in a reduced overlap. In section 3.8, I have discussed how this can be overcome by using a special optical dipole trap with a carefully chosen wavelength. All the experiments presented in this chapter were performed using the external confinement of the magnetic trap which is characterized by the same absolute potential for ^{40}K and ^{87}Rb . In order to reduce the central density as much as possible, but at the same avoid a reduction in overlap due to the presence of the differential gravitational sag, the following scheme for loading the mixture into the optical lattice has been developed: When the mixture is close to degeneracy after the initial rf-induced sympathetic cooling, the shape of the elongated magnetic trap is adjusted adiabatically to come closer to an isotropic situation. The idea is to decrease the radial confinement (about 250 Hz for ^{87}Rb) of the magnetic trap to about 150 Hz by increasing the offset field. In order not to lose too much in terms of collisions for the final evaporation stage and to make the geometry more isotropic, the axial trap frequency needs to be increased at the same time. In principle, this could be achieved by increasing the overall magnetic trap current, but for 11 Hz axial ^{87}Rb trap frequency used during evaporation, the trap is already running at the maximum current. The answer is therefore to increase the axial confinement by means of an additional dipole trap beam. In the experiment, this is performed by using one of the diagonal lattice beams and blocking the retroreflection using an EOM between the collimation lens and the mirror. The additional dipole beam increases confinement in the axial direction to about 50 Hz. In the combined potential of the laser beam and the magnetic trap, one last step of rf-induced sympathetic cooling leads to degeneracy of the mixture in a trap which is as isotropic as possible but not too weak against gravity. The next step is to ramp up the optical lattice potential. For one diagonal axis and for the horizontal beam, this is done just by increasing the power in the beam. For the second diagonal axis which is in use for the additional dipole trap, the lattice potential is increased by changing the voltage at the EOM so that the back-reflected fraction of the light increases.

For all three lattice axes, this ramp-up procedure is performed simultaneously.

Below, I will discuss measurements for pure bosonic atoms and with a variable admixture of fermionic atoms. In order to make the direct comparison as clear as possible, the pure bosonic system is prepared in the same way as the mixture, only that the fermionic component is removed immediately before ramping up the optical lattice using a resonant light pulse. Final samples contain about 10^5 ^{87}Rb atoms (pure BEC with no discernible thermal cloud) and a variable 0-20% fermionic impurity component subsequently loaded into the lowest Bloch band of the optical lattice. The amount of ^{40}K is controlled by adjusting initial laser cooling parameters.

Due to the additional harmonic confinement by the magnetic trap and the Gaussian lattice laser profiles, the mixture occupies a few ten thousand lattice sites with an occupation rising from 0 in the outer regions to 1 fermion and >5 bosons per site at the center. Experimental parameters have been chosen such that the fermionic impurities always stay within the bosonic cloud. For $2 \cdot 10^4$ fermions at $T = 0$, the radial ensemble radius in the harmonic trap (before lattice ramp-up) is roughly $8.6 \mu\text{m}$ with a central density just reaching the unity filling density. For the assumption of a most compressed Fermi cloud with unity filling, the corresponding radius is approximately $7 \mu\text{m}$. These numbers have to be compared to the extension of a pure BEC of $\approx 10^5$ atoms, whose radial radius is $\approx 8.2 \mu\text{m}$ for $25 E_r^{\text{Rb}}$ lattice depth.

After sudden switch-off of the lattice potential and a period of free expansion of 15-20 ms, we record the interference pattern which builds up in the density distribution of the bosonic component. The fermionic component is simultaneously imaged after 3-5 ms time of flight and is used to determine the impurity concentration. In order to study the behavior of the system, this procedure is repeated for several different final lattice depths.

6.2 Loss of coherence for deep lattices

Fig. 6.2 shows the evolution of the boson interference pattern for about 20% impurity concentration (bottom row) in comparison to a pure bosonic sample created under the same experimental conditions but with a removal of the fermionic atoms just before the lattice ramp-up sequence (top row). The lattice depths are given in units of the recoil energy for the ^{87}Rb component $E_r^{\text{Rb}} = (\hbar^2 k^2)/(2m_{\text{Rb}}) \approx h \cdot 2.14 \text{ kHz}$ where k is the lattice wavenumber. The loss of interference contrast which accompanies the breakdown of long range order is clearly visible in both cases. In case of the pure bosonic gas, the loss of coherence accompanies the well-known superfluid to Mott-insulator phase transition [119, 120]. The latter occurs as a result of competition between the minimization of kinetic energy, parametrized by the tunneling matrix element J which tends to delocalize the atomic wavefunction over the crystal and the minimization of interaction energy U (Fig. 6.2a). As can be clearly seen from Fig. 6.2b, the presence of fermionic impurities induces a loss of coherence at much lower lattice depths than for a pure BEC.

6.3 Quantitative analysis

In the following, I will study the influence of the fermionic component quantitatively. Taking the interference contrast in the above pictures as a measure of coherence and putting it into mathematical terms, one can define the visibility of the matter wave interference pattern as

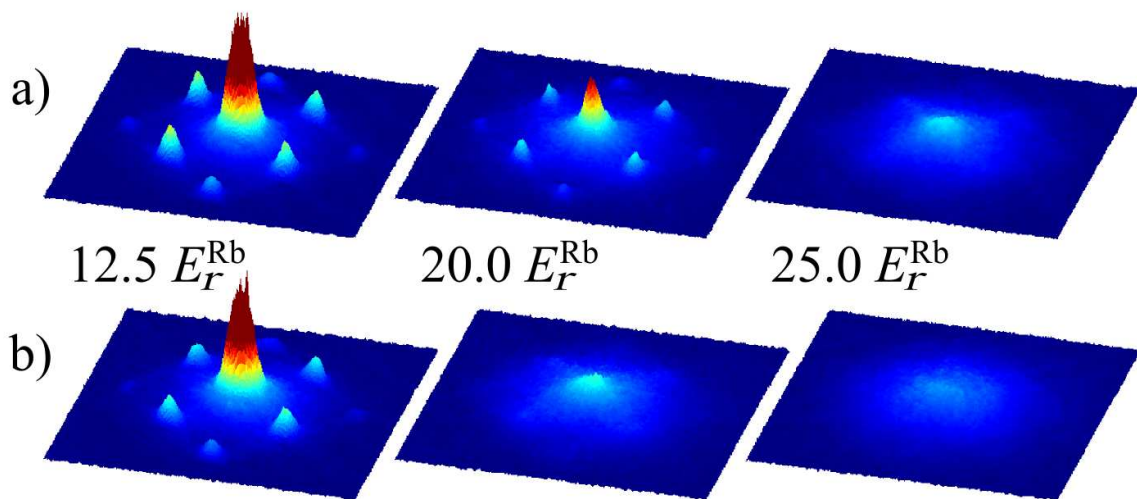


Figure 6.2: Time of flight absorption images of the bosonic component 15 ms after switching off the lattice and trap potentials. **a.** Pure bosonic ensemble for three different lattice depths. **b.** Fermi-Bose mixture for the same lattice depths and 20% fermionic impurity concentration. The reduction of interference contrast visible in the images accompanies the onset of localization. This loss of coherence is shifted to lower lattice depth in the presence of fermionic impurities.

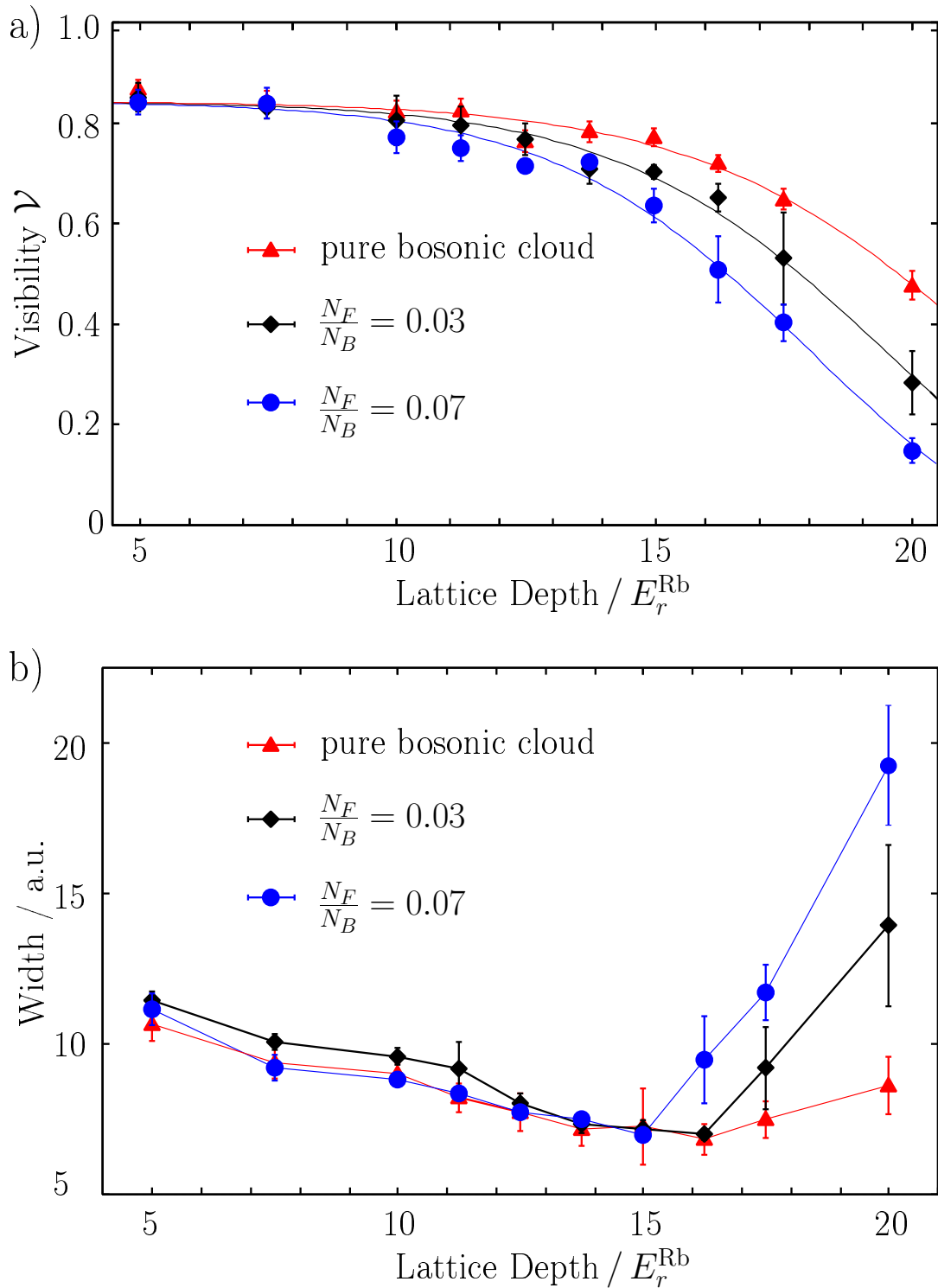


Figure 6.3: Visibility \mathcal{V} (a) and central peak width (b) of the bosonic interference pattern for different fermionic impurity concentrations.

[125]

$$\mathcal{V} = \frac{N_{peaks} - N_{int}}{N_{peaks} + N_{int}}. \quad (6.1)$$

Here N_{peaks} denotes the sum of the number of atoms within the first order interference maxima, while N_{int} is the sum of the number of atoms in equivalent areas at intermediate positions between the maxima. Complementary information can be extracted from the width of the central interference peak which is related to the correlation length of the bosonic system [120, 126]. Fig. 6.3 shows sample data comparing the behavior of ensembles with 3% and 7% impurity concentrations to a pure bosonic ensemble. The loss of coherence marked by a loss of interference contrast and a decrease of correlation length is clearly visible in the visibility curve as well as in the width data. Fig. 6.3 also shows that the loss of coherence is shifted by an amount depending on the impurity concentration. Already for 3% impurity concentration, the visibility data shows a significant shift. The corresponding width data, however, essentially exhibits a steeper slope for the deep lattices with no pronounced shift as compared to the pure bosonic system. This indicates a qualitative difference in the type of transition for the pure bosonic system and the system with fermionic impurities.

We use two different methods to extract quantitative information about the shift of the coherence loss from our experimental data. For the visibility data, we use a phenomenological fit function

$$\mathcal{V}(s) = \frac{1}{1 + \exp(\alpha \cdot (s - s_{crit}))} - \mathcal{V}_0 \quad (6.2)$$

where s is the lattice depth in units of E_r^{Rb} , s_{crit} is a measure for the onset of the coherence reduction, and α is an additional fit parameter. The value of α always ranges around 0.35 ± 0.05 and has no significant influence on the observed shift in s_{crit} (fixing α to its mean causes changes below $0.5 E_r^{Rb}$). \mathcal{V}_0 is the visibility offset for small lattice depth which essentially reflects the choice of the circle size around the interference peaks. For data as in Fig. 6.3, we compare s_{crit} for a pure bosonic sample recorded under the same experimental conditions to the impurity induced transition and extract the shift of the transition. Resulting shifts are plotted as a function of impurity concentration in Fig. 6.4. The corresponding width data is analyzed by extracting the intersection point of two linear fits to the descending and ascending branches of the data. As can be seen from Fig. 6.4, an increasing impurity concentration leads to a considerable shift of the coherence breakdown. For 20% impurity concentration, the shift is on the order of $5E_r^{Rb}$.

6.4 Understanding the role of the fermions

In a pure bosonic system, the loss of coherence for deeper optical lattices accompanies the superfluid to Mott-insulator phase transition. The simplest attempt to understand the origin of the shift might be to explain it as a shift of a localized phase due to the heteronuclear interaction.

In order to assess the size of a possible shift to an insulating phase, one can calculate the value of the on-site Fermi-Bose interaction matrix element

$$U_{FB} = \frac{2\pi\hbar^2 a_{FB}}{\mu} \cdot \int w_F(x)^2 w_B(x)^2 d^3x = 1.1E_r^{Rb} \quad (6.3)$$

The value on the right-hand side is calculated in the tight binding limit (i.e. using harmonic oscillator ground state wavefunctions for $w_F(x)$ and $w_B(x)$) at the localization transition

point for our lattice parameters, based on a scattering length of $a_{\text{FB}} = -205(7)a_0$ [113]. This matrix element characterizes the additional potential felt by bosonic atoms due to the presence of a fermionic impurity atom in a single potential well. It is thus on the order of the expected shift of the localization transition for unity fermionic filling in the simple mean field picture shown in Fig. 6.1e.

Another way of looking at this picture is to calculate the quantum critical point for the onset of the Mott phase for a lattice potential modified by the interaction. The calculation results in essentially the same shift on the order of one recoil energy.

On the other hand, in a trapped geometry, the fermionic atoms may tend to sit in the center of the trap which can in turn increase the central bosonic density due to the attractive interaction. An increased occupation number would result in an onset of a ‘‘Mott’’ phase of the mixture for deeper optical lattices. The opposite has been observed in the experiment.

Quasi-exact one-dimensional DMRG calculations and quantum Monte Carlo simulations [127] have recently shown that the expected shift would be towards deeper lattices and also very small. The results have been interpreted in terms of an effective reduction of the Bose-Bose repulsion by the Fermi-Bose attraction. Given the 1D nature of these calculations, it is still unclear what the 3D result would be. Preliminary data from mean field calculations performed by Marcus Cramer at Potsdam show that one would also expect a shift towards deeper lattices, and a very small one.

Other effects may strongly influence the size of the shift and may even induce a loss of coherence all by themselves. The role of the trap has an influence on the thermodynamic behavior of the system, since the ramp up sequence of the optical lattice may affect both absolute temperatures and critical temperatures. Depending on regimes, either adiabatic cooling upon ramp-up of the lattice or adiabatic heating can occur. Note that the term ‘‘adiabatic’’ means that this is not parametric heating due to imperfections of the system but a fundamental process which is due to thermodynamic properties of the system and which is fully reversible [128, 129, 130].

Similar experimental data as in this thesis have been obtained in Zürich with an important shift towards shallower lattices [65], and the origin of the shift is currently by no means clear. The large shift towards shallower lattices may indicate that disorder or any other of the effects mentioned above may play a significant role.

It would be interesting to map out the nature of the transition by using further diagnostic tools such as Bragg spectroscopy and look for the presence of an excitation gap. Other possible diagnostics include spectroscopy of occupation numbers and correlation measurements.

A detailed understanding of the possible localization scenarios is a challenging task and the measurements presented in this chapter are a promising starting point for further experimental and theoretical studies on Fermi-Bose localization physics.

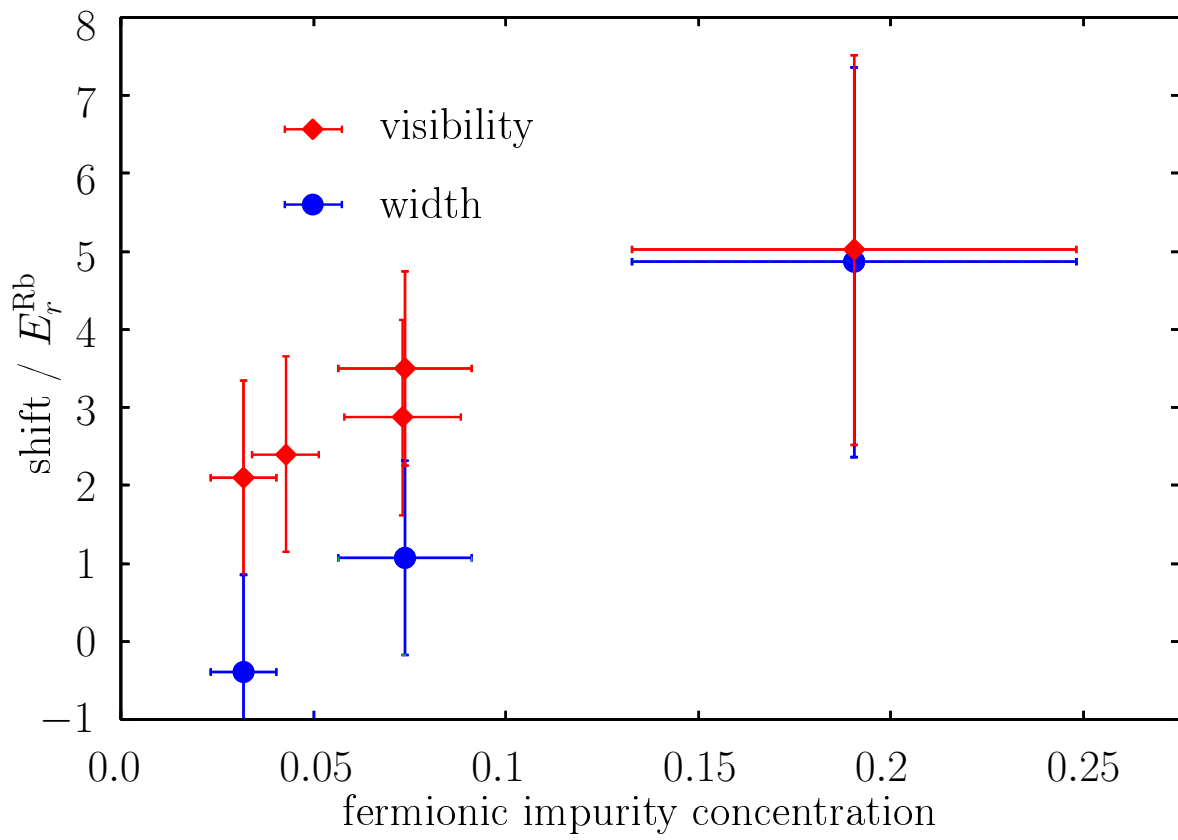


Figure 6.4: Observed shift of coherence loss as a function of fermionic impurity concentration.

Chapter 7

Heteronuclear molecules in a 3D optical lattice

Being able to perform experiments with ultracold polar molecules is one of the outstanding challenges in atomic, molecular and optical physics [131]. The increasing interest in this problem is motivated by a wide range of research directions which would directly benefit from the availability of such molecular samples. In the following, I will discuss possible applications of ultracold polar molecules, possible routes currently being followed towards this goal and then describe groundbreaking experiments performed within this thesis on the first creation of ultracold heteronuclear molecules within a single well of an optical lattice by means of Feshbach resonances. As will become clear from my discussion of current experimental efforts, this is a crucial step towards advances in quantum computation, dipolar gases and fundamental measurements.

7.1 The quest for ultracold polar molecules

7.1.1 Polar molecules and anisotropic interactions

A diatomic polar molecule is characterized by the presence of a permanent internal dipole moment occurring as a result of the electronic charge distribution not having the same “center of mass” as the nuclear charge distribution¹. The dipole moment associated with this electronic charge distribution gives rise to a long-range dipolar interaction. This interaction is novel in two senses: it is long range, and the interaction depends on the relative alignment of the scattering partners. In a sample of aligned dipoles, it is energetically more favorable for two dipoles to sit in front of each other than side by side. To date, all quantum gas experiments have studied effects of internal interactions which are short-range and isotropic, with the exception of experiments performed with ultracold Cr [132] which has a noticeable *magnetic* dipole moment². Studies of dipole-dipole interacting quantum gases are expected to reveal novel fascinating physics. For example, in the presence of dipolar interactions, the elementary excitations and the stability of the gas in various dimensions are expected to strongly depend

¹In chemistry, the concept of electronegativity of an element is used to estimate the degree of polarity present in a covalent bond.

²In this case, the long range dipolar interaction [133] is relatively weak compared to the short range contact interaction, although there is the perspective of tuning the short range part through Feshbach resonances [134] and working with a fixed dipolar interaction.

on the dimensionality, the external confinement and the ratio of long range to short range interactions. To name only a few of the predicted effects, Quantum hall states of dipolar gases have been considered, both for fermionic and bosonic particles [135, 136], phases of gases with dipolar interactions in optical lattices [137] and novel solitonic behavior [138].

7.1.2 Polar molecules and quantum computation

It has been suggested by D. DeMille in 2001 [55] to use polar molecules for quantum computation. The idea is to encode quantum information in the orientation of the molecular dipole moment relative to an external field. Using the dipole alignment of a single molecule, a single qubit can be realized. A qubit register, i. e. multiple qubits can be realized by loading dipolar molecules into a 1D optical lattice. In order to make this quantum information storage register a quantum computer, some degree of coupling needs to be introduced between the qubits. This is where the long range dipolar interaction becomes important: it couples molecules at different lattice sites and is used as the quantum bus. Following the initialization of the quantum register and the proper register operation, the readout of individual qubit states can be achieved by adding an electric field gradient along the direction of the optical lattice to separately address lattice sites through the Stark effect.

The suggested quantum computation scheme is currently being considered as a very promising candidate for future scalable quantum computers with a low decoherence time.

7.1.3 Polar molecules and the EDM

Polar molecules are currently being considered for precision experiments testing upper limits on the permanent electric dipole moment of the electron. While the standard model sets an upper limit on such an EDM which is vanishingly small (about 10^{-40} em), supersymmetric theories predict values of the EDM which are getting within reach of current experimental efforts. Improving the upper limit of the EDM would thus eventually enable certain new theories to be ruled out, while finding a non-zero EDM would be an exciting signature of T-violating physics beyond the standard model. It has initially been pointed out by Sanders [139] that the electronic EDM signature (a linear Stark effect) could be enhanced in heavy paramagnetic atoms, which is expressed by the so-called “enhancement factor”. Several experiments are under way testing limits on the EDM using e. g. atomic fountains, atoms confined in solid helium matrices and beam experiments. In almost all atomic experiments, the achievable sensitivity is limited by the electric fields that can be applied without initiating a discharge. In paramagnetic heavy polar molecules, an enormous degree of polarization can be achieved due to the internal electric field with only moderate external fields. Experiments on polar molecules and the EDM are currently under way using e. g. PbO, TlF, and also molecular ions. Measurements of the EDM of polar molecules would greatly benefit from the availability of ultracold samples with long interrogation times, and the counting rate would be substantially increased by having all molecules in a well defined quantum state.

7.1.4 Possible routes to molecular degeneracy

Actively pursued routes to molecular degeneracy fall into two different categories, depending on whether the starting point is a deeply bound molecular sample or whether molecules are assembled from precooled and possibly degenerate atoms. The different approaches will be discussed in the following sections.

The molecular way to molecular degeneracy

The key obstacle in obtaining ultracold or even degenerate molecular samples compared to atomic Bose-Einstein Condensates or degenerate Fermi gases is the lack of laser cooling techniques for molecular gases. The main issue is the wealth of molecular energy levels, enhanced by rotational and vibrational degrees of freedom and the corresponding lack of clear cycling transitions for laser cooling of molecules. Currently followed routes to molecular degeneracy starting with deeply bound molecules therefore either rely on cryogenic techniques bringing the sample into contact with a thermal reservoir or on interaction with external electric fields slowing down the external degrees of freedom or filtering out low velocity classes. All of these can be followed by subsequent evaporative cooling of a trapped sample, but the temperature gap into the ultracold and even degenerate regime has yet to be bridged.

Buffer gas cooling Buffer gas cooling [140] is a very general technique for cooling anything that can be held in a magnetic trap, i. e. any paramagnetic atom or molecule. It has been pioneered by the group of J. Doyle at Harvard. Buffer gas cooling involves cryogenic techniques in order to produce cold vapors of Helium which cools atoms and molecules through elastic collisions. Buffer gas cooling can eventually be combined with evaporative cooling in order to bridge the temperature gap into the ultracold.

Stark deceleration Stark deceleration [141] is based on the interaction of molecules with an external electric field. A high field seeking molecule runs up a potential hill formed by a pair of electrodes. Upon reaching the highest potential, it has lost kinetic energy, and this loss in kinetic energy is conserved when the field is rapidly switched off. Through a cleverly designed timing sequence and a suitable configuration of electrodes, molecular bunches with greatly reduced longitudinal velocity can thus be produced from a collimated molecular beam.

Velocity filtering Velocity filtering [142] selects low-energy molecules from an effusive source by means of Stark deflection as a first step to electrostatic trapping of this low-energy tail of the velocity distribution.

The atomic route to molecular degeneracy

The technical difficulties associated with slowing down the external degrees of freedom of molecules have made another route to molecular degeneracy attractive. This approach is based on ultracold atomic samples which are routinely produced in laboratories today. The goal is to assemble ultracold molecules in both their external and internal (rovibrational) ground state from ultracold atoms by means of a coherent photoassociation step.

Photoassociation The idea behind photoassociation is to excite two colliding atoms into an excited molecular state using a “pump” pulse and then to dump the excited state population into the internal ground state by means of a second “dump” pulse. Formation of vibronic ground state molecules from a MOT has been demonstrated in 2005 [143]. Several important parameters such as the Franck-Condon overlap between initial and final states, pulse shape, excitation bandwidth etc. influence this process. The currently most promising route is to use femtosecond lasers for the pump/dump-scheme. These lasers have the advantage of offering arbitrary frequency synthesis, combined with the benefit of coherent accumulation techniques

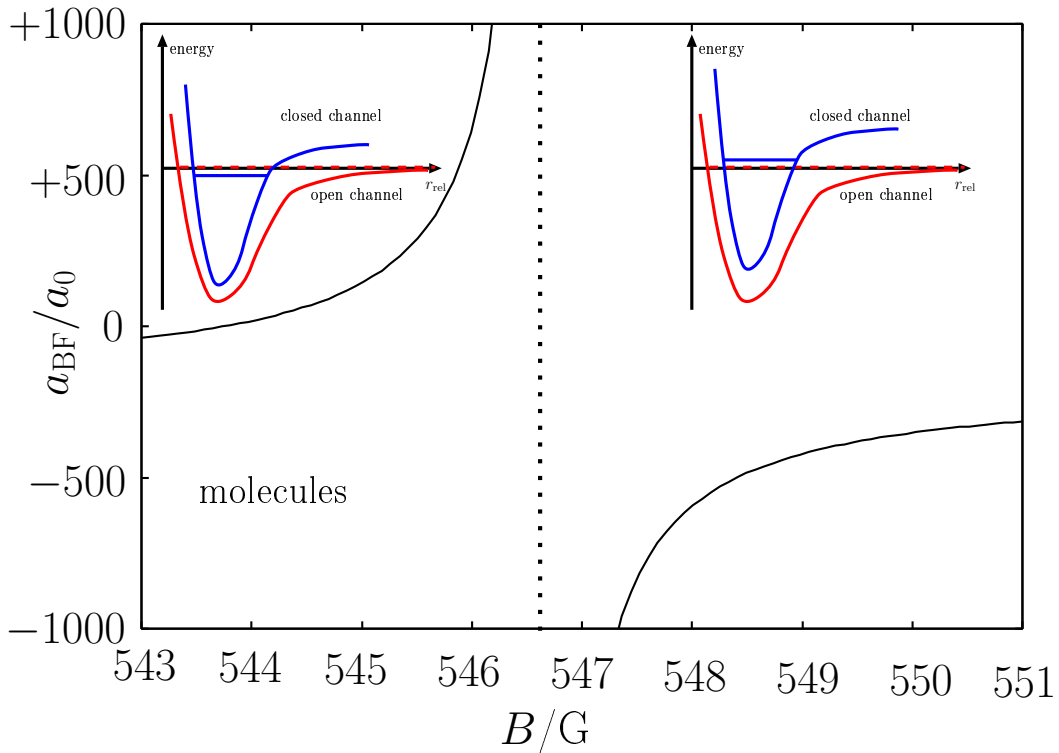


Figure 7.1: Cartoon picture of a Feshbach resonance. When bound molecular state is below the open channel (left), molecules are formed. Interactions are repulsive in this case. When the molecular bound state is above the resonance, no stable Feshbach molecules are formed in free space.

which can be used to increase the overall efficiency. The excitation bandwidth can be varied by tuning pulse length and shape.

Parallel to the above mentioned work on photoassociation, recent years have seen a lot of progress in molecule formation based on Feshbach resonances. Molecule creation at Feshbach resonances is based on the fact that the occurrence of the resonance itself is due to the coupling between a bound molecular state energetically close to the incoming energy of two free atoms.

Feshbach molecules Feshbach resonances in scattering between atoms occur when the energy of a bound molecular state is close to degeneracy with the open channel of two colliding atoms. In this case, the coupling between the two states at the resonance allows the s wave scattering to be tuned to large and attractive or large and repulsive by tuning the respective position of the two energy levels using e. g. magnetic fields.

When the energy of the bound molecular state is above the free-atom threshold, the coupling between the two close to degenerate states gives rise to strong attractive interactions. In free space, no two-body bound state exists (see Fig. 7.1 right).

When the energy of the bound molecular state is below the open channel, the interaction between atoms is large and repulsive, and pairs of atoms can occupy the two-body bound state and form a weakly bound molecule with typical binding energies between a few 10 kHz and a few MHz. Starting from an atomic sample, such molecules can e. g. be created by

sweeping a magnetic field from attractive interactions through the resonance center position over to repulsive interactions. (see Fig. 7.1 left).

In a groundbreaking experiment performed in the group of C. Wieman [144], this magnetic field sweep technique was first used to create a coherent atom-molecule superposition. In this and following experiments with bosonic atoms and Feshbach resonances, it was observed that the resulting molecular lifetime was rather low and on the order of about 1ms, limited by collisional losses.

Molecules created from fermions are surprisingly stable! A big step forward in Feshbach chemistry was achieved when it was realized that bosonic molecules created from two fermionic atoms using the magnetic field sweep technique would be collisionally stable due to the Pauli exclusion principle [145]. The argument is as follows: These weakly bound molecules have a relatively large spatial extent, and the atomic character of the two constituents still plays a major role. In order for inelastic collisional losses to occur, two molecules need to come close to each other. This necessarily implies that two identical fermions come close to one another, which is prohibited by the Pauli exclusion principle. The experimental demonstration of long-lived bosonic molecules created from fermionic atoms was soon to follow [24, 25, 26, 27, 28]. While there was some initial controversy about the scattering length a_{MM} between these bosonic molecules, it soon became clear that $a_{MM} \approx 0.6 \cdot a_{FF}$, where a_{FF} is the Feshbach-resonant scattering length between the constituents [145].

The next landmark in the field was evaporative cooling of these long-lived bosonic molecules and resulted in the creation of a molecular BEC [29, 30, 31], clearly visible in the bimodal distribution of time of flight absorption images. These experiments thus realized the BEC limit of the BCS-BEC crossover. The development culminated in early 2004 [32, 33, 34, 35, 36] when fermionic condensates were created on the BCS side of the Feshbach resonance by ramping the magnetic field back to the other side of the Feshbach resonance where the interaction is attractive and no bound two-body state exists. Following studies revealed both the excitation spectrum of the system [34], the expansion behavior [36, 35], and established the superfluid nature of the fermionic condensates through the observation of vortices [146]. Hence, the system of two non-identical fermions interacting at a Feshbach resonance realizes the full BEC-BCS crossover discussed by Eagles, Nozières, Schmidt-Rinck, Leggett [147, 148, 149] and others and constitutes a continuous crossover between bosonic and fermionic superfluidity.

Molecules and lattices Parallel to this development, it was realized that the lifetime limitation of molecules created from bosonic atoms [144, 150, 151, 152, 153] can be overcome in 3-dimensional lattices by creating molecules from atom pairs in isolated wells of the lattice and thus inhibiting inelastic collisions [154, 155].

Creation of molecules in optical lattices highlighted the role of the external trapping potential in molecule formation. A model system of two particles in a harmonic trap was already considered in 1997 [156], and in 2005 experiments with optical lattices demonstrated that the existence of the external trapping potential shifts the free-atom threshold, resulting in the existence of molecules on the attractive side of the Feshbach resonance where no stable molecules exist in free space [41], also seen later in the behavior of repulsively interacting pairs [157].

Today, many people consider molecule creation through magnetic field sweeps as *the* way to create molecules at Feshbach resonances. In recent years, however, a number of techniques

has been used to create Feshbach molecules. For example, it seems to be a unique property of ${}^6\text{Li}$ that molecule formation can be achieved by evaporative cooling of thermal lithium atoms on the repulsive side of the Feshbach resonance without any magnetic field sweeps [30]. Another technique which has been demonstrated is magnetic field modulation at a Feshbach resonance [158]. When the modulation frequency corresponds to the binding energy of the bound molecular state at the time average value of the magnetic field, free atoms can be converted into molecules on the repulsive side of a Feshbach resonance. Another possibility of creating molecules is rf association of atoms into molecules as developed within this thesis.

7.2 Ultracold heteronuclear Feshbach molecules

While heteronuclear Feshbach resonances were already predicted in 2003 [159] (for ${}^{40}\text{K}$ — ${}^{87}\text{Rb}$) and experimentally identified through collisional losses in the middle of 2004 [63, 62], all of the fascinating physics which has become accessible through Feshbach resonances has been limited to homonuclear systems. As a crucial step towards the exploration of dipole-dipole interacting molecular systems, novel quantum computation schemes and fundamental measurements, this thesis presents the first experimental demonstration of ultracold long-lived heteronuclear molecules. Molecules are created within the single well of an optical lattice at a heteronuclear Feshbach resonance by means of a novel technique developed for this purpose and based on rf spectroscopy. The technique avoids magnetic field ramps and precisely determines the energy spectrum of pairs composed of one ${}^{40}\text{K}$ and one ${}^{87}\text{Rb}$ atom in the optical lattice close to a Feshbach resonance. Lifetime and molecule creation efficiency have been measured and are consistent with a physical picture of lattice occupation. Both molecules stable in the absence of any external potential, confinement-induced molecules and repulsively interacting pairs with a positive “binding energy” have been identified. A detailed understanding of this model system has been developed based on a pseudopotential approach for the atomic interaction in cooperation with F. Deuretzbacher, K. Plassmeier and D. Pfannkuche. The model consistently treats both the anharmonicity of the lattice potential and the general case of particles with unequal trapping frequencies; excellent agreement with numerical simulations has been obtained. By implementing coherent deexcitation schemes based on femtosecond technology, it may be possible to convert these Feshbach molecules into deeply bound molecules in both their internal rovibrational and external ground state. This work thus opens up intriguing perspectives both for dipolar quantum gases, fundamental measurements and novel quantum computation schemes. Parallel to this work, efforts at JILA have resulted in the production of short-lived heteronuclear ${}^{40}\text{K}$ - ${}^{87}\text{Rb}$ molecules in an optical dipole trap and later in heteronuclear ${}^{87}\text{Rb}$ - ${}^{85}\text{Rb}$ molecules [160].

7.2.1 Rf association of molecules

As discussed above, various techniques have been employed for molecule production at Feshbach resonances in the literature. Within this thesis, rf association in an optical lattice as a novel technique for molecule production has been used. The idea of this association scheme is to start with a non Feshbach-resonant mixture in one spin state. In another spin state, a Feshbach resonance occurs at the same magnetic field, and the difference between this state’s energy and the non-interacting limit in the same spin state is precisely the binding energy. By shining in an rf photon which provides the undisturbed energy corresponding to the spin

flip plus the additional interaction or binding energy, we can populate the two-body bound molecular state (see Fig. 7.4).

This section discusses experimental techniques developed for molecule production based on rf spectroscopy [22, 23]. In the presence of an optical lattice, molecule production through rf association provides us with a precise measurement of the binding energy at the same time, thus extracting a maximum of information about the energy spectrum. Rf association allows molecule production without rapid magnetic field sweeps and uncertainties associated with magnetic field settling, thereby removing technical complications which can make a measurement of the binding energy quite cumbersome.

Rf association as a method for molecule production is inspired by rf spectroscopy. In my eyes, rf spectroscopy together with the advent of Feshbach resonances is one of the key techniques that has pushed the understanding of resonant strong interactions in recent years. The idea behind rf spectroscopy is to observe collisional shifts in atomic ensembles as interaction induced frequency changes on rf and microwave transitions between sub-states of the atomic ground states. Consider the simple case of a complete transition (π pulse) between two states 1 and 2 in a Bose-Einstein condensate with density n . The size of the collisional shift is given by

$$\Delta\nu_{12} = \frac{2\hbar}{m}n(a_1 - a_2)$$

The size of the collisional shift is proportional both to the density and to the difference in scattering length between initial and final state. For Feshbach-resonant two-component Fermi gases in strongly confining dipole traps, typical collisional shifts are on the order of a few kHz [22]. Measured collisional frequency shifts in the optical lattice as discussed below in the context of heteronuclear molecule formation have been between a few kHz and up to about 150 kHz, and in both cases the difference in scattering length is thousands of Bohr radii. Spectroscopy of lattice site occupation in the optical lattice [161] has been used to detect scattering length differences of a few Bohr radii only by making use of magnetic-field insensitive clock transitions. These had been used at JILA [162] to study interaction shifts in magnetic traps.

7.2.1.1 ^{40}K and ^{87}Rb in external magnetic fields

In order to understand rf spectroscopy as used for molecule creation in this thesis, let us first look at the energy levels of ^{87}Rb and ^{40}K in the presence of a homogeneous external magnetic field. For $J = I \pm 1/2$, the well-known Breit-Rabi formula yields the energy levels in the presence of an external magnetic field:

$$E_B = -\frac{\Delta E_{HFS}}{2(2I+1)} + m_F g_K \mu_K B \pm \frac{\Delta E_{HFS}}{2} \begin{cases} 1 - x \cdot \text{sgn}(A) & -m_F \cdot \text{sgn}(A) = I + 1/2 \\ \sqrt{1 + \frac{4m_F}{2I+1}x + x^2} & \text{otherwise} \end{cases} \quad (7.1)$$

where x is defined by

$$x = \frac{g_j \mu_b - g_K \mu_K}{\Delta E_{HFS}} \cdot B \quad (7.2)$$

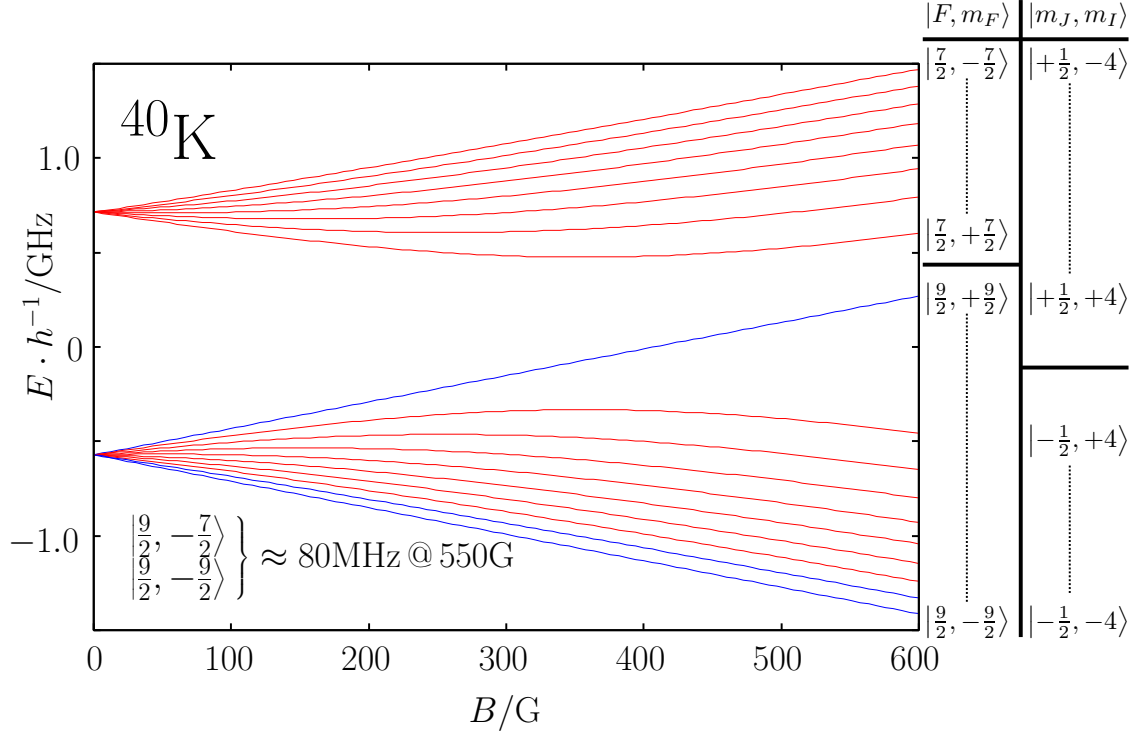


Figure 7.2: ^{40}K $4^2S_{1/2}$ energy levels in the presence of an external magnetic field. The magnetically trapped $|\frac{9}{2}, \frac{9}{2}\rangle$ state and the $|\frac{9}{2}, -\frac{7}{2}\rangle / |\frac{9}{2}, -\frac{9}{2}\rangle$ states used for rf spectroscopy are highlighted in blue.

ΔE_{HFS} is related to the Landé interval constant A according to:

$$\Delta E_{HFS} = A \cdot \left(I + \frac{1}{2} \right) \quad (7.3)$$

Values of the A and B constants for ^{87}Rb and ^{40}K as well as other atomic parameters can be found appendix B.

In Figs. 7.2 and 7.3, I have plotted the resulting energy structure for both ^{40}K and ^{87}Rb , clearly showing both the linear Zeeman regime and the Paschen-Back limit. Due to the lower hyperfine splitting, much lower fields are required to drive ^{40}K into the Paschen-Back regime than for ^{87}Rb . The resulting magnetic field insensitivity of transitions between neighboring levels at experimental fields is one of the reasons for the success of rf spectroscopy in this system. States are labelled both by their low-field ($F = I + J$) limit F and m_F quantum numbers and by the independent m_I and m_J quantum numbers in the Paschen-Back regime.

7.2.1.2 Transition for rf spectroscopy

The Feshbach resonance that was used for molecule production in this work occurs between ^{87}Rb atoms in the $|1, 1\rangle$ and ^{40}K atoms in the $|9/2, -9/2\rangle$ absolute ground states at a magnetic field of 547 G. The idea for determining the energy spectrum of the $|9/2, -9/2\rangle \otimes |1, 1\rangle$ state is to drive a transition between the ^{40}K $|9/2, -7/2\rangle$ state and the Feshbach-resonant $|9/2, -9/2\rangle$ state. The former features a scattering length which is independent of B over the magnetic

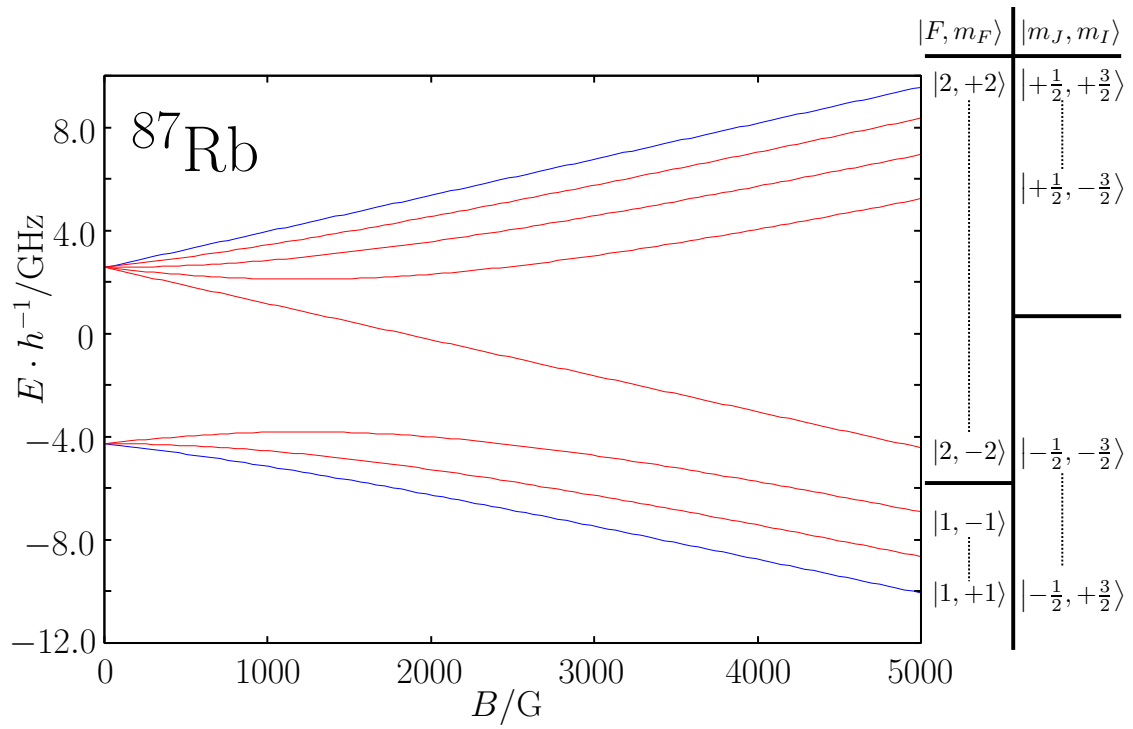
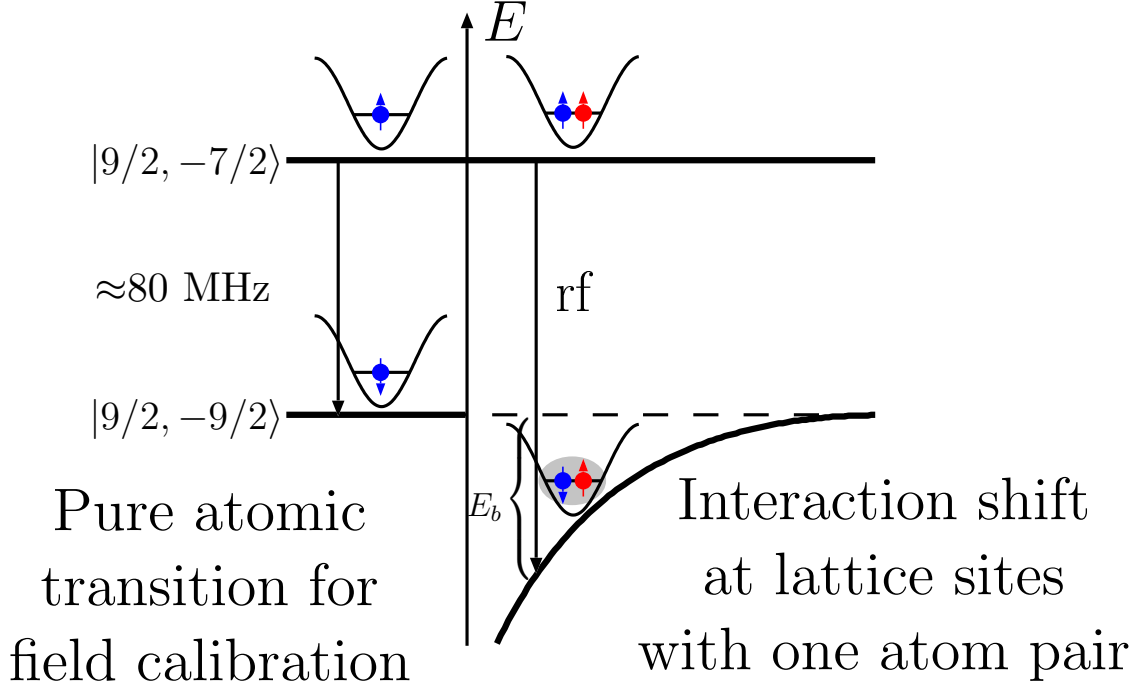


Figure 7.3: $^{87}\text{Rb } 5^2S_{1/2}$ energy levels in the presence of an external magnetic field. The magnetically trapped $|2, 2\rangle$ state and the Feshbach-resonant absolute ground state $|1, 1\rangle$ used in this thesis are highlighted in blue.

Figure 7.4: Illustration of rf spectroscopy for ^{87}Rb - ^{40}K

field range studied in the experiment and small (given approximately by the background scattering length)³; the energy of the latter strongly varies as a function of B across the resonance compared to the undisturbed $|9/2, -9/2\rangle$ energy level. The interaction energy (binding energy) of the Feshbach-resonant state $|9/2, -9/2\rangle$ is thus given as the difference of the observed $|9/2, -7/2\rangle \rightarrow |9/2, -9/2\rangle$ transition frequency compared to the undisturbed transition frequency which can be calculated from the Breit-Rabi formula or extracted from a measurement where no bosons causing the collisional shift are present (see Fig. 7.4). Note that this measurement of the collisional shift is up to the small constant offset caused by the non-resonant $|9/2, -7/2\rangle \otimes |1, 1\rangle$ interactions.

7.2.2 Experimental protocol

The experimental implementation of this scheme is as follows: A quantum degenerate mixture of ^{40}K and ^{87}Rb in the $|9/2, 9/2\rangle \otimes |2, 2\rangle$ state is prepared in the crossed magic dipole trap (see section 3.8) using the procedure discussed in chapter 5. Using a current of 1 A through the main Helmholtz coils, a field of approximately 21 G is created for state preparation. In the following, the rf and microwave manipulation setup discussed in section 3.9.1 is used to prepare the mixture in the initial state of the rf association process. A 10 ms microwave sweep over 400 kHz on the hyperfine transition transfers ^{87}Rb atoms from $|2, 2\rangle$ to $|1, 1\rangle$ (see section 3.9.2). Directly afterwards, a 870 kHz rf sweep from 7.7 MHz to 6.83 MHz transfers ^{40}K from $|9/2, 9/2\rangle$ to $|9/2, -7/2\rangle$ within 40 ms. Any remaining atoms in ^{87}Rb $|2, X\rangle$ states

³The closest known heteronuclear Feshbach resonances in this state are located at 522 G and 584 G [109] and have theoretical widths of below 1 G.

are removed using a resonant light pulse. Afterwards, the magnetic field is ramped up to a value close to the Feshbach resonance occurring at 547 G. In total, we allow 150 ms for the field to stabilize close to its final value. During the last 100 ms, the 3D optical lattice intensity is increased from zero to its final value using a linear ramp. At magnetic field values of 547 G, the ^{40}K $|9/2, -7/2\rangle \rightarrow |9/2, -9/2\rangle$ transition occurs at about 80 MHz. In order to probe the energy spectrum for a given magnetic field, an rf pulse with durations between 400 and 800 μs is irradiated using the standard evaporation antenna (a discussion of rf pulse shapes and the achieved resolution follows in section 7.2.8.2).

About 1 ms after the end of the pulse, the lattice intensity is ramped down using a linear ramp within 1 ms in order to reduce the kinetic energy, and the dipole trap is then suddenly switched off, marking the beginning of the time of flight. During time of flight, we detect both remaining ^{40}K $|9/2, -7/2\rangle$ atoms and ^{87}Rb $|1, 1\rangle$ atoms as well as weakly bound molecules and ^{40}K atoms in the $|9/2, -9/2\rangle$ channel.

I will first discuss how a maximum of sensitivity is achieved for the detection of weakly bound molecules and $|9/2, -9/2\rangle$ ^{40}K atoms, since this signal is used to extract rf spectra for the determination of the binding energy. During the time of flight, the magnetic field is left at its current value. After 4 ms time of free expansion, we image the $|9/2, -9/2\rangle$ component at a detuning of -764 MHz with respect to the zero field detection frequency ($F = 9/2 \rightarrow F' = 11/2$ at $B = 0$) on the main imaging system perpendicular to the magnetic field (for a discussion of high field imaging, see section 3.11.3.2 and appendix A). The linear polarization is perpendicular to the magnetic field, such that it can be represented as a superposition of left- and right- circular polarizations in the direction of the magnetic field. The corresponding cycling transition is a $|m_J = -1/2, m_I = -4\rangle \rightarrow |m_J = -3/2, m_I = -4\rangle$ transition and requires circular polarization. Thus, about every second photon contributes to the signal. While this represents a potential disadvantage (lower signal), this is by far outweighed by the fact that this imaging axis usually gave the lowest mechanical vibrations and hence less interference fringes in the image. The interference fringes are further suppressed on this axis by quickly switching off the magnetic field after the absorption image using IGBTs and directly taking the reference image within 500 μs (see section 3.11.2.3). As the laser detuning is held constant, the imaging laser does not “see” any remaining atoms at zero magnetic field, although they have not had time to leave the imaging area. As our main interest is in detecting small numbers of molecules and atoms down to a few hundred, this detection scheme achieved best sensitivity for our purposes.

^{40}K atoms in the $|9/2, -7/2\rangle$ and ^{87}Rb atoms are imaged in the direction of the magnetic field using one CCD chip and the two-species imaging technique (see section 3.11.2.2). With the magnetic field still switched on, the ^{40}K $|9/2, -7/2\rangle$ absorption image is taken after 3 ms at a detuning of -833 MHz, corresponding to a $|m_J = -1/2, m_I = -3\rangle \rightarrow |m_J = -3/2, m_I = -3\rangle$ transition, and the ^{87}Rb $|1, 1\rangle$ atoms are transferred into $|2, 2\rangle$ using a short 40 μs repumper pulse and imaged immediately afterwards with a total TOF of 15 ms close to zero magnetic field. The chip with the two absorption images is then read out, and corresponding reference and dark images are taken after delays of 200 ms.

7.2.3 Rf spectrum

At fixed magnetic field, the rf pulse frequency is varied in the vicinity of the undisturbed ^{40}K $|9/2, -7/2\rangle \rightarrow |9/2, -9/2\rangle$ rf transition to obtain rf spectra as in Fig. 7.5 for $B=547.13$ G. The spectrum shows the number of ^{40}K atoms in the $|9/2, -9/2\rangle$ state and weakly bound

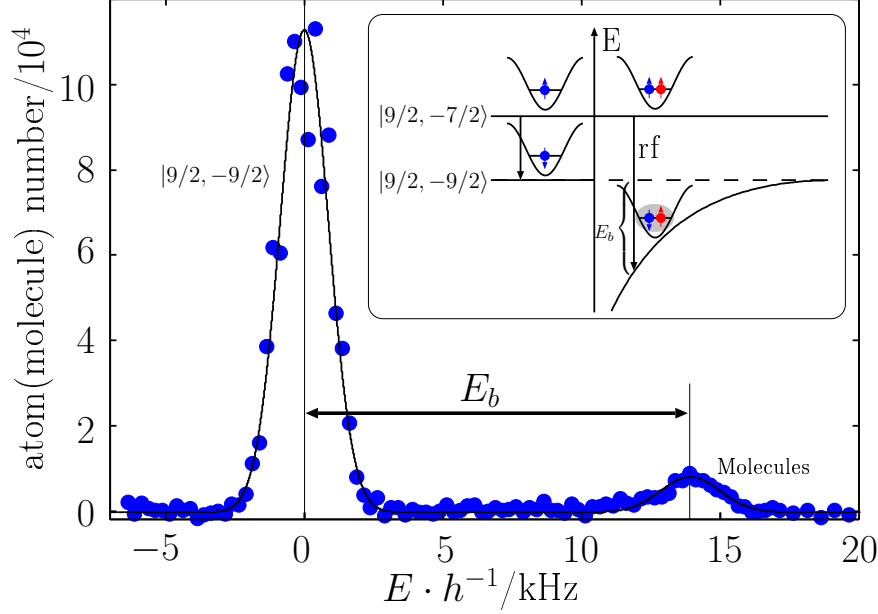


Figure 7.5: Rf spectroscopy of ^{40}K - ^{87}Rb at 547.13 G in a $40 E_r$ deep optical lattice.

Feshbach molecules as a function of rf detuning from the frequency corresponding to the pure ^{40}K $|9/2, -7/2\rangle \rightarrow |9/2, -9/2\rangle$ transition at the set value of the magnetic field. The large peak at zero detuning occurs whether bosons are present in the optical lattice or not. It stems from lattice sites where only one fermion and no boson is present and is used as a precise magnetic field calibration in connection with the Breit-Rabi formula eq. 7.1.

The second peak occurring about 14 kHz above the undisturbed peak is due to the existence of a collisional shift at lattice sites where one boson and one fermion are present. The strong interaction between the two at the Feshbach resonance introduces a strong differential collisional shift between the $|9/2, -7/2\rangle$ and the $|9/2, -9/2\rangle$ levels. In this case, additional energy is required to drive the rf transition. This implies that in the presence of a bosonic atom, the energy of the target state $|9/2, -9/2\rangle$ is lower than in the reference level, which shows that the target state has a negative binding energy and that heteronuclear molecules have been formed through rf association. Forming heteronuclear molecules through rf association thus measures the binding energy of these molecules at the same time. In the particular case of Fig. 7.5 recorded at a magnetic field of 547.13 G, the interaction between ^{40}K and ^{87}Rb is attractive which, in free space, would not allow molecules to be created because the bound molecular state is above threshold. As we shall see, the negative binding energy of the molecules in Fig. 7.5 is due to the presence of the optical lattice which admits the presence of a bound state even for attractive interactions. The resulting molecule is a confinement-induced molecule which will decay into free particles when the lattice potential is removed.

7.2.4 Energy spectrum

In order to extract information about the energy spectrum over the whole magnetic field range of the Feshbach resonance, spectra as in Fig. 7.5 have been recorded for a number of magnetic fields around 547 G. For each of the spectra, the molecular binding energy has been

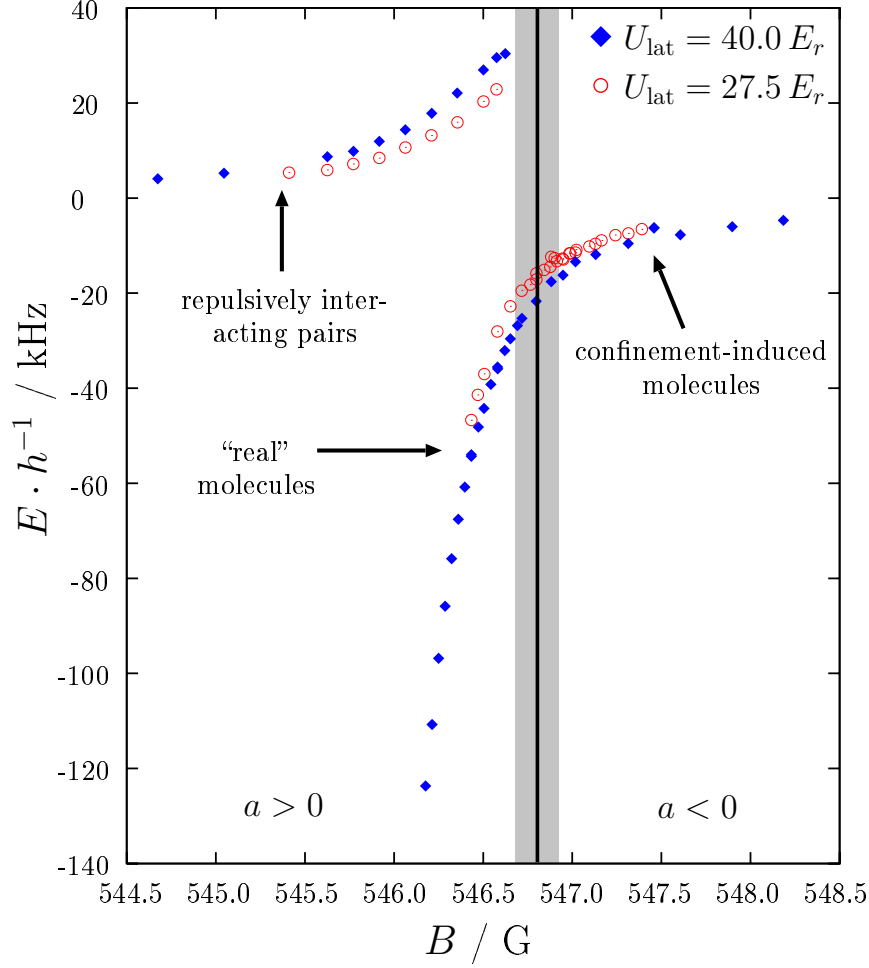


Figure 7.6: Observed energy spectrum of ^{40}K ^{87}Rb atom pairs at an individual lattice site for two different values of the lattice depth.

extracted by fitting both atomic and molecular peaks and taking the difference in position between the atomic and the molecular peak. The resulting spectrum is shown in Fig. 7.6, recorded for two different values of the lattice depth, $40.0 E_r$ and $27.5 E_r$.

The vertical bar in Fig. 7.6 represents the center position B_0 of the Feshbach resonance as determined from ^{40}K - ^{87}Rb interactions in an optical dipole trap (chapter 5). In the magnetic field range considered here, the interaction is attractive above B_0 and repulsive below B_0 .

The energy spectrum shows two basic branches. The lower branch or molecular branch is characterized by the presence of a negative binding energy, and the upper branch, which is only observed for repulsive interactions, is characterized by a positive “binding energy”. In a system of pure bosons confined in an optical lattice, the behavior of these repulsively interacting pairs has been studied in recent experiments in Innsbruck [157].

In the molecular branch, one can distinguish between attractive and repulsive interactions. Above B_0 , we access an energy branch of confinement-induced molecules [41, 43] which exhibit a negative binding energy due to the presence of the lattice potential. The sample rf spectrum in Fig. 7.5 has been recorded in this regime. As the resonance center is crossed, there is a

smooth transition into “real” molecules which are stable even in the absence of an external potential. As the scattering length decreases from infinity (at the resonance) towards zero, these molecules become more and more deeply bound. The maximum binding energy observed in the experiment is about -130 kHz.

7.2.5 Modelling strong heteronuclear interactions in the lattice

In order to qualitatively and quantitatively understand the observed energy spectrum, let us consider a model which was considered in 1997 to describe two interacting particles in a harmonic potential [156]. The model describes the atomic interaction as a regularized delta-type interaction potential. The Hamiltonian of the system thus consists of the kinetic energy of the two atoms, of the trapping potential and the interaction potential:

$$H = -\frac{\hbar^2}{2m_1}\Delta_1 - \frac{\hbar^2}{2m_2}\Delta_2 + \frac{1}{2}m_1\omega_1^2 r_1^2 + \frac{1}{2}m_2\omega_2^2 r_2^2 + \frac{2\pi\hbar^2 a}{\mu}\delta(r)\frac{\partial}{\partial r}r + V_{anh}(\vec{r}_1, \vec{r}_2) \quad (7.4)$$

where a is the s-wave scattering length between the two atoms, $m_{1,2}$ the respective mass, $\mu = m_1 \cdot m_2 / (m_1 + m_2)$ the reduced mass, $\vec{r}_{1,2}$ the respective single particle coordinate, $\omega_{1,2}$ the harmonic trap frequency for atom 1 and 2 and V_{anh} contains anharmonic correction to the external trapping potential. Reference [156] proceeds by introducing relative and center of mass coordinates $\vec{r} = \vec{r}_1 - \vec{r}_2$ and $\vec{R} = \frac{m_1\vec{r}_1 + m_2\vec{r}_2}{M}$ where $M = m_1 + m_2$ is the total mass. By introducing frequencies

$$\omega_{CM} := \sqrt{\frac{m_1\omega_1^2 + m_2\omega_2^2}{M}} \quad (7.5)$$

$$\omega_{rel} := \sqrt{\frac{m_2\omega_1^2 + m_1\omega_2^2}{M}} \quad (7.6)$$

$$\Delta\omega := \sqrt{\omega_1^2 + \omega_2^2} \quad , \quad (7.7)$$

the resulting Hamiltonian takes the form

$$H = -\frac{\hbar^2}{2M}\Delta_{CM} + \frac{1}{2}M\omega_{CM}^2 R^2 \quad (7.8)$$

$$-\frac{\hbar^2}{2\mu}\Delta_{rel} + \frac{1}{2}M\omega_{rel}^2 r^2 + \frac{2\pi\hbar^2 a}{\mu}\delta(r)\frac{\partial}{\partial r}r \quad (7.9)$$

$$+\mu\Delta\omega^2 \vec{R} \cdot \vec{r} + V_{anh}(\vec{R}, \vec{r}) \quad (7.10)$$

$$= H_{CM} + H_{rel} + H_{co} \quad (7.11)$$

with one part H_{CM} involving only center of mass coordinates, one term H_{rel} containing only relative coordinates and a final term H_{CO} potential coupling the two coordinates. Ref. [156] makes the assumption of equal masses and equal trapping frequencies and considers purely harmonic trapping. In this case, the coupling term vanishes and the solution of the center of mass motion are harmonic oscillator states with trapping frequency ω_{CM} . The eigenvalues and eigenfunctions of H_{rel} are determined using a harmonic oscillator representation of the unknown wave function to solve the problem of relative motion⁴. The result for the energy

⁴Ref. [156] introduces unconventional factors of $\sqrt{2}$ in center of mass and relative coordinates in order to obtain simpler final expressions. In this thesis, the textbook definition is used.

eigenvalues E_{rel} of the relative motion is implicitly given by

$$2 \frac{\Gamma[-E_{rel}/(2\hbar\omega_{rel}) + 3/4]}{\Gamma[-E_{rel}/(2\hbar\omega_{rel}) + 1/4]} = \frac{1}{a/l_{rel}} \quad (7.12)$$

where $l_{rel} = \sqrt{\hbar/(\mu\omega_{rel})}$ is the harmonic oscillator length associated with the relative motion. Equation 7.12 allows us to plot a as a function of E_{rel} or, alternatively, by changing axes, the various energy eigenvalues as a function of the dimensionless scattering length a/l_{rel} as shown in Fig. 7.7. Note that for two identical particles, $\omega_{rel} \equiv \omega_{CM} \equiv \omega_{1,2} \equiv \omega$, and that Fig. 7.7 shows the energy of relative motion in units of $\hbar\omega$. The regularized delta potential only affects s states with zero angular momentum; only these are shown in Fig. 7.7. From the treatment of the quantum mechanical harmonic oscillator, we know that these s states all correspond to an even number of quanta. All other states are not affected by the interaction and are not shown in the figure.

In order to understand the spectrum of Fig. 7.7, let us first consider the non-interacting limit. In this case, for s states, $E_{rel} = (2n + 3/2)\hbar\omega_{rel}$, and the absolute ground state has an energy of relative motion of $3/2\hbar\omega_{rel}$, as can be seen in Fig. 7.7.

For strong attractive interactions $a < 0$, these harmonic oscillator states approach the lower lying states with non-zero angular momentum and an energy lower by one quantum. When talking about the lowest level, this corresponds to confinement-induced molecules, since the energy is lower than the energy of the noninteracting limit, resulting in a negative value of the binding energy with a unitary limit of $-\hbar\omega$ for $a \rightarrow -\infty$.

For strong repulsive interactions $a > 0$, the s states approach the higher lying states with $l \neq 0$ characterized by one additional quantum of relative motion. In this case, we obtain repulsively interacting atom pairs characterized by a positive “binding energy” of $+\hbar\omega_{rel}$ in the unitary limit $a \rightarrow +\infty$.

For repulsive interactions, there is a special branch of the energy spectrum which, in the limit $a \rightarrow +\infty$, is energetically degenerate with the $n = 0, l = 0, a \rightarrow -\infty$ state. For small values of a , this branch features a diverging binding energy, corresponding to the formation of molecules which are bound even in the absence of the external trapping potential. The degeneracy of the two aforementioned energy levels in the limit of strong interactions is the origin of the smooth transition from confinement-induced molecules to “real” molecules in the experimentally observed energy spectrum of Fig. 7.6, as we shall see.

Next, let us look at the influence of the anharmonicity and of the difference in trap frequency between the two particles, which both lead to a coupling between the relative and center of mass motion through H_{CO} . In this case, a numerical solution to the full problem can be found by diagonalizing H_{CO} in the basis of the decoupled problem corresponding to the energy eigenvalues of eq. 7.12 and the wavefunctions given in [156]. This approach has been developed in close collaboration with K. Plassmeier, F. Deuretzbacher and D. Pfannkuche.

Fig. 7.8 shows the resulting energy spectrum as a solid line. The calculation is based on experimental parameters used for molecule production as described above, i. e. for a lattice depth of $40.0 E_r$ for ^{87}Rb . For reference, Fig. 7.8 also shows the energy spectrum without the coupling term. As can be seen, the effect of the coupling term is substantial and most pronounced in the repulsively interacting pair branch. The effect of the coupling term decreases the closer one comes to the “real molecule” part of the spectrum. An intuitive picture is that in the molecular branch of the spectrum, the particles become more and more deeply bound, get closer to each other and behave more and more like *one* particle. In this

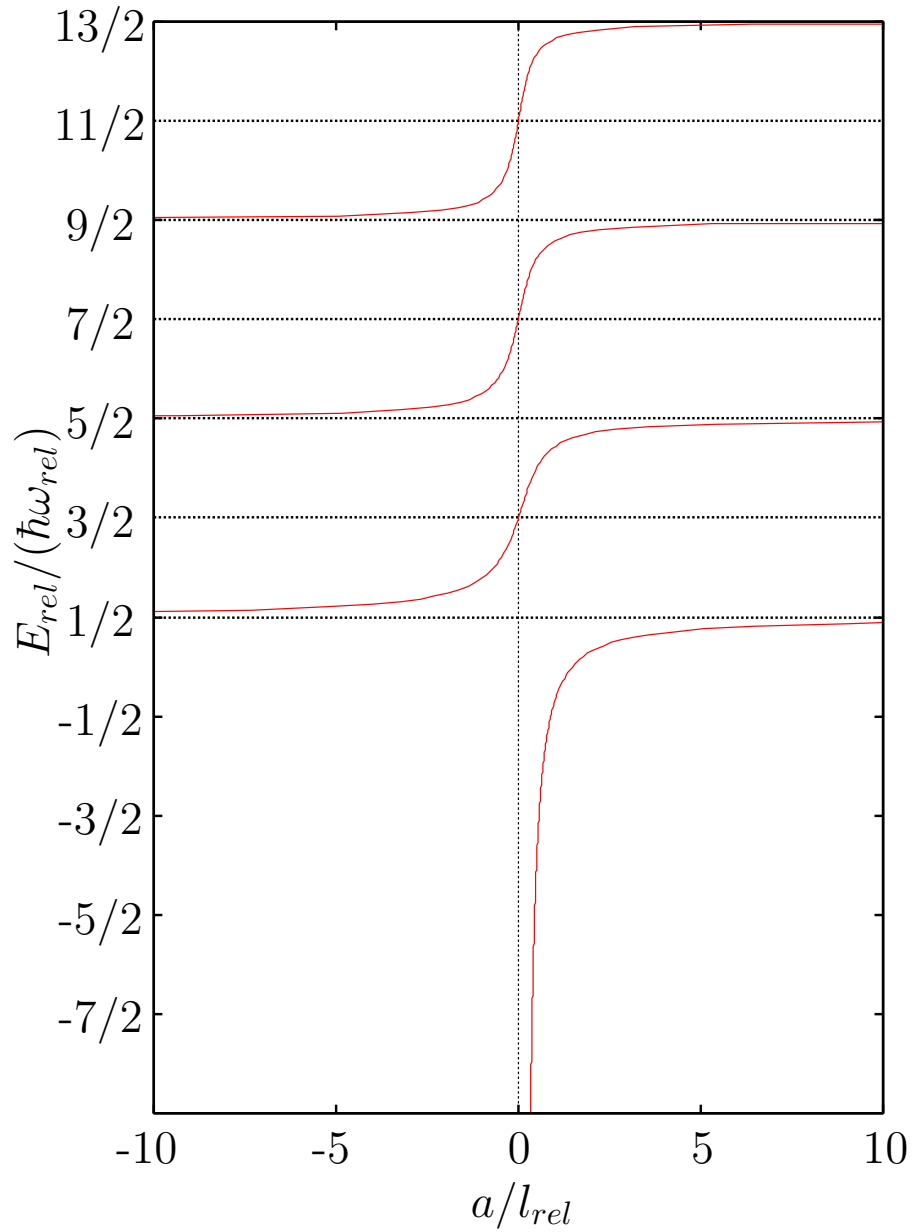


Figure 7.7: Energy spectrum of two interacting particles in an arbitrarily deep harmonic trap. Both particles have equal trap frequencies, and the energy plotted is the energy stored in the relative motion degree of freedom in units of the corresponding energy quantum.

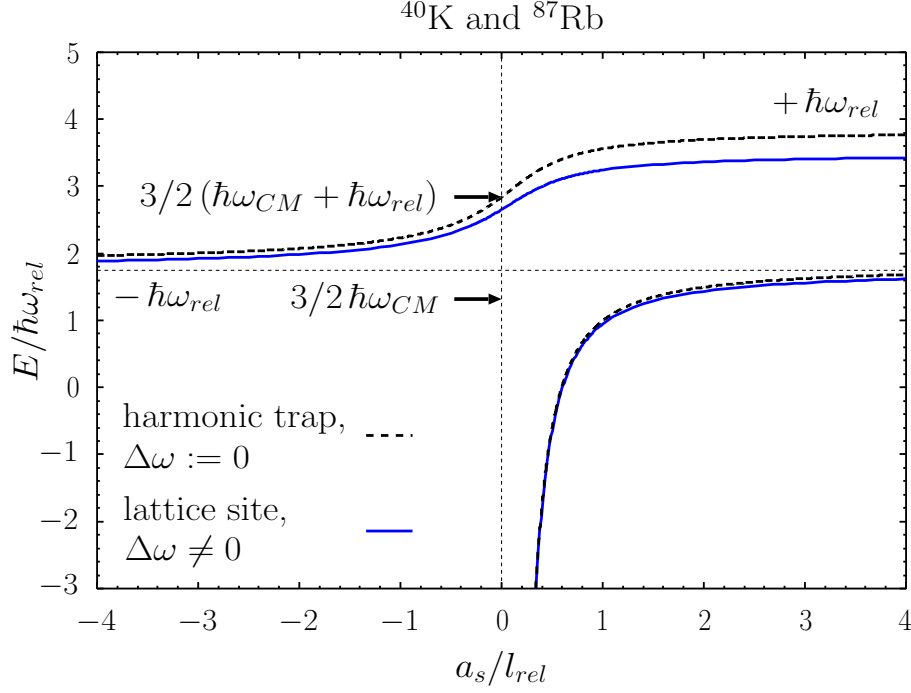


Figure 7.8: Energy spectrum of a heteronuclear system (^{40}K - ^{87}Rb) for the pseudopotential model. The calculation has been performed for a lattice depth of $40.0 E_r$ for ^{87}Rb . For comparison, the spectrum without the coupling terms and the anharmonicity is also shown (dashed line).

limit, the difference in trap frequency and the anharmonicity of the potential begin to lose their importance, and the binding energy is close to the free space binding energy. Note that the binding energy shown in Fig. 7.8 includes the center of mass energy quanta, but is normalized to the energy of relative motion.

Now, let us look at the energy spectrum not as a function of scattering length, but as a function of magnetic field at an atomic Feshbach resonance. At the Feshbach resonance, the scattering length varies according to

$$a = a_{bg} \cdot \left(1 - \frac{w}{B - B_0} \right) \quad (7.13)$$

where a_{bg} is the background scattering length, and w the width of the Feshbach resonance, characterizing the magnetic field separation between infinite a at the resonance position B_0 on the one hand and the noninteracting limit $a = 0$ at $B = B_0 + w$ on the other hand. In the case of the resonance used for molecule formation in this thesis, $w \approx -2.9\text{G}$, and a_{bg} is expected to be approximately equal to the scattering length measured for the magnetically trapped states, i. e. between 200 and $300 a_0$. When combining the pseudopotential solution with equation 7.13, one obtains the binding energy of the various energy branches as a function of magnetic field as seen in Fig. 7.9. The dotted line shows the result of the numerical solution, together with the experimental data for a lattice depth of $40.0 E_r$. As can be seen, the above treatment qualitatively reproduces the energy spectrum very well; both the smooth transition from confinement-induced molecules to “real” molecules and the repulsively interacting pair

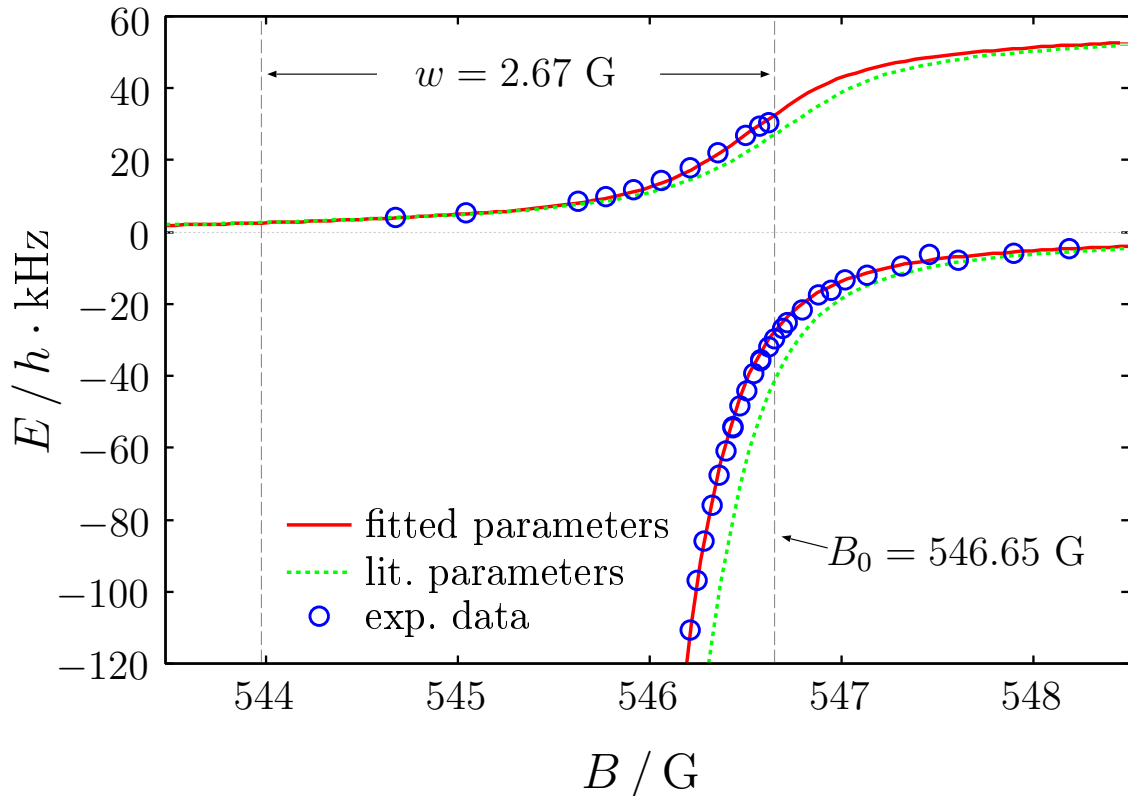


Figure 7.9: Energy spectrum as a function of magnetic field at the Feshbach resonance for the pseudopotential model. The calculation shows both a result based on literature values for the Feshbach resonance parameters (dashed line) and a fit of the theoretical model to the experimental data allowing a precise determination of the resonance position (solid line).

branch are clearly visible.

A few words on the parameters a_{bg} , w and B_0 used in obtaining Fig. 7.9 are appropriate here. The studies of tunable interactions in a dipole trap which I have presented in chapter 5 constrained B_0 to 546.8(1) G. It has been pointed out in ref. [32] that molecule formation and dissociation can allow a very precise determination of a Feshbach resonance position. In the case of lattice molecules, the resonance position shows no particular discontinuity in the observed energy spectrum; the energy spectrum is nevertheless very sensitive to B_0 . Feshbach parameters which are in a sense orthogonal to B_0 are w and a_{bg} . For strong resonant interactions as observed in the experiment, the leading 1 in equation 7.13 becomes small to the second term, and a_{bg} and w become mostly equivalent parameters. Fig. 7.9 has been obtained by using the Feshbach resonance center position and the width w a_{bg} as fit parameters; $a_{bg} = -189 a_0$ has been taken from ref. [113]. Note that due to the uncertainty in our knowledge of a_{bg} , the above procedure only allows the precise determination of B_0 . The resulting fit parameter for w is merely shown as an illustration. The resulting resonance center position of 546.65 G lies slightly outside the confidence interval from the observation of mean-field tuning of interactions (see chapter 5), which may be due to some sweep imperfections in those measurements.

Looking closely at Fig. 7.9, there is one outlier at 547.4 G. This data point has been verified

several times. After completion of the experimental work discussed here, a very narrow spin resonance (width ca. 100 mG) located at this magnetic field value has been brought to our attention by the LENS group, which may explain this feature. Also, looking at magnetic field values close to the resonance position, the pseudopotential binding energy curve seems to lie slightly above the experimental data points. This may be due to the fact that when the scattering length becomes on the order of the harmonic oscillator length, energy-dependent pseudopotentials may introduce corrections to the regularized δ potential.

7.2.6 Transfer efficiency

The maximum expected efficiency of molecule creation in the optical lattice can be estimated by looking at the number of ^{40}K atoms occupying a lattice site where exactly one boson is sitting, compared to the total number of ^{40}K atoms in the lattice at sites where no more than one boson is present. This fraction has to be compared to the ratio of transfer amplitudes of rf association on the molecular peak, compared to the atomic peak. We estimate the fraction of ^{40}K atoms which can undergo rf association to be about 10%, which is by no means a rigorous result, but sets the scale of what can be expected. Fig. 7.10 shows experimental results for the transfer efficiency of the rf association process as a function of magnetic field, both for the molecular branch and for the repulsively interacting pair branch. The experimental data is compared to a theory curve which has been calculated using the overlap integral between the initial state wavefunction of rf association (confinement-induced molecule with almost vanishing binding energy due to the small background scattering length) and the final state using the waveforms resulting from the pseudopotential model. Experimentally observed transfer efficiencies have been scaled by a global normalization factor in order to be able to compare them to the theory curve.

As can be seen, the rf association process is most efficient for confinement-induced molecules where the initial and final state wave functions are very similar. The observed efficiency drops to about 20% for the more deeply bound molecules, which is in agreement with the calculation based on the pseudopotential model.

In the repulsively interacting pair branch, the highest transfer efficiencies are observed for small scattering lengths at low magnetic fields, where the initial and final state are still close to each other; it also drops to about 20% as we approach the resonance where the scattering length is large and positive. Again, the behavior of the transfer efficiency is well described by the pseudopotential model.

7.2.7 Lifetime of the molecular sample

In my introductory remarks on Feshbach molecules, I have already mentioned an aspect of Feshbach chemistry which is of extreme experimental relevance: the lifetime of the resulting molecular sample. In general, these molecules are very fragile objects due to their highly excited internal state, leading to large collisional losses, possibly both molecule-molecule and atom-molecule collisions. Initial experiments with molecules created from bosonic atoms [144, 150, 151, 152, 153] correspondingly showed a very short lifetime, meaning that degeneracy could be achieved, but not thermal equilibrium. This limitation has been overcome in the presence of a deep 3D optical lattice [154, 155]. Molecules created from two fermionic atoms have shown a long lifetime close to Feshbach resonances due to Pauli-forbidden inelastic decay [145]. For heteronuclear molecules composed of a bosonic and a fermionic atom, the situ-

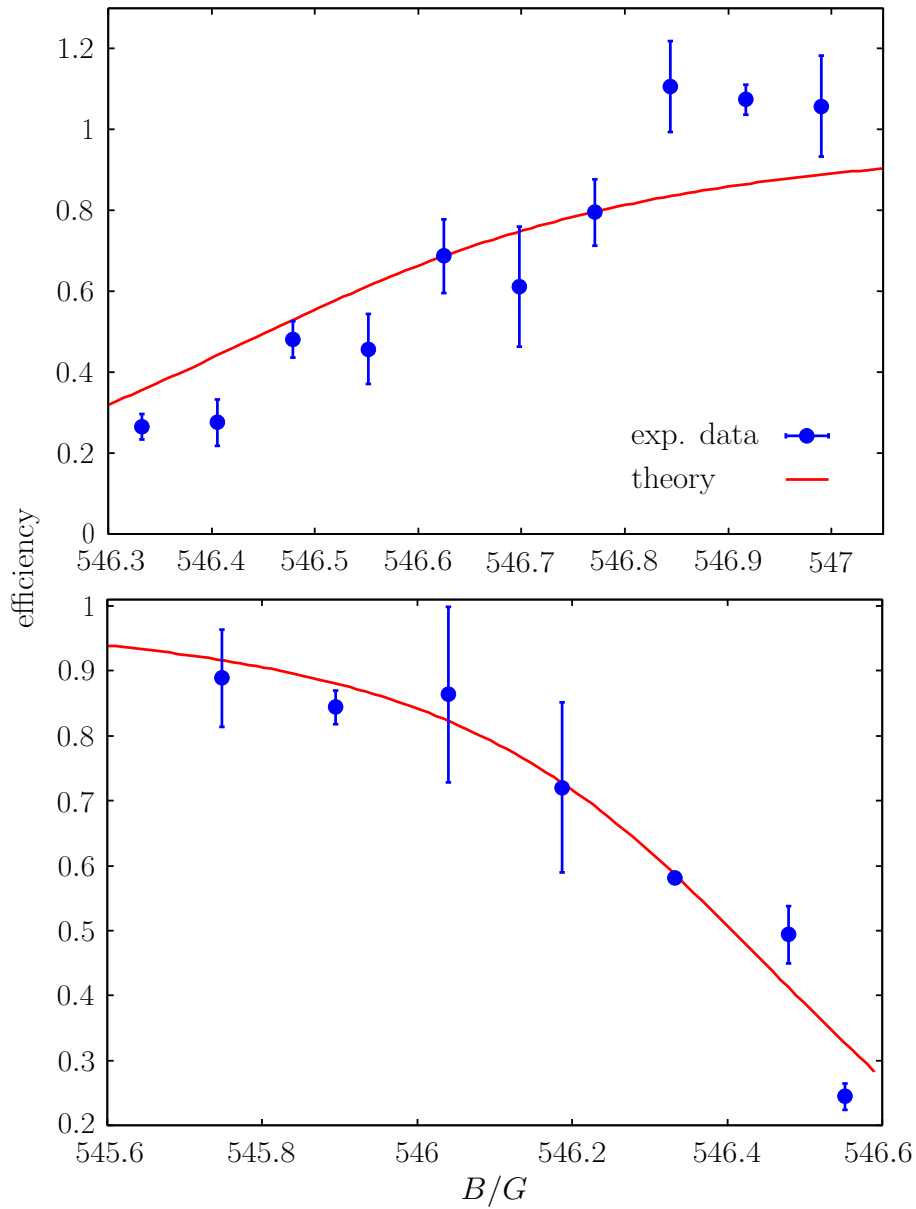


Figure 7.10: rf association efficiency for ^{40}K and ^{87}Rb in the optical lattice as a function of magnetic field

ation is somewhat more complicated; suppression of collisions due to their fermionic character is expected for more deeply bound molecules [62]. In addition collisions with the remaining free atoms are expected to strongly limit the lifetime of the molecules, and this effect will tend to become more important the deeper the molecule is bound.

In the experiment described here, heteronuclear molecules are produced within 3D optical lattices where the large tunneling time strongly reduces inelastic collisional losses. Fig. 7.11 shows a measurement of the lifetime of the heteronuclear molecular sample in an optical lattice with a depth of $40.0 E_r$ as a function of magnetic field. The lifetimes are the $1/e$ times obtained from exponential fits to the molecule number decay curves. We find a lifetime of about 120 ms for weakly bound confinement-induced molecules. In the vicinity of the resonance, the lifetime is about 80 ms, and drops to 20 to 40 ms for more deeply bound molecules. The measurement is performed by rf associating atoms originally in the $|1, 1\rangle \otimes |9/2, -7/2\rangle$ state into molecules via a π pulse on the molecular rf transition and observing them on the high-field $^{40}\text{K } |9/2, -9/2\rangle$ detection frequency.

Exactly on the molecular resonance, rf association creates only molecules and does not transfer unpaired ^{40}K atoms initially in the $|9/2, -7/2\rangle$ state. However, high-field imaging does not distinguish between atoms and weakly bound molecules, as long as they are in the $|9/2, -9/2\rangle$ channel. It is therefore of potential concern that molecules may fall apart and form unpaired $^{40}\text{K } |9/2, -9/2\rangle$ atoms which would be taken for a false molecular signal. In order to exclude this scenario, after molecule formation, we transfer any remaining $^{40}\text{K } |9/2, -7/2\rangle$ atoms into the $|9/2, -5/2\rangle$ state using an rf sweep at 85 MHz. A resonant light pulse on the $^{40}\text{K } |9/2, -7/2\rangle$ detection frequency ensures that no atoms in this state are left⁵. We then introduce a slot with a variable hold time which is used to extract the lifetime. With the $|9/2, -7/2\rangle$ state completely empty, we can now shine in an rf π pulse on the atomic $|9/2, -9/2\rangle \rightarrow |9/2, -7/2\rangle$ transition in order to transfer any possibly remaining unpaired $^{40}\text{K } |9/2, -9/2\rangle$ into the $|9/2, -7/2\rangle$ state which has been emptied before. Should there be any unpaired $|9/2, -9/2\rangle$ before this procedure, they can now be detected on the $|9/2, -7/2\rangle$ high field detection transition and distinguished from the molecular signal. We have however never found a significant atomic contribution in the $|9/2, -9/2\rangle$ channel. This proves that the lifetime measurement really measures the lifetime of the molecular sample.

In order to understand the lifetime, let us look at atom-molecule collisions. Here we need to distinguish between ^{40}K and ^{87}Rb atoms. Remaining ^{87}Rb atoms can scatter with the molecular sample, no matter how deeply bound; there is no Pauli blocking of collisions here. On the other hand, in units of the atomic recoil energy, the lattice is considerably deeper for ^{87}Rb than for ^{40}K , so one would expect these ^{87}Rb atoms to remain localized on the time scales discussed here. ^{40}K atoms are still relatively mobile at the lattice depths which we study here, and their tunneling time in the lattice is on the order of 10 ms. In the lifetime measurement discussed above, ^{40}K atoms not assembled into molecules remain in a different spin state ($|9/2, -5/2\rangle$) and are thus “distinguishable” from the fermionic constituents of the molecules which are in the $|9/2, -9/2\rangle$ channel. Hence, there is nothing which can prevent these atoms from tunneling to lattice sites occupied by molecules and causing inelastic losses. This effect can explain the observed lifetime of about 20 ms for the more deeply bound Feshbach molecules. The observed dependency of the lifetime on the binding energy

⁵This two-step cleaning sequence for the $^{40}\text{K } |9/2, -7/2\rangle$ state was necessary since the corresponding optical detection frequency is not far enough detuned from the $^{40}\text{K } |9/2, -9/2\rangle$ transition to allow a blasting pulse reducing the $^{40}\text{K } |9/2, -7/2\rangle$ population below the percent level without affecting the $^{40}\text{K } |9/2, -9/2\rangle$ population.

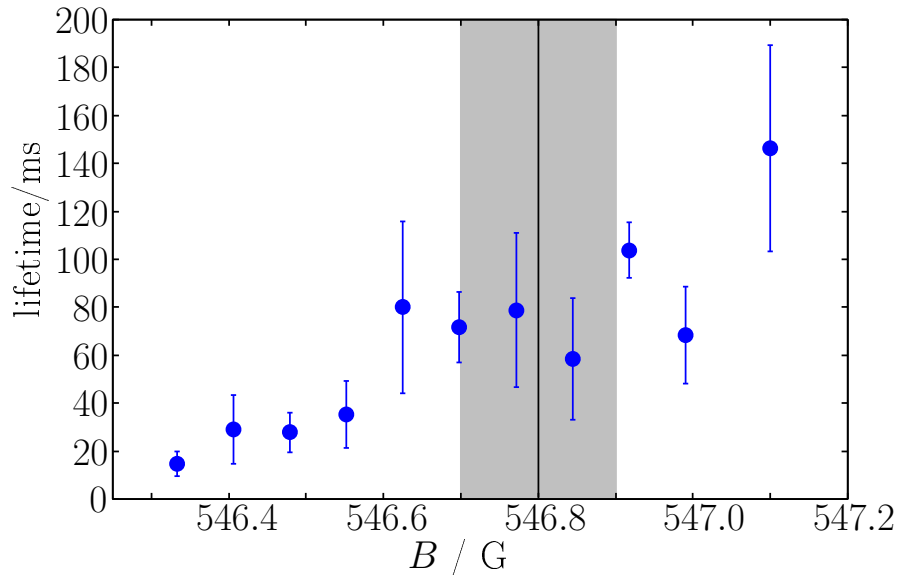


Figure 7.11: Lifetime of heteronuclear ^{40}K - ^{87}Rb molecules as a function of magnetic field

or magnetic field is still an open question.

If a further increase in lifetime is desired in future experiments, it may be beneficial to remove any of the remaining atoms. For this to be possible, ^{40}K atoms would have to be transferred to the upper hyperfine manifold, where they could be removed using a resonant light pulse. Very promising steps in this direction have been undertaken towards the end of this thesis. In the available time, the experiment lacked the possibility to shine in a resonant “blasting” pulse in the upper hyperfine manifold. For ^{87}Rb , this is slightly more difficult – available rf transitions are relatively sensitive to magnetic fields which may limit the possibility to separately address atoms and molecules using rf to the more deeply bound regime, but this is by no means a fundamental limitation.

7.2.8 Experimental implementation of rf spectroscopy

In the previous part, I have explained the idea of determining energy spectrum, lifetime and transfer efficiency of heteronuclear molecules in the previous part and discussed experimental results in comparison to a pseudopotential model for the interactions. I will now discuss the conditions for success of this technique, i. e. the obtained lineshape, the particular choice of transition for rf spectroscopy and the achieved magnetic field stability.

7.2.8.1 Choice of transitions for rf spectroscopy

In principle, one might imagine doing this spectroscopic experiment using other transitions, and I discuss several of the possible alternatives here. As a first criterion for choosing a transition, either the initial or final state should be the $|1, 1\rangle \otimes |9/2, -9/2\rangle$ Feshbach-resonant absolute ground state. Based on this argument, it could in principle be equally favorable to perform the spectroscopy using the ^{87}Rb microwave transition from $|2, 2\rangle$ to $|1, 1\rangle$ or a ^{87}Rb $|1, 0\rangle \rightarrow |1, 1\rangle$ transition, in particular since the former is used anyway to transfer from the magnetically trapped to the absolute ground state. The advantage of using the ^{40}K transition

Transition		Sensitivity in kHz/G	
		at 0 G	at 547 G
⁴⁰ K	$ 7/2, -7/2\rangle \leftrightarrow 9/2, -9/2\rangle$	2491	2736
⁴⁰ K	$ 9/2, -7/2\rangle \leftrightarrow 9/2, -9/2\rangle$	311	67
⁸⁷ Rb	$ 1, 0\rangle \leftrightarrow 1, 1\rangle$	702	594
⁸⁷ Rb	$ 2, 2\rangle \leftrightarrow 1, 1\rangle$	2100	2300

Table 7.1: Magnetic field sensitivity of candidate transitions for rf spectroscopy

for rf spectroscopy is that it has a much lower magnetic field sensitivity at the magnetic fields of the heteronuclear Feshbach resonance. The magnetic sensitivity is of concern because magnetic field drifts and AC magnetic noise, multiplied by the sensitivity, can easily be on the order of the interaction shifts that are to be measured or even larger. As seen from Figs. 7.2 and 7.3, neighboring levels with the same m_J run parallel as a function of magnetic field in the Paschen-Back regime, which makes such transitions totally magnetic-field independent in the limit of very large fields. For ⁴⁰K at 547 G, we are already in the Paschen-Back regime, whereas much larger fields would be required for ⁸⁷Rb, and this is the reason for the choice of transition. For comparison, table 7.1 gives magnetic field sensitivities of the various transitions mentioned above both in the Zeeman regime and at the magnetic fields of interest (547 G).

7.2.8.2 Rf spectroscopy lineshape

The transitions that are commonly used for rf spectroscopy are usually characterized by a natural lifetime of the atomic states which is on the order of years. The linewidth and thus the resolution of collisional shifts observed in the experiment is thus determined by the interaction time of the atomic sample with the rf field, unless limited by magnetic field noise. Here, I will discuss the lineshape of the rf transitions that have been used in this work and the relation to the corresponding pulse rf shape. At the same time, this illustrate two textbook examples on time of flight linewidth broadening both in the linear and π pulse regime. Let us first look at the case of a square pulse of duration T , which is the rf pulse shape used for the very first rf spectroscopy experiments performed within this thesis. The finite length of the pulse is associated with a frequency spread of the rf spectrum. In order to obtain this spread, we need to Fourier transform the magnetic field

$$B(t) = \begin{cases} B_0 \cdot \cos(-2\pi\nu_0 t) & |t| < T/2 \\ 0 & \text{otherwise} \end{cases} \quad (7.14)$$

and obtain the associated intensity distribution as a function of frequency by taking the square modulus. The result is

$$I(\nu) = I_0 \cdot \frac{\sin^2(\pi T \delta\nu)}{(\pi T \delta\nu)^2} \quad (7.15)$$

where $\delta\nu = \nu - \nu_0$ is the detuning from the carrier frequency. This expression is well known from time of flight broadening of a molecular beam with a single velocity v intersecting with a transverse laser beam with rectangular intensity profile and width L . The above intensity distribution is only proportional to the achieved population transfer in the so-called linear regime of small Rabi flopping angles, not for a π pulse. In the latter case, the exact result

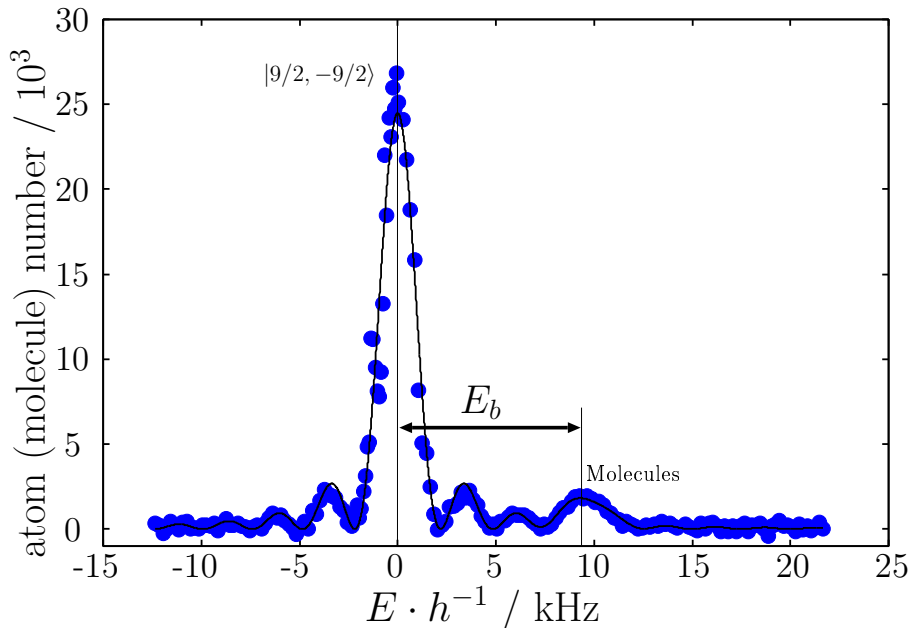


Figure 7.12: Rf spectroscopy of ^{40}K - ^{87}Rb atom pairs using a square pulse of $400 \mu\text{s}$ duration.

for the population transfer is obtained from the well-known solution for a two-level atom interacting with an oscillatory field (e. g. [163]). Let P be the transition probability, χ the Rabi flopping frequency (i. e. not the angular frequency). Then,

$$P = \frac{\chi^2}{\chi^2 + \delta\nu^2} \sin^2 \left[\sqrt{\chi^2 + \delta\nu^2} \pi T \right] . \quad (7.16)$$

Note that eq. (7.16) approaches the linear regime of eq. 7.15 when $\delta\nu$ is always small compared to χ for experimentally interesting $\delta\nu$. The difference between the linear and the π pulse regime is plotted in Fig. 7.13a. It is generally most pronounced in the height of the side lobes compared to the on-resonance amplitude. The width of the feature remains essentially unaffected.

Fig. 7.12 shows the experimentally observed rf spectrum of the ^{40}K $|F = 9/2, m_F = -7/2\rangle \rightarrow |F = 9/2, m_F = -9/2\rangle$ transition at a finite pulse duration of $T=400 \mu\text{s}$ together with the prediction of eq. 7.16⁶. The spectrum shows both the characteristic atomic peak at zero detuning, the appearance of two to three clearly visible side lobes due to the \sin^2 modulation term in eq. 7.16 and the molecular peak above the atomic resonance frequency which has been modelled as a Gaussian in Fig. 7.12. The agreement between the predicted lineshape and the experimental result is excellent. The appearance of side lobes in the rf spectroscopy signal when using a square rf pulse can lead to ambiguities in the identification of molecular features, especially when the molecular feature is close to the atomic feature, and make a simultaneous least square fit for both cumbersome.

As the Fourier transform argument in the linear regime demonstrates, the appearance of the side lobes in the spectrum is due to the abrupt change in rf amplitude at the beginning

⁶The amplitude at the VFG output is -25 dBm, compared to -20 dBm for evaporation. These may not be directly comparable, since the frequency range is different and the magnetic field produced by our coil-shaped antenna is probably smaller at 80 MHz than at 1-40 MHz. The Rabi flopping frequency is $\chi = 1250 \text{ Hz}$.

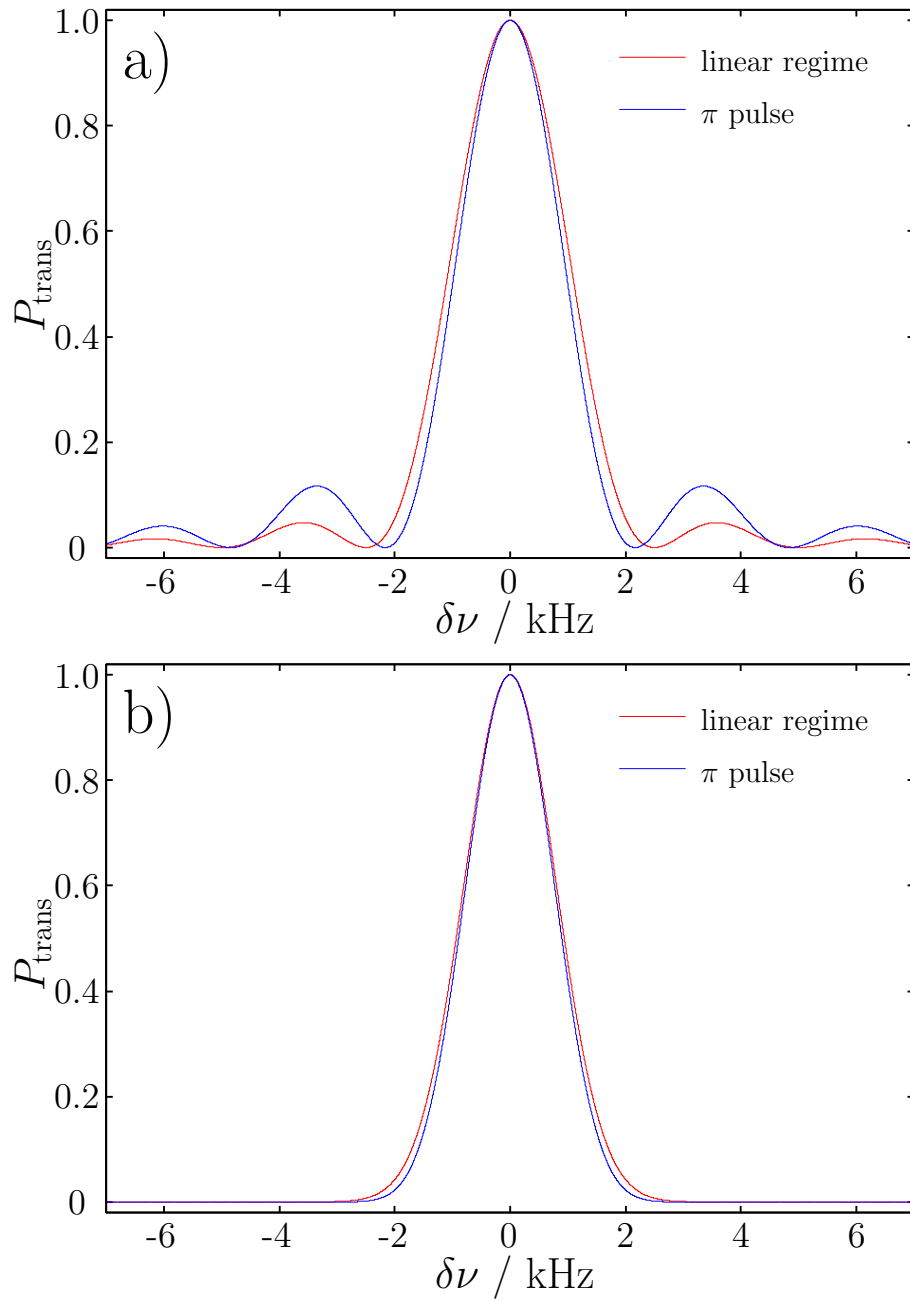


Figure 7.13: Rf spectroscopy lineshape arising as a result of a) square rf pulse shape b) Gaussian rf pulse shape

and end of the pulse. A smoother rf envelope would hence result in the elimination of the side lobes. In order to choose a suitable pulse shape, let us look at the linear regime of small Rabi flopping angles again. In this regime, the line shape is simply the modulus of the Fourier transformed temporal rf power envelope. It is well known that the Fourier transform of a Gaussian will again produce a Gaussian pulse. Hence, this is a very natural choice for the rf amplitude envelope. Let the rf power in the pulse as a function of time be given by

$$P(t) = P_0 \cdot \exp(-2t^2/w_t^2) \quad (7.17)$$

where w_t is the $1/e^2$ half width. Fourier transforming the square root of this expression (which is proportional to the magnetic field) and again taking the square modulus of the result, we obtain

$$P(\nu) = P_0 \cdot \exp(-2t^2/w_\nu^2) \quad (7.18)$$

with a $1/e^2$ frequency half width

$$w_\nu = 1/(\pi w_t) \quad . \quad (7.19)$$

Coming back to the initial time of flight broadening analogy, this is the direct analogon of a monochromatic atomic beam transversely intersecting with a Gaussian shaped laser beam. As in the case of the square pulse, the Fourier argument is not really valid for situations close to π pulses. In the case of the Gaussian pulse, calculating the resulting rf spectrum will require a numerical solution (see e. g. [164] or the plot of Fig. 7.13b). Nevertheless, as in the case of the square pulse, the basic shape of the spectrum is similar to the linear response regime. This is illustrated in Fig. 7.13b, where I have plotted the spectrum in the linear regime together with the solution for the π pulse obtained through a numerical integration of the Bloch equations. As can be seen, the spectrum can very well be approximated by using the Gaussian result from the linear regime, even for π pulses.

The experimental spectrum of the Gaussian pulse has been shown in Fig. 7.5 with the corresponding Gaussian fit for the atomic and molecular peak. The Gaussian $1/e^2$ half width from the spectrum of Fig. 7.5 is 1.7 kHz; the prediction of the linear regime (eq. 7.19) is 1.6 kHz, and no sidelobes are present in the spectrum, demonstrating that the Gaussian pulse has the desired effect on the rf spectrum.

In the experiment, the complication arises that in contrast to the square pulse, the Gaussian pulse has in principle infinite wings. Thus, some temporal cutoff has to be chosen. The cutoff is a compromise between the requirements that the initial increase in power is not too sudden and that the overall pulse duration should not be too long. For this work, the following choice was made: Given w_t , the total length T of the pulse was $4 \cdot w_t$, resulting in almost the same area under the truncated pulse and the full pulse. The rf power as a function of time is then given by

$$P(t) = P_0 + 7.0697 \text{ dBm} - \frac{t^2}{T^2} \cdot 138.974 \text{ dBm} \quad (7.20)$$

where P_0 is the power in dBm of a square pulse with the same area under the $B(t)$ curve as the Gaussian pulse. In order to produce the desired pulse shape, the VFG-150 rf generator setup presented in section 3.9.1 has been used without any hardware modifications or external pulse shaping hardware, demonstrating the versatility and performance of this setup for advanced manipulations on atomic rf and microwave transitions.

7.2.8.3 Magnetic field control

In order to achieve a maximum spectroscopic resolution, several steps to reduce magnetic field drifts and AC magnetic noise have been crucial in the experiment. The first step consisted in removing sources of AC magnetic fields (typically 50 Hz noise) from the proximity of the glass cell. In identifying sources of noise, a flux-gate probe connected to a line triggered scope was of great help. The origin of the dominant AC noise contribution were power supplies for lattice and dipole trap intensity stabilization which had large internal transformers. In a next step, a technique developed by J. Kronjäger for the spinor BEC experiment in our group was adapted for this experiment: The experiment is synchronized with the 50Hz mains frequency. Shortly before starting the rf association pulse, the cycle is paused for a variable time between 0 and 20 ms until a zero crossing of the mains frequency occurs.

With these improvements of AC noise, the remaining challenge is to produce a magnetic field which is stable and reproducible enough at 547 G to allow precision rf spectroscopy. First experiments were performed using the external current programming input of the magnetic trap bias field power supply, but it soon became clear that this would not provide the required stability - partly also due to the precision of isolation amplifiers used in between the analog output of our DSP system and the analog input of the power supply. The conclusion was that a precision external regulator would best fulfill the needs of precision rf spectroscopy. Inspired by techniques used at JILA, I have developed a magnetic field servo based on a DANFYSIK Ultrastab 867-200I transducer measuring the current in the bias coils. Based on this input signal, a precision regulator controls the current in the bias coils by means of a Powerex CM200HA-24H IGBT module. Note that care has to be taken in order not to exceed the device's power handling capability. The current transducer has a bandwidth of 100 kHz and a temperature coefficient of < 1 ppm/K. In order not to compromise these excellent specifications in the regulator or computer control, the input stage of the regulator, in particular any amplifier in the input signal path up to and including the difference amplifier comparing to the set value needs to be carefully designed. Precision resistors used in the regulator have temperature coefficients of < 50 ppm/K; the housing of the regulator was therefore temperature stabilized. The set value of the regulator is provided by an internal precision bandgap reference and a combination of fixed divider resistors. In order to be able to vary the current in the region of 547 G, a modulation input allows variations of the set value of ± 2 A to be controlled from the computer through an isolation amplifier. Not controlling the full current range from the computer but only this tiny modulation ΔI around a fixed set value greatly reduces the influence of the modest performance of isolation amplifiers etc. The result is a mean deviation of the measured magnetic field (based on the atomic peak from rf spectroscopy) from the magnetic field calibration of 2.7 mG at 547 G (57 measurements on 11 consecutive days), corresponding to a magnetic field reproducibility of $\approx 5 \cdot 10^{-6}$ which is the main key to the excellent quality of the rf spectroscopy data. The resulting field calibration is shown in Fig. 7.14.

One source of systematic error which could possibly influence the magnetic field calibration is the reference frequency for the VFG generator used for the rf spectroscopy. This device, a HAMEG8131-2 which also produces the 100 kHz event source for the DSP system, has a specified absolute accuracy of 10 ppm. Given the magnetic field sensitivity of 67 kHz/G and an absolute frequency of 80 MHz, the resulting magnetic field uncertainty is

$$\Delta B = \frac{80 \text{ MHz} \cdot 10^{-5}}{67 \text{ kHz/G}} = 12 \text{ mG} \quad (7.21)$$

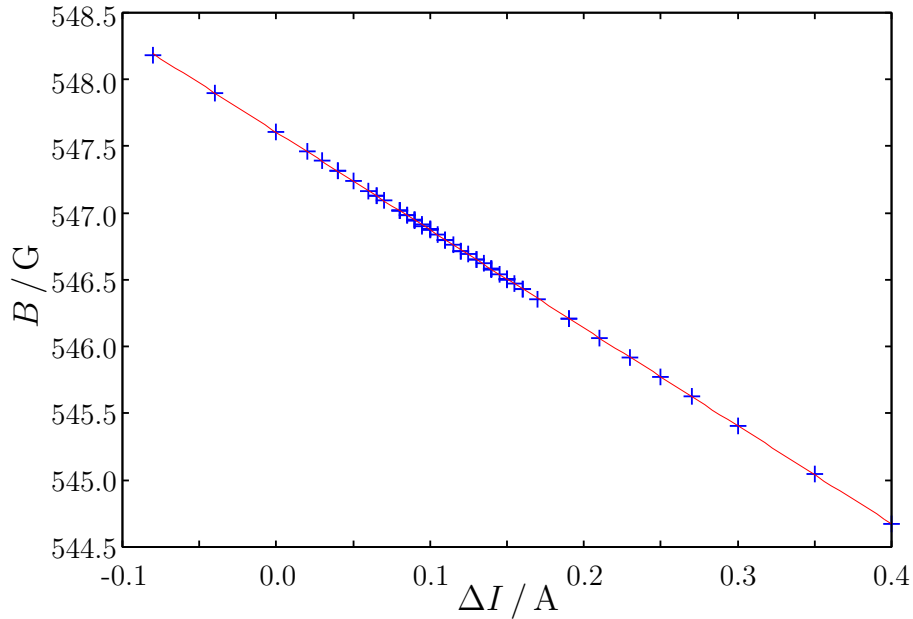


Figure 7.14: Magnetic field calibration. Magnetic fields are determined from the single-atom peak in rf spectroscopy, and the current is the modulation current around the fixed regulator set value entered into the experiment control software.

which is a factor of four above the achieved field reproducibility. When we started our experiments on rf spectroscopy, we did not expect to reach a magnetic field control at the 2.7 mG level, and did not expect the synthesizer to be the ultimate limit. For future experiments, it may therefore be desirable to use a common high-accuracy 10 MHz source such as the one available in our SMR microwave generator or a GPS-disciplined reference oscillator and to synchronize all other rf equipment relative to that source. For the DSP experiment control system requiring a 100 kHz event source, this could be done using a 1:100 frequency divider.

Chapter 8

Conclusions and Outlook

In the previous chapters, I have looked at trapped heteronuclear quantum gases, in this case Fermi-Bose mixtures of ^{40}K and ^{87}Rb from several perspectives. Since a large part of the effort which went into this thesis has been spent on setting up an experiment, the first perspective has been the production of such ultracold mixtures with all of the experimental details which have resulted in the so far largest ^{40}K - ^{87}Rb mixtures. Equipped with a 3D optical lattice setup, sophisticated rf manipulation and spectroscopy techniques and excellent optical access as well as four detection systems, the experiment which I have described allows a plethora of phenomena to be studied, and the field is currently wide open.

Harmonically trapped mixtures and Feshbach resonances

In chapters 2, 4 and 5, I have looked at a mean-field picture of trapped Fermi-Bose mixtures. Mixtures are trapped in a global harmonic trap under the influence of heteronuclear background (chapter 4) and tunable (chapter 5) interactions. I have discussed what we can learn about the role of interactions from time of flight images in two cases: when the role of interactions is enhanced through densities or through tuning of interactions. In the first case, I have shown that for large particle numbers, we can unambiguously observe a mean field collapse of the mixture as a localized phenomenon in the overlap region with the condensate with a sudden drop in atom number. This fascinating phenomenon, where the Fermi-Bose attraction overcomes both the outward bound Fermi pressure and the internal repulsion of the BEC, is possibly enhanced through excitations and the large reservoir of the thermal cloud; yet the measurements have provided us with an important upper limit on the scattering length and shown that large ^{40}K - ^{87}Rb mixtures can be created, which was not believed to be possible for a long time.

I have shown how we have made use of heteronuclear Feshbach resonances for the first time to tune heteronuclear interactions over a wide range and observe all phases of harmonically trapped mixtures discussed in chapter 2 – stable attractively and repulsively interacting mixtures as well as an induced collapse and phase separation. The latter occurs preferentially in the upward direction in the presence of the symmetry-breaking gravitational force. The measurements of Feshbach resonance positions performed in this context have had important implications in the context of the ^{40}K - ^{87}Rb collisional model.

Already in my introduction on harmonically trapped mixtures, I have talked about the possibility of observing bright soliton-like structures in Fermi-Bose mixtures [107]. With

the advent of Feshbach resonances, it may be possible to realize these self-trapping states. Depending on experimental regimes, it may be beneficial to realize these in 1D optical lattices. In the same regime, one may also look at collective excitations in the vicinity of the mean field collapse, which are predicted to be strongly affected in this regime.

Leaving the mean field discussion, the availability of tunable interactions may bring us a lot closer to the observation of boson-induced cooper pairing in Fermi-Bose mixtures. An open question is the detection of pairing phases – possibilities include excitation spectroscopy, noise correlations, Bragg spectroscopy, formation of vortices and possibly many more.

Mixtures in lattices – the many-body limit

In chapter 6, I have reported on the first demonstration of heteronuclear systems in 3D optical lattices and on interesting many-body phenomena: already a few percent admixture of a fermionic component in the optical lattice destroys the bosonic coherence in shallow lattices. The origin of this dramatic loss in coherence is currently the subject of intense theoretical discussions, and thermodynamical, advanced mean field and disorder related scenarios are discussed as possible explanations.

Further insight into the origin of this drastic effect may be gained by excitation spectroscopy and Bragg spectroscopy and by looking for an excitation gap in the spectrum. Noise correlation analysis may also be used. Given the availability of Feshbach resonances, this impurity-induced decoherence may also be studied as a function of scattering length.

Optical lattices allow the realization of lower dimensional systems by freezing out some of the degrees of freedom. In the case of pure bosonic systems, this has raised interesting questions, starting with the possibility of condensation itself and the occurrence of phase fluctuations. A lot of the appeal of low-dimensional systems stems from the fact that many results can be obtained analytically or through quasi-exact DMRG calculations. Under conditions of reduced dimensionality, an interacting Bose gas can effectively assume the character of a non-interacting Fermi gas as seen in the observation [165, 166] of a Tonks-Girardeau gas [167, 168, 169]. In the case of Fermi-Bose mixtures, one-dimensional systems [170] may exhibit charge-density wave phenomena [171]. It may be possible to observe such phases as the appearance of a second periodicity in bosonic time of flight images or correlation analysis.

Boson-induced Cooper pairing has been predicted to be enhanced in the presence of an optical lattice potential. In principle, the same discussion as with boson-enhanced Cooper pairing in dipole traps applies, mostly concerning diagnostics. In optical lattices, transport measurements may provide evidence of superfluidity in this system. Transport properties can be measured in moving lattices, and this experiment has been developed to allow moving optical lattices to be studied. In appendix C, I have collected some of the ideas for transport studies, moving lattices and more general phase stabilized interference patterns. Some of the technological ideas have been used by the spinor BEC experiment in our group, resulting in a very compact hexagonal lattice setup.

Mixtures in lattices – heteronuclear molecules

In chapter 7, I have reported on the first observation of ultracold heteronuclear Feshbach molecules. Forming these molecules within individual sites of an optical lattice greatly enhances the lifetime of the sample; at the same time, it has allowed a very precise measurement of

the binding energy of these molecules. I have shown how we can explain the energy spectrum and the transfer efficiency of the molecules in a pseudopotential model. In a heteronuclear system, the possible different trapping frequencies of the two atoms raise interesting questions with respect to universality and unitarity for strongly interacting pairs. In fact, this chapter realizes a third perspective on heteronuclear mixtures – the two-body limit, compared to the global mean field limit and the many-body lattice perspective discussed above.

One of the most immediate things that one can do with these molecules is to study their lifetime in the optical lattice when the residual atoms are removed using resonant light beams. The necessary microwave technology in order to first transfer these atoms into the higher lying hyperfine manifold was already demonstrated, and a minor modification of the ^{40}K and ^{87}Rb laser systems is necessary in order to be able to shine in two detection laser beams with a respective detuning of a few GHz within some 100 ms. The necessary offset-locking technology has already been implemented during this thesis. Once these atoms have been removed, the lifetime in the lattice should improve even more. One can then think about ramping the optical lattice down and studying molecule-molecule collisions and eventually prove the fermionic character of these molecules.

The molecules that have been produced in this thesis are still relatively weakly bound, which becomes apparent in the fact that their binding energies are so well predicted by a pseudopotential model. Nevertheless, production of heteronuclear Feshbach molecules is generally considered as an important step forwards towards ultracold polar molecules. In forming ultracold ground state polar molecules from ultracold atoms, there is currently a similar “phase space density gap” as the one which separated laser cooled atoms from degeneracy before the advent of evaporative cooling. The phase space density gap is the small Franck-Condon overlap between the initial and final states of a two-color photoassociation experiment bringing two atoms to form a molecule.

The gap may ultimately be bridged using a combination of techniques: performing the experiment in an optical lattice as in this thesis may increase the lifetime of the sample and hence relax experimental constraints. The fact that in lattice Feshbach association as demonstrated in chapter 7, molecules come out in a well-defined ro-vibrational state may be beneficial since it provides definite starting conditions in comparison to e. g. dipole traps. This makes these Feshbach molecules ideal candidates for subsequent transfer into the internal ground state using two-color pulsed photoassociation. The transfer efficiency may be significantly enhanced by using concepts developed for coherent control and coherent accumulation, thereby tailoring excited state wave packets in the association process which lead to optimum overlap. This may be done using readily available femtosecond technology.

The fact that these ultracold polar molecules would be associated within the single well of an optical lattice makes them direct candidates for quantum computation schemes relying on long-range dipolar interactions [55] and for implementations of lattice spin models [172], opening new perspectives for scalable quantum computation and quantum simulation.

Together, the measurements presented in this thesis demonstrate the wide range of phenomena which can be studied in heteronuclear systems, in particular Fermi-Bose mixtures, and the bright perspectives of these systems for ultracold chemistry, fascinating many-body phenomena and quantum simulation.

Appendix A

High field detection and frequency offset lock

In this appendix, I derive the relevant laser detunings for imaging ^{40}K at high magnetic fields close to the 547 G Feshbach resonance. I also discuss the frequency offset lock which has been used to produce the required detunings in the experiment.

In the presence of magnetic fields around 500 G, both the ground state $4^2S_{1/2}$ sublevels and the excited state $4^2P_{3/2}$ sublevels are strongly affected by the presence of the magnetic field. In the case of the ground state, the shift can be calculated using the Breit-Rabi formula (equation 7.1). In the excited state, the energy structure as a function of magnetic field can be calculated numerically by diagonalizing the magnetic field interaction operator. The intermediate regime between Zeeman effect and Paschen-Back effect is plotted in Fig. A.1.

Compared to Fig. 7.2 which shows the ground state magnetic field dependence, one can see that the Paschen-Back regime is entered much earlier in the excited state than in the ground state, which is due to the much smaller hyperfine constant. At 547 G, we can therefore safely assume the validity of the Paschen-Back formula for the excited state in order to calculate the optical detection frequency shift:

$$E_{PB}(B) = g_J \mu_B m_J B + A m_I m_J \quad (\text{A.1})$$

Fig. A.2 shows the relevant frequency shifts. We consider two transitions, one for atoms in the (low field) $|F = 9/2, m_F = -9/2\rangle$, $|m_J = -1/2, m_I = -4\rangle$ (high field) absolute ground state and one for atoms in the $|F = 9/2, m_F = -7/2\rangle$ (low field), $|m_J = -1/2, m_I = -3\rangle$ (high field) state. The relevant cycling transitions are $\Delta m_I = 0$, $\Delta m_J = -1$ transitions, and the respective detunings from the zero field $F = 9/2 \rightarrow F' = 11/2$ cycling are given in Fig. A.2 both for the ground and excited state. Altogether, we obtain a detuning of

$$1531.1 \text{ MHz} - 767.0 \text{ MHz} = 764.1 \text{ MHz} \quad (\text{A.2})$$

for detection of atoms in $|m_J = -1/2, m_I = -4\rangle$ (which would be $|F = 9/2, m_F = -9/2\rangle$ at low field) and

$$1519.7 \text{ MHz} - 687.0 \text{ MHz} = 832.7 \text{ MHz} \quad (\text{A.3})$$

for detection of atoms in $|m_J = -1/2, m_I = -3\rangle$ (which would be $|F = 9/2, m_F = -7/2\rangle$ at low field).

In order to generate these detunings, a frequency offset lock has been implemented together with Leif Humbert [173] allowing the frequency of the Ti:Sa laser used for detection to be

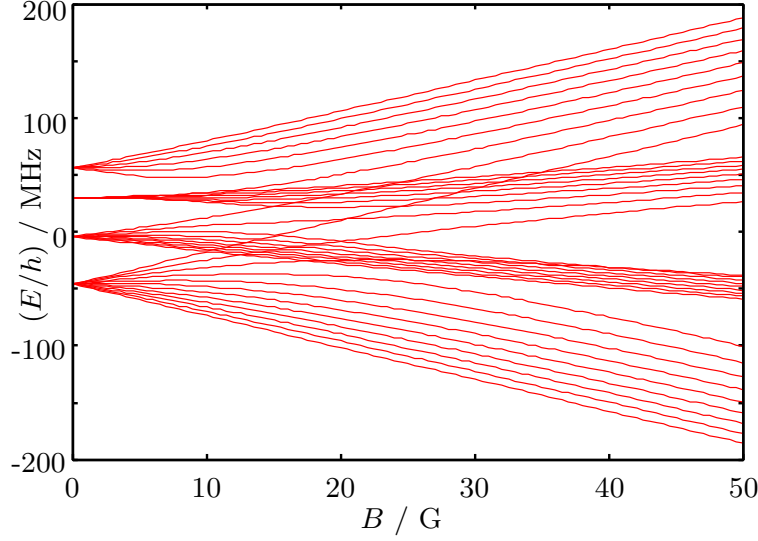


Figure A.1: Crossover from Zeeman to Paschen-Back regime for ^{40}K in the $4^2P_{3/2}$ state.

varied over a wide range while it is locked relative to the fixed ^{40}K repumping TA laser system. The scheme is based on [90]. The basic idea has been mentioned in chapter 3, and the setup is shown in Fig. A.3. The beat note $\Delta\nu$ between the Ti:Sa and the TA laser system is mixed with a variable frequency reference ν_{SMT} (Rohde & Schwarz SMT02), and the product is stabilized to a reference frequency using an error signal circuit generating a dispersive lineshape. The error signal circuit compares the rf levels of a high pass and a -3 dB attenuator to a -6 dB attenuator and thus has zero output voltage when the input signal has a frequency equal to the -3 dB point of the high pass. This dispersive signal is fed back to the Ti:Sa tuning input through a PI regulator in order to stabilize the system to zero error signal circuit output voltage, i. e. in our case

$$\nu_{SMT} - \Delta\nu = 161 \text{ MHz} \quad (\text{A.4})$$

(161 MHz is the frequency where the error signal circuit output is zero). By changing the SMT output frequency from the experiment control software over GPIB, the detuning of the Ti:Sa relative to the TA laser system can be varied over almost one GHz. We use this scheme in order to red-detune the Ti:Sa (i. e. lower ν_{SMT}) relative to the zero magnetic field $|F = 9/2\rangle \rightarrow F' = 11/2$ cycling transition for detection at high magnetic fields as outline above, and the tuning range is fully sufficient for the detunings calculated above.

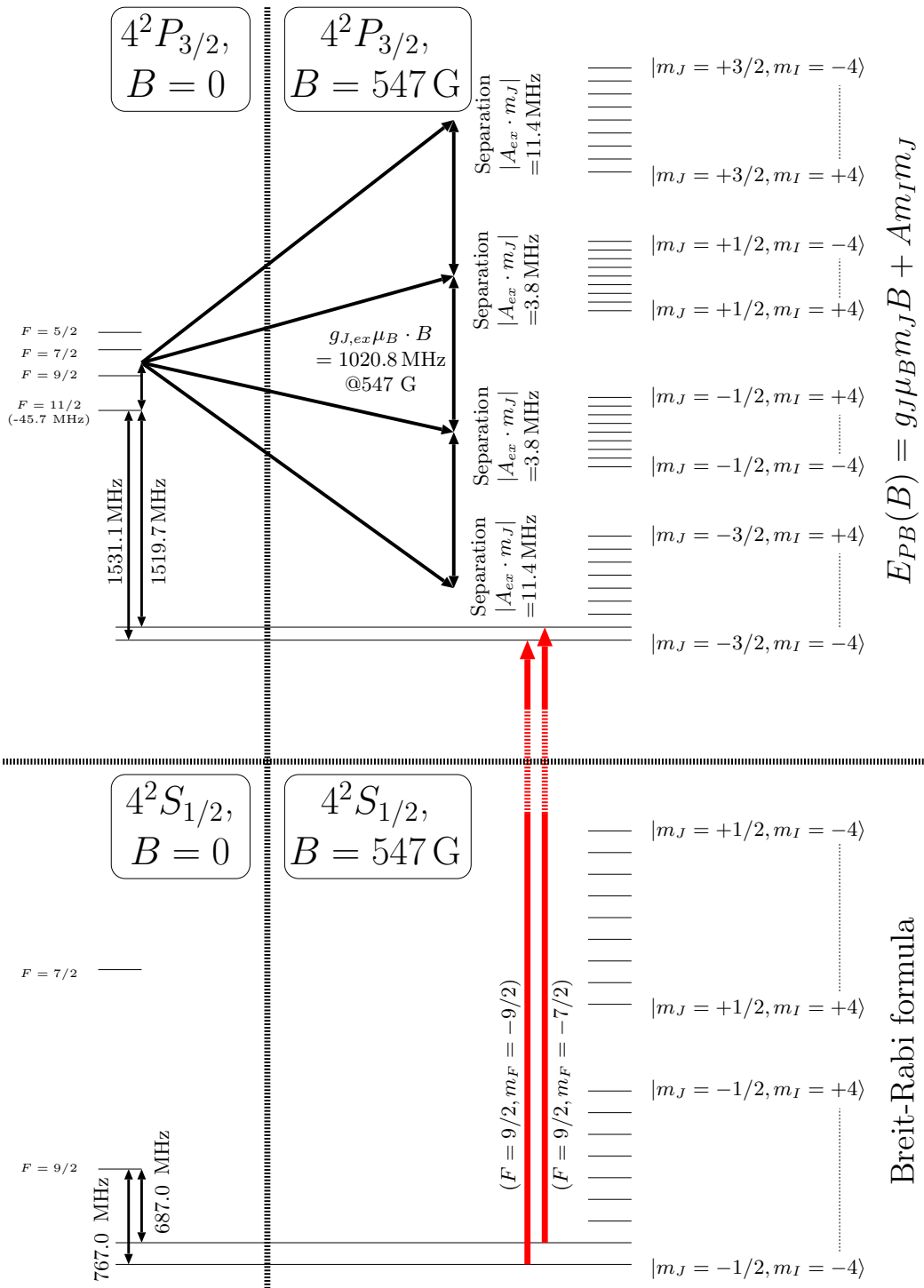


Figure A.2: Calculation of detunings for detection of ^{40}K at high magnetic fields.

Appendix B

Atomic parameters

This appendix lists some of the atomic parameters and fundamental constants that have been used in calculations in this thesis, in particular for magnetic field calibrations using the Breit-Rabi formula and for calculation of detunings for detection at high magnetic fields. All values have been taken from ref. [174].

Symbol	Description	Value
I	Nuclear spin	4
g_J	Electron gyromagnetic ratio	2.002 294 21(24)
g_I	Nuclear gyromagnetic ratio	0.000 175 490(34)
$A (4^2S_{1/2})$	Hyperfine constant	-285.7308(24) MHz
$A (4^2P_{3/2})$	Hyperfine constant	-7.59(6) MHz

Table B.1: Atomic parameters for ^{40}K used in this thesis.

Symbol	Description	Value
I	Nuclear spin	3/2
g_J	Electron gyromagnetic ratio	2.002 331 13(20)
g_I	Nuclear gyromagnetic ratio	0.000 176 490(34)
$A (5^2S_{1/2})$	Hyperfine constant	3417.341 306 42(15) MHz

Table B.2: Atomic parameters for ^{87}Rb used in this thesis.

Appendix C

Transport in lattices and phase stabilization

While BEC and superfluidity are intimately connected, they do not necessarily occur together. Superfluidity has been intensely discussed in the context of dilute bosonic gases; formation of vortices and transport measurements provide striking evidence of superfluidity in ultracold atomic gases. When setting up this experiment, transport measurements have been of particular interest with respect to future experiments studying the onset of fermionic superfluidity in Fermi gases and interacting Fermi-Bose mixtures. In a system of atoms confined in a trap with an overlapped lattice potential, transport can be studied either by displacing the trap and leaving the lattice stationary or by displacing the lattice and leaving the trap stationary¹.

One can then observe the response of the atomic cloud to the displacement. The former technique has been demonstrated e. g. in experiments in 1D optical lattices performed at LENS in Florence [175]. In these experiments, the underlying magnetic trap has been displaced by applying additional magnetic fields. To make use of every possible degree of freedom, in particular Feshbach resonances as used in proposals for boson-induced cooper pairing, the use of an underlying trap is impracticable, and optical traps are not displaced as easily. In these situations, one would therefore prefer the second approach over the first one. When designing the 3D optical lattice setup for this experiment, I have therefore looked into possibilities of implementing moving optical lattices.

The idea of a moving lattice is as follows: When using two independent, counterpropagating laser beams with a difference frequency $\delta\nu$, one obtains a moving interference pattern with a velocity $v = \delta\nu/2 \cdot \lambda$. At a wavelength of $1 \mu\text{m}$, a shift of 1 kHz therefore corresponds to a lattice velocity of 0.5 mm/s. Thus, by increasing the detuning between two counterpropagating beams from zero to v , one can accelerate the lattice and subsequently bring it to rest by lowering the detuning again.

In the experiment, it is usually desirable to use optical fibers in lattice setups. On the one hand, this separates the adjustment of the lattice laser source from the adjustment of the lattice itself, and on the other hand, it provides mode cleaning of the optical lattice beams. In order to realize two counterpropagating laser beams with the possibility to tune the difference frequency, two scenarios are possible:

- **Single fiber.** In this case, the light from the laser source is sent through a single

¹Man kann den Propheten zum Berg tragen oder den Berg zum Propheten...

fiber and then split up into two beams, sent through two different AOMs to control the relative frequency and then delivered to the atoms on counterpropagating beam paths. The presence of the AOM may affect beam quality, and the beam path from the splitting of the two beams to the overlap region is potentially very long, possibly leading to issues with adjustment and mechanical vibrations. The experiment has been designed to allow this scenario with a beam path as short as possible on the horizontal axis of the apparatus using the flexible stainless steel boards (see Fig. C.2a)).

- **Two fibers.** Both beams can also be sent through separate fibers. This only requires two fiber output and focussing units on each side of the apparatus. In this situation, one immediately faces the issue of a relative phase jitter of the interference pattern after passing through two separate fibers. This effect is due to coupling of mechanical vibrations to the fiber. The jitter can easily be on the order of a few kHz, thereby on the order of the desired detuning, and is a main source of concern in optical clock experiments when a narrow linewidth laser beam is to be transmitted over an optical fiber [176]. One therefore needs to come up with a method of relative phase separation after the fiber. Phase stabilization can be achieved by putting a beam splitter into the path of the two counterpropagating beams, and directing the two outputs onto a common photodiode. Using the beat signal, the relative phase can be stabilized using an actuator.

However, the case of two counterpropagating beams is only a special case of a more generalized class of optical lattice geometries based on interference of separate beam paths with an arbitrary angle where phase stabilization is required. For a review, see [177]. To give only one example, in experiments on condensates in 2D lattices in Munich, the relative phase of two orthogonal retroreflected beams has been stabilized using a an actuator on one of the retroreflection mirrors [178].

Another geometry is the well known tetrahedron configuration made up of four independent laser beams [177]. Within one plane, it is also possible to use three beams at an angle of 120° and create a hexagonal lattice pattern ([177], see below). The latter approach is currently being pursued in the spinor BEC experiment in our group. In all of these experiments, one benefits from phase stabilization techniques which will not require bulky equipment at the experiment itself in addition to detection systems, MOT optics, dipole traps, magnetic trap,... . This would almost certainly occur due to complicated beam paths to overlap light from the different lattice beam paths, particularly for the not counterpropagating setups.

I have already mentioned that the noise introduced by an optical fiber has been seen in optical clock experiments [176]. For phase stabilization in optical lattices, we can adopt techniques which are currently used in many optical clock and frequency standard distribution experiments (e. g. [176, 179, 180]) to stabilize the beam path through an optical fiber. The basic idea is shown in Fig. 2.6. Let ν_L be the frequency of the laser light. An AOM in single pass configuration with frequency ν_A in front of the optical fiber allows control of the frequency of the light sent into the optical fiber. This AOM is needed anyway for intensity control, and it is not specific to this scheme. The light is coupled into a fiber, which introduces time-dependent frequency jitter $\delta\nu$. At the end of the fiber, we have $\nu_L + \nu_A + \delta\nu$, and a small fraction of the light is coupled back into the fiber and passes the AOM in double pass configuration on its way back to the laser. The simplest way of achieving this is to use the light which is reflected anyway from the end of an optical fiber. This avoids any additional elements in the beam path at the experiment proper.

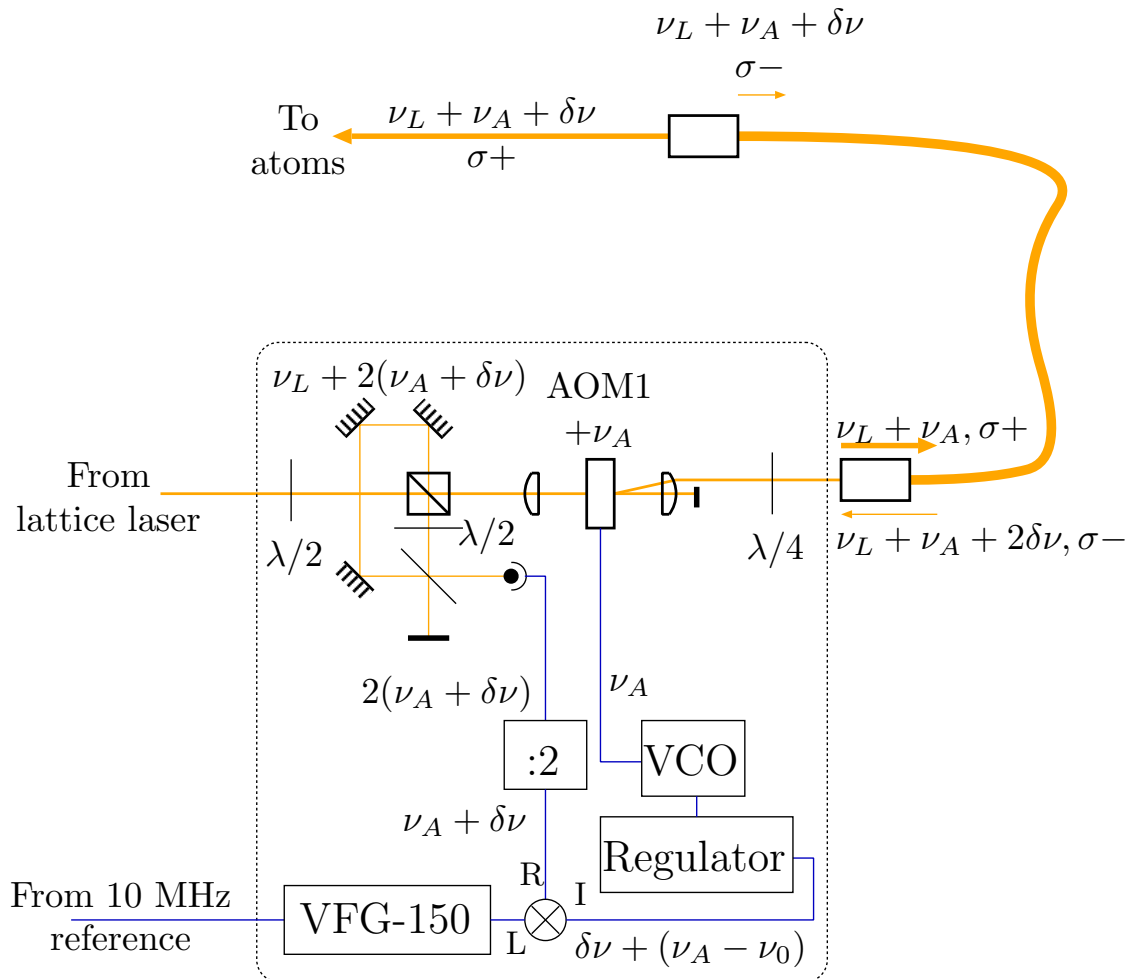


Figure C.1: Phase stabilization setup for moving lattices and lattices created through interference from separate fibers.

Between the AOM and the laser itself, the retroreflected fraction has a frequency $\nu_L + 2(\nu_A + \delta\nu)$. The retroreflected light can be separated from the main beam path if a quarter wave plate is introduced in front of the fiber or if the fiber is adjusted such that it acts like a waveplate. The retroreflected light now has orthogonal polarization and can be split from the main beam path using a polarizing beam splitter cube in front of the AOM. If this light is overlapped with the main beam on a photodiode, we obtain a beat note with frequency $2(\nu_A + \delta\nu)$. Using this beat note, the fiber-induced shift can be compensated by acting on the AOM frequency ν_A using standard rf phase locking techniques. One can for example divide the beat note by two and obtain $\nu_A + \delta\nu$. Mixing this with a frequency ν_0 close to the AOM VCO frequency ν_A , one obtains a low frequency signal proportional to $\delta\nu + \nu_A - \nu_0$ ². Using a regulator, we can control ν_A such that $\delta\nu + \nu_A - \nu_0 \equiv 0$ by acting on the AOM VCO source. This corresponds to $\nu_L + \nu_A + \delta\nu \equiv \nu_L + \nu_0$ behind the fiber, and we have effectively canceled the fiber noise and stabilized the phase at the output of the fiber with respect to the phase at the beam splitter in front of the AOM.

While this setup may look complicated at first sight, there is really not a lot of additional optical equipment compared to “traditional” lattice branch as shown in section 3.10. There is just one interferometer in front of the fiber and some standard rf equipment. The particular advantage of this scheme for optical lattices is that the whole phase stabilization setup can be placed in front of the fiber, and that it allows a very compact lattice beam collimation and focussing unit without any bulky equipment near the experiment, which is particularly relevant if multiple phase stabilized beams are required such as for moving lattices or the tetrahedron lattice (which would require *three* phase stabilization setups directly at the experiment).

Another way to close the feedback loop is to drop the frequency divider stage and mix the rf signal with a reference source with frequency $2\nu_0$ close to $2\nu_A$. One obtains a low frequency signal $2(\nu_A - \nu_0 - \delta\nu)$. The latter can again be fed back to the VCO generating ν_A in a feedback loop in order to compensate $\delta\nu$ via ν_A .

The latter approach avoids the frequency divider stage and has been implemented by Jochen Kronjäger and Christoph Becker at the spinor BEC experiment in our group in a hexagonal lattice configuration. Beat notes below one Hz width have been observed between beams passing different stabilized fibers. In addition, Jochen has added an automatic gain compensation setup which provides stable operation of the phase lock over a wide range of output intensities which is important for the lattice ramp-up sequence. In this case, a common rf source for $2\nu_0$ is used for all three lattice beams, and this phase stabilization approach has resulted in a very compact lattice setup. This approach also separates the adjustment of phase control from the adjustment of the lattice itself.

When not using one common source for ν_0 but several synthesizers which are stabilized relative to a common 10 MHz reference, we can achieve a controlled detuning between the individual beams by detuning one synthesizer with respect to another. This detuning will lead to a moving interference pattern for the optical lattice. Let us look at the simple case of two counterpropagating phase stabilized beams. We will have one fixed frequency synthesizer operated at 140 MHz providing $2\nu_0$ for one beam. The second phase stabilization setup could obtain its modulation frequency from a VFG rf synthesizer as described in section 3.9.1 with a frequency equal to or close to $2\nu_0$. By connecting 10 MHz frequency reference inputs of both synthesizers to a common source, both would be phase stable with respect to each other. The techniques discussed in section 3.9.1 can then be used to control the detuning and phase

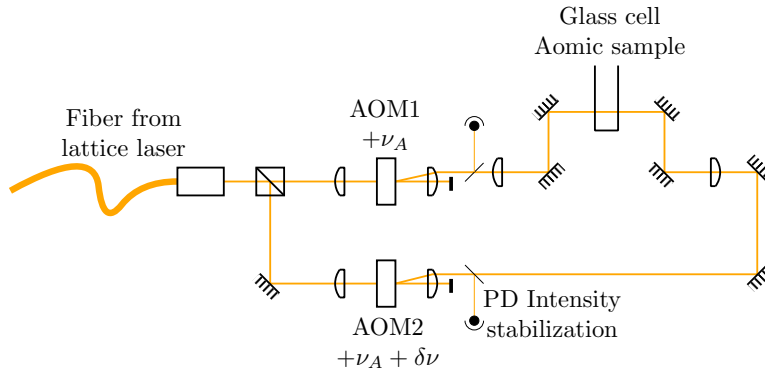
²A phase detector might be more appropriate here.

between two beams through the VFG output frequency and phase and thus the velocity and position of a moving lattice very precisely, thereby enabling future transport measurements in a very elegant setup shown in Fig. C.2b).

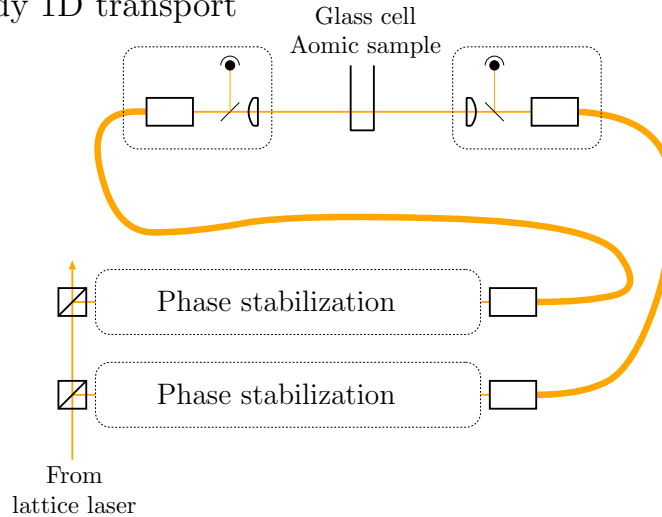
With the above mentioned setup, transport would be restricted to one dimension. When implementing the above-mentioned velocity control with the hexagonal lattice, requiring one fixed oscillator and two VFG synthesizers, one would be able to move around 1D tubes of the lattice in a plane with a high degree of control (Fig. C.2c)), eventually in combination with polarization manipulation. This may be particularly interesting for creation of rotating lattices as has recently observed at JILA using a rotating diaphragm [181].

The above technique of relative phase stabilization may also be used for experiments studying atomic transport over large distances, such as through hollow core fibers. By creating an accelerated lattice of two counterpropagating beams in the fiber, one may transfer atoms into the fiber in a controlled fashion, bring them to rest, perform a wide variety of manipulation and cooling schemes within the steep potential formed by the longitudinal lattice and the tight transverse dipole trap and subsequently accelerate the atoms and transport them out of the fiber. For a recent demonstration of transport over more than 20 cm using moving lattices and free lattice beams, see [182].

a) Study 1D transport (without active phase stabilization)



b) Study 1D transport



c) Rotating lattice, controlled through rf!

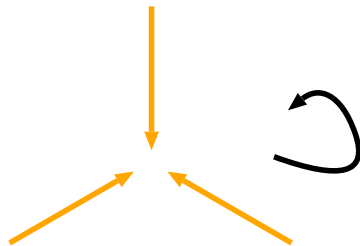


Figure C.2: Moving lattice scenarios. a) Shows a moving lattice scenario which requires relatively bulky equipment near the experiment. b) Shows an elegant setup for 1D transport measurements with active phase stabilization. c) Extends this to a moving 2D configuration of 1D tubes pointing out of the plane.

Appendix D

Numerical algorithms and software

The purpose of this appendix is to list software libraries, packages and algorithms and recipes which have been used for data analysis in this thesis.

- The **GNU Scientific Library (GSL)** is a numerical library for C / C++ programs. The implementations of Fermi-Dirac functions `gsl_sf_fermi_dirac_*` contained in this library have been used in data analysis. Note that

$$-Li_n(-\zeta) = \text{gsl_sf_fermi_dirac_}(n-1)(\ln\zeta) \quad .$$

- From the **CEPHES** mathematical function library available through `netlib`, the `spence()` function implementing spencers's integral (related to the dilogarithm) has been used in the 2-dimensional Fermi-Dirac fit. I have also used implementations of Bose-Einstein functions and Fermi-Dirac functions given in [183, 184], in particular for $g_{5/2}$.
- Also from the **CEPHES** library, the `lmdif()` function implementing the Marquardt-Levenberg nonlinear least squares algorithm has been used in all of the one- and two-dimensional fits for absorption images.
- `libjpeg`, `libtiff` and `libpng` have been used for image in- and output in all of the data processing software.
- The `mingw` cross-compiler has been used under `linux` to develop the VFG-controller software, along with `flex` and `bison` to parse the VFG language.
- The `mingw` windows port of some of the above-mentioned libraries was used e. g. in the CCD control software.
- The `openafs` distributed filesystem, together with the `Heimdal` Kerberos implementation and `openldap`, has allowed setting up a linux cluster which has hosted the 1.2 TB of image data recorded during this thesis.

Bibliography

- [1] C. Ospelkaus, S. Ospelkaus, L. Humbert, P. Ernst, K. Sengstock and K. Bongs: *Ultracold Heteronuclear Molecules in a 3D Optical Lattice*. Phys. Rev. Lett. **97**, 120402 (2006). doi:10.1103/PhysRevLett.97.120402.
- [2] S. Ospelkaus, C. Ospelkaus, L. Humbert, K. Sengstock and K. Bongs: *Tuning of Heteronuclear Interactions in a Degenerate Fermi-Bose Mixture*. Phys. Rev. Lett. **97**, 120403 (2006). doi:10.1103/PhysRevLett.97.120403.
- [3] S. Ospelkaus, C. Ospelkaus, O. Wille, M. Succo, P. Ernst, K. Sengstock and K. Bongs: *Localization of Bosonic Atoms by Fermionic Impurities in a Three-Dimensional Optical Lattice*. Phys. Rev. Lett. **96**, 180403 (2006). doi:10.1103/PhysRevLett.96.180403.
- [4] C. Ospelkaus, S. Ospelkaus, K. Sengstock and K. Bongs: *Interaction-Driven Dynamics of $^{40}\text{K} - ^{87}\text{Rb}$ Fermion-Boson Gas Mixtures in the Large-Particle-Number Limit*. Phys. Rev. Lett. **96**, 020401 (2006). doi:10.1103/PhysRevLett.96.020401.
- [5] S. Ospelkaus, C. Ospelkaus, R. Dinter, J. Fuchs, M. Nakat, K. Sengstock and K. Bongs: *Degenerate K-Rb Fermi-Bose gas mixtures with large particle numbers*. Journal of Modern Optics **prEview** (2006). doi:10.1080/09500340600777763.
- [6] Bose: *Plancksches Gesetz und Lichtquantenhypothese*. Zeitschrift für Physik **26**, 178 (1924). doi:10.1007/BF01327326.
- [7] Albert Einstein: *Quantentheorie des einatomigen idealen Gases. I*. Sitzungsberichte der Preussischen Akademie der Wissenschaften **22**, 261 (1924).
- [8] Albert Einstein: *Quantentheorie des einatomigen idealen Gases. II*. Sitzungsberichte der Preussischen Akademie der Wissenschaften **1**, 3 (1925).
- [9] W. Pauli: *Über den Zusammenhang des Abschlusses der Elektronengruppen im Atom mit der Komplexstruktur der Spektren*. Zeitschrift für Physik **31**, 765–783 (1925).
- [10] E. Fermi: *Über den Zusammenhang des Abschlusses der Elektronengruppen im Atom mit der Komplexstruktur der Spektren*. Zeitschrift für Physik **36**, 902 (1926). doi:10.1007/BF01400221.
- [11] F. London: *The λ -phenomenon of liquid helium and the Bose-Einstein degeneracy*. Nature **141**, 643 (1938).
- [12] F. London: *On the Bose-Einstein Condensation*. Phys. Rev. **54**, 947–954 (1938). doi:10.1103/PhysRev.54.947.

- [13] C. E. Hecht: *The possible superfluid behaviour of hydrogen atom gases and liquids*. Physica **25**, 1159 (1959).
- [14] William C. Stwalley and L. H. Nosanow: *Possible "New" Quantum Systems*. Phys. Rev. Lett. **36**, 910–913 (1976). doi:10.1103/PhysRevLett.36.910.
- [15] M. H. Anderson, J. R. Ensher, M. R. Matthews, C. E. Wieman and E. A. Cornell: *Observation of Bose-Einstein Condensation in a Dilute Atomic Vapor*. Science **269**, 198–201 (1995). doi:10.1126/science.269.5221.198.
- [16] K. B. Davis, M. O. Mewes, M. R. Andrews, N. J. van Druten, D. S. Durfee, D. M. Kurn and W. Ketterle: *Bose-Einstein Condensation in a Gas of Sodium Atoms*. Phys. Rev. Lett. **75**, 3969–3973 (1995). doi:10.1103/PhysRevLett.75.3969.
- [17] C. C. Bradley, C. A. Sackett, J. J. Tollett and R. G. Hulet: *Evidence of Bose-Einstein Condensation in an Atomic Gas with Attractive Interactions*. Phys. Rev. Lett. **75**, 1687–1690 (1995). doi:10.1103/PhysRevLett.75.1687.
- [18] B. DeMarco and D. S. Jin: *Onset of Fermi Degeneracy in a Trapped Atomic Gas*. Science **285**, 1703–1706 (1999). doi:10.1126/science.285.5434.1703.
- [19] T. Loftus, C. A. Regal, C. Ticknor, J. L. Bohn and D. S. Jin: *Resonant Control of Elastic Collisions in an Optically Trapped Fermi Gas of Atoms*. Phys. Rev. Lett. **88**, 173201 (2002). doi:10.1103/PhysRevLett.88.173201.
- [20] K. Dieckmann, C. A. Stan, S. Gupta, Z. Hadzibabic, C. H. Schunck and W. Ketterle: *Decay of an Ultracold Fermionic Lithium Gas near a Feshbach Resonance*. Phys. Rev. Lett. **89**, 203201 (2002). doi:10.1103/PhysRevLett.89.203201.
- [21] K. M. O'Hara, S. L. Hemmer, S. R. Granade, M. E. Gehm, J. E. Thomas, V. Venturi, E. Tiesinga and C. J. Williams: *Measurement of the zero crossing in a Feshbach resonance of fermionic ^6Li* . Phys. Rev. A **66**, 041401 (2002). doi:10.1103/PhysRevA.66.041401.
- [22] C. A. Regal and D. S. Jin: *Measurement of Positive and Negative Scattering Lengths in a Fermi Gas of Atoms*. Phys. Rev. Lett. **90**, 230404 (2003). doi:10.1103/PhysRevLett.90.230404.
- [23] S. Gupta, Z. Hadzibabic, M. W. Zwierlein, C. A. Stan, K. Dieckmann, C. H. Schunck, E. G. M. van Kempen, B. J. Verhaar and W. Ketterle: *Radio-Frequency Spectroscopy of Ultracold Fermions*. Science **300**, 1723–1726 (2003). doi:10.1126/science.1085335.
- [24] Cindy A. Regal, Christopher Ticknor, John L. Bohn and Deborah S. Jin: *Creation of ultracold molecules from a Fermi gas of atoms*. Nature **424**, 47 (2003). doi:10.1038/nature01738.
- [25] J. Cubizolles, T. Bourdel, S. J. J. M. F. Kokkelmans, G. V. Shlyapnikov and C. Salomon: *Production of Long-Lived Ultracold Li_2 Molecules from a Fermi Gas*. Phys. Rev. Lett. **91**, 240401 (2003). doi:10.1103/PhysRevLett.91.240401.

- [26] C. A. Regal, M. Greiner and D. S. Jin: *Lifetime of Molecule-Atom Mixtures near a Feshbach Resonance in K*. Phys. Rev. Lett. **92**, 083201 (2004). doi:10.1103/PhysRevLett.92.083201.
- [27] Kevin E. Strecker, Guthrie B. Partridge and Randall G. Hulet: *Conversion of an Atomic Fermi Gas to a Long-Lived Molecular Bose Gas*. Phys. Rev. Lett. **91**, 080406 (2003). doi:10.1103/PhysRevLett.91.080406.
- [28] S. Jochim, M. Bartenstein, A. Altmeyer, G. Hendl, C. Chin, J. Hecker Denschlag and R. Grimm: *Pure Gas of Optically Trapped Molecules Created from Fermionic Atoms*. Phys. Rev. Lett. **91**, 240402 (2003). doi:10.1103/PhysRevLett.91.240402.
- [29] Markus Greiner, Cindy A. Regal and Deborah S. Jin: *Emergence of a molecular Bose-Einstein condensate from a Fermi gas*. Nature **426**, 537 (2003). doi:10.1038/nature02199.
- [30] M. W. Zwierlein, C. A. Stan, C. H. Schunck, S. M. F. Raupach, S. Gupta, Z. Hadzibabic and W. Ketterle: *Observation of Bose-Einstein Condensation of Molecules*. Phys. Rev. Lett. **91**, 250401 (2003). doi:10.1103/PhysRevLett.91.250401.
- [31] S. Jochim, M. Bartenstein, A. Altmeyer, G. Hendl, S. Riedl, C. Chin, J. Hecker Denschlag and R. Grimm: *Bose-Einstein Condensation of Molecules*. Science **302**, 2101–2103 (2003). doi:10.1126/science.1093280.
- [32] C. A. Regal, M. Greiner and D. S. Jin: *Observation of Resonance Condensation of Fermionic Atom Pairs*. Phys. Rev. Lett. **92**, 040403 (2004). doi:10.1103/PhysRevLett.92.040403.
- [33] M. W. Zwierlein, C. A. Stan, C. H. Schunck, S. M. F. Raupach, A. J. Kerman and W. Ketterle: *Condensation of Pairs of Fermionic Atoms near a Feshbach Resonance*. Phys. Rev. Lett. **92**, 120403 (2004). doi:10.1103/PhysRevLett.92.120403.
- [34] M. Bartenstein, A. Altmeyer, S. Riedl, S. Jochim, C. Chin, J. Hecker Denschlag and R. Grimm: *Collective Excitations of a Degenerate Gas at the BEC-BCS Crossover*. Phys. Rev. Lett. **92**, 203201 (2004). doi:10.1103/PhysRevLett.92.203201.
- [35] T. Bourdel, L. Khaykovich, J. Cubizolles, J. Zhang, F. Chevy, M. Teichmann, L. Tarruell, S. J. J. M. F. Kokkelmans and C. Salomon: *Experimental Study of the BEC-BCS Crossover Region in Lithium 6*. Phys. Rev. Lett. **93**, 050401 (2004). doi:10.1103/PhysRevLett.93.050401.
- [36] J. Kinast, S. L. Hemmer, M. E. Gehm, A. Turlapov and J. E. Thomas: *Evidence for Superfluidity in a Resonantly Interacting Fermi Gas*. Phys. Rev. Lett. **92**, 150402 (2004). doi:10.1103/PhysRevLett.92.150402.
- [37] C. Chin, M. Bartenstein, A. Altmeyer, S. Riedl, S. Jochim, J. Hecker Denschlag and R. Grimm: *Observation of the Pairing Gap in a Strongly Interacting Fermi Gas*. Science **305**, 1128–1130 (2004). doi:10.1126/science.1100818.
- [38] Martin W. Zwierlein, Andre Schirotzek, Christian H. Schunck and Wolfgang Ketterle: *Fermionic Superfluidity with Imbalanced Spin Populations*. Science **311**, 492–496 (2006). doi:10.1126/science.1122318.

- [39] Guthrie B. Partridge, Wenhui Li, Ramsey I. Kamar, Yean-an Liao and Randall G. Hulet: *Pairing and Phase Separation in a Polarized Fermi Gas*. Science **311**, 503–505 (2006). doi:10.1126/science.1122876.
- [40] Michael Köhl, Henning Moritz, Thilo Stöferle, Kenneth Günter and Tilman Esslinger: *Fermionic Atoms in a Three Dimensional Optical Lattice: Observing Fermi Surfaces, Dynamics, and Interactions*. Phys. Rev. Lett. **94**, 080403 (2005). doi:10.1103/PhysRevLett.94.080403.
- [41] Henning Moritz, Thilo Stöferle, Kenneth Günter, Michael Köhl and Tilman Esslinger: *Confinement Induced Molecules in a 1D Fermi Gas*. Phys. Rev. Lett. **94**, 210401 (2005). doi:10.1103/PhysRevLett.94.210401.
- [42] Kenneth Günter, Thilo Stöferle, Henning Moritz, Michael Köhl and Tilman Esslinger: *p-Wave Interactions in Low-Dimensional Fermionic Gases*. Phys. Rev. Lett. **95**, 230401 (2005). doi:10.1103/PhysRevLett.95.230401.
- [43] Thilo Stöferle, Henning Moritz, Kenneth Günter, Michael Köhl and Tilman Esslinger: *Molecules of Fermionic Atoms in an Optical Lattice*. Phys. Rev. Lett. **96**, 030401 (2006). doi:10.1103/PhysRevLett.96.030401.
- [44] H. Ott, E. de Mirandes, F. Ferlaino, G. Roati, G. Modugno and M. Inguscio: *Collisionally Induced Transport in Periodic Potentials*. Phys. Rev. Lett. **92**, 160601 (2004). doi:10.1103/PhysRevLett.92.160601.
- [45] L. Pezzè, L. Pitaevskii, A. Smerzi, S. Stringari, G. Modugno, E. de Mirandes, F. Ferlaino, H. Ott, G. Roati and M. Inguscio: *Insulating Behavior of a Trapped Ideal Fermi Gas*. Phys. Rev. Lett. **93**, 120401 (2004). doi:10.1103/PhysRevLett.93.120401.
- [46] H. Ott, E. de Mirandes, F. Ferlaino, G. Roati, V. Türck, G. Modugno and M. Inguscio: *Radio Frequency Selective Addressing of Localized Atoms in a Periodic Potential*. Phys. Rev. Lett. **93**, 120407 (2004). doi:10.1103/PhysRevLett.93.120407.
- [47] G. Roati, E. de Mirandes, F. Ferlaino, H. Ott, G. Modugno and M. Inguscio: *Atom Interferometry with Trapped Fermi Gases*. Phys. Rev. Lett. **92**, 230402 (2004). doi:10.1103/PhysRevLett.92.230402.
- [48] S. R. Granade, M. E. Gehm, K. M. O'Hara and J. E. Thomas: *All-Optical Production of a Degenerate Fermi Gas*. Phys. Rev. Lett. **88**, 120405 (2002). doi:10.1103/PhysRevLett.88.120405.
- [49] F. Schreck, L. Khaykovich, K. L. Corwin, G. Ferrari, T. Bourdel, J. Cubizolles and C. Salomon: *Quasipure Bose-Einstein Condensate Immersed in a Fermi Sea*. Phys. Rev. Lett. **87**, 080403 (2001). doi:10.1103/PhysRevLett.87.080403.
- [50] Andrew G. Truscott, Kevin E. Strecker, William I. McAlexander, Guthrie B. Partridge and Randall G. Hulet: *Observation of Fermi Pressure in a Gas of Trapped Atoms*. Science **291**, 2570–2572 (2001). doi:10.1126/science.1059318.
- [51] G. Roati, F. Riboli, G. Modugno and M. Inguscio: *Fermi-Bose Quantum Degenerate $^{40}\text{K} - ^{87}\text{Rb}$ Mixture with Attractive Interaction*. Phys. Rev. Lett. **89**, 150403 (2002). doi:10.1103/PhysRevLett.89.150403.

- [52] Z. Hadzibabic, C. A. Stan, K. Dieckmann, S. Gupta, M. W. Zwierlein, A. Görlitz and W. Ketterle: *Two-Species Mixture of Quantum Degenerate Bose and Fermi Gases*. Phys. Rev. Lett. **88**, 160401 (2002). doi:10.1103/PhysRevLett.88.160401.
- [53] J. Goldwin, S. Inouye, M. L. Olsen, B. Newman, B. D. DePaola and D. S. Jin: *Measurement of the interaction strength in a Bose-Fermi mixture with ^{87}Rb and ^{40}K* . Phys. Rev. A **70**, 021601 (2004). doi:10.1103/PhysRevA.70.021601.
- [54] G. Modugno, M. Modugno, F. Riboli, G. Roati and M. Inguscio: *Two Atomic Species Superfluid*. Phys. Rev. Lett. **89**, 190404 (2002). doi:10.1103/PhysRevLett.89.190404.
- [55] D. DeMille: *Quantum Computation with Trapped Polar Molecules*. Phys. Rev. Lett. **88**, 067901 (2002). doi:10.1103/PhysRevLett.88.067901.
- [56] F. Matera: *Fermion pairing in Bose-Fermi mixtures*. Phys. Rev. A **68**, 043624 (2003). doi:10.1103/PhysRevA.68.043624.
- [57] Fabrizio Illuminati and Alexander Albus: *High-Temperature Atomic Superfluidity in Lattice Bose-Fermi Mixtures*. Phys. Rev. Lett. **93**, 090406 (2004). doi:10.1103/PhysRevLett.93.090406.
- [58] F. Ferlaino, E. de Mirandes, G. Roati, G. Modugno and M. Inguscio: *Expansion of a Fermi Gas Interacting with a Bose-Einstein Condensate*. Phys. Rev. Lett. **92**, 140405 (2004). doi:10.1103/PhysRevLett.92.140405.
- [59] G. Modugno, G. Roati, F. Riboli, F. Ferlaino, R. J. Brecha and M. Inguscio: *Collapse of a Degenerate Fermi Gas*. Science **297**, 2240 (2002). doi:10.1126/science.1077386.
- [60] M. Modugno, F. Ferlaino, F. Riboli, G. Roati, G. Modugno and M. Inguscio: *Mean-field analysis of the stability of a K-Rb Fermi-Bose mixture*. Phys. Rev. A **68**, 043626 (2003). doi:10.1103/PhysRevA.68.043626.
- [61] J. Goldwin, S. Inouye, M. L. Olsen and D. S. Jin: *Cross-dimensional relaxation in Bose-Fermi mixtures*. Phys. Rev. A **71**, 043408 (2005). doi:10.1103/PhysRevA.71.043408.
- [62] C. A. Stan, M. W. Zwierlein, C. H. Schunck, S. M. F. Raupach and W. Ketterle: *Observation of Feshbach Resonances between Two Different Atomic Species*. Phys. Rev. Lett. **93**, 143001 (2004). doi:10.1103/PhysRevLett.93.143001.
- [63] S. Inouye, J. Goldwin, M. L. Olsen, C. Ticknor, J. L. Bohn and D. S. Jin: *Observation of Heteronuclear Feshbach Resonances in a Mixture of Bosons and Fermions*. Phys. Rev. Lett. **93**, 183201 (2004). doi:10.1103/PhysRevLett.93.183201.
- [64] M. Zaccanti, C. D'Errico, F. Ferlaino, G. Roati, M. Inguscio and G. Modugno: *Control of the interaction in a Fermi-Bose mixture*. Phys. Rev. A **74**, 041605 (2006). doi:10.1103/PhysRevA.74.041605.
- [65] Kenneth Günter, Thilo Stöferle, Henning Moritz, Michael Köhl and Tilman Esslinger: *Bose-Fermi Mixtures in a Three-Dimensional Optical Lattice*. Phys. Rev. Lett. **96**, 180402 (2006). doi:10.1103/PhysRevLett.96.180402.

- [66] Silke Ospelkaus-Schwarzer: *Quantum Degenerate Fermi-Bose Mixtures of ^{40}K and ^{87}Rb in 3D Optical Lattices*. Ph.D. thesis, Universität Hamburg (2006).
- [67] Brian DeMarco: *Quantum Behaviour of an Atomic Fermi Gas*. Ph.D. thesis, Graduate School of the University of Colorado (2001).
- [68] D. A. Butts and D. S. Rokhsar: *Trapped Fermi gases*. *Phys. Rev. A* **55**, 4346–4350 (1997). doi:10.1103/PhysRevA.55.4346.
- [69] Lev Pitaevskii and Sandro Stringari: *Bose-Einstein Condensation*. Oxford University Press (2003).
- [70] C. J. Pethick and H. Smith: *Bose-Einstein Condensation in Dilute Gases*. Cambridge University Press (2002).
- [71] Klaus Mølmer: *Bose Condensates and Fermi Gases at Zero Temperature*. *Phys. Rev. Lett.* **80**, 1804 (1998). doi:10.1103/PhysRevLett.80.1804.
- [72] Robert Roth: *Structure and stability of trapped atomic boson-fermion mixtures*. *Phys. Rev. A* **66**, 013614 (2002). doi:10.1103/PhysRevA.66.013614.
- [73] R. K. Pathria: *Statistical Mechanics*. Butterworth-Heinemann (1972).
- [74] Jonathan Michael Goldwin: *Quantum Degeneracy and Interactions in the ^{87}Rb - ^{40}K Bose-Fermi Mixture*. Ph.D. thesis, Faculty of the Graduate School of the University of Colorado (2005).
- [75] W. Ketterle, D. S. Durfee and D. M. Stamper-Kurn: *Making, probing and understanding Bose-Einstein condensates*. In M. Inguscio, S. Stringari and C. E. Wieman, editors, *Proceedings of the International School of Physics - Enrico Fermi*, page 67. IOS Press (1999).
- [76] R. Roth and H. Feldmeier: *Mean-field instability of trapped dilute boson-fermion mixtures*. *Phys. Rev. A* **65**, 021603 (2002). doi:10.1103/PhysRevA.65.021603.
- [77] E. G. M. van Kempen, S. J. J. M. F. Kokkelmans, D. J. Heinzen and B. J. Verhaar: *Interisotope Determination of Ultracold Rubidium Interactions from Three High-Precision Experiments*. *Phys. Rev. Lett.* **88**, 093201 (2002). doi:10.1103/PhysRevLett.88.093201.
- [78] C. A. Sackett, J. M. Gerton, M. Welling and R. G. Hulet: *Measurements of Collective Collapse in a Bose-Einstein Condensate with Attractive Interactions*. *Phys. Rev. Lett.* **82**, 876–879 (1999). doi:10.1103/PhysRevLett.82.876.
- [79] E. A. Donley, N. R. Claussen, S. L. Cornish, J. L. Roberts, E. A. Cornell and C. E. Wieman: *Dynamics of collapsing and exploding Bose-Einstein condensates*. *Nature* **412**, 295 (2001). doi:10.1038/35085500.
- [80] K. Dieckmann, R. J. C. Spreeuw, M. Weidemüller and J. T. M. Walraven: *Two-dimensional magneto-optical trap as a source of slow atoms*. *Phys. Rev. A* **58**, 3891 (1998). doi:10.1103/PhysRevA.58.3891.

- [81] G. Ferrari, M. Inguscio, W. Jastrzebski, G. Modugno, G. Roati and A. Simoni: *Collisional Properties of Ultracold K-Rb Mixtures*. Phys. Rev. Lett. **89**, 053202 (2002). doi:10.1103/PhysRevLett.89.053202.
- [82] Holger Schmaljohann: *Spindynamik in Bose-Einstein-Kondensaten*. Ph.D. thesis, Universität Hamburg (2004).
- [83] B. DeMarco, H. Rohner and D. S. Jin: *An enriched ^{40}K source for fermionic atom studies*. Rev. Sci. Instr. **70**, 1967 (1999). doi:10.1063/1.1149695.
- [84] Michael Erhard: *Experimente mit mehrkomponentigen Bose-Einstein-Kondensaten*. Ph.D. thesis, Universität Hamburg (2004).
- [85] I. Shvarchuck, K. Dieckmann, M. Zielonkowski and J. T. M. Walraven: *Broad-area diode-laser system for a Rubidium Bose-Einstein condensation experiment*. Appl. Phys. B **71**, 475–480 (2000). doi:10.1007/s003400000395.
- [86] Jürgen Fuchs: *Aufbau und Charakterisierung einer 2D und 3D magneto-optischen Fallenkombination für ^{87}Rb* . Diplomarbeit, Universität Hamburg (2004).
- [87] Wolfgang Ketterle, Kendall B. Davis, Michael A. Joffe, Alex Martin and David E. Pritchard: *High densities of cold atoms in a dark spontaneous-force optical trap*. Phys. Rev. Lett. **70**, 2253–2256 (1993). doi:10.1103/PhysRevLett.70.2253.
- [88] Robert Sylvester III Williamson: *Magneto-optical trapping of potassium isotopes*. Ph.D. thesis, University of Wisconsin-Madison (1997).
- [89] Quang-Viet Nguyen, Robert W. Dibble and Timothy Day: *High-resolution oxygen absorption spectrum obtained with an external-cavity tunable diode laser*. Optics Letters **19**, 2134–2136 (1994).
- [90] G. Ritt, G. Cennini, C. Geckeler and M. Weitz: *Laser frequency offset locking using a side of filter technique*. Appl. Phys. B **79**, 363–365 (2004). doi:10.1007/s00340-004-1559-6.
- [91] Marlon Nakat: *Kohärente Grundzustandsmanipulation von fermionischem Kalium bei hoher Teilchenzahl*. Diplomarbeit, Universität Hamburg (2004).
- [92] David E. Pritchard: *Cooling Neutral Atoms in a Magnetic Trap for Precision Spectroscopy*. Phys. Rev. Lett. **51**, 1336–1339 (1983). doi:10.1103/PhysRevLett.51.1336.
- [93] M.-O. Mewes, M. R. Andrews, N. J. van Druten, D. M. Kurn, D. S. Durfee and W. Ketterle: *Bose-Einstein Condensation in a Tightly Confining dc Magnetic Trap*. Phys. Rev. Lett. **77**, 416–419 (1996). doi:10.1103/PhysRevLett.77.416.
- [94] Lene Vestergaard Hau, B. D. Busch, Chien Liu, Zachary Dutton, Michael M. Burns and J. A. Golovchenko: *Near-resonant spatial images of confined Bose-Einstein condensates in a 4-Dee magnetic bottle*. Phys. Rev. A **58**, R54–R57 (1998). doi:10.1103/PhysRevA.58.R54.
- [95] Markus Kottke: *Magnetfallen und Signaturen der Eindimensionalität für Bose-Einstein-Kondensate*. Ph.D. thesis, Universität Hannover (2004).

- [96] Ralf Dinter: *Aufbau und Charakterisierung einer Magnetfalle zur simultanen Speicherung von ^{40}K und ^{87}Rb* . Diplomarbeit, Universität Hamburg (2004).
- [97] Markus Greiner, Olaf Mandel, Theodor W. Hänsch and Immanuel Bloch: *Collapse and revival of the matter wave field of a Bose-Einstein condensate*. *Nature* **419**, 51–54 (2002). doi:10.1038/nature00968.
- [98] Tino Weber, Jens Herbig, Michael Mark, Hanns-Christoph Nagerl and Rudolf Grimm: *Bose-Einstein Condensation of Cesium*. *Science* **299**, 232–235 (2003). doi:10.1126/science.1079699.
- [99] Manuel Succo: *Degenerate Quantum Gases in Optical Lattice Potentials*. Diplomarbeit, Universität Hamburg (2006).
- [100] Oliver Wille: *Aufbau eines 3D-optischen Gitters für quantenentartete Fermi-Bose-Mischungen aus ^{40}K und ^{87}Rb* . Diplomarbeit, Universität Hamburg (2005).
- [101] R. W. P. Drever, J. L. Hall, F. V. Kowalski, J. Hough, G. M. Ford, A. J. Munley and H. Ward: *Laser Phase and Frequency Stabilization Using an Optical Resonator*. *Appl. Phys. B* **31**, 97–105 (1983). doi:10.1007/BF00702605.
- [102] M. R. Andrews, M.-O. Mewes, N. J. van Druten, D. S. Durfee, D. M. Kurn and W. Ketterle: *Direct, Nondestructive Observation of a Bose Condensate*. *Science* **273**, 84–87 (1996). doi:10.1126/science.273.5271.84.
- [103] W. Gerlach and O. Stern: *Der experimentelle Nachweis der Richtungsquantelung im Magnetfeld*. *Zeitschrift für Physik* **9**, 349–352 (1922). doi:10.1007/BF01326983.
- [104] J. Söding, D. Guéry-Odelin, P. Desbiolles, F. Chevy, H. Inamori and J. Dalibard: *Three-body decay of a rubidium Bose-Einstein condensate*. *Appl. Phys. B* **69**, 257 (1999). doi:10.1007/s003400050805.
- [105] E. A. Burt, R. W. Ghrist, C. J. Myatt, M. J. Holland, E. A. Cornell and C. E. Wieman: *Coherence, Correlations, and Collisions: What One Learns about Bose-Einstein Condensates from Their Decay*. *Phys. Rev. Lett.* **79**, 337–340 (1997). doi:10.1103/PhysRevLett.79.337.
- [106] Sadhan K. Adhikari: *Mean-field description of a dynamical collapse of a fermionic condensate in a trapped boson-fermion mixture*. *Phys. Rev. A* **70**, 043617 (2004). doi:10.1103/PhysRevA.70.043617.
- [107] T. Karpiuk, M. Brewczyk, S. Ospelkaus-Schwarzer, K. Bongs, M. Gajda and K. Rzażewski: *Soliton Trains in Bose-Fermi Mixtures*. *Phys. Rev. Lett.* **93**, 100401 (2004). doi:10.1103/PhysRevLett.93.100401.
- [108] D. M. Jezek, M. Barranco, M. Guilleumas, R. Mayol and M. Pi: *K-Rb Fermi-Bose mixtures: Vortex states and sag*. *Phys. Rev. A* **70**, 043630 (2004). doi:10.1103/PhysRevA.70.043630.
- [109] Francesca Ferlaino, Chiara D’Errico, Giacomo Roati, Matteo Zaccanti, Massimo Inguscio, Giovanni Modugno and Andrea Simoni: *Erratum: Feshbach spectroscopy of a*

- K – Rb atomic mixture* [*Phys. Rev. A* **73**, 040702 (2006)]. *Phys. Rev. A* **74**, 039903 (2006). doi:10.1103/PhysRevA.74.039903.
- [110] L. Viverit: *Boson-induced s-wave pairing in dilute boson-fermion mixtures*. *Phys. Rev. A* **66**, 023605 (2002). doi:10.1103/PhysRevA.66.023605.
- [111] M. J. Bijlsma, B. A. Heringa and H. T. C. Stoof: *Phonon exchange in dilute Fermi-Bose mixtures: Tailoring the Fermi-Fermi interaction*. *Phys. Rev. A* **61**, 053601 (2000). doi:10.1103/PhysRevA.61.053601.
- [112] D. V. Efremov and L. Viverit: *p-wave Cooper pairing of fermions in mixtures of dilute Fermi and Bose gases*. *Phys. Rev. B* **65**, 134519 (2002). doi:10.1103/PhysRevB.65.134519.
- [113] Francesca Ferlaino, Chiara D’Errico, Giacomo Roati, Matteo Zaccanti, Massimo Inguscio, Giovanni Modugno and Andrea Simoni: *Feshbach spectroscopy of a K – Rb atomic mixture*. *Phys. Rev. A* **73**, 040702 (2006). doi:10.1103/PhysRevA.73.040702.
- [114] C. Ticknor, C. A. Regal, D. S. Jin and J. L. Bohn: *Multiplet structure of Feshbach resonances in nonzero partial waves*. *Phys. Rev. A* **69**, 042712 (2004). doi:10.1103/PhysRevA.69.042712.
- [115] C. A. Regal, C. Ticknor, J. L. Bohn and D. S. Jin: *Tuning p-Wave Interactions in an Ultracold Fermi Gas of Atoms*. *Phys. Rev. Lett.* **90**, 053201 (2003). doi:10.1103/PhysRevLett.90.053201.
- [116] C. H. Schunck, M. W. Zwierlein, C. A. Stan, S. M. F. Raupach, W. Ketterle, A. Simoni, E. Tiesinga, C. J. Williams and P. S. Julienne: *Feshbach resonances in fermionic ${}^6\text{Li}$* . *Phys. Rev. A* **71**, 045601 (2005). doi:10.1103/PhysRevA.71.045601.
- [117] J. Zhang, E. G. M. van Kempen, T. Bourdel, L. Khaykovich, J. Cubizolles, F. Chevy, M. Teichmann, L. Tarruell, S. J. J. M. F. Kokkelmans and C. Salomon: *P-wave Feshbach resonances of ultracold ${}^6\text{Li}$* . *Phys. Rev. A* **70**, 030702 (2004). doi:10.1103/PhysRevA.70.030702.
- [118] Hui Hu, Xia-Ji Liu and Michele Modugno: *Expansion of a quantum degenerate boson-fermion mixture*. *Phys. Rev. A* **67**, 063614 (2003). doi:10.1103/PhysRevA.67.063614.
- [119] D. Jaksch, C. Bruder, J. I. Cirac, C. W. Gardiner and P. Zoller: *Cold Bosonic Atoms in Optical Lattices*. *Phys. Rev. Lett.* **81**, 3108–3111 (1998). doi:10.1103/PhysRevLett.81.3108.
- [120] Markus Greiner, Olaf Mandel, Tilman Esslinger, Theodor W. Hänsch and Immanuel Bloch: *Quantum phase transition from a superfluid to a Mott insulator in a gas of ultracold atoms*. *Nature* **415**, 39–44 (2002). doi:10.1038/415039a.
- [121] M. Cramer, J. Eisert and F. Illuminati: *Inhomogeneous Atomic Bose-Fermi Mixtures in Cubic Lattices*. *Phys. Rev. Lett.* **93**, 190405 (2004). doi:10.1103/PhysRevLett.93.190405.

- [122] M. Lewenstein, L. Santos, M. A. Baranov and H. Fehrmann: *Atomic Bose-Fermi Mixtures in an Optical Lattice*. Phys. Rev. Lett. **92**, 050401 (2004). doi:10.1103/PhysRevLett.92.050401.
- [123] L. Fallani, J. E. Lye, V. Guarrera, C. Fort and M. Inguscio: *Onset of a Bose-Glass of ultracold atoms in a disordered crystal of light*. arXiv:cond-mat/0603655 (2006).
- [124] Uri Gavish and Yvan Castin: *Matter-Wave Localization in Disordered Cold Atom Lattices*. Phys. Rev. Lett. **95**, 020401 (2005). doi:10.1103/PhysRevLett.95.020401.
- [125] Fabrice Gerbier, Artur Widera, Simon Fölling, Olaf Mandel, Tatjana Gericke and Immanuel Bloch: *Phase Coherence of an Atomic Mott Insulator*. Phys. Rev. Lett. **95**, 050404 (2005). doi:10.1103/PhysRevLett.95.050404.
- [126] C. Kollath, U. Schollwöck, J. von Delft and W. Zwerger: *Spatial correlations of trapped one-dimensional bosons in an optical lattice*. Phys. Rev. A **69**, 031601 (2004). doi:10.1103/PhysRevA.69.031601.
- [127] Lode Pollet, Corinna Kollath, Ulrich Schollwoeck and Matthias Troyer: *Mixture of bosonic and spin-polarized fermionic atoms in an optical lattice*. arXiv:cond-mat/0609604 (2006).
- [128] P. B. Blakie and J. V. Porto: *Adiabatic loading of bosons into optical lattices*. Phys. Rev. A **69**, 013603 (2004). doi:10.1103/PhysRevA.69.013603.
- [129] P. B. Blakie and A. Bezett: *Adiabatic cooling of fermions in an optical lattice*. Phys. Rev. A **71**, 033616 (2005). doi:10.1103/PhysRevA.71.033616.
- [130] Ana Maria Rey, Guido Pupillo and J. V. Porto: *The role of interactions, tunneling, and harmonic confinement on the adiabatic loading of bosons in an optical lattice*. Phys. Rev. A **73**, 023608 (2006). doi:10.1103/PhysRevA.73.023608.
- [131] J. Doyle, B. Friedrich, R. V. Krems and F. Masnou-Seeuws: *Editorial: Quo vadis, cold molecules?* Eur. Phys. J. D **31**, 149 (2004). doi:10.1140/epjd/e2004-00151-x.
- [132] Axel Griesmaier, Jörg Werner, Sven Hensler, Jürgen Stuhler and Tilman Pfau: *Bose-Einstein Condensation of Chromium*. Phys. Rev. Lett. **94**, 160401 (2005). doi:10.1103/PhysRevLett.94.160401.
- [133] J. Stuhler, A. Griesmaier, T. Koch, M. Fattori, T. Pfau, S. Giovanazzi, P. Pedri and L. Santos: *Observation of Dipole-Dipole Interaction in a Degenerate Quantum Gas*. Phys. Rev. Lett. **95**, 150406 (2005). doi:10.1103/PhysRevLett.95.150406.
- [134] J. Werner, A. Griesmaier, S. Hensler, J. Stuhler, T. Pfau, A. Simoni and E. Tiesinga: *Observation of Feshbach Resonances in an Ultracold Gas of ^{52}Cr* . Phys. Rev. Lett. **94**, 183201 (2005). doi:10.1103/PhysRevLett.94.183201.
- [135] M. A. Baranov, Klaus Osterloh and M. Lewenstein: *Fractional Quantum Hall States in Ultracold Rapidly Rotating Dipolar Fermi Gases*. Phys. Rev. Lett. **94**, 070404 (2005). doi:10.1103/PhysRevLett.94.070404.

- [136] E. H. Rezayi, N. Read and N. R. Cooper: *Incompressible Liquid State of Rapidly Rotating Bosons at Filling Factor $3/2$* . Phys. Rev. Lett. **95**, 160404 (2005). doi:10.1103/PhysRevLett.95.160404.
- [137] K. Góral, L. Santos and M. Lewenstein: *Quantum Phases of Dipolar Bosons in Optical Lattices*. Phys. Rev. Lett. **88**, 170406 (2002). doi:10.1103/PhysRevLett.88.170406.
- [138] P. Pedri and L. Santos: *Two-Dimensional Bright Solitons in Dipolar Bose-Einstein Condensates*. Phys. Rev. Lett. **95**, 200404 (2005). doi:10.1103/PhysRevLett.95.200404.
- [139] P. G. H. Sandars: *The electric dipole moment of an atom*. Physics Letters **14**, 194–196 (1965). doi:10.1016/0031-9163(65)90583-4.
- [140] Jonathan D. Weinstein, Robert deCarvalho, Thierry Guillet, Bretislav Friedrich and John M. Doyle: *Magnetic trapping of calcium monohydride molecules at millikelvin temperatures*. Nature **395**, 148 (1998). doi:10.1038/25949.
- [141] Hendrick L. Bethlem, Giel Berden and Gerard Meijer: *Decelerating Neutral Dipolar Molecules*. Phys. Rev. Lett. **83**, 1558–1561 (1999). doi:10.1103/PhysRevLett.83.1558.
- [142] S. A. Rangwala, T. Junglen, T. Rieger, P. W. H. Pinkse and G. Rempe: *Continuous source of translationally cold dipolar molecules*. Phys. Rev. A **67**, 043406 (2003). doi:10.1103/PhysRevA.67.043406.
- [143] Jeremy M. Sage, Sunil Sainis, Thomas Bergeman and David DeMille: *Optical Production of Ultracold Polar Molecules*. Phys. Rev. Lett. **94**, 203001 (2005). doi:10.1103/PhysRevLett.94.203001.
- [144] Elizabeth A. Donley, Neil R. Claussen, Sarah T. Thompson and Carl E. Wieman: *Atom-molecule coherence in a Bose-Einstein condensate*. Nature **417**, 529 (2002). doi:10.1038/417529a.
- [145] D. S. Petrov, C. Salomon and G. V. Shlyapnikov: *Weakly Bound Dimers of Fermionic Atoms*. Phys. Rev. Lett. **93**, 090404 (2004). doi:10.1103/PhysRevLett.93.090404.
- [146] M. W. Zwierlein, J. R. Abo-Shaeer, A. Schirotzek, C. H. Schunck and W. Ketterle: *Vortices and superfluidity in a strongly interacting Fermi gas*. Nature **435**, 1047 (2005). doi:10.1038/nature03858.
- [147] D. M. Eagles: *Possible Pairing without Superconductivity at Low Carrier Concentrations in Bulk and Thin-Film Superconducting Semiconductors*. Phys. Rev. **186**, 456–463 (1969). doi:10.1103/PhysRev.186.456.
- [148] A. J. Leggett: *Cooper pairing in spin-polarized Fermi systems*. J. Phys. C (Paris) **41**, 19 (1980).
- [149] P. Nozières and S. Schmitt-Rink: *Bose condensation in an attractive fermion gas: From weak to strong coupling superconductivity*. Journal of Low Temperature Physics **59**, 195 (1985).
- [150] Cheng Chin, Andrew J. Kerman, Vladan Vuletic and Steven Chu: *Sensitive Detection of Cold Cesium Molecules Formed on Feshbach Resonances*. Phys. Rev. Lett. **90**, 033201 (2003). doi:10.1103/PhysRevLett.90.033201.

- [151] K. Xu, T. Mukaiyama, J. R. Abo-Shaeer, J. K. Chin, D. E. Miller and W. Ketterle: *Formation of Quantum-Degenerate Sodium Molecules*. Phys. Rev. Lett. **91**, 210402 (2003). doi:10.1103/PhysRevLett.91.210402.
- [152] Jens Herbig, Tobias Kraemer, Michael Mark, Tino Weber, Cheng Chin, Hanns-Christoph Nagerl and Rudolf Grimm: *Preparation of a Pure Molecular Quantum Gas*. Science **301**, 1510–1513 (2003). doi:10.1126/science.1088876.
- [153] Stephan Dürr, Thomas Volz, Andreas Marte and Gerhard Rempe: *Observation of Molecules Produced from a Bose-Einstein Condensate*. Phys. Rev. Lett. **92**, 020406 (2004). doi:10.1103/PhysRevLett.92.020406.
- [154] G. Thalhammer, K. Winkler, F. Lang, S. Schmid, R. Grimm and J. Hecker Denschlag: *Long-Lived Feshbach Molecules in a Three-Dimensional Optical Lattice*. Phys. Rev. Lett. **96**, 050402 (2006). doi:10.1103/PhysRevLett.96.050402.
- [155] T. Volz, N. Syassen, D. M. Bauer, E. Hansis, S. Dürr and G. Rempe: *Preparation of a quantum state with one molecule at each site of an optical lattice*. Nature Physics **2**, 692 (2006). doi:10.1038/nphys415.
- [156] Thomas Busch, Berthold-Georg Englert, Kazimierz Rzążewski and Martin Wilkens: *Two Cold Atoms in a Harmonic Trap*. Found. Phys. **28**, 549 (1998). doi:10.1023/A:1018705520999.
- [157] K. Winkler, G. Thalhammer, F. Lang, R. Grimm, J. Hecker Denschlag, A. J. Daley, A. Kantian, H. P. Büchler and P. Zoller: *Repulsively bound atom pairs in an optical lattice*. Nature **441**, 853 (2006). doi:10.1038/nature04918.
- [158] M. Greiner, C. A. Regal and D. S. Jin: *Probing the Excitation Spectrum of a Fermi Gas in the BCS-BEC Crossover Regime*. Phys. Rev. Lett. **94**, 070403 (2005). doi:10.1103/PhysRevLett.94.070403.
- [159] A. Simoni, F. Ferlaino, G. Roati, G. Modugno and M. Inguscio: *Magnetic Control of the Interaction in Ultracold K-Rb Mixtures*. Phys. Rev. Lett. **90**, 163202 (2003). doi:10.1103/PhysRevLett.90.163202.
- [160] S. B. Papp and C. E. Wieman: *Observation of Heteronuclear Feshbach Molecules from a $^{85}\text{Rb} - ^{87}\text{Rb}$ Gas*. Phys. Rev. Lett. **97**, 180404 (2006). doi:10.1103/PhysRevLett.97.180404.
- [161] Gretchen K. Campbell, Jongchul Mun, Micah Boyd, Patrick Medley, Aaron E. Leanhardt, Luis G. Marcassa, David E. Pritchard and Wolfgang Ketterle: *Imaging the Mott Insulator Shells by Using Atomic Clock Shifts*. Science **313**, 649–652 (2006). doi:10.1126/science.1130365.
- [162] D. M. Harber, H. J. Lewandowski, J. M. McGuirk and E. A. Cornell: *Effect of cold collisions on spin coherence and resonance shifts in a magnetically trapped ultracold gas*. Phys. Rev. A **66**, 053616 (2002). doi:10.1103/PhysRevA.66.053616.
- [163] Peter W. Milonni and Joseph H. Eberly: *Lasers*. Wiley Interscience (1988).

- [164] Christopher Bauer, Ray Freeman, Tom Frenkiel, James Keeler and A. J. Shaka: *Gaussian Pulses*. Journal of Magnetic Resonance **58**, 442 (1983).
- [165] Belén Paredes, Artur Widera, Valentin Murg, Olaf Mandel, Simon Fölling, Ignacio Cirac, Gora V. Shlyapnikov, Theodor W. Hänsch and Immanuel Bloch: *Tonks-Girardeau gas of ultracold atoms in an optical lattice*. Nature **429**, 277–281 (2004). doi:10.1038/nature02530.
- [166] Toshiya Kinoshita, Trevor Wenger and David S. Weiss: *Observation of a One-Dimensional Tonks-Girardeau Gas*. Science **305**, 1125–1128 (2004). doi:10.1126/science.1100700.
- [167] M. Girardeau: *Relationship between systems of impenetrable bosons and fermions in one dimension*. J. Math. Phys. **1**, 516–523 (1960).
- [168] Lewi Tonks: *The Complete Equation of State of One, Two and Three-Dimensional Gases of Hard Elastic Spheres*. Phys. Rev. **50**, 955–963 (1936). doi:10.1103/PhysRev.50.955.
- [169] Elliott H. Lieb and Werner Liniger: *Exact Analysis of an Interacting Bose Gas. I. The General Solution and the Ground State*. Phys. Rev. **130**, 1605–1616 (1963). doi:10.1103/PhysRev.130.1605.
- [170] Adilet Imambekov and Eugene Demler: *Exactly solvable case of a one-dimensional Bose-Fermi mixture*. Phys. Rev. A **73**, 021602 (2006). doi:10.1103/PhysRevA.73.021602.
- [171] L. Mathey, D.-W. Wang, W. Hofstetter, M. D. Lukin and Eugene Demler: *Luttinger Liquid of Polarons in One-Dimensional Boson-Fermion Mixtures*. Phys. Rev. Lett. **93**, 120404 (2004). doi:10.1103/PhysRevLett.93.120404.
- [172] A. Micheli, G. K. Brennen and P. Zoller: *A toolbox for lattice-spin models with polar molecules*. Nature Physics **2**, 341 – 347 (2006). doi:10.1038/nphys287.
- [173] Leif Humbert: *Untersuchung und Manipulation von Quantengasmischungen aus ^{40}K und ^{87}Rb* . Diplomarbeit, Universität Hamburg (2006).
- [174] E. Arimondo, M. Inguscio and P. Violino: *Experimental determinations of the hyperfine structure in the alkali atoms*. Rev. Mod. Phys. **49**, 31–75 (1977). doi:10.1103/RevModPhys.49.31.
- [175] S. Burger, F. S. Cataliotti, C. Fort, F. Minardi, M. Inguscio, M. L. Chiofalo and M. P. Tosi: *Superfluid and Dissipative Dynamics of a Bose-Einstein Condensate in a Periodic Optical Potential*. Phys. Rev. Lett. **86**, 4447–4450 (2001). doi:10.1103/PhysRevLett.86.4447.
- [176] L. S. Ma, P. Jungner, J. Ye and J. L. Hall: *Delivering the same optical frequency at two places: accurate cancellation of phase noise introduced by optical fiber or other time-varying path*. Optics Letters **19**, 1777 (1994).
- [177] P. S. Jessen and I. H. Deutsch: *Optical lattices*. In B. Bederson and H. Walther, editors, *Advances in Atomic, Molecular, and Optical Physics*, volume 37, page 95 (1996).

- [178] Markus Greiner: *Ultracold quantum gases in three-dimensional optical lattice potentials*. Ph.D. thesis, Ludwig-Maximilians-Universität München (2003).
- [179] Jun Ye, Jin-Long Peng, R. Jason Jones, Kevin W. Holman, John L. Hall, David J. Jones, Scott A. Diddams, John Kitching, Sebastien Bize, James C. Bergquist, Leo W. Hollberg, Lennart Robertsson and Long-Sheng Ma: *Delivery of high-stability optical and microwave frequency standards over an optical fiber network*. J. Opt. Soc. Am. B **20**, 1459–1467 (2003).
- [180] M. Eichenseer, J. von Zanthier and H. Walther: *Common-mode-free frequency comparison of lasers with relative frequency stability at the millihertz level*. Optics Letters **30**, 1662–1664 (2005).
- [181] S. Tung, V. Schweikhard and E. A. Cornell: *Observation of Vortex Pinning in Bose-Einstein Condensates*. arXiv:cond-mat/0607697 (2006).
- [182] Stefan Schmid, Gregor Thalhammer, Klaus Winkler, Florian Lang and Johannes Hecker Denschlag: *Long distance transport of ultracold atoms using a 1D optical lattice*. New Journal of Physics **8**, 159 (2006). doi:10.1088/1367-2630/8/8/159.
- [183] Allan J. MacLeod: *Accurate and efficient computation of the Bose-Einstein functions $g(3/2)$ and $g(5/2)$* . Computers in Physics **11**, 385–387 (1997).
- [184] Allan J. MacLeod: *Fermi-Dirac functions of orders $-1/2$, $1/2$, $3/2$, and $5/2$* . ACM Trans. Math. Soft. **24**, 1–12 (1998).

List of publications

This thesis has partly been published in the following research publications:

1. C. Ospelkaus, S. Ospelkaus, L. Humbert, P. Ernst, K. Sengstock, and K. Bongs: *Ultracold Heteronuclear Molecules in a 3D Optical Lattice*. Phys. Rev. Lett. **97**, 120402 (2006) [1].
2. S. Ospelkaus, C. Ospelkaus, L. Humbert, K. Sengstock, and K. Bongs: *Tuning of Heteronuclear Interactions in a Degenerate Fermi-Bose Mixture*. Phys. Rev. Lett. **97**, 120403 (2006) [2].
3. S. Ospelkaus, C. Ospelkaus, R. Dinter, J. Fuchs, M. Nakat, K. Sengstock and K. Bongs: *Degenerate K-Rb Fermi-Bose gas mixtures with large particle numbers*. Journal of Modern Optics, advanced online publication (2006) [5].
4. S. Ospelkaus, C. Ospelkaus, O. Wille, M. Succo, P. Ernst, K. Sengstock, and K. Bongs: *Localization of Bosonic Atoms by Fermionic Impurities in a Three-Dimensional Optical Lattice*. Phys. Rev. Lett. **96**, 180403 (2006) [3].
5. C. Ospelkaus, S. Ospelkaus, K. Sengstock, and K. Bongs: *Interaction-Driven Dynamics of ^{40}K - ^{87}Rb Fermion-Boson Gas Mixtures in the Large-Particle-Number Limit*. Phys. Rev. Lett. **96**, 020401 (2006) [4].